The Manufacture and Mechanical Properties of Poly(ethylene terephthalate) Fibers filled with Organically Modified Montmorillonite

David W. Litchfield

Dissertation submitted to the Faculty of
Virginia Polytechnic Institute and State University
In partial fulfillment of the requirements for the degree of

DOCTOR OF PHILOSOPHY
in
Chemical Engineering

Dr. Donald G. Baird, Chairman
Dr. Richey M. Davis
Dr. John J. Lesko
Dr. John Y. Walz
Dr. Garth L. Wilkes

April 21, 2008
Blacksburg, VA

Keywords: nanocomposites, fiber spinning, fiber drawing, morphology, orientation, drawability

The Manufacture and Mechanical Properties of Poly(ethylene terephthalate) Fibers filled with Organically Modified Montmorillonite

David W. Litchfield

ABSTRACT

This work is concerned with mechanical property improvements to poly(ethylene terephthalate), PET, fibers by the addition of layered silicate nanoparticles and by drawing the un-oriented nanocomposite filaments in a second step. No previous studies on PET fibers filled with montmorillonite (MMT) nanoclay examined fiber drawability at temperatures above the glass transition. Therefore, the primary objective of this research was to determine 1) if PET nanocomposite fibers could be drawn to finer diameters and 2) whether drawing imparted improved Young's modulus and tenacity (i.e. strength) relative to un-filled PET fibers. Of equal importance to this work, the subsequent objective was to discern and understand the role of nanoclay in 1) the production of improved or reduced mechanical properties and 2) the ability to draw PET to lower or higher than normal draw ratios.

In the first part of this thesis, the improvements in Young's modulus and tenacity of PET fibers filled with various types of organically modified montmorillonite is shown and the method to produce them is discussed. Greater improvements in mechanical properties occurred when the MMT stacks were intercalated with PET. A nominal 1 wt% loading of dimethyl-dehydrogenated tallow quaternary ammonium surface modified

MMT in drawn PET fiber showed a 28% and 63% increase in Young's modulus and strength, respectively. Relative to an un-filled PET fiber, these results exceeded the upper-bound of the rule of mixtures estimate. Therefore, both the type of surface modification and concentration of MMT were shown to affect the degree of PET orientation and crystallinity. Furthermore, drawability above T_g and elongation-at-break increased upon the addition of organically modified MMT to un-oriented PET fibers, which was a key distinction of this work from others examining similar systems.

Interestingly, the mechanical properties of modulus and tenacity showed a maximum with concentration of alkyl modified clay, but drawability did not show significant variation with increasing nanoclay content. Thermal analysis and Raman spectroscopy was used to examine the role of nanoclay in creating this maximum in mechanical properties. At low loadings, nanoclay was shown to intercalate with PET and enhance amorphous orientation. At higher concentrations of nanoclay the presence of large agglomerates prevented efficient orientation to the fiber axis and acted as stress concentrators to aid in cavitation and failure during testing. Raman spectroscopy showed that the as-spun unfilled PET fibers possessed significantly more trans conformer content of the ethylene glycol moiety than the nanocomposite fibers. The greater gauche content of the nanocomposite fibers delayed crystalline development during non-isothermal DSC scans to higher temperatures was associated with the increased drawability.

Acknowledgements

The author wishes to thank Dr. Donald G. Baird for his support, guidance, and confidence in me, the result of which has lead to the completion of this dissertation. The author sincerely thanks the unwavering patience and enthusiasm of Performance Fibers Inc. and particularly Dr. Peter B. Rim, who approved the funding of this work and our continued efforts. In addition, the author wishes to thank his committee members for their guidance: Dr. Garth Wilkes, Dr. Jack Lesko, Dr. Richey Davis, and Dr. John Walz.

The author wishes to thank the following people:

- First and foremost his love and soon to be wife, Lindsey for her enthusiastic support.
- His parents for their love and who shared with me their experiences of graduate school and kept things in perspective.
- His brother for his example of character, advice, guidance, humor, and beach house that made the few days of time off immeasurably enjoyable, especially when installing the weed barrier.
- All the members of the Polymer Processing Lab (PPL) past and present whose antics and advice have helped the time pass: Chris, Aaron, Brent, Chris, Joe, Dave, Desmond, Gregorio, Myoungbae, Jianhua, Quang, Matt, and Wade.
- Phil for his peer pressure and perspectives on life and swimming.

- The old guy crew at War Memorial Pool: Dr. Westman, Dr. Hicks, Dr. Riley, Dr. Eick, Dr. Peairs, Dr. Lesko, Dr. Roy and Fred, for the bi-daily escape from the mundane routine.
- To those in the Department of Chemical Engineering that have made the accomplishment of this feat easier: Diane, Chris, Amanda, Riley, and Mike (to whom I must also thank for the trout fishing tips.)
- And everyone else that has shown me support, which is a list too long to detail in full.

Original Contributions

The following are considered to be significant original contribution of this research:

- A method for producing PET nanocomposite fibers, using montmorillonite nanoparticles, with improved drawability and drawn fiber mechanical properties was established.

- It was demonstrated that solid state polymerization of the PET nanocomposite resins filled with various nanoclays of different surface modifications was a) possible and b) increased the thermal stability of the PET matrix during further melt processing steps.

- Mechanical properties of drawn PET fibers were reported as a function of both nanoclay concentration and surface modification type (i.e. none, polar, or non-polar).

- The role of nanoclay in the development of mechanical property improvements and reductions relative to un-filled PET fibers was disclosed. By Raman spectroscopy, the first measurements of the effect of nanoclay on the average PET chain and crystal orientations were made on drawn fibers. It was shown that the presence of nanoclay led to greater gauche content in as-spun PET, and that this larger amorphous phase improved the drawability of the PET chains.

Format of Dissertation

This dissertation is written in journal format. Chapters 3 and 4 are self contained papers that separately describe the experiments, results, and conclusions relative to each chapter. With the exception of the literature review, the figures and tables are inserted after the reference section of each chapter.

Table of Contents

1 Introduction……..……..……1

1.1 References……..……9

2 Literature Review……10

2.1 The Rheology of High Aspect Ratio Nano-particle Filled Liquids…..…….10

2.1.1 Abstract……...11

2.1.2 Introduction to Nanocomposite Rheology…….…….12

2.1.3 Structure and Properties of Nanoparticles…….…….15

2.1.3.1 Nanoclays…… 15

2.1.3.2 Carbon Nanotubes (CNT) and Nanofibers (CNF)……18

2.1.3.3 Particle Surface Treatments……..21

2.1.3.4 Other Nanoparticles……..22

2.1.4 Rheology of Nanoparticle Suspensions in Low Molecular Weight Liquids…….23

2.1.4.1 Layered-Silicate Suspensions……...26

2.1.4.2 Thermosetting Layered-Silicate Nanocomposites, Newtonian Precursors……..32

2.1.4.3 Nano-Fibrous Suspensions……...34

2.1.5 Rheology of Nanoparticle Filled Polymer Liquids…….....38

2.1.5.1 Polymer Layered-Silicate Nanocomposites…….38

2.1.5.1.1 Dynamic Storage Modulus in Linear and Nonlinear Oscillatory Shear…….39

2.1.5.1.2 Shear Thinning and Yield Stress Behavior……..48

2.1.5.1.3 Thermal Effects on Viscoelasticity in Nanoclay Polymer Composites……55

2.1.5.1.4 Transient Rheology……..57

2.1.5.1.5 Normal Stresses and Flow Phenomena……61

2.1.5.1.6 Extensional Rheology……..66

2.1.5.2 Rheology of CNT and CNF Polymer Nanocomposites……...69

2.1.5.2.1 Dynamic Oscillatory Shear Measurements……..69

2.1.5.2.2 Normal Stress Difference and Elastic Effects……..74

2.1.6 Constitutive Theories for Nanoparticle filled Polymer Melts…….76

2.1.6.1 Rheology and Structure……. ..76

2.1.6.2 Modeling the Rheology……79

2.1.7 Summary of the Rheology of High Aspect Ratio Nanoparticle Filled Liquids……..86

2.2 Fiber Spinning and Processing of PET and PET Nanocomposite Fibers……..87

2.2.1 The Synthesis of PET Nanocomposites…….88

2.2.1.1 In-situ Intercalative Polymerization Methods……..89

2.2.1.2 Melt Intercalation Methods……..91

2.2.1.3 The Effect of sc-CO_2 on Nanoparticle Dispersion in Thermoplastic Matrices……96

2.2.1.4 The Effect of Nanofiller on Solid State Polymerization……..98

2.2.2 Post-processing of PET-nanocomposite Fibers……103

2.2.2.1 Fiber Drawing Methods for Increased Tensile Properties……..103

2.2.2.1.1 Drawing Processes……..103

2.2.2.1.2 Drawing Aids for Higher Orientation…….115

2.2.2.2 The Effect of Nanoparticles on Crystallinity and Related Thermal Behaviors……..116

2.3 Mechanical Property Improvements of PET and Related Step-Growth Polymer Nanocomposites……..126

2.3.1 Predicting the Moduli of Polymer Nanocomposites by Composite Theory……..128

2.3.2 Examination of the Factors Leading to Property Improvement of PET Nanocomposites……...138

2.3.2.1 The Effect of Mineral Filler Type……...139

2.3.2.2 The Effect of Particle Concentration……...141

2.3.2.3 The Effect of Particle Surface Treatment……142

2.3.2.4 The Effect of Compatibilizers…….143

2.3.2.5 The Effect of Spinning Speed……..145

2.3.2.6 Conclusions on Modulus and Tenacity Improvements……152

2.4 References……154

3.0 Improved Mechanical Properties of PET Nanocomposite Fibers……165

Abstract…….……...165

3.1 Introduction ……..…….……...……166

3.2 Experimental….…….……..……...170

3.2.1 Materials….……..……..170

3.2.2 Melt Compounding……..……171

3.2.3 Solid State Polymerization, SSP…….……171

3.2.4 Fiber Spinning……172

3.2.5 Fiber Drawing…..……..…….173

3.2.6 Characterization…….…….173

3.3 Results and Discussion…….…….…..175

3.3.1 General Features of Solid State Polymerization of

PET Nanocomposites……..……...175

3.3.2 Morphological Characterization of Nanoparticle Dispersion….……179

3.3.3 Mechanical Properties of Solid Stated PET

Nanocomposite Melt-Spun Fibers…….……182

3.4 Conclusions……..……..188

Acknowledgements……189

3.5 References……190

4.0 The Role of Nano-clay in the Generation of Poly(ethylene terephthalate) Fibers with Improved Modulus and Tenacity ……..208

Abstract……..208

4.1 Introduction……...209

4.2 Experimental…….……213

4.2.1 Materials…….…….…….213

4.2.2 Melt-Compounding, Fiber Spinning, and Fiber Drawing…….……..…213

4.2.3 Characterization……..214

4.3 Results and Discussion…….216

4.3.1 Nanoparticle Morphology……216

4.3.2 Thermal Behaviors …….…….218

4.3.3 Molecular Orientation and Mechanical Property Improvement…..……..222

4.3.4 Molecular Conformation and Drawability Improvement…….……226

4.4 Conclusions ……..…..…….230

4.5 References……..……233

5.0 Recommendations…….254

5.1 The use of dispersion agents such as super-critical carbon dioxide to improve the degree of nanoclay exfoliation in the PET matrix.……..…….….254

5.2 The use of rod-like carbon nanofibers and nanotubes in replacement of disk-shaped layered silicate nanoclays.…….……....259

5.3 Simulation of the melt spinning dynamics of nanoparticle filled viscous poly-condensate polymers. ……262

5.4 References……..265

Appendix A. Materials and Methods Summary……266

Appendix B. Rheological data……..273

Appendix C. Thermal Analysis…….……311

Appendix D. Raman Spectroscopy…….……..316

Appendix E. Nanocomposite Fiber Morphology…….…….335

List of Figures

Chapter 1

Figure 1.1. Schematic representation of montmorillonite type layered silicates, adapted from van Olphen [8]……..……...2

Figure 1.2. Schematic illustration of two morphologies expected of layered-silicate dispersed in a polymer matrix: (a) intercalated some particle-particle interactions persist, (b) exfoliated, only particle polymer interactions giving the highest aspect ratio per particle volume……...……..3

Figure 1.3. Schematic of the effect of particulate size on filament formation……4

Chapter 2

Figure 2.1. Schematic representation of layered silicates of the 2:1 phyllosilicate or smectite group. Lines are not scale representations of covalent bonds [11]……..17

Figure 2.2. Schematic illustrations of two types of polymer-layered silicate morphologies: (a) intercalated, (b) flocculated edge-edge interactions between platelets, and (c) exfoliated [12]……18

Figure 2.3. The effect of CNF concentration on the relative viscosity of 90% glycerol/water and the prediction accuracy of the semi-empirical Kreiger-Dougherty (K-D) equation over the hydrodynamic based Einstein-Bachelor (E-B) equation [39]……...……..26

Figure 2.4. Schematic of creep and recovery results of a 4 wt% nanoclay suspension from Zong and Wang [45]. The curves show creep compliance and viscosity of suspension as a function of silicate loading. The nanoclay modifier used in this case is dehydrogenated tallow quaternarty ammonium chloride…….28

Figure 2.5. Schematic of nanoclay platelet mesostructures adapted from Pignon et al. [50] and Luckham and Rossi [5]. a – the percolation of platelet clusters under rest; b – upon deformation rodlike aggregates form along the direction of the velocity gradient; c – under further deformation the aggregates break up into individual clusters; d – exfoliated platelets; e – face-to-face aggregates; f – face-to-face “band-like” aggregates to form a network; g – edge-to-face percolated network; h – edge-to-edge “house of cards” percolated network structure…….30

Figure 2.6. Complex viscosity of a 10 wt% nanoclay/epoxy suspension showing the significant effect surface treatment on favorable interactions [57]……..……..33

Figure 2.7. Storage and Loss Moduli as a function of angular frequency at 1% strain and for various CNT loadings, adapted from [61] Dashed lines – G'', solid lines – G'……36

Figure 2.8. Viscosity and primary normal stress difference as a function of steady shear rate in a cone-plate rheometer for a 3.5 wt% single-walled nanotube suspension in 102% H_2SO_4. The authors draw the similarity to the triple zone LCP behavior [66]…….……37

Figure 2.9. Role of polymer molecular weight on the G'. of melt intercalated 3 wt% hydroxyl modified nanoclay/nylon 6 composites. T = 240C, HMW ~ 30K, MMW ~ 22K, LMW ~ 16K. [76]…….……41

Figure 2.10. G' as a function of angular frequency for various PC and nanoclay (NC) composites as evidence of molecular weight loss, either by chain scission or depletion of continuous phase [82]……43

Figure 2.11. Effect of ternary compatibilizer on tallow modified nanoclay/PP composites, showing a maximum in G' with maleic anhydride concentration at low frequencies [95]……...……..45

Figure 2.12. Effect of preshear on storage and loss moduli of (top) a 4 wt% hydroxyl modified nanoclay/PBT and (bot) 4 wt% hydroxyl-modified-nanoclay/ 4 wt% epoxy/ PBT composites [85]……..47

Figure 2.13. Failure of the Cox-Merz relation and the increased onset of shear thinning for three different molecular weights of nylon 6 and its nanocomposite of 3 wt% hydroxyl modified nanoclay [76]…….…….….51

Figure 2.14. Decrease in apparent steady shear viscosity from capillary data on a acrylonitrile (34%) butadiene rubber (NBR) and its nanocomposite with unmodified (N4) and alkyl modified (OC4) nanoclays [76,115]……..52

Figure 2.15. Relative viscosity and glass transition temperature as a function of filler mass fraction, for tightly crosslinked PS nanoparticles in a linear PS matrix [128]……...……53

Figure 2.16. Yield stress as a function of clay loading and (inset) the correlation of experiment data to Casson's equation, for a PS-PI block copolymer. Yield stresses indicate the presence of solid-like behavior and some microstructural order [108]…….……..55

Figure 2.17. (Top) Low strain relaxation modulus $G(t)$ as a function of clay loading, line represents the fit to calculated relaxation spectra (Bottom) Characteristic damping

function as a function of clay loading, line represents fit to PSM damping model [103]……...……58

Figure 2.18. Magnitude of stress overshoot (represented as the difference between the peak stress and steady stress values) as functions of rest time (time allotment for structural reformation) and clay loading in PP/MAH matrix [89]…….……59

Figure 2.19. Stress-strain scaling of stress overshoot upon inception of steady shear flow for alkyl modified nanoclay/maleic anhydride/ PP composite.[89]…….……..61

Figure 2.20. Primary normal stress difference as functions of shear stress and organoclay (NC) content in EVA nanocomposites [101]……..……...63

Figure 2.21. Suppression of critical shear rate for the onset of melt fracture for a pure PP melt, a 0.1 wt% and 0.5 wt% onium ion modified nanoclay/PP composite [97]…….……65

Figure 2.22. Extensional viscosity as a function of Hencky strain for 8wt% nanoclay (MMT) and fluorohectorite (FH) suspensions in a 50/50 copolymer of PMMA and PMAA [102]. In terms of size: FH >> MMT……..……..68

Figure 2.23. Extensional viscosity as function of Hencky strain and nanoclay loading for an alkyl ammonium modified clay melt blended with EVA [101]…….…….…….69

Figure 2.24. (Top) Electrical conductivity and inverse loss tangent, expressed as G'/G'', as a function of CNT volume fraction in a PP matrix. (Bottom) G' as a function of angular frequency and CNT loading (vol%) melt blended with PP [137]……..…….71

Figure 2.25. Negative normal stress difference from parallel plate rheometry ($\Delta N = N_1 - N_2$, where N_1 was deemed the more negative quantity) as a function of nanotube (NT) loading melt blended with PP [137]…….…..75

Figure 2.26. Schematic from Sarvestani and Picu [155]. The polymers bridge, loop, and dangle as they come in contact with and adsorb on to the nanoparticles……..85

Figure 2.27. Schematic of crosslinking and possible branching reactions of PET to the silanol surface (hydroxyl groups) of nanosilicates [187, 190]…….102

Figure 2.28. True stress as a function of draw ratio, λ, at two strain rates and draw temperature of 90 °C [193]…….….106

Figure 2.29. Schematic diagram of a proposed mechanism for the extension of PET under high stress [194]……..…….……..107

Figure 2.30. General stress as a function of draw ratio, strain, for an amorphous unoriented polymer [191]……108

Figure 2.31. Schematic representations of commercially viable constant force drawing mechanisms. The bottom diagram shows a three step draw-annealing process with heat conduction to the fiber by a fluid medium……...……109

Figure 2.32. The effect of applied force on the rate of deformation of PET film drawn above the T_g (80 °C): (a) 1.5, (b) 3.8, (c) 5.0, (d) 6.3, (e) 7.5, (f) 10.5 MPa [200]…….110

Figure 2.33. Schematic diagram of zone drawing/annealing deformation versus hot draw deformation of a polymer film…….112

Figure 2.34. The "split billet" assemblies for solid state co-extrusion of films (top) and fibers (bottom), note the required taper to fit the conical die……..……114

Figure 2.35. Schematic of the influence of strain-rate, temperature, or molecular weight on the crystalline content during a constant rate of extension draw of PET [191]……..……119

Figure 2.36. Volume fraction of crystal content as a function of draw ratio for PET film drawn at 90°C at constant force (A) with an average strain rate of 5 s^{-1}, at constant extension rate (B and C) with strain rates of 0.42 s^{-1} and 0.042 s^{-1} respectively……..…….120

Figure 2.37. Schematic representation of the predominance of the γ-crystalline phase due to increased hydrogen bonding of the amide linkages to the silicate surface for nylon 6 nanocomposites depicting epitaxial crystallization, adapted from [242]…….122

Chapter 3

Fig. 3.1. Complex viscosity, $|\eta^*|$ vs. frequency, ω for the melt-compounded Cloisite 30B nanocomposites before SSP……..……..193

Fig. 3.2. Molecular weight as a function of solid stating time for a nominal loading 3 wt% of various nanoclays……195

Fig. 3.3. Relative complex viscosity loss as a function of time for the Cloisite 30B series of nanocomposites with and without SSP……..……..196

Fig. 3.4. Relative complex viscosity loss as a function of time for the Cloisite 20A series of nanocomposites with and without SSP……..……..197

Fig. 3.5. (Left axis) complex viscosity, |η*| vs. frequency, ω for the melt-compounded Cloisite 30B nanocomposites after SSP and (right axis) experiment time elapsed for measurement of the respective data points……..……198

Fig. 3.6. (Left axis) storage modulus, G' vs. frequency, ω for the melt-compounded Cloisite 30B nanocomposites after SSP and (right axis) experiment time elapsed for measurement of the respective data points……199

Fig. 3.7. X-ray diffraction spectra for a representative 3 wt% loading of Cloisite 20A in PET as a function of SSP time, scaled for clarity. Inset: XRD spectra of pure Cloisite 20A…….200

Fig. 3.8. XRD patterns for the as-spun, un-oriented nanocomposite fibers at 1 and 3 wt% loadings of various nanoclays, scaled for clarity. Inset: XRD spectra of the pure nanoclays Cloisite 30B, 20A, and Na^+ as references for determining intercalation…..201

Fig. 3.9. XRD patterns for the drawn nanocomposite fibers at various loadings of Cloisite 20A, scaled for clarity……202

Fig. 3.10. Young's modulus of the drawn nanocomposite fibers as a function of nanoclay loading weight % for the different nanoclay surface treatments compared to a simple rule of mixtures estimate……205

Fig. 3.11. Drawn fiber strength at maximum load versus nanoclay concentration in weight % for the various nanoclay surface treatments…..…….206

Fig. 3.12. True stress versus draw ratio of pure PET and a 1 wt% loading of Cloisite 20A at a draw temperature of 85 °C……207

Chapter 4

Fig. 4.1 XRD for the as-spun nanocomposite fibers (a) pure PET, (b) 0.5 wt% 20A, (c) 1 wt% 20A, (d) 1.5 wt% 20A, (e) 3 wt% 20A. Inset – pure Cloisite 20A nanoclay……237

Fig. 4.2. XRD for the drawn nanocomposite fibers (a) pure PET, (b) 0.5 wt% 20A, (c) 1 wt% 20A, (d) 1.5 wt% 20A, (e) 3 wt% 20A……..238

Fig. 4.3. SEM images of large agglomerates in the as-spun (a) and drawn (b) 3 wt% 20A nanocomposite fiber and a smooth section (c) of the drawn fiber……..239

Fig. 4.4. Cooling from the melt at 20 °C/min, heat flow as a function of temperature for various nanoclay concentrations…….240

Fig. 4.5. Complex viscosity as a function of temperature for the PET nanocomposite chips cooled at 40 °C/min, 100 rad/s, under nitrogen…….241

.
Fig. 4.6. Cooling from the melt at 20° C/min, non-isothermal crystallization, X, as a function of time for various nanoclay loadings…..……242

Fig. 4.7. 1st Heating of the as-spun nanocomposite fibers at 20 °C/min, heat flow as a function of temperature for various nanoclay loadings (scaled for clarity)……..…243

Fig. 4.8. 1st Heating of the as-spun nanocomposite fibers at 20 °C/min, non-isothermal crystallization, X, as a function of time for various nanoclay loadings……244

Fig. 4.9. 1st and 2nd Heating of the as-spun nanocomposite fibers at 20 °C/min, heat flow as a function of temperature for various nanoclay concentrations……245

Fig. 4.10. Thermal shrinkage in % of the drawn nanocomposite fibers at 177 °C…..247

Fig. 4.11. Raman spectra of as-spun fibers of Pure PET (a), 1 wt% 20A (b), and 3wt% 20A (c) with the fiber samples parallel to the vector of polarized light…….248

Fig. 4.12. Raman Spectra of parallel and perpendicular arrangements of the wt% 20A as-spun and drawn fibers (a) parallel spectra of drawn 1 wt% 20A, (b) perpendicular spectrum of drawn 1 wt% 20A, (c) parallel spectra of as-spun 1 wt% 20A, (d) perpendicular spectrum of as-spun 1 wt% 20A……..250

Fig. 4.13. Molecular orientation factor of the PET backbone (–C–C– stretch at 1616 cm^{-1}), f_{1616}, for the as-spun and drawn nanocomposite fibers and the orientation of the ethylene glycol units (stretch at 998 cm^{-1}), f_{998} for the drawn case only……251

Fig. 4.14. 1727 cm^{-1} band as a function of nanoclay loading in the as-spun and drawn states, (a) Pure PET, (b) 1 wt% 20A, (c) 3 wt% 20A…….252

Fig. 4.15. Raman spectrum from 720-1550 cm^{-1} for the as-spun nanocomposite fibers, (a) pure PET, (b) 0.5 wt% 20A, (c) 1 wt% 20A, (d) 1.5 wt% 20A, (e) 3 wt% 20A……253

List of Tables

Chapter 1

Table 1.1. Typical properties of fibers melt spun commodity fibers versus solution spun engineering fibers [10]…….6

Chapter 2

Table 2.1. Effect of unmodified and surface treated (modified) nanoclay (NC) on the extrudate swell response from a capillary at constant shear rate given in the reference…….64

Table 2.2. Tensile properties of zone drawn and zone annealed PET film…….……...……112

Chapter 3

Table 3.1. Zero shear viscosity reduction of the PET matrix as a function of nanoclay surfactant and particle concentration……194

Table 3.2. Tensile properties of as-spun (un-oriented) PET/MMT nanocomposite fibers with true clay content and molecular weight by intrinsic viscosity……..203

Table 3.3. Tensile properties of oriented PET/MMT nanocomposite fibers drawn in a second step above Tg…….204

Chapter 4

Table 4.1. Tensile properties of as-spun (un-oriented) PET/MMT nanocomposite fibers with true clay content and molecular weight by intrinsic viscosity……..……..236

Table 4.2. PET nanocomposite fiber crystallinity, X_c, from DSC heating scans at 20 °C/min…….246

Table 4.3. Raman Bands of Interest for Semicrystalline PET and Montmorillonite….249

1 Introduction

Although mixing a rigid anisotropic filler into a soft isotropic matrix was a concept known by the ancients, the addition of rigid nanometer scale mineral particles to a polymer melt has been a subject of interest for only the past 15 years. Specifically, research efforts directed toward forming nanocomposite fibers, a subset of the materials mentioned above, have occurred relatively recently, within the past four years. Complete knowledge of these materials is years away with the current science of nanocomposite polymeric fibers slowly blossoming into a field of intense discovery. This section will introduce the subject of polyester layered silicate nanocomposites and the aspects of these materials that are to date relatively unknown. It is the goal of this study to fill the dearth of understanding of the properties of polyester nanocomposite fibers and the role of nano-fillers in the manufacturing process.

It can be argued as to who discovered the first polymer layered silicate nanocomposites [1-3], but current opinion holds the Toyota research group [4,5] accountable for the first successful breakthroughs in this area of composite science. The Toyota research group is credited with successfully preparing the first exfoliated nylon-6 layered silicate nanocomposites from the *in-situ* polymerization of organically modified montmorillonite in ε-caprolactam. The synthesized nanocomposites showed exceedingly high thermo-mechanical properties at particle volume loadings much less than that exhibited by conventionally filled polymer matrices. In the years to follow, many research groups have experimented with developing layered silicate nanocomposites with

nearly every polymer matrix available [6,7]. Yet, nylon-6 nanocomposites have shown the best exfoliation results, while most other matrices have yielded an intercalated morphology. Theoretically, the more homogenous the dispersion of single platelets in the polymer matrix the better the exfoliation of platelet galleries, and in turn the greater the property improvement in strength and modulus can be expected.

Figure 1.1 shows the chemical structure of a model layered silicate such as montmorillonite, and Figure 1.2 shows the two morphologies expected of polymer nanocomposites (neglecting the completely phase separated system). The interlamellar space in figure 1.1 is naturally occupied by Na^+ ions but these ions can be displaced by quaternary-ammonium surfactants to expand the distance between silicate sheets. This organic modification allows for more favorable interactions between inorganic nanoparticle and organic polymer. The stack height, or the thickness of a single sheet is roughly 1 nm, where the length and width dimensions can range between 50 and 300 nm.

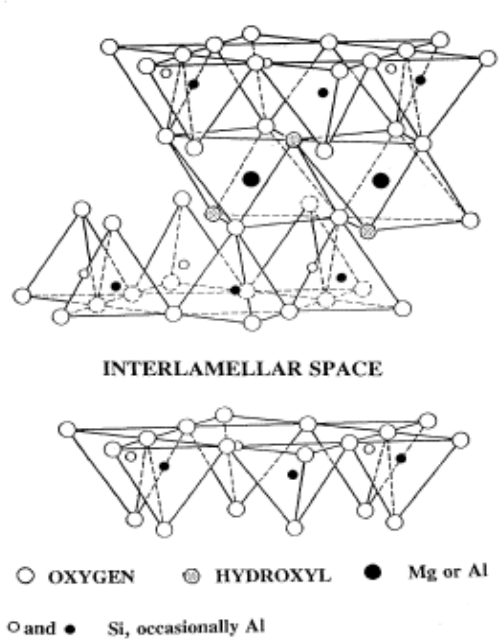

Figure 1.1. Schematic representation of montmorillonite type layered silicates, adapted from van Olphen [8].

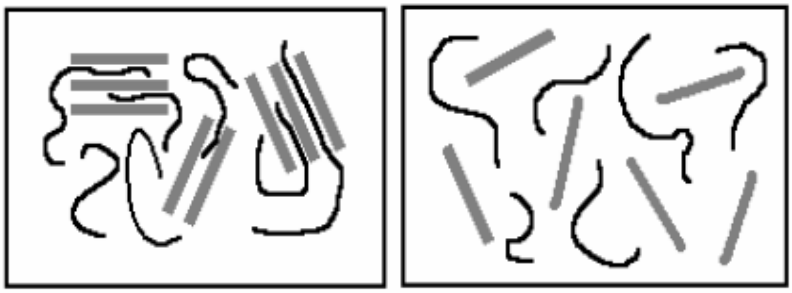

a. b.

Figure 1.2. Schematic illustration of two morphologies expected of layered-silicate dispersed in a polymer matrix: (a) intercalated some particle-particle interactions persist, (b) exfoliated, only particle polymer interactions giving the highest aspect ratio per particle volume.

However, the benefits of nano-fillers have been exploited to fulfill the demands of injection molded articles. The particular benefit to crystal nucleation rates that layered silicate induce allows for more dimensional stability to be imparted to the part, which boosts turnover times in the injection molding process. Although injection molding is an operation crucial to polymer processing, fiber spinning is of equal significance but has received less attention as a process to form polymer layered silicate nanocomposites. Nanocomposite fibers have possibly been neglected because of the relative unfamiliarity of the industry to inorganically filled fibers, whereas the injection molding industry has been filling polymers with glasses and other particles for many years. The polyester fibers industry is obsessed with product purity, and spin-packs consisting of filter media are typically used to remove dust particles and gel-like polymer agglomerates, such that the extruded filament of micrometer diameter can be effectively taken-up. In the conventional filler sense, in which these particles are on the order of magnitude as the thickness of the filament, the composite can not be processed too quickly or cohesive fracture will occur in the spin-line. Figure 1.3 illustrates this phenomenon schematically.

The fiber on the left consists of rigid particles on the order of magnitude of the un-drawn filament diameter (spinneret diameter) and shows the capillary break-up of the filament when take-up force is applied. The fiber on the right idealizes a nanoparticle filled fiber in which the particles have no effect on spin instabilities.

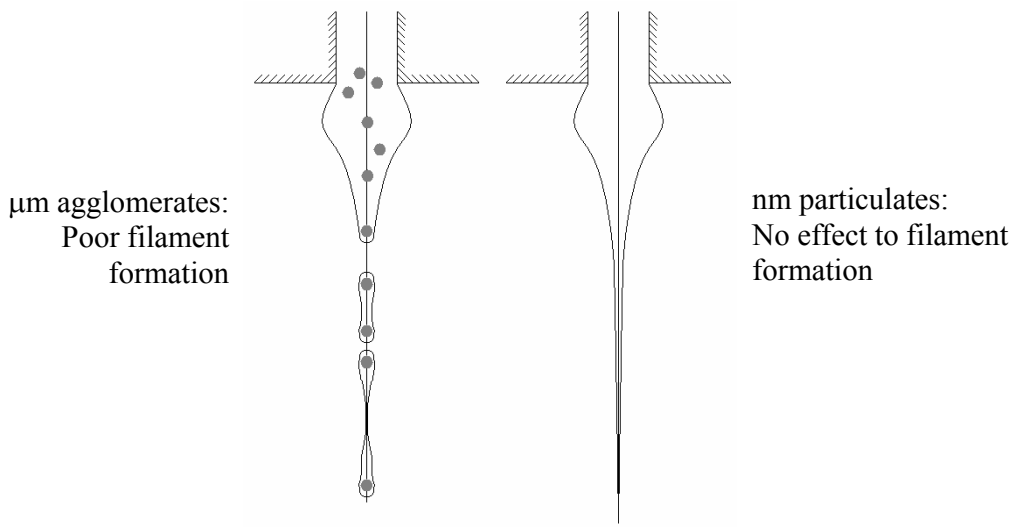

Figure 1.3. Schematic of the effect of particulate size on filament formation.

In the historical context, the polymeric fibers industry supersedes the injection molding industry by a number of decades. Although it could be debated who developed the first synthetic polymer, Carothers and Hill in the 1930's synthesized the first few aliphatic polyester polymers [9]. These materials were tested for their polymeric nature by the ability to pull fibers from the molten product and cold draw them for orientation and strength [9].

The aliphatic polyesters synthesized by Carothers possessed too low of a melting point for practical utility and for a few decades nylon fibers dominated the industry. The discovery of aromatic polyesters of high melting point, like poly(ethylene terephthalate) PET and poly(butylenes terephthalate) PBT, was made by DuPont in the United States

and ICI in the United Kingdom simultaneously in the 1940's. However, the widespread use of PET fibers did not occur until cheap feedstocks of terephthalic intermediates were made available. Then during the 1970's the full potential of PET fibers became realized in both the textile and technical yarn industries. The relatively high modulus of PET played a large part in making it suitable for blending with wool and cotton staple fibers and for industrial uses such as tire cordage or rope cordage.

Yet the key in forming usable aromatic polyester yarns has been in the drawing process, in which the fiber is drawn or extended to a lower cross sectional area while the molecular chains are oriented and crystallized (depending on the process temperature) to the direction of deformation. All types of fibers benefit from a second stage draw, except of course for gel-spun and solution spun ultra-high molecular weight polymers and liquid crystalline polymers. Although the spinning speed can be increased to eliminate the draw requirement, the ultimate properties of fibers spun at high speed are lower than those spun at a lower speed and draw accordingly in a second step. Table 1.1 shows that a two stage spin-draw imparts better mechanical properties such as strength (tenacity) and modulus than a single step high speed spinning process.

Table 1.1. Typical properties of fibers melt spun commodity fibers versus solution spun engineering fibers [10].

Property	PET		UHMWPE	Aramid
	OSP (6000 m/min)	TSP (conventional)	Spectra 1000	Kevlar 149
Density (g/cm^3)	1.38	1.375	0.97	1.47
Tensile strength (MPa)	460-550	610	3000	3450
Tenacity (gf/d)	3.8-4.5	5.0		
Modulus of elasticity (GPa)	13-14	18	172	172
Modulus of elasticity (gf/d)	75-80	120		
Elongation at break (%)	45-50	35	2.7	1.5

(OSP – One step process by the formation of a partially oriented yarn at high take-up. TSP - two step process of spin-draw. UHMWPE – ultra high molecular weight polyethylene.)

To date using the most efficient drawing processes and polyester of ultra-high molecular weight, the achieved drawn modulus has reached only 30% of the crystalline modulus of PET, which theoretically is 140 GPa [11]. On more commercial style equipment a modulus value of 10% of the crystalline modulus is typically achieved. Comparatively, a 15 GPa PET fiber filled with a 5 vol% loading of nanoparticles with a modulus of 178 GPa could give a modulus improvement in the estimate of 50%. Theoretically, higher concentrations of particles could give the 30% of the crystalline modulus that has been so far only achieved with high molecular weight polymers and drawn under un-conventional techniques. Therefore filling a PET fiber with a layered silicate filler particle of high modulus and high aspect ratio is a worthy exercise.

Although it is a worthy exercise in principal, the current and past literature has shown that synthesizing PET nanocomposite fibers is a difficult exercise in practicum. The current literature and available patents do not show any convincing mechanical property improvements [12-23]. Yet the shortcomings of nearly all of the studies are that

(1) care is not taken in the accounting of the layered silicate's effect on polyester molecular weight and that (2) no study has taken into full account the effect of second step draw on the final properties of PET nanocomposite fibers. The amine surfactants, used to create more thermodynamically favorable interactions between the polymer and inorganic filler, certainly have a negative effect on molecular weight in the polymer melt phase. As mentioned previously, drawing in a second step is essential to imparting usable properties to PET fibers and it is unclear as to why prior researchers have neglected to explore the effect of drawing on PET nanocomposite mechanical properties.

In tandem with the investigations of second step drawing on PET nanocomposite fibers, there is a relative lack in understanding of the structure-property relationships in nanocomposite fibers in general. In particular relatively little work has been published on the role of nano-fillers in affecting composite properties. For instance one might question whether the particle acts as a drawing or processing aid. Only one research group has provided insight into the role of montmorillonite in the drawing of nylon 6 nanocomposite fibers using small angle x-ray scattering [24,25]. The authors concluded that the particles acted to increase the maximum achievable draw ratio but did not contribute to property enhancement. However, the effect of nano-fillers as both a processing aid in the melt formation of fiber and a drawing aid in nucleating crystallinity under deformation in the rubbery and glassy states for PET fibers has not been addressed.

Although the knowledge base for polymer layered-silicate nanocomposites in injection molded form is increasing due to the considerable amount of ongoing research, the amount of effort made toward understanding nanocomposites in fiber form is increasing at a much slower rate. This work represents an effort to breakthrough to

mainstream applications of nanocomposite fibers. The primary goal is to establish the effect of second step drawing on the Young's modulus, tenacity, and heat distortion temperature of PET nanocomposite fibers as a function of filler loading level, filler surface treatment. The secondary objective of this work is to assess the role of the nanoparticle in the polymer matrix during processing from the melt and drawing in the solid state. To determine the role of nanoparticles during second step drawing and discern their specific ability to increase molecular orientation or accelerate strain-induced crystallinity, this work examines the structure-property relationships through microscopy, diffraction and spectroscopy of PET nanocomposite fibers. The results from each objective and discussed in whole should shed the first glimmers of understanding on nanocomposite fibers from manufacturing to properties.

1.1 REFERENCES

1. National Lead: US Patent 2531396. 1950.
2. Union Oil. US Patent 3084117. 1963.
3. Unitika. Japanese Patent application 109998. 1976.
4. Fukushima, Y. and Inagaki, S. J. Inclus. Phenom. 1987, **5**, 473.
5. Kojima, Y.; Usuki, A.; Kawasumi, M.; Okada, A.; Fukushima, Y.; Karauchi, T.; Kamigaito, O. J. Mater. Res. 1993, **8,** 1185.
6. Ray, S.S. and M. Okamoto, *Polymer/layered silicate nanocomposites: areview from preparation to processing.* Prog. Polym. Sci., 2003. **28**: p. 1539-1641.
7. Tjong, S.C. *Structural and mechanical properties of polymer nanocomposites.* Mater. Sci. and Eng. Rev. 2006, **53**, 73-197.
8. Carothers, W.H. and Hill, J.W. J. Amer. Chem. Soc. 1932, **54**, 1579.
9. van Olphen, H., *Clay Colloid Chemistry*. 1977, New York: Wiley & Sons.
10. Baird, D.G. and Collias, D.I. *Polymer Processing Principles and Design*. Wiley, New York; 1998.
11. Ito, M., K. Takahashi, and K. Kanamoto, *Effects of sample geometry and draw conditions on the mechanical properties of drawn poly(ethylene terephthalate).* Polymer, 1990. **31**: p. 58-63.
12. Lee, W.D., et al., *Preparation and properties of layered double hydroxide/poly(ethylene terephthalate) nanocomposites by direct melt compounding.* Polymer, 2006. **47**: p. 1364-1371.
13. Sanchez-Solis, A., et al., *Mechanical and Rheological Studies on Polyethylene Terephthalate-Montmorillonite Nanocomposites.* Polym. Eng. & Sci., 2004. **44**: p. 1094-1102.
14. Chang, J.H., M.K. Mun, and I.C. Lee, *Poly(ethylene terephthalate) Nanocomposite Fibers by In Situ Polymerization: The Thermomechanical Properties and Morphology.* J. Appl. Polym. Sci., 2005. **98**: p. 2009-2016.
15. McConnell, D.C., et al., *Structure Property Relationships in PET Nanocomposite Fibres.* Ann. Tech. Conf. Society of Plastic Engineers, Technical Papers, 2006: p. 387-392.
16. Sanchez-Solis, A., A. Garcia-Rejon, and O. Manero, *Production of Nanocomposites of PET-Montmorillonite Clay by an Extrusion Process.* Macromol. Symp., 2003. **192**: p. 281-292.
17. Pegoretti, A., et al., *Recycled poly(ethylene terephthalate)/layered silicate nanocomposites: morphology and tensile mechanical properties.* Polymer, 2004. **45**: p. 2751-2759.
18. Chang, J.H., et al., *Poly(ethylene terephthalate) nanocomposites by insitu interlayer polymerization: the thermo-mechanical properties and morphology of the hybrid fibers.* Polymer, 2004. **45**: p. 919-926.
19. Chang, J.H., et al., *Poly(butylene terephthalate)/organoclay nanocomposites prepared by in situ interlayer polymerization and its fiber (II).* Polymer, 2003. **44**: p. 5655-5661.
20. Chang, J.H. and S.J. Kim, *Polyester nanocomposite fibers: comparison of their properties with poly(ethylene terephthalate) and poly(trimethylene terephthalate) (II).* Poymer Bulletin, 2004. **52**: p. 289-296.
21. Matayabas, J.C.; Turner, S.R.; Jones, S.B.; Wayne, C.G.; Gilmer, J.W.; Boyde, B.B. *US Patent 6084019.* 2000.
22. Gilmer, J.W.; Matayabas, J.C.; Wayne, C.G.; Owens, J.T.; Turner, S.R.; Piner, R.L. *Europena Patent 1144500.* 2000.
23. Dugan, J.S. *US Patent* 6726989. 2004.
24. Ibanes, C., et al., *Structure and Mechanical Behavior of Nylon-6 Fibers Filled with Organic and Mineral Nanoparticles. I. Microstructure of Spun and Drawn Fibers.* J. Polym. Sci. Part B: Polym. Phys., 2004. **42**: p. 3876-3892.
25. Ibanes, C., et al., *Structure and Mechanical Behavior of Nylon-6 Fibers Filled with Organic and Mineral Nanoparticles. II. In-Situ Study of Deformation Mechanisms.* J. Polym. Sci, Part B: Polym. Phys., 2004. **42**: p. 2633-2648

2 Literature Review

2.1 THE RHEOLOGY OF HIGH ASPECT RATIO NANO-PARTICLE FILLED LIQUIDS

The following review of high aspect ratio nanoparticle filled liquids was originally written for and accepted to the 2006 edition of *Rheology Reviews* published under the British Society of Rheology and edited by D.M. Binding and K. Walters. This entry was co-authored by D.G. Baird, whose main contribution to the review pertained to the theoretical constitutive equations of suspended anisotropic particles. The document is reproduced for completeness of the topic, yet the reader may appreciate the abstract and summary, the rheology of layered silicates in low molecular weight liquids, and the rheology of layered silicates in polymeric liquids (sections 2.1.1 & 2.1.7, 2.1.4.1-2, and 2.1.5.1 respectively) as an abridged version that retains the main concepts. However, the title is not restricted to layered silicates. Therefore, the article includes rheological aspects of nanotubes and nanofibers as a comparison to layered silicates. After review of both types of particles, it is clear that layered silicates, at present, are more conducive for reinforcement of melt-spun fibers, based on cost per pound, ease of dispersion, degree of strain-hardening, and availability of current literature. Much is still unknown about the benefits of nanotubes in composite form. This section leads this review because rheology and rheological methods are very specific in their ability to probe the structure and mobility of molten polymer materials on the molecular level. As filler particle dimensions approach and become smaller than the radius of gyration of the polymer molecules, few methods other than rheology can give a complete picture of the specific

polymer-filler interactions. For nanoparticles, solid fillers of nanometer dimensions and of high aspect ratio and large surface area, a series of unique rheological responses have been observed and interpreted to paint the wildly interesting microstructure of these nanocomposite materials. It is from these conclusions on the fluid behavior that one can understand the mechanical and processing behaviors.

2.1.1 ABSTRACT

The objective of this review is to elucidate the recent developments in the rheology of suspensions containing high aspect ratio (> 100) nano-scale fillers. In particular, this review focuses on industrially important nanoparticles, namely layered silicates or nanoclays, carbon nanotubes, and carbon nanofibers, suspended in low and high molecular weight liquids. This review begins with the critical aspects of nanoparticle structure. In addition, the surface chemistry is discussed in the context of particle-particle interactions leading to flocculation or aggregation, because optimum suspension properties occur in well-dispersed, non-aggregated systems. A comprehensive review of large aspect ratio nanoparticles in low and high molecular weight liquids is then presented, with discussions of the effects of particle size, surface treatment, meso-structural development on linear and non-linear viscoelastic properties (complex, steady shear, and extensional viscosity; shear thinning; stress overshoot; and primary normal stress difference where applicable). These sections elaborate on the following results of nanoparticle suspensions. First, nanocomposites require much lower concentrations for the same rheological effects as conventional micro-composites, because of the

nanoparticle's larger available surface area and the development of a meso-structural polymer-nanoparticle network. Second, the linear viscoelastic properties generally increase with the addition of nanofiller, and the nanoparticles profoundly broaden the relaxation dynamics of the polymer melt. Third, the primary normal stress difference (N_1) becomes negative at high stresses and high nanoparticle loadings. Finally, nanoparticles increase the values of extensional viscosity as a function of Hencky strain to a greater extent than micron sized fillers. This review concludes with a discussion of recent theory concerning particle network development and the nature of particle-polymer interactions with an emphasis on what types of constitutive relations are needed to describe the rheology of fluids containing high aspect ratio nanoparticles.

2.1.2 INTRODUCTION TO NANOCOMPOSITE RHEOLOGY

In recent years there has been considerable interest in the use of nanoparticles to improve the mechanical, electrical, and barrier properties of polymers. Furthermore, nano-sized particles have been used as thickening agents for low viscosity Newtonian fluids. With the addition of nano-sized particles to fluids, it is desirable to know what their effect is on the rheology of the composite and what type of approach is needed to model the rheology of these systems. In addition, rheology may provide a means to determine the degree of exfoliation (i.e. degree of dispersion) of the nanoparticles in a polymer melt. Rheological properties of particulate suspensions are sensitive to structure, particle size and shape, and surface modification. Although most studies include forms of x-ray diffraction and/or electron micrographs to quantify and qualify nanoparticle

dispersion, representations are made on a sampling basis and may differ from the bulk. Rheological properties change significantly with favorable particle-matrix interactions compared to non-interacting systems or strong particle-particle attractions. Thus, the study of the rheological properties of a nanocomposite system may yield an invaluable tool in structure characterization and property prediction, but the connection of structures to flow is not completely understood.

The addition of particles to a flowing liquid, with the complementary local disturbance of the flow lines, will result in the simplest flows becoming rather complicated. The flow pattern changes to a situation where locally in the liquid phase in the vicinity of the particle there is an increase and spatial variation of the shear rate in the continuous phase and transient behavior of local liquid elements. In the melt phase, the attractive van der Waals forces between particles encourage agglomeration and significantly influence flow properties from the increase in phase volume. Aggregated domains of nanoparticles increase the distortion of flow lines and have profound effects on rheological properties such as viscosity and normal stresses. Well-dispersed domains may be a result of favorable interaction between matrix and particle surfactant, such as the hydrogen bonding between hydroxyl modified nanosilicates and nylon polymers. At an equal particle concentration, exfoliated or well-dispersed nanoparticles exhibit different rheological behavior compared to their agglomerated counterparts. These complications invalidate any assumptions governing macroscopic homogeneity, forcing the application of complex constitutive equations over the heterogeneous phase to account for additional spatial and time derivatives as well as particle-particle and particle-matrix molecular interactions.

The complexity of filled liquids has created much scientific interest, especially in the rheological properties of particle suspensions on the nano-scale. Pieces of the available reviews of colloid suspensions and filled viscoelastic systems from some authors [1-10] provide some perspective but not the complete rheological picture of high aspect ratio nanoparticle suspensions. Such reviews have focused on spherical, near spherical or fibrous micron-sized particles, but as the particle size decreases and the particle shape elongates rheological behaviors begin to change, i.e. primary normal stress difference (N_1). The most recent review of nanoparticle rheology was completed as a chapter of layered-silicate polymer composite science by Ray and Okamoto [2] in 2003, and focused on 2-dimensional nanoclay particles in polymer matrices. Yet, a complete review of both shear and shear-free material functions for high aspect ratio (1- and 2-D) nanoparticle suspensions in low molecular weight and polymeric liquids from both an experimental and a theoretical standpoint has yet to be accomplished and is the major aim of this work.

The following review of the observed phenomena in nanoparticle filled systems is presented in a format to cover the multitude of matrices and particles and their surface treatments discussed in the recent literature. The main body of text for a given rheological property covers the most prevalent filler type, nanosilicates, or platelet shaped particles including natural and synthetic clays for different matrices. Then the effects of carbon nanotubes and nanofiber are covered, as these fillers are the least abundant in the current literature. Covered under the filler types will be their effects on the rheological properties of the various types of polymer matrices and small molecule solvents. The most common thermoplastic matrices are polyamides, polyvinyls including

polyolefins, polycarbonates, and polyesters. Aqueous suspensions are the most common in studies of nanoparticles suspended in mall molecule liquids. Yet thermosetting polymer nanocomposites begin as suspensions in low molecular weight organic liquids and are covered in sections entitled Newtonian precursors. Because the rheology is so dependent on the structure and properties of the particles, the inherent geometric and chemical structures of the most studied nanoparticles must be discussed.

2.1.3 STRUCTURE AND PROPERTIES OF NANOPARTICLES

2.1.3.1 *Nanoclays*

To better understand the complex morphologies that occur in layered silicate nanocomposites, the structural details of the layered silicates, i.e. nanoclays, and their properties are briefly reviewed. The structure in figure 2.1, and for the nanoclays in this review, refers to a 2:1 phyllosilicate called montmorillonite (MMT). The structures of MMTs have two tetrahedral sheets surrounding a single octahedral sheet that form a single layer of 0.6 nm thickness. The tetrahedrons, pictured in figure 2.1, are composed of silicon-oxygen bonds that share a single oxygen bond with the octahedrons of aluminum- or magnesium-oxygen-hydroxyl bonds. In a real system six tetrahedrons form a hexagonally symmetric ring; the rendering in figure 2.1 has been flattened for simplicity. MMT has the generic formula of $M_y^+ nH_2O\left(Al_{2y}Mg_y\right)Si_4O_{10}\left(OH\right)_2$. For example, sodium montmorillonite, i.e. Na^+MMT, has the general chemical composition of $Na_{1/3}\left[\left(Al_{5/3}Mg_{1/3}\right)Si_4O_{10}\left(OH\right)_2\right]$. Tetrahedral ($Si^{4+}$) and octahedral ($Al^{3+}$ or Mg^{2+}) cations

may be substituted by different valence ions to create a surface charge, which in the presence of water aids in the stacking layers together.

Layers are held together by van der Waals forces of attraction generated from charge balancing interlayer complexes. The inherent surface charge of the clay originates primarily from adsorption of ions through the silicate. For example, Si^{4+} is typically replaced by Al^{3+} or Fe^{3+} in the tetrahedral sheets, and Al^{3+} is substituted by Mg^{2+}, Fe^{2+}, or other cations in the octahedral sheets [1]. Yet, any smaller valence atom may replace a higher valence atom; for example tetrahedral Al may be substituted by K ions. For the clays of interest, the surface charge is naturally balanced by larger hydrated cationic complexes that adsorb on to the silicate surfaces and expand the interlayer distance. The amount of these interlayer cations is described in their unit of measure commonly called the charge exchange capacity (CEC) expressed in milliequivalents per 100g of dry clay. A reason for MMT's wide application in composites is its particularly high CEC (~ 90 mequiv/100g). Therefore, MMT is prone to cation exchange reactions that add surfactant molecules to improve particle-liquid interactions and, thus, the properties of the composite.

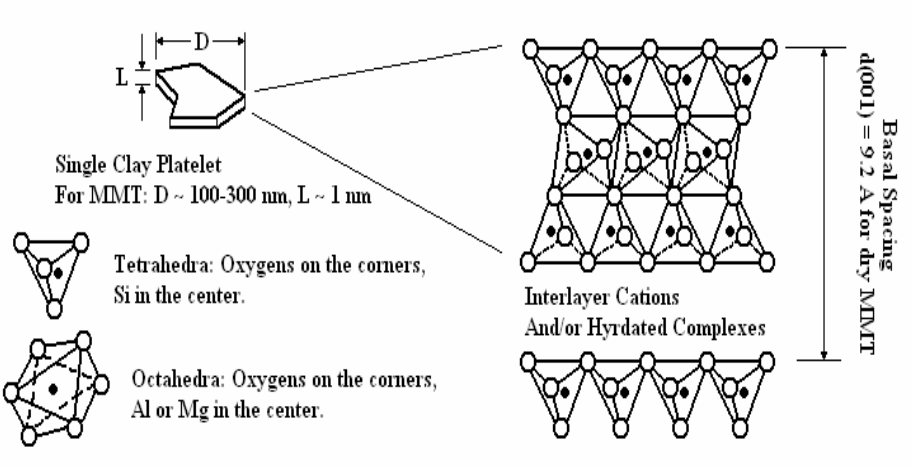

Figure 2.1. Schematic representation of layered silicates of the 2:1 phyllosilicate or smectite group. Lines are not scale representations of covalent bonds [11].

In general, the degree of dispersion of the clay platelets into the polymer matrix determines the super-structure of the nanocomposites. Depending on the interaction between the clay and the polymer matrix, two main idealized types of polymer-clay morphologies, intercalated and exfoliated, and a third less ideal flocculated morphology can be obtained (figure 2.2). Flocculation is more readily found in suspensions of charged particles in low viscosity, low molecular weight liquids, in which edge-edge interactions are significant. The intercalated structure results from penetration of a few polymer chains into the silicate interlayers. Face-to-face attractions persist resulting in formation of alternate layers of polymer and inorganic layers. The platelets are exfoliated when the individual silicate layers are completely separated and dispersed randomly in a polymer matrix, where no electrostatic interactions between surfaces exist. The best property improvements in polymer composites and the least influence to viscosity for low molecular weight suspensions results from the exfoliated morphologies.

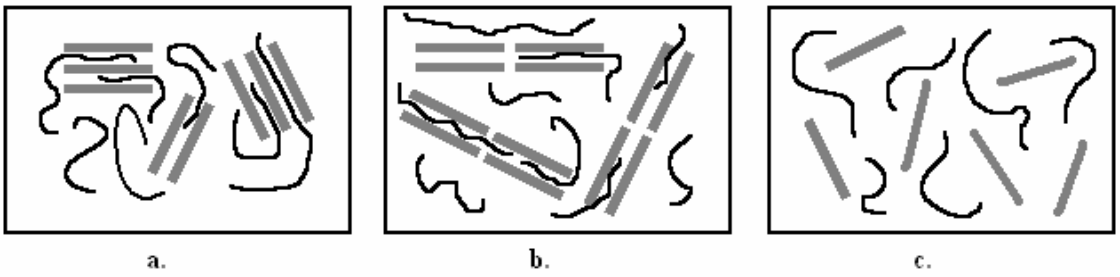

Figure 2.2. Schematic illustrations of two types of polymer-layered silicate morphologies: (a) intercalated, (b) flocculated edge-edge interactions between platelets, and (c) exfoliated [12].

2.1.3.2 *Carbon Nanotubes (CNT) and Nanofibers (CNF)*

Carbon nanotubes (CNTs) are cylindrically shaped carbon molecules with properties that make them useful in electronics, optics, and materials applications. The exceptional mechanical and transport properties of CNTs provide useful insight into the potential for nanoparticle additives in liquids and solid polymers to achieve significant improvements in bulk properties at low volume concentrations. The uniqueness of CNT properties arises from the structure and molecular arrangement of the carbon atoms.

Single-walled nanotubes have diameters close to 1nm, with a length that can possibly reach the millimeter scale. The structure of a single-walled nanotube is composed of a seamless wrap of a single nanometer thick graphene sheet. The graphene sheet wraps into a cylinder characterized by two integer indices (n,m) to form a chiral vector normal to the tube axis. The wrapping structure or orientation of the chiral vector dictates the electronic properties of the tube. Any "metallic" nanotube (for which (n-m)/3 = integer) has a current density 1,000 times stronger than copper [13]. Otherwise, the remaining nanotube population is semi-conductive. Yet, the tensile properties of single-

walled and multi-walled nanotubes are weak functions of the chiral vector. For single-walled nanotubes the tensile strength is an order of magnitude greater than steel and the elastic modulus is in the tera-Pascal range (10^{12} Pa) [14].

Multi-walled nanotubes are composed of repeated sheaths, or cylinders within cylinders, of single-walled nanotubes. Multi-walled nanotubes have diameters on the order of tens of nanometers with length ranges in the thousands of nanometers. Typically the reported properties are lower than their single-walled constituents because of the increased probability of critical defects. An abundance of defects often produces tensile properties two or three orders of magnitude lower than their more perfect counter parts. A review by Hidling [15] provides a detailed comparison of calculated versus experimental mechanical and transport properties of single- and multi- walled nanotubes.

The method of nanotube synthesis will dictate the formation and concentration of single- or multi-walled nanotubes, as well as the morphology of the CNT product. Chemical vapor deposition [16], electric arc discharge [17], and solid pyrolysis [18] are among the documented processes used in CNT formation. Aspect ratio, purity, defects, and degree of physical or chemical entanglements depend on the CNT synthesis method and significantly effect melt rheology. Until nanotube manufacturing yields CNTs suitable for direct end applications, nanotube ropes must be dispersed or exfoliated within a given matrix or substrate for further processing. Formation of CNT aggregates prevents efficient distribution of mechanical loads and isotropic transport coefficients by reducing interaction between the polymer and nanotube. However, entangled aggregates can be difficult to disperse without causing fragmentation and reducing the aspect ratio. In the un-entangled state, the high aspect ratio leads to physical contacts between particles in

the fluids creating a network to improve thermal and electrical conductivity of the composite. In addition to increasing tensile and mechanical properties, the viscosity of suspensions of such high aspect ratio nanoparticles increases. Understanding the rheology of these filled materials will shed light on the composite properties after processing in unit operations necessary for large-scale production. For now and the near future, the use of CNTs is confined to high-end engineering applications and research interests because of their high cost.

Carbon nanofibers (CNF) possess similar chemical composition to nanotubes and present a cheaper alternative without sacrificing the majority of attractive mechanical and transport properties in composite form. One method of CNF preparation is the chemical deposition of ethylene gas on a copper catalyst to produce vapor grown nanofibers [19]. A CNF can be visualized as a thick single-walled nanotube, in which the center may be hollow, but carbon atoms are bonded in the radial direction. Reported CNF diameters range from 50-200 nm with lengths ranging from 20-100 μm [20]. Like nanotubes, purification and functionalization processes are required to remove by-products and to disperse the highly entangled nanofibers without truncating the aspect ratio by shortening the fiber length. Solvent casting or melt blending are two convenient methods for dispersion of nanofibers in polymeric matrices. Solvent casting methods, such as ultra-sonication in an appropriate solvent and dissolved polymer, disperse the nanofiber with less truncation of fiber ends than melt compounding in a polymer matrix under high shear [20]. The advantage of a larger aspect ratio provides greater probability of nanofiber contacts with the suspending matrix, which leads to greater improvements of composite properties over a lower aspect ratio, or more agglomerated nanofiber filler. Nevertheless,

CNFs can be produced in large quantities and are relatively inexpensive, which are two factors propelling their interest in current research.

2.1.3.3 *Particle Surface Treatments*

A common observation in nanocomposite rheology is that flocculated or agglomerated particles produce larger viscosity increases than well-dispersed or exfoliated systems of equal particle loading. Therefore, one may state that flocculation or agglomeration artificially increases particle concentration. Thus, to optimize mechanical property improvements, the particles (platelets, tubes, or spheres) must be exfoliated. This task is not easily accomplished because the particle surfaces and suspending liquid may have unmatched chemical affinity. For example, layered-silicates are naturally hydrophilic, and do not interact favorably with a non-polar, polypropylene, matrix. Nevertheless, such obstacles are overcome with the addition of ionic and/or organic compounds to more effectively wet the particle surfaces.

In terms of clay composites, exfoliation of the platelets in low molecular weight liquids depends on the electric double layer thickness of the platelet faces, whereas polymer suspensions require larger steric hindrances between plates. At low salt (or organic anions) concentrations (and depending of pH for aqueous systems), the compression of the electric double layer repulses other clay platelets and promotes exfoliation. Highly adsorbed polyelectrolytes and non-ionic polymers on clay surfaces provide an “entropic” repulsion due to the steric barrier that the dangling ends provide [1]. For polymer suspensions, cationic quaternary alkyl ammonium salts (or bases) are the most used surfactants, because the compounds strongly adsorb to the platelet surfaces,

displacing interlayer water and increasing basal spacings to allow for easier polymer chain intercalation [21, 22]. Different groups may be added to the amine to improve polymer-clay interactions, such as hydroxyls to promote hydrogen bonding.

For nanotube suspensions, acid treatments leave functional sites that promote dispersion in polar solvents, but shorten tube/fiber lengths. Surfactants, such as sodium dodecyl benzene sulfonate [23], surround the tube surface in long alkyl tails headed by hydrophilic sulfonate anions that increase aqueous interactions and provide enough steric hindrance to prevent aggregation, or roping, of single-walled nanotubes. Islam et al. [23] were able to disperse up to 65% nanotubes into single tubes of 1 nm diameter using dodecyl benzyl sulfonate among other less effective surfactants.

2.1.3.4 *Other Nanoparticles*

Novel nanoparticles are continually being developed by researchers but, to limit the scope of this review, the focus lies on the high aspect ratio particles discussed above because these structures are of immense industrial and academic interest. Yet, other nanoparticles that could be considered as significant but that are not discussed are listed below. Low aspect ratio, carbon fullerenes have been found to be suspendible in a number of small molecule liquids but only in dilute concentrations. At these solubility limits, the particles do not influence the elastic properties of the fluid [24], and higher concentrations of particles precipitate creating an inhomogeneous mixture. For these reasons, fullerene applications involve drug delivery and high performance solid lubricants [25-29], but not as polymer composites. As an interesting alternative to fullerenes, crosslinked polymer particles of nano-scale diameters that are mixed with

linear chains of the same polymer demonstrate some unusual rheology. The particles are synthesized by a method of intra-molecular collapse, in which functional groups on originally linear polymer chains chemically bond to form a 3-dimensional nanoparticle [30]. These particles are becoming realized as ideal for computational thermodynamic simulations, because of the absence of enthalpy restrictions. Calcium carbonate and titanium oxide particles possess large specific surface energies and strongly agglomerate to produce broad size distributions. Therefore, these particles are traditionally considered as having low aspect ratios and near spherical geometries. In terms of other high aspect ratio nanoparticles, inorganic nanotubes of tungsten sulfide, molybdenum sulfide, etc. are nanoparticles that have been studied in dispersed situations but omitted because scientific applications have been limited to solid tribology and atomic imaging [31].

2.1.4 RHEOLOGY OF NANOPARTICLE SUSPENSIONS IN LOW MOLECULAR WEIGHT LIQUIDS

Attention from industry on nanoparticle solutions has stemmed from past interest in the viscosity thickening properties of particle suspensions. The simplest cases arise from nanoparticles suspended in mediums of constant viscosity. Yet, these suspensions are far from being completely understood, as factors such as particle size distribution, volume fraction, and charge influence rheological behaviors. The properties of the medium, such as pH, polarity, and inherent functionality, also dictate flow behavior by regulating the degree of flocculation or aggregation. There are other factors that can influence results, for example the plate roughness or vane geometry of the testing device, which dictates

the degree of slip at the wall and the amount of phase separation due to gravity or poor liquid-particle interactions.

The general trend in viscosity, as a function of particle concentration, has been semi-empirically modeled by several authors [32-37]:

$$\eta_{sp} = \eta_r - 1 = \eta/\eta_s - 1 = 2.5\phi \qquad \text{.....(1)}$$

$$\frac{\eta}{\eta_s} = 1 + 2.5\phi + 6.2\phi^2 \qquad \text{.....(2)}$$

$$\frac{\eta}{\eta_s} = \left(1 - k\phi\right)^x \qquad \text{.....(3)}$$

$$\frac{\eta}{\eta_s} = \left(\frac{1}{1 - \phi/\phi_m}\right)^{\phi_m[\eta]} \qquad \text{.....(4)}$$

The analysis began with Einstein's early 20th century relation (equation (1)) and has since been developed by Baker and later authors to include non-spherical geometries and shear thinning continuous phases [7]. The more often applied, semi-empirical models for high aspect ratio particles in suspension are of the type in equation (3), in which a common analogue is the Krieger Dougherty equation (4). Most analyses include a comparison to the hydrodynamicly based Einstein equation of the form in equation (2), referred to as the Einstein-Batchelor equation. Such comparisons usually favor the Baker type equations because of the onset of shear thinning in more concentrated suspensions. At high particle loadings the Einstein type equations perform expectedly poor, although their parameters are more straightforward than those of Baker. For example, the equation of Krieger and Dougherty [35] requires a maximum packing volume fraction, ϕ_m, of the particulate and an intrinsic viscosity parameter, $[\eta]$, to empirically model the effect of

particle concentration on the suspension viscosity. The effects of particle size distribution are carried into ϕ_m, and the effects of shear thinning are absorbed into the $[\eta]$ term. Xu and coworkers [38] studied the effect of aspect ratio on the relative viscosity of CNFs in glycerol and water. Figure 2.3 shows the Krieger-Dougherty equation fitted their data well at high concentrations of filler, contrary to the Einstein-Batchelor equation. The authors examined a high and low aspect ratio CNF suspension and determined as the aspect ratio increases, the maximum packing fraction decreases. As a comparison, a suspension of 30x700 μm glass rods, the maximum packing fraction was $\phi_m = 0.27$ [39]; yet, for a suspension of non-interacting CNFs, $\phi_m = 0.05$ [38].

However, these semi-empirical models do not account for particle interactions or particle alignment under shear. Attempts can be made to place particle-particle interactions into the maximum packing factor, because particles typically agglomerate to increase the effective particle size. Yet, particle-liquid interactions combined with particle-particle interactions generate flocculates and aggregates that are formed and broken down during flow. Thus, the effective volume fraction could change as a function shear rate. In addition, high aspect ratio particles align in the direction of flow, and, therefore, the maximum packing factor increases as the particles align.

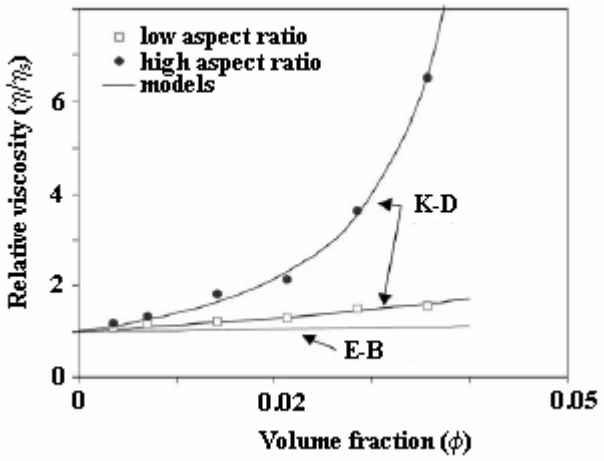

Figure 2.3. The effect of CNF concentration on the relative viscosity of 90% glycerol/water and the prediction accuracy of the semi-empirical Kreiger-Dougherty (K-D) equation over the hydrodynamic based Einstein-Bachelor (E-B) equation [39].

2.1.4.1 *Layered-Silicate Suspensions*

For dilute sols and suspensions, where the concentration of clay is so low that the platelets are non-interacting, the behavior is Newtonian. Einstein derived an equation for the viscosity increase from non-interacting spherical solids in suspension (see equation 1 above). However, for large aspect ratio, anisometric, platelets a larger proportionality constant is warranted. Van Olphen [1] suggested for large thin disks with small height to diameter ratios:

$$\eta_{sp} = 32\phi/(15\pi p)\ ; \qquad \text{.....(5)}$$

$$\phi = m_c/(2.85(100-a))\ , \qquad \text{.....(6)}$$

where p is the aspect ratio, m_c is the mass in grams of dry clay per 100 cm^3 of suspension, 2.85 g/cm^3 is the density of dry clay, and a is the volume percent of water in the expanded clay derived from hydration basal spacings. Thus, according to theory, for dilute suspensions only the volume of clay influences the rheological response, not the

number of platelets or degree of agglomeration. Kislenko and Verlinskaya [40] observed that agglomerated nanoclay suspensions behave as featureless Newtonian liquids.

For this section only the rheology of Na^+ MMT suspensions are discussed in detail. Although rheological experiments have been conducted on other types of clay suspensions such as illitites and kaolinites, the smectite clays, especially Na^+ MMTs, show the best swelling behavior [1, 41-43]. An inherent swelling ability is energetically favored in particle exfoliation, as larger swelling creates greater interlayer distances. Additionally, for aqueous suspensions of MMT, the presence of yield stress has been directly related to Na^+ ion concentration, because of sodium's ability to form strongly hydrated complexes within the interlayer spacing [44].

Exfoliated nanoclay filled liquids typically exhibit a non-Newtonian yield stress above the percolation limit and, hence, the gel phase is of prevalent interest in the recent literature. The yield behavior is related to the mesostructure of the suspension, in which the applied stress can result in a sol-gel transition to change the structure of the suspension from a solid to a flowing liquid over time in a narrow stress range. In a study of organically modified montmorillonite clay and xylene, the yield stress, which was determined by creep testing of clay suspensions containing clay weights from 1-6%, was found to increase rapidly with concentration [45]. The yield stress and critical shear are measures of the degree of particle association and are indicators of changes in inter-particle interaction modes [46]. The breakdown of particle-particle interactions is a result of shear or hydrodynamic forces, but the time-dependent buildup of particle interactions leading to yield stress values is solely related to Brownian motion as the particles collide with each other.

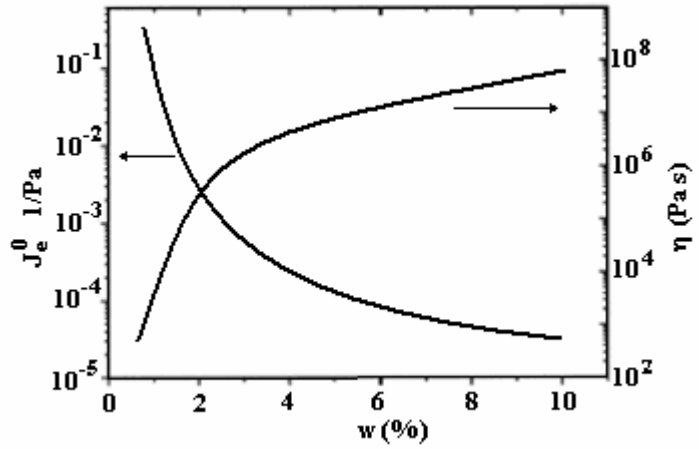

Figure 2.4. Schematic of creep and recovery results of a 4 wt% nanoclay suspension from Zong and Wang [45]. The curves show creep compliance and viscosity of suspension as a function of silicate loading. The nanoclay modifier used in this case is dehydrogenated tallow quaternarty ammonium chloride.

Studies on creep compliance of nanoclay solutions have attempted to elucidate the mechanism network reformation. Zhong and Wang [45] scaled the viscosity to the volume fraction of clay as $\eta \sim \phi^3$ and the equilibrium creep compliance as $J_e^\circ \sim \phi^{-3}$, implying that relaxation is nearly constant with respect to clay concentration, as shown in figure 2.4. The retardation time or lifetime of network entanglements is observed to be nearly constant for clay loading greater than 3 wt%, such that the increased number of entanglements from higher clay concentrations leads to higher viscosities. The authors proposed that nano-confinement of liquid xylene between the clay platelets increases the solid volume and leads to elastic solid-like response. Time dependent studies have shown that higher concentrations of clay slow the kinetics of quiescent structure recovery [45],[47]. Yet, as figure 2.4 implies, the relaxation is unaffected.

The addition of electrolytes to a suspension of clay platelets influences the double layer thickness, which dictates the mechanism of particle association. The addition of sodium hydroxide in low concentrations lowers an unmodified clay/water solution viscosity, suggesting the electrolyte weakens attractive forces between clay surfaces and the clay platelets are aligned along their positive ends. At high concentrations the apparent viscosity increases as the repulsion energy is reduced and clay platelets interact face to face to confine the solvent in tighter spaces producing a more solid-like response [46]. Additionally, at high salt concentrations the yield stress was reduced due to the decrease in network links from increased platelet agglomeration. Maino and Rabaioli [48] observed a transition from edge-face to face-face platelet interactions with increasing salt loading. Yet others [49] have shown that particles associate only edge-to-edge or face-to-face.

Pignon et al. [50] explored the mesostructural aspects of nanoclay/water suspensions of weak electrolyte concentration in a coupled rheological and light scattering study. The authors suggested a fractal arrangement of nanometric units of clay that extend to the tens of nanometers and form larger micrometer sized agglomerates at rest (for example, see figure 2.5). The sol-gel transition of their laponite clay and water system was about 0.5 vol %. Typical micron sized particles begin to form gels at much higher volume fractions, which were usually in the 20-50 vol % range. Yet, under shear, the fibrous structure of the isotropic phase was broken into rod-like aggregates perpendicular to the flow direction, which in turn they dispersed into micrometer flocculations upon longer or stronger deformation.

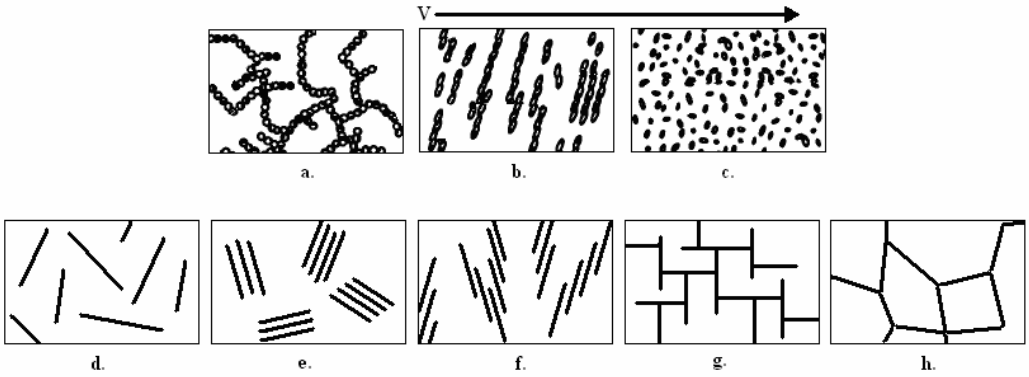

Figure 2.5. Schematic of nanoclay platelet mesostructures adapted from Pignon et al. [50] and Luckham and Rossi [5]:
a – the percolation of platelet clusters under rest;
b – upon deformation rodlike aggregates form along the direction of the velocity gradient;
c – under further deformation the aggregates break up into individual clusters;
d – exfoliated platelets;
e – face-to-face aggregates;
f – face-to-face "band-like" aggregates to form a network;
g – edge-to-face percolated network;
h – edge-to-edge "house of cards" percolated network structure.

This interpretation was built on observations from previous authors [51-53]. Pignon and coworkers noted that as the shear rate increased, the dispersion of clay concentration increased to suggest the breakup of larger rod-like aggregates of flocs to smaller moieties. The proposed mechanism of network deformation of nanoclay/water suspensions suggested two time scales for the breakdown of structure. During the first few moments of shear the nanoclay aggregates oriented perpendicular to flow until the peak stress in the material was exceeded, depicted in figure 2.5(a-c). The long time scale of dis-aggregation and elimination of fractal characteristics began after the critical strain was exceeded. Then during the recovery under quiescence, the anisotropic disks orient to collective aggregates followed by a deformation history dependent rearrangement to a

fractal structure. This structure was marked by a time dependent increase in viscoelastic moduli, which under due time gave an equal behavior to the original gel.

The discussion so far has mainly pertained to charge stabilization, yet steric stabilization by polymer surfactants dictates rheological response. Ionic steric stabilizers, such as the popular quaternary ammonium salts or bases ($R_4N^+Cl^-$ or $R_4N^+OH^-$), substitute the interlayer cations and displace water to form a diffuse double layer of non-polar chains, which makes the clay suspensions stable in non-polar solvents. The discussions of Zhong and Wang [45] above involved an alkyl-ammonium quaternary cation to stabilize MMT in xylene. Non-ionic steric stabilizers are typically low molecular weight polymers that loop on, train along, and dangle off platelet surfaces and prevent agglomeration by reducing van der Waals forces between faces. In very dilute suspensions of Na^+MMT in polyethylene glycol (PEG) the viscosity was shown to decrease with increasing polymer concentration until a minimum, at which the de-flocculated particles, now arranged face-to-face, adsorb more polymer surfactant ultimately bridging platelets together [54]. In more concentrated silica/PEG suspensions the viscosity increased with polymer concentration until a maximum, at which the number of bridges between particles was reduced as the PEG polymer filled the available interactive sites on platelet surface [55, 56]. As expected the apparent yield stress reached a maximum of a critical polymer concentration due to the rising number of bridges. These bridges acted as effective gel points that trap solvent molecules and produce a more solid-like response until the saturation. At this point progressive micelles began to form and induced the deterioration of the network structure.

2.1.4.2 *Thermosetting Layered-Silicate Nanocomposites, Newtonian Precursors*

The majority of thermoset-layered silicate research has focused on epoxy-based precursors, which by themselves are Newtonian fluids. Similar to their non-reactive analogues, the control of exfoliation for epoxy suspensions depends upon the nanoparticle composition, the curing rate, and the compatibility of the two phases. Processing variables such as temperature and initial dispersion play an important role in the formation epoxy composites. An increase in temperature lowers the viscosity to improve the interlayer diffusion of monomer within the platelets and upon cure aids in delamination producing exfoliated thermoset composites. The addition of modified montmorillonite increases dynamic viscosity values with increasing clay content in an uncured epoxy monomer. The viscosity versus angular frequency curve reflects similar shear thinning behavior of particulate suspensions and weakly agglomerated gels, where larger contents of clay produce steeper shear thinning regimes.

As mentioned before, the epoxy nanoclay compatibility influences the degree of viscosity enhancement. Brown et al [57] compared the degree of exfoliation of hydroxyl modified silicate to a long alkyl chain or tallow modified silicate. The authors found that not only were the hydroxyl-modified clays exfoliated in the final cured matrix, and the tallow-modified clays intercalated, but that the surface modification influenced the kinetics of the curing time. At equal concentrations of clay loading, the larger magnitude of viscosity, for an alkyl modified clay over an hydroxyl modification, was attributed to the formation of larger aggregates, which occlude more liquid between the platelet surfaces. Smaller aggregate sizes showed smaller increases in the magnitude of viscosity. The subsequent addition of diamine to crosslink and form the final matrix had little effect

on shear thinning characteristics of either clay modifier, but the ability of the hydroxyl modified clay to hydrogen bond to the hydroxyl-amine group produced a 2-3 order of magnitude upward shift in viscosity [57]. The tallow-modified clay showed little interaction with the crosslinking agent and marginally increased the viscosity, as shown in fig 3.4.

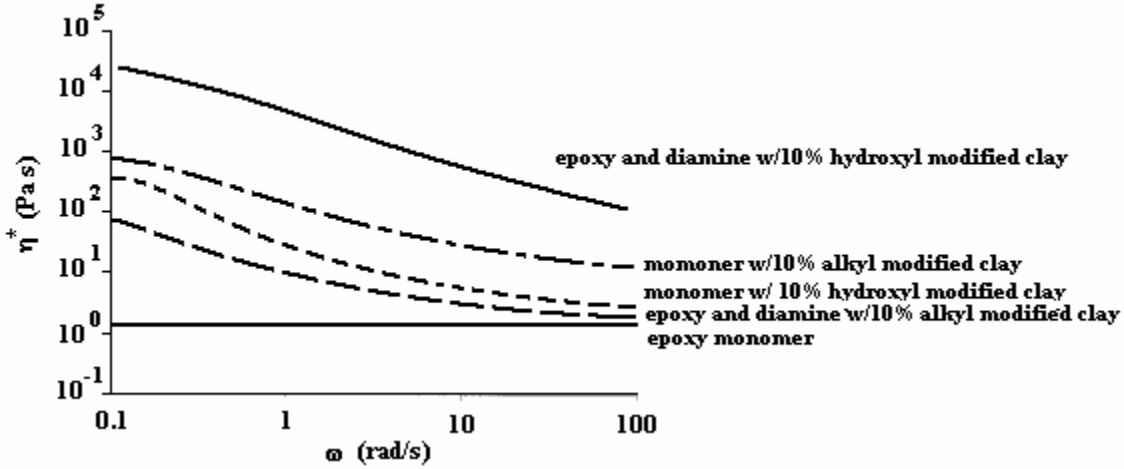

Figure 2.6. Complex viscosity of a 10 wt% nanoclay/epoxy suspension showing the significant effect surface treatment on favorable interactions [57].

In recent articles, the time-dependent shear rheology of organically modified layer-silicate and epoxy nanocomposites was examined. Dean et al. [58] conducted time sweeps of dynamic moduli that showed the expected behavior of slowly rising storage, G', and loss moduli, G'', followed by a steep increase as the gel point was reached and then a flattening out to final properties as the composite vitrified. Their gel time decreased with increasing hydroxyl-modified clay content. The authors found that the balance between solution and particle polarity dictated the strength of inter-particle forces and the length of platelet separation available for diffusion of crosslinking agent. Similar results were obtained by le Pluart et al. [59], who built on the work of Moraru [60], to

extend the observations of particle-solvent pairing to epoxy precursors. At equal clay concentrations, good organic modifier-solvent interactions produced weak gels with thixotropic behavior, whereas poor interactions produced strong gels with characteristic Newtonian behavior due to aggregate formation [59].

2.1.4.3 *Nano-Fibrous Suspensions*

The application of CNT and CNF reinforced composites share potential in the electronics industry as well as engineering materials in general. Processing nanotube or nanofiber suspensions must be understood to produce optimal properties. The addition of CNTs of CNFs to Newtonian liquids leads to non-Newtonian behavior strictly as an effect of the presence of filler. Therefore, the study of nanotube and nanofiber suspensions in small molecule liquids can be extended to more complex polymeric nanocomposites. Only a small volume fraction of nanotubes added to a Newtonian liquid is enough to dramatically change the rheological properties. Typical non-Newtonian behaviors, such as yield stress and shear thinning, have been shown to occur at volume fractions less than 1% [61]. Similar to other particles in suspension, the percolation threshold and rheological response (for example, onset and degree of shear thinning) are functions of nanotube orientation, aspect ratio, concentration, and even surface treatment [61], [62]. Advani and Fan [62] have recently discussed the effect of such variables for single-walled CNTs in epoxy suspensions.

Hough and coworkers [61] have achieved some success in effectively dispersing single-walled CNTs in water using a surface treatment, which produced aggregates no larger than 10 nm in diameter and a percolation volume fraction of 0.0026. Of the

dynamic responses probed, the increased storage modulus, shown in figure 2.7, for these suspensions at low frequency was due to the formation and strengthening of a percolated network of physical, freely rotating nanotube-nanotube interactions. At a strain amplitude greater than 1% strain thinning occurs; as such $G'' > G'$, depending on the CNT concentration. Hough et al. contrasted their nanotubes against actin suspensions [63] that flex and stretch, rather than bond together, to increase G' with concentration. At large strains liquid-like behavior exceeded the initial solid like response ($G'' > G'$) and suggested that the nanotube rods underwent rotations from their major axis to debond and disentangle from their nearest neighbors, and therefore the enhancement of G' is not due to flexing or stretching of the nanotube particles. Hough et al. also showed success in developing a model for the yield stress, based on arguments of Doi-Edwards theory [64] and stress-strain scaling, of the form:

$$\sigma_y \approx \frac{40k_bT}{V_{rod}}\left(\phi - \phi^*\right)^{3/2}, \qquad \text{.....(7)}$$

and, therefore, calculated a storage modulus that agreed reasonably with their data:

$$G' \approx \frac{\sigma_y}{\varepsilon} \approx \frac{40k_bT}{D_{eff}^3}\left(\phi - \phi^*\right)^2, \qquad \text{.....(8)}$$

where the quantity $40k_bT$ is the nanotube-nanotube bond energy [65], ϕ is the volume fraction, ϕ^* is the percolation volume fraction, V_{rod} is the volume of the rod and surface coating, and D_{eff} is the rotary diffusion coefficient from the theory of Doi and Edwards.

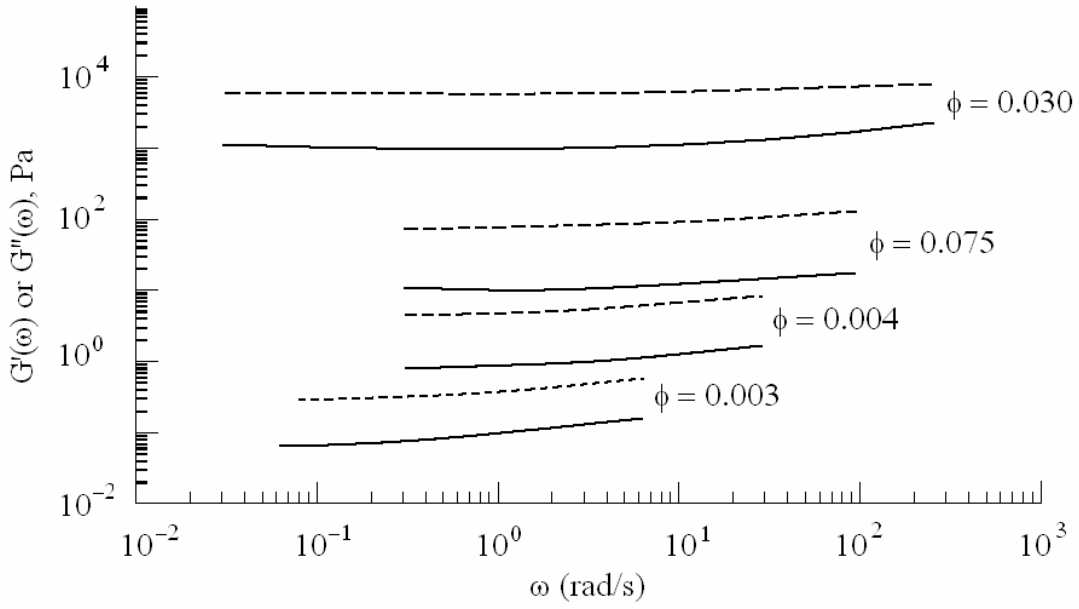

Figure 2.7. Storage and Loss Moduli as a function of angular frequency at 1% strain and for various CNT loadings, adapted from [61] Dashed lines – *G″*, solid lines – *G′*.

CNTs suspended in low molecular weight liquids show a negative primary normal stress difference similar to that observed in lyotropic rod-like liquid crystalline polymers. Davis et al. [66] suspended single walled nanotubes in highly concentrated acids and observed a positive primary normal stress difference at low steady shear rates but became largely negative at higher shear rates. In figure 2.8 is shown the shear dependency of both viscosity and N_1 for CNTs suspended in super-sulfuric acid. The explanation for such behavior was adapted from discussions of N_1 behavior found in the liquid crystalline polymer (LCP) literature [67-70]. For an oversimplified explanation, the negative N_1 was attributed to the transition from the rod-like structure rotating or "tumbling" to fluctuating or "wagging" about an axis under appropriate stress. The N_1 values turned out to be positive as the rods or tubes aligned in the flow direction. Larson [4] provided an in depth

general discussion of LCP rheology. Recent Stokesian dynamics simulations by Brady and Sierou [71] of low viscosity suspensions of concentrated low aspect ratio particles have shown large negative normal stresses under high deformation from interparticle lubrication, which could be the case for large aspect ratio fibers.

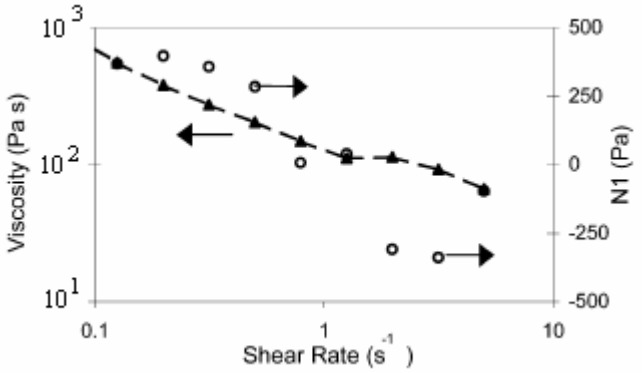

Figure 2.8. Viscosity and primary normal stress difference as a function of steady shear rate in a cone-plate rheometer for a 3.5 wt% single-walled nanotube suspension in 102% H_2SO_4. The authors draw the similarity to the triple zone LCP behavior [66].

In general, CNFs are larger than CNTs and push the limits of nanoparticle definitions of size. A recent paper by Xu et al. [39] examined the effect of CNF dispersant method on rheological properties, where the dispersant method is defined as the treatment applied to the nanofibers by acid wash, sonication, or both, before mixing with a glycerol and water solution. The authors observed that $G' > G''$ for low frequency shear rates and that suspension viscosity increased with nanofiber loading. The development of a yield stress combined with the prior two effects led to the suggestion of a percolated CNF entanglement network. Xu et al. [39] reaffirmed the entanglement

network from the observation of > 5 wt% CNF suspensions being too viscous for measurement. Yet, the suspensions tested shear- and strain-thinned, which was attributed to CNF alignment in the flow direction. Certainly alignment may occur, but an alternative may be from a lubrication effect of the small molecule solvent between the shearing (slip) planes of the CNF aggregates. Shear thinning diminished with decreasing particle concentration and aspect ratio, as previously noted by Brenner [72], and was caused by increased packing ability (see figure 2.3). In addition, all suspensions were non-thixotropic. Any breakdown of network structure due to alignment rapidly reformed because of the weak interactions between nanofiber agglomerates of non-Brownian nature.

2.1.5 RHEOLOGY OF NANOPARTICLE FILLED POLYMER LIQUIDS

2.1.5.1 *Polymer Layered-Silicate Nanocomposites*

The recent literature has examined the linear and non-linear viscoelastic properties of several clay-polymer combinations such as polyamides [73-79], polycarbonates [80-82], polyesters [83-86], polyolefin [87-97], polyvinyls [98-104], polystyrene [12, 105-107], polystyrene-polyisoprene block copolymers [108-111], thermotropic liquid crystalline polymers [112], [113], elastomers [114, 115], other copolymers [116, 117], and biodegrable polymers [11, 118] among others [119-121]. The majority of rheological studies have focused on using the rheological properties to assess the state of nanoparticle dispersion. G' from oscillatory shear flow in the linear viscoelastic regime gives the most obvious indicator of nanoparticle dispersion, because the composite will show a more

solid-like response as the percolation network limit is reached. Transient shear experiments probe the microstructure development for the effects of inter-particle interactions. However, dispersion or exfoliation of anisotropic nanoclay platelets in polymer matrices depends on many variables such as composite preparation, molecular weight of the polymer, nanoclay surface treatment, nanoclay aspect ratio distribution, particle-particle interactions, and particle-polymer interactions, to name a few.

2.1.5.1.1 Dynamic Storage Modulus in Linear and Nonlinear Oscillatory Shear

In the linear viscoelastic region, dynamic moduli reflect the viscous and elastic character of complex liquids through the quantities of G'' and G' respectively. Most studies focus on the development of the elastic character, G', with the addition of nanoparticle filler because these studies are ultimately searching for enhanced mechanical properties. Typically, if the polymer is inherently viscous in nature, G'' exceeds G', but when rigid and semi-flexible solid particles are added G' approaches or exceeds G''. Although a change in loss modulus may occur, the change in storage modulus is typically much more sensitive. Therefore, much of the discussion of dynamic moduli pertains to the effects on G'.

The specific interest in G' is based on the development and extent of a low frequency plateau, or non-terminal slope, where essentially the elastic character is independent of angular frequency. In general, in the terminal region the storage and loss moduli scale as $G' \sim \omega^2$ and $G'' \sim \omega$. The formation of the low frequency plateau indicates gelation of the particles into mesostructural domains, which dictate the solid-like response. Whether the mesostructure exists as a percolated or critically entangled

network or the solid-like response is due to geometric confinement is still under debate [87], [98], [108]. Rheology alone cannot determine the exact morphology, for example, between a soft-glass and gel [122]. Most rheological studies are complemented with electron imaging and light scattering to assess the degree of dispersion. The concentration at which this liquid-like to solid-like transition occurs depends upon the exfoliation or dispersion of the nanoclay within the polymer. Some of the factors dictating exfoliation observed in the literature are polymer matrix molecular weight, particle-particle interactions, particle-polymer affinity, platelet aspect ratio, etc. Associated with each of these factors are the effects of processing such as the method of nanocomposite formation (in-situ polymerization, solvent casted, melt blended) [see [2] for more examples], the surface treatment of the clays that allows for larger gallery spacing and functional sites for interaction, and the temperature of the test as some polymers are unstable at their melt temperature.

For conventionally filled composites, with greater than micron-sized particles, an increase in matrix molecular weight increases the magnitude of the low frequency storage modulus response at equal particulate concentrations greater than 30 weight percent. Nanocomposites require much lower amounts of filler to observe the same behavior. In a 3 wt% hydroxyl modified nanoclay and nylon 6 melt blended system, the terminal zone slope decreased with increasing molecular weight, as shown in figure 2.9 [76]. The authors believed that the increased shear from the longer and more entangled chains of the high molecular weight polymer aided the diffusion of chains into the platelet gaps, and exfoliated the nanoclays better than the lower molecular weights. Increased

exfoliation led to a greater number of stronger particle-polymer interactions that served to increase G'.

For aggregated systems of particles at equal molecular weight and filler loading, the stacked platelets have a smaller aspect ratio and interact less with the polymer chains so that the terminal slope scales near to $G \sim \omega^2$. In-situ polymerization typically produces well-dispersed nanoclay composites, whereas melt blending leaves some intercalated stacks. Although studies of in-situ and melt-blended composites of the same molecular weight and polydispersity index and clay concentration have yet to be conducted, the end-tetherment of polyamide to the clay during polymerization has shown qualitatively a more pronounced elastic response than the melt blended counterparts [73], [75], [76], [79], [80].

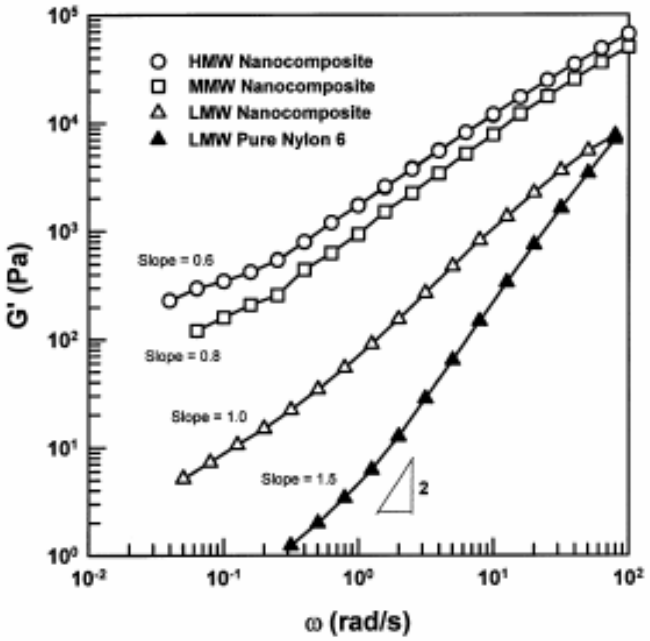

Figure 2.9. Role of polymer molecular weight on the G'. of melt intercalated 3 wt% hydroxyl modified nanoclay/nylon 6 composites. T = 240C, HMW ~ 30K, MMW ~ 22K, LMW ~ 16K. [76].

The literature has instead focused on the effect of organic modifier of the clay surface on the strength of particle-particle and particle-polymer interactions. Lee and Han [80] investigated the effect of hydroxyl-modified nanoclay on the storage modulus of polycarbonates. The authors reported very little change in the low frequency behavior of unmodified clay, but a low frequency plateau in storage modulus developed and broadened in frequency range for hydroxyl modified clay. The broadening of the plateau with clay concentration indicated the favorable interaction of PC and organically modified-nanoclay due to hydrogen bonding [80]. Yoon et al. [81] tested a myriad of clay surface treatments ranging from phenyl groups, long alkyl chains, and hydroxyl groups. However, direct comparison of the surface treatments was convoluted with significant molecular weight degradation of the PC phase. Even though the hydroxyl modified nanoclay preformed best in tensile tests, the molecular weight loss was greater than for some of the other composites tested, which showed higher G' plateaus in oscillatory shear [81]. Others observed degradation when dealing with polycondensates possessing carboxylic acid linkages [80], [82], [84]. A symptom of molecular weight degradation was manifested in dynamic moduli experiments when the low frequency storage modulus of the nanocomposites exceed that of the virgin polymer, but at higher frequencies the storage moduli of the nanocomposites are lower than those of the neat polymer, as shown in figure 2.10.

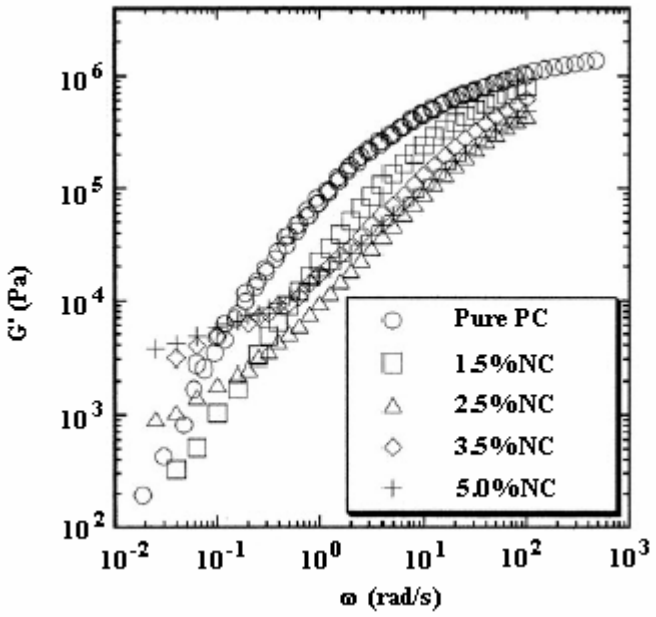

Figure 2.10. G' as a function of angular frequency for various PC and nanoclay (NC) composites as evidence of molecular weight loss, either by chain scission or depletion of continuous phase [82].

The cationic exchange of montmorillonite surface metals with organic salts lengthens inter-gallery spacing and provides better wetability between the polymer and clay. Sodium ions between galleries of fluoromica sheets were displaced by a long amine terminated polystyrene and a very short phenylethylamine to examine the effect of modifier length on exfoliation in a linear polystyrene of narrow polydispersity [105]. The lengths of the modifiers differed by a factor of 50. The results show for equal loadings of silicate a plateau in G' in the long chain modified composite and G' behavior no different than that of the matrix for the shorter modifier chains. Electron imaging confirmed the significantly more exfoliated platelets for the long-chain-modified clay, indicating that large agglomerates do not significantly contribute to composite viscoelasticity at low concentrations.

Additional compatibility between phases aids in nanoclay dispersion and enhancement of rheological properties. Nanoclay/polypropylene composites typically involve a polypropylene grafted maleic anhydride plasticizer to compatiblize the hydrophilic clay surface and the hydrophobic polyolefin. As in most systems, nanoclay content increases the storage modulus of polypropylene melts at low frequency [89], [90], [93-95]. At high angular frequency, the inclusion of maleic anhydride produces a decrease in G' at some concentrations, due to the possibility of maleic anhydride's ability to degrade polypropylene [89], [123]. A recent study by Lertwimolnun and Vergens [95] showed the plasticizing effect of maleic anhydride as the elastic response was reduced, but the ternary mixture of PP-MAH-nanoclay showed a maximum in the low frequency storage modulus with increasing anhydride loading, as shown in figure 2.11. This maximum corresponded to the optimal amount of compatibilizer required for the best exfoliation of a long alkyl-modified nanoclay/PP composite [95]. Polyethylene-g-maleic anhydride nanoclay composites showed enhanced low frequency moduli over PE/clay composites at equal clay loadings [96], [12]. Similar results were obtained with polystyrene [12].

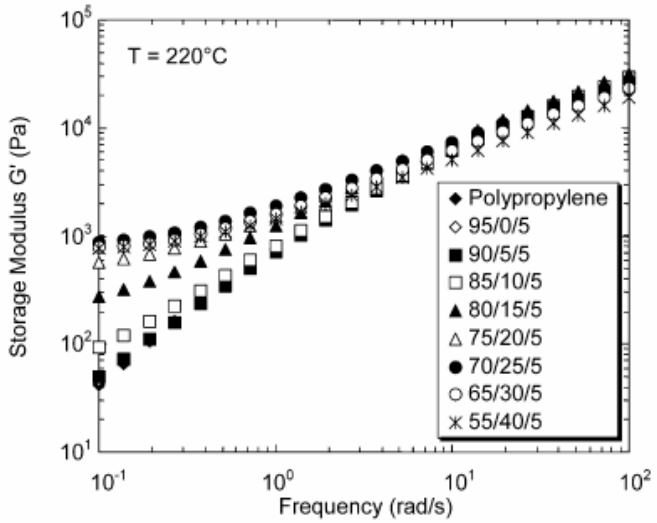

Figure 2.11. Effect of ternary compatibilizer on tallow modified nanoclay/PP composites, showing a maximum in G' with maleic anhydride concentration at low frequencies [95].

In terms of polyesters, maleic anhydride and pentaerythritol were used as compatibilizers in nanoclay/PET composites, but the effects of molecular weight degradation were too severe to draw any conclusions on the effect on G' [84]. A recent study by Wu et al. [85] examined the effect of a reactive epoxy on dispersing an organically modified nanoclay/PBT composite. At a constant nanoclay level the increase in epoxy compatibilizer increased the low frequency storage modulus response due to the greater number of PBT-epoxy-nanoclay interactions, which reduced the critical concentration for solid-like network formation compared to that of the PBT-nanoclay alone. Transesterification of the ester linkage of PBT was not observed by the authors.

Pre-alignment and pre-orientation of clay platelets to the flow direction before oscillatory shear decreases values of G' relative to those for the unoriented composites. The shear rate or strains required to align the platelets depends upon the numerous factors listed above. As the preshear rate increases subsequent oscillatory shear reveals a

reduction in solid-like behavior (i.e. plateau in G'). A recent study on nanoclay/PBT composites showed the strength of particle-compatibilizer-polymer interactions dictated the magnitude of preshear needed for orientation [85]. The authors also showed (figure 2.12) the crossover frequency, where $G' = G''$, decreased with alignment reflecting the loss of elastic modulus due to orientation as the viscous polymer controls rheological response. Not only is the terminal zone slope eliminated with preshear, but the elastic response diminishes as the particles orient with surface normals perpendicular to the flow direction [85]. Lim and Park [12] examined on the effect of particle alignment on polystyrene and polyethylene composites. Total alignment of clay sheets was observed when all the viscoelastic properties reach steady state and the moduli reflected attributes of the neat polymer.

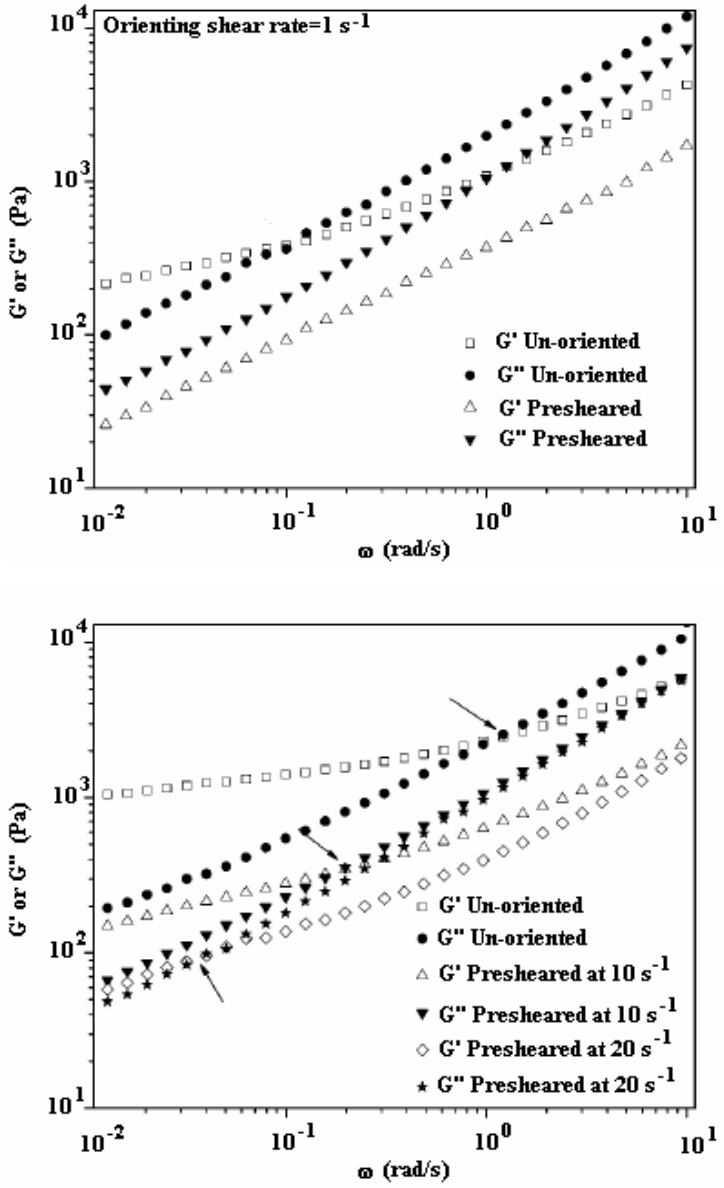

Figure 2.12. Effect of preshear on storage and loss moduli of (top) a 4 wt% hydroxyl modified nanoclay/PBT and (bot) 4 wt% hydroxyl-modified-nanoclay/ 4 wt% epoxy/ PBT composites [85].

Studies outside the linear regime are not as common. Dynamic moduli that decrease with increasing strain amplitude in filled systems have been known for many years and generally the phenomenon is referred to as the Payne effect [124]. Sternstein and Zhu [98] developed a mesostructural mechanism from the observed Payne effect in nanoclay

reinforced poly(vinyl acetate) and poly(vinyl alcohol) composites. The authors proposed the clay surfaces serve as contact points, and with the aid of Monte Carlo simulations [125] verified the “bridging’ and “training” of polymer chains between and along clay surfaces that effectively increased the entanglement distribution. In another study, nanoclay-polycaprolactam end-tethered polymer-brushes strain-hardened after alignment to the direction of shear flow [74]. Strain hardening behavior was attributed to the pull and push of chains attached to the silicate surface from in situ polymerization [74]. The critical strain amplitude for the onset of strain hardening decreases with addition of silicate surfaces available for attachment. In other words, smaller strains were required to raise the viscosity of more densely entangled, tethered nanocomposites, similar to the jammed colloid of Cates et al. [126].

2.1.5.1.2 Shear Thinning and Yield Stress Behavior

The addition of anisotropic nanoclay platelets enhances the low shear rate and low frequency viscosity of stable polymer matrices regardless of particle morphology. Subsequently, for a given concentration the degree of enhancement depends on the exfoliation with essential sub-factors such as surface treatment of the clay and the method of composite preparation. Typically as the clay concentration rises, the Newtonian plateau, if present in the neat polymer, gradually disappears until the percolation concentration is reached. At and beyond the percolation concentration, the composites exhibit strong non-Newtonian shear thinning at low angular frequencies and shear rates. Many authors reference the absence of Newtonian behavior as the presence of an apparent yield stress. Existence of a true yield stress may only be probed at very low

controlled stresses, and some believe true yield is fiction as all materials flow given a large enough time scale [127]. Nonetheless, the apparent yield stress occurs simultaneously with the observations of meso-structural networks and solid-like behavior. Larger apparent yield stresses indicate stronger inter-particle and/or particle polymer interactions. Thus, electrostatic charge and particle-polymer affinity play significant roles in viscosity behavior, which are very much similar to the effects on storage modulus.

Interestingly, at high shear rate or frequency there is little increase in viscosity, if not a decrease as in cases of continuous phase depletion. At large deformations the network can no longer hold together and viscous polymer behavior dominates the response. The polymer chains then open and intercalate platelet layers simultaneously aligning them to flow. Alignment to flow has been checked by imposing steady shear for prescribed periods followed by dynamic oscillations, which show a decrease in the composite viscosity from the destruction of the network. Light scattering methods have verified the orientation of clay platelets to the shear flow direction [92].

Furthermore, the Cox-Merz rule is generally invalid for these nanocomposites. Briefly, the Cox-Merz rule empirically states the equivalence of complex and steady shear viscosities, $|\eta^*(\omega)| \approx \eta(\dot{\gamma})$ for $\omega = \dot{\gamma}$, and works well for many homopolymers. Typically, complex viscosity data are greater than steady shear data, indicating network destruction by steady deformation in the low shear region, $< 10^2$ s^{-1}, and orientation of platelets in flow. Failure of the Cox-Merz rule is not unique to nanofilled materials, but has been observed in many conventionally filled polymer composites and liquid crystalline polymers among others.

In general, as molecular weight of the continuous phase increases shear thinning of the complex and shear viscosity become more pronounced. Fornes et al. [76] examined the effects molecular weight on viscosity for a melt compounded nanoclay/nylon6 system. Figure 2.13 shows that although all neat resins exhibited Newtonian behavior, shear thinning increased with molecular weight. The shear thinning behavior was attributed to increased stress that the higher molecular weight polymer exerts on the platelets, which effectively peels the layers and allows intercalation of polymer into the galleries [76]. At high angular frequencies the composites of each molecular weight do not show a significant difference in shear thinning, because of platelet alignment. Tung and coworkers [79] drew rough comparison between melt blended and in-situ polymerized nanoclay/nylon6 composite viscosities. In their study, at approximately equal clay concentrations the more exfoliated composite showed a greater steady shear viscosity, but equal shear thinning exponent. Many others have observed similar effects with different surface modifications [77], [80], [86], [93], [99], [119]. Lee and Han [80], [116] showed stronger particle-polymer interactions led to stronger shear thinning correlating to the presence of a stronger network. Hyun and coworkers [119] showed directly that an increase in clay modifier length produced a concomitant increase in exfoliation and complex viscosity in a PEO matrix.

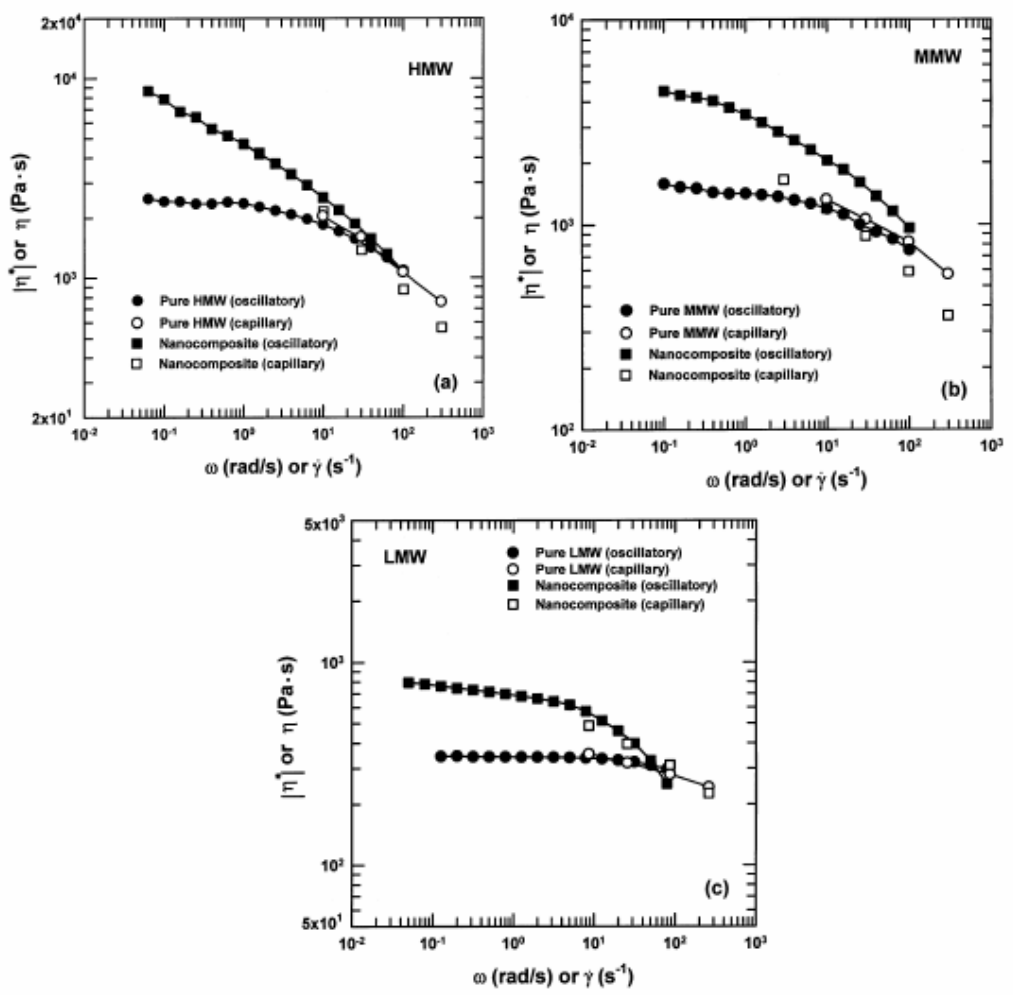

Figure 2.13. Failure of the Cox-Merz relation and the increased onset of shear thinning for three different molecular weights of nylon 6 and its nanocomposite of 3 wt% hydroxyl modified nanoclay [76].

Exceptions to the general observation of viscosity concomitantly increasing with filler loading do occur. Typically, these contrary observations occur in systems which degrade with filler addition. However, cases in which the molecular weight remains stable have been observed in capillary measurements of rubber-based nanocomposites and in dynamic measurements of soft-polymer particles suspended in the same linear polymer.

Sadhu and Bhowmick [115] observed that an apparent shear viscosity decrease may result from slip at the wall for nanoclay reinforced rubbers. The authors noted that the shear viscosity curve shifts downward to lower viscosities as the level of filler rose and decreases further when organically modified interacting clays were added. The processability of the rubber improved up to a critical concentration, at which particle agglomeration increased the shear viscosity (range $10\text{-}10^2$ s^{-1}). Figure 2.14 shows that the organically modified clay breaks up hydrogen bonds in the polar rubber and leads to a decrease in viscosity as rubber chains are more loosely bound in composites. Thus, Sadhu and Bhowmick [115] suggested the improved processability resulted from the nonpolar and unmodified nanoclays impeding the polar interactions between nitrile rubber chains. As an aside, the shear viscosity values increased for non-polar rubber/nanoclay composites.

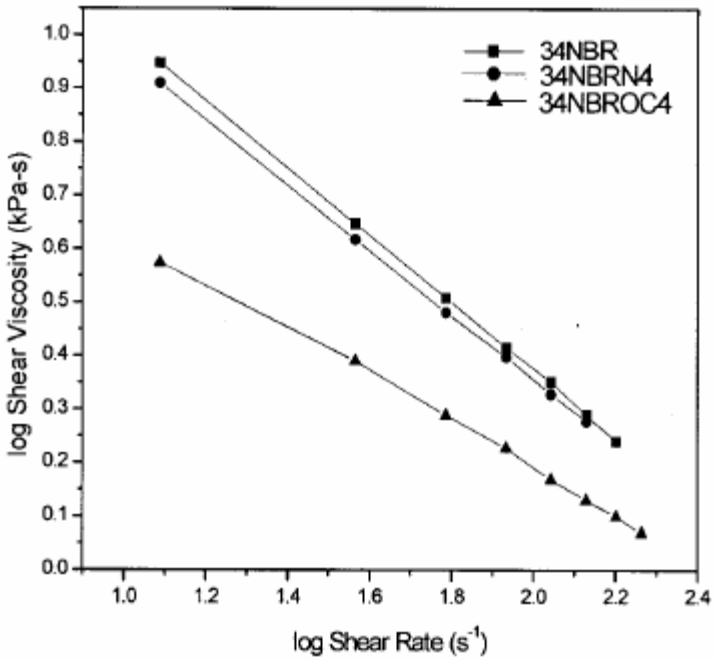

Figure 2.14. Decrease in apparent steady shear viscosity from capillary data on a acrylonitrile (34%) butadiene rubber (NBR) and its nanocomposite with unmodified (N4) and alkyl modified (OC4) nanoclays [76, 115].

Although collapsed or tightly crosslinked polymer particles may not be of high aspect ratio, these particles in suspension show viscosity decreases with increasing filler concentration. Mackay [128] has shown that in the absence of enthalpic restrictions dilute suspensions of well-dispersed crosslinked polystyrene nanospheres in a linear polystyrene matrix do not comply with Einstein predictions, i.e. relative viscosity decreases with filler concentration. A recent molecular dynamics simulation showed a qualitative agreement with the results of Mackay and coworkers [129]. The simulations showed that when the particles are smaller than the root-mean-squared radius of gyration, the particles act as a plasticizer to produce a viscosity decrease. Figure 2.15 shows the general trend of decreasing terminal viscosity with T_g as a function of tightly crosslinked PS nanoparticle concentration in linear PS. The zero shear or terminal viscosity was determined from the low frequency dynamic data. This genre of nanospheres increases the suspension free volume to decrease the composite glass transition.

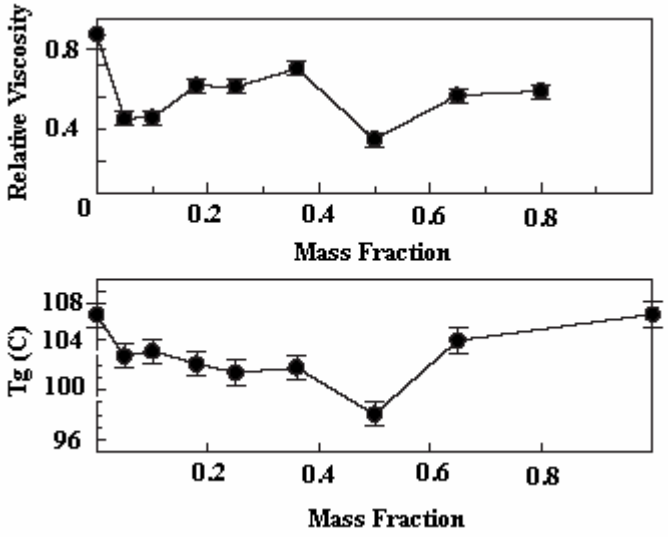

Figure 2.15. Relative viscosity and glass transition temperature as a function of filler mass fraction, for tightly crosslinked PS nanoparticles in a linear PS matrix [128]

In terms of yield stress in polymer layered silicate nanocomposites, Galgali and coworkers [87] observed the Newtonian behavior followed by a 3 order of magnitude decrease in viscosity within 500 Pa of shear stress of a relatively highly loaded (9 wt%) nanoclay/PP/maleic anhydride composite. The presence of a yield stress coincided with the low frequency nonterminal plateau in the storage modulus. The authors concluded that the solid-like or network response was a consequence of frictional drag imparted on the surfaces of the clay platelets. Yield stresses have been determined from phenomenological equations fit to low shear rate data. Ren and Krishnamoorti [108] applied Casson's equation:

$$\sqrt{\sigma_{12}} = \sqrt{\sigma_0} + \beta\sqrt{\dot{\gamma}}\,, \qquad \text{.....(9)}$$

to low shear rate data of a polystyrene-polyisoprene/organoclay composite. Here, σ_{12} is the shear stress, σ_0 is the yield stress, and β is a fitting parameter. Casson's equation provided an excellent fit to their data, as shown in the inset in figure 2.16. The yield stress increased slowly at low clay concentration and then accelerated at high loadings indicating the existence of strong solid-like behavior and a network-type of mesostructure. Lertwimolnun and Vergnes [95] used a five parameter modified Careau-Yasuda model (equation 10) to determine the yield stress from dynamic frequency data for PP-g-maleic anhydride nanocomposites:

$$\eta(\omega) = \frac{\sigma_0}{\omega} + \eta_0[1 + (\lambda\omega)^a]^{(n-1)/a}\,, \qquad \text{.....(10)}$$

where η_0 is the zero shear viscosity, λ is a time constant, a is the Yasuda exponent, and n is the power law index. The presence of compatibilizer increased the yield behavior of the PP/nanoclay composite, although the intercalation distance between platelets did not

significantly increase. Recently Zhong et al. [107] observed an apparent yield stress in polystyrene nanocomposites from superimposable scaling ($\eta \sim \dot{\gamma}$) of capillary and parallel-plate steady shear viscosity data. Reported yield stresses in electro-rheological fluids, such as polyaniline polymers, are enhanced with the addition of modified nanoclays beyond the percolation limit [120], [121].

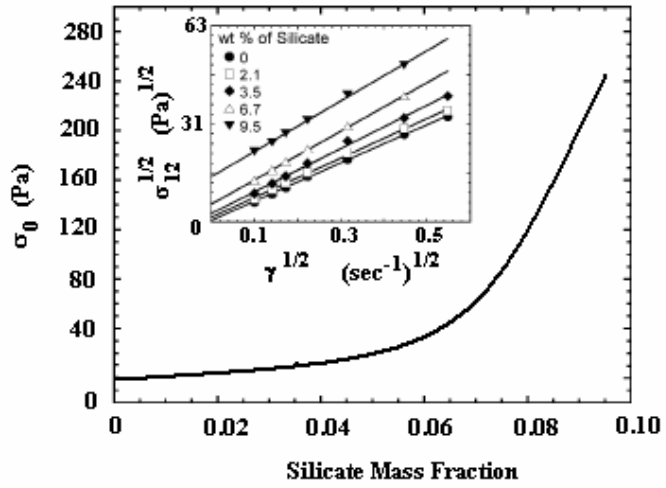

Figure 2.16. Yield stress as a function of clay loading and (inset) the correlation of experiment data to Casson's equation, for a PS-PI block copolymer. Yield stresses indicate the presence of solid-like behavior and some microstructural order [108].

2.1.5.1.3 Thermal Effects on Viscoelasticity in Nanoclay Polymer Composites

Time-temperature superposition (TTS) is used to probe linear viscoelastic behavior at frequencies out of the typical range of oscillatory rheometers via shift factors relative to a given temperature. Thermorheologically simple polymer layered-silicate nanocomposites have been formed from several polymer-clay combinations [73], [89, 94, 103, 108]. In each case the shift factors are, to good approximation, independent of clay

loading. A lack of temperature dependent relaxation of the silicate layers in the exfoliated composite leaves polymer chain relaxation to account for the superimposability of dynamic moduli [73]. Ren and co-workers [108] later added that intercalated chains between platelets relax on time scales much longer than those of the experiment and, therefore, show no contribution to TTS. This suggestion has led others to observe and recount the same non-Brownian effect from multilayered clay domains in polymer matrices [89], [94], [103].

TTS has not held for every polymer-nanoclay combination. The reasons for failure are different in each case. For a polystyrene-polyisoprene block copolymer above its order-disorder transition temperature, the moduli are superimposable. However, below this transition the changing matrix microstructure coupled with increasing agglomeration of particles with temperature lead to the failure of TTS at low frequencies [110]. Less exfoliated solvent casted PS/clay nanocomposites showed non-superimposable low frequency dynamic moduli, where the moduli of better dispersed in-situ polymerized composites proved superimposable, because of possible desorption of polystyrene chains from the clay surface as a function of temperature [107]. Gelfer et al. [99] proposed the formation of physical crosslinks between the clay surface treatment and the EVA chains, so that the polymer chains replace surfactant molecules on the clay surfaces. Yet, no spectroscopy was used to verify their hypothesis. In studies of PC/clay composites failure of TTS was proposed to be as a result of severe molecular weight degradation with increasing clay content and temperature dependent formation of a percolated network [82]. Furthermore, TTS failure was attributed to the formation of a temporarily hydrogen bonded network between polar clay surfactant and carbonyl oxygens in the PC backbone

that created divergent dynamic moduli at low frequencies [80]. Interestingly, Lee and Han [80] showed unmodified nanoclay/PC composites followed TTS, which could be due to of the hydrodynamic constraints lengthening the relaxation time as explained by Ren and co-workers [108]. Comparing the organic modified and unmodified cases, the weight loss of surfactant and/or polymer as a function of temperature could lead to low frequency non-superimposability.

2.1.5.1.4 Transient Rheology

Time-dependent rheology probes the transient effects of nanoclay loading on the temporal mesostructure development. The stress relaxation function from step strain and intermittent stress growth from the onset of steady shear shed insight into the relaxation processes and network formation behavior of the nanocomposites. In general, the curves of time dependent relaxation modulus, $G(t)$, increase and flatten in slope as the concentration of reasonably dispersed nanoclay increases [77], [93], [100], [103], [107], [111]. The upward shift and decreasing slope of $G(t)$ indicate longer relaxation times caused by the retardation of chain conformations from the presence of rigid two-dimensional clay platelets. Figure 2.17 (top) shows the retardation of PMMA chains by nanoclay particles that slow the relaxation dynamics shown by an increasing shift in linear relaxation modulus and onset of nonlinear strain amplitude [103]. Zhong and coworkers [107] found that the linear relaxation modulus of a PS/nanoclay composite was independent of temperature, suggesting that the colloidal interactions between platelets dominated the Brownian motions of the polymer chains.

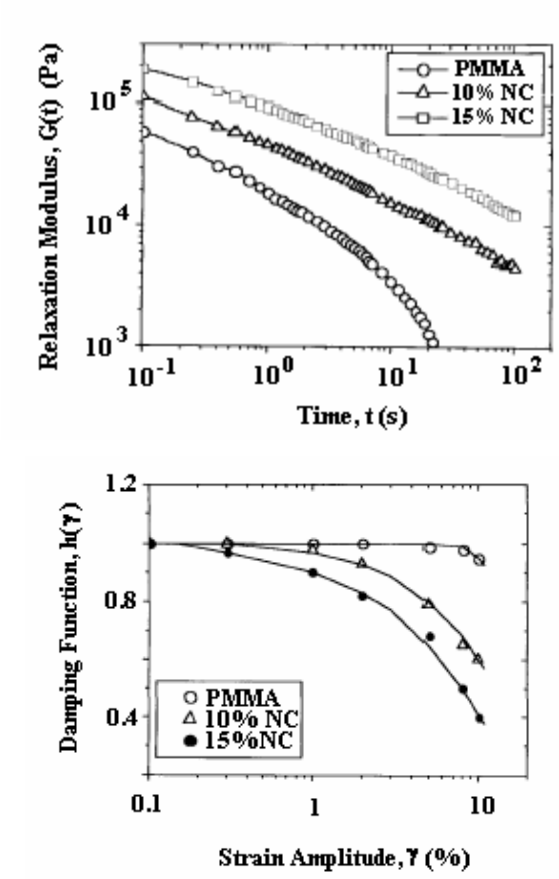

Figure 2.17. (Top) Low strain relaxation modulus $G(t)$ as a function of clay loading, line represents the fit to calculated relaxation spectra (Bottom) Characteristic damping function as a function of clay loading, line represents fit to PSM damping model [103].

The stress relaxation function, $G(t,\gamma)$, is typically expressed as a product of separable functions of time, $G(t)$, and strain, $h(\gamma)$ [130]. The damping function, $h(\gamma)$, is generally a non-linear function of strain at high amplitudes. Figure 2.17 (bottom) and subsequent studies conducted on $h(\gamma)$ revealed much stronger damping behavior characterized by the onset of non-linear behavior at lower strain amplitudes as the clay concentration increased [100], [103], [111]. The strain induced alignment of clay stacks was alleged to lead to such non-linear behavior.

The transient reformation behavior of nanocomposite mesostructure is typically quantified through stress growth observations as a function of time. Flow reversal experiments investigate the effect of nanoclay content and surface modification on the magnitude of stress overshoot, or the strength of network interactions, and the recovery time, the kinetics of network reformation. As expected, the magnitude of the stress overshoot and the time for recovery of the initial overshoot increased with the nanoclay concentration, as shown in figure 2.18 [80], [85], [89], [90]. An increase in nanoclay content increased the recovery time of stress overshoot, indicating that upon cessation of shear flow microstructural domains reformed and then strengthened depending on amount of clay-clay and clay-polymer interactions as well as time [89]. Surface modified organoclays that share favorable interactions with the matrix polymer also enhanced overshoot and recovery time more than unmodified nanoclay composites [80]. The stress overshoot in startup of shear depends on the distribution of particles and particle orientations that control particle-particle interactions [80], [89].

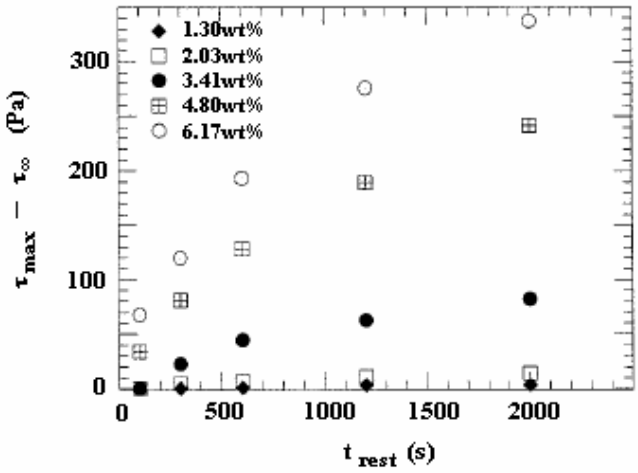

Figure 2.18. Magnitude of stress overshoot (represented as the difference between the peak stress and steady stress values) as functions of rest time (time allotment for structural reformation) and clay loading in PP/MAH matrix [89].

Solomon and coworkers scaled the stress overshoot with strain to probe the strain reliance of the particle-particle mesostructure and eliminate time-dependency (figure 2.19). The methods are similar to those used for evaluating the behaviors of LCPs except that the overshoots of Solomon's data did not scale in magnitude as they would for LCPs [4]. Low concentrations of intercalated clay in PP/MAH have shown no significant effect on stress overshoot indicating that the separation distance between dispersed stacks negated network formation. Furthermore, the recovery of stress for an unmodified clay/PC composite was found independent of deformation and rest time, while a possibly hydrogen bonded nanoclay/PC composite depended on adequate the time of recovery [80]. Wu et al. [85] found that a higher degree of flocculation between polymer and nanoclay prior to steady shear increased the magnitude of stress overshoot. Discussions in the recent literature have focused on colloidal reformation mechanisms as opposed to the Brownian motion of individual platelets [89]. Shear deformation is believed to break down and orient the intercalated clay stacks, which are too large for significant Brownian motion effects during flow. After cessation of shear flow, the local particulate domains aggregate and reorganize through interparticle interactions, which rupture and align upon subsequent steady shear.

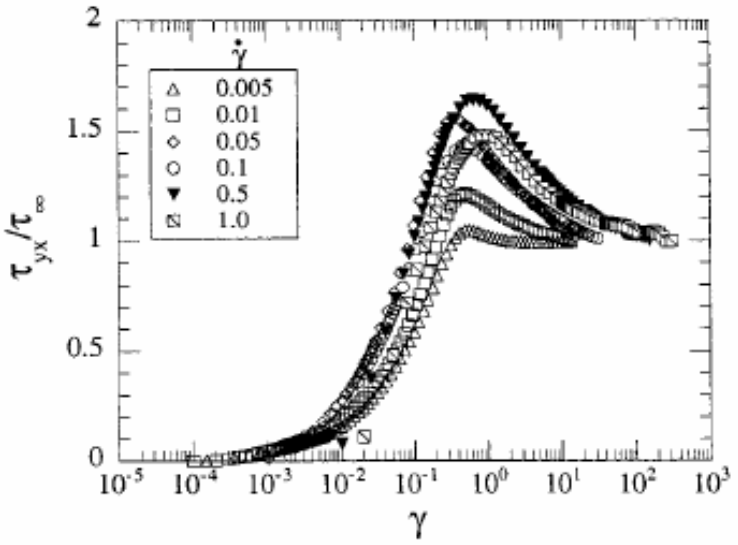

Figure 2.19. Stress-strain scaling of stress overshoot upon inception of steady shear flow for alkyl modified nanoclay/maleic anhydride/ PP composite.[89].

Rheopexy at very small shear rates has been observed for nanoclay filled polybutylene succinate [11]. The viscosity as a function of shear rate, between 10^{-3} and 10^{-2} s^{-1}, and nanoclay loading increased with time. The initial shear thickening, at steady shear, indicates the time scale of platelet alignment and orientation to the flow direction. Comparable to oscillatory shear, the particles dictate rheological response at low steady shear rate, but as the rate of deformation increases the polymer's contribution dominates and leads to shear thinning.

2.1.5.1.5 Normal Stresses and Flow Phenomena

A limited number of studies have examined the elastic behavior of layered-silicate nanocomposites. Current interest lies in understanding the significance of exfoliation as it applies to true elastic behavior. Yet, the scarcity of actual studies of N_1 results from suggestions that materials exhibiting large yield stresses complicate measurements of the

normal stress [131, 132]. Therefore, the already difficult to measure normal stress depends on the distribution of platelets orientations that cause yield stresses among other factors.

In the current literature on the primary normal stress difference, the available studies have shown that nanoclay concentration has either no effect on N_1 or reduces N_1 relative to the neat polymer within an equal stress range. In both studies the shear viscosity did not depend on clay concentration at high shear rates, which has been shown to reduced elasticity in conventionally filled composites [101]. Additionally, matrix degradation with clay content was not observed, and polymer/clay compatibility produced well-dispersed intercalated composites. The influence of clay on N_1 may then depend on a relationship between the polymer and particle surface treatment. A block copolymer may not wet the particle surfaces sufficiently, because of the possible difference in block affinity for surface treatment, which creates weak polymer block-to-particle interactions and relatively little effect on elasticity. Therefore, in the case a strongly interacting polymer-particle systems, a decrease N_1 should be expected, but further studies are required to verify these conclusions.

However, the presence of nanoclay up to 9.5 wt% in a polystyrene-1,4 polyisoprene block copolymer showed no effect on the steady state values of N_1 [109]. Krishnamoorti et al. [109] ruled out the complications due to yield stress and confined local stress gradients that would produce slip between layers, because of the independence of viscosity and N_1 on nanoclay concentration. Instead the authors suggested that the absence of any influence of clay concentration was due to the alignment of the two-dimensional silicate layers under shear flow. It was reported that the orientation of the

fillers in the flow direction eliminated surface to surface interactions between platelets and reduced the elastic energy.

Yet the observations of Gupta et al. [101] showed a decrease in N_1 with increasing clay content at high shear stresses on the order of 10^3 Pa (see figure 2.20). Figure 2.20 shows that increased nanoclay content restricted relaxation and reduced the elasticity of the composite melt compared to the neat polymer. Thus, the reduced N_1 reflected the strong tendency of the exfoliated platelets to restrict the motion of polymer chains [101].

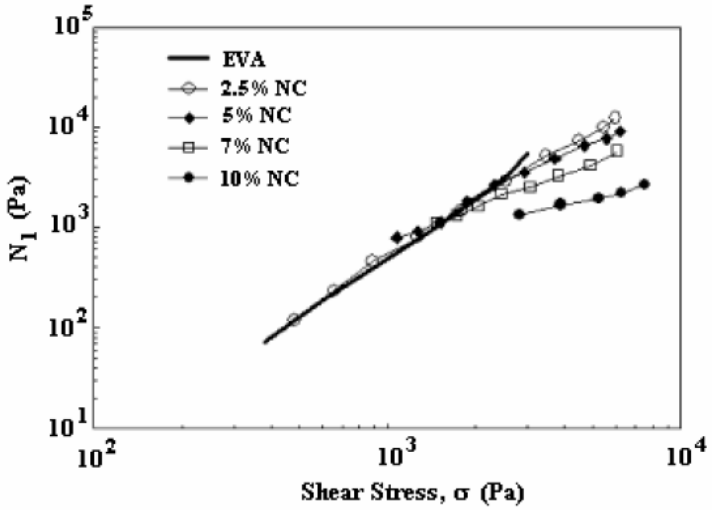

Figure 2.20. Primary normal stress difference as functions of shear stress and organoclay (NC) content in EVA nanocomposites [101].

The phenomenon associated with the increase of the diameter of an extrudate as a melt leaves a capillary is known as die swell or extrudate swell, and defined as:

$$Die\ Swell\ \% = (D/D_o - 1) \times 100 \qquad .....(11)$$

where D is the extrudate diameter and D_o is the die diameter. Consistent with the observations of decreasing N_1 with increasing clay content, the die swell of nanoclay

composites was less than that of their neat polymers [107]. Die swell was also reduced in more exfoliated elastomeric polymers because of favorable polar interactions between clay surface treatment and acrylonitrile butadiene rubber [115]. Table 2.1 shows that for the case of nonpolar polybutadiene, die swell increased with clay loading and was attributed to poor particle-polymer interactions leading to particle agglomeration. For PS composites an increase in surface modified nanoclay concentration significantly reduces extrudate swell percentage. The overall reduction in die swell is a reflection of the retardation effect that the nanoclays have on the polymer relaxation time, much like the increase in time-dependent relaxation modulus.

Matrix	Filler	Conc.	Die Swell (%)	Ref.
Polystyrene	None	-	57.0	106
	Alkyl modified NC	4 wt %	20.0	106
	Alkyl modified NC	9 wt %	4.0	106
Polybutadiene	None	-	52.9	114
	Unmodified NC	4 wt %	46.4	114
	Modified NC	4 wt %	59.7	114
Poly(styrene-butadiene) rubber	None	-	39.1	114
	Unmodified NC	4 wt %	38.4	114
	Modified NC	4 wt %	34.8	114
Poly(butadiene-acrylonitrile) rubber	None	-	62.2	114
	Unmod. NC	4 wt %	52.0	114
	mod. NC	4 wt %	49.1	114

Table 2.1. Effect of unmodified and surface treated (modified) nanoclay (NC) on the extrudate swell response from a capillary at constant shear rate given in the reference.

In terms of flow stability, the critical shear rate for the onset of melt fracture was delayed up to 2-3 times the original threshold for an onium ion modified nanoclay in linear low density polyethylene (LLDPE) with a large reduction in extrusion pressure [97]. Figure 2.21 shows the critical shear rate for the onset of gross melt fracture for a PP melt was delayed up to 170% the original shear rate when melt blended with 0.5wt% nanoclay. A combination of nanoclay with a fluoropolymer, known to be a processing aid, postponed critical shear for appearance of sharkskin to 10 times the critical value of neat LLDPE [97]. Interestingly the authors observed no or little change in critical shear rate for unmodified clays at equal concentrations as the modified nanoclays.

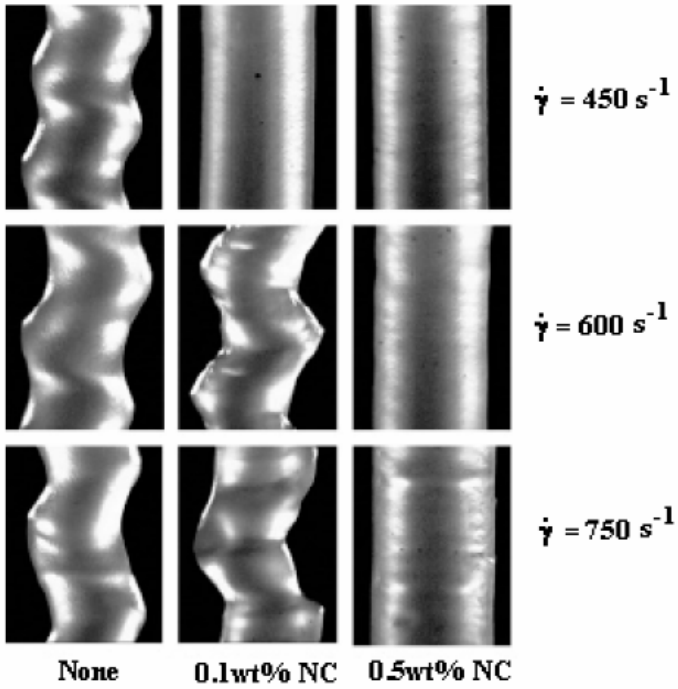

Figure 2.21. Suppression of critical shear rate for the onset of melt fracture for a pure PP melt, a 0.1 wt% and 0.5 wt% onium ion modified nanoclay/PP composite [97].

2.1.5.1.6 Extensional Rheology

Most rheological studies have focused on the effect of nanoclay concentration on the time-dependent uniaxial elongation viscosity expressed in units of time or Hencky strain [88], [101], [103], [104]. Predictions from linear viscoelasticity indicated that the extensional viscosity curve at low extension rates was equal to 3 times the zero shear viscosity, frequently called Trouton's ratio. Some studies have reported that this ratio holds for nanoclay composites in cases where a near steady state extensional viscosity is observed [103]. Others attributed the failure of Trouton's ratio to different mechanisms of mesostructural formation in shear compared to uniaxial elongation [88], [101]. No matter the system, the onset of strain hardening is always increased with the addition of nanoclay compared to the neat polymer. To draw an analogy, pure polyethylenes, with varying degrees of long chain branching, showed increases in strain hardening with the addition of polymer chain entanglements [133]. Thus, the presence of clay in the polymer matrix may create more entanglements or stronger polymer-clay networks that resist extensional deformation.

Early literature suggested the clays took a house of cards structure in an intercalated PP composite [88]. The card house reflected the flocculated edge to face colloidal interactions between the clay layers, which may have been a result of the presence of small amounts of maleic anhydride [88]. A shift in polarity of the suspending medium results in a change of interaction between the clay platelets, from face-face to edge-face attractions [1]. Yet, Okamoto and coauthors [88], by transmission electron microscopy (TEM) imaging, revealed platelets arranged with faces normal to the flow direction after deformation and not as a function of deformation time. Thus, localized stress variations

between intercalated sheets may have created forces insufficient to induce alignment of all platelets in the flow direction.

More recent extensional viscosity studies have shown that the platelets align in the flow direction [104], [134]. Electrospun unmodified montmorillonite nanoclay and poly(MMA-co-MAA) copolymer composites showed (figure 2.22) a greater degree of strain hardening than larger sized particle composites and neat copolymer [104]. The increased strain hardening aided the formation of finer filaments of less than 500 nm in diameter [104]. Such a thin and uniform fiber could have only been produced from clay platelets aligning to the flow direction, because the length scale of a single platelet is of the diameter order of magnitude. Alignment of the platelets in the flow direction has been considered critical for stable fiber formation of nanocomposites [134]. The authors observed that less exfoliated larger platelets, which produced less uniform "drops" of large agglomerates still aligned in the flow direction. TEM analysis confirmed the exfoliated and aligned nanoclay structure. TEM and WAXD experiments on drawn polypropylene nanocomposites have verified the orientation of clay platelets in the flow direction [91], [94].

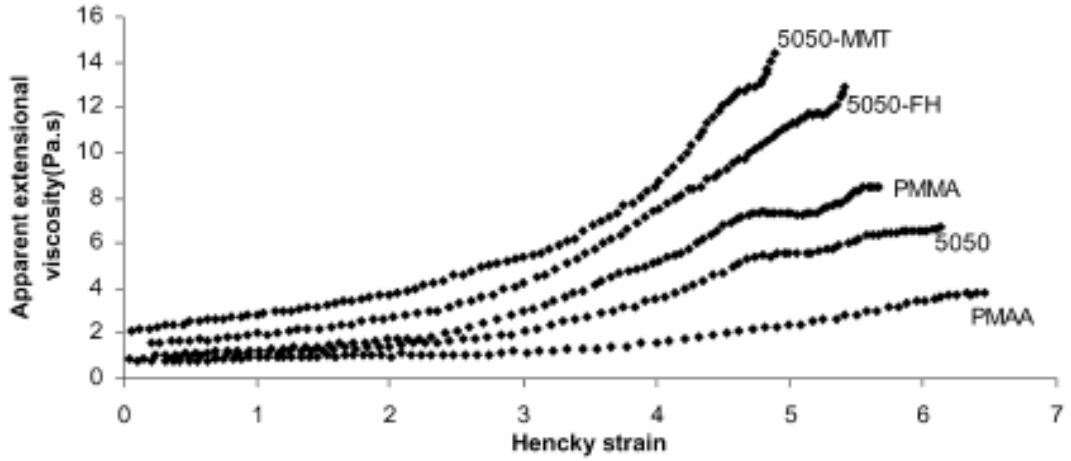

Figure 2.22. Extensional viscosity as a function of Hencky strain for 8wt% nanoclay (MMT) and fluorohectorite (FH) suspensions in a 50/50 copolymer of PMMA and PMAA [102]. In terms of size: FH >> MMT.

Gupta et al. [101] observed that although the onset of strain hardening was increased by the addition of nanoclay, at large Hencky strains the viscosity of the composites was less than that of the neat EVA matrix. The behavior, as shown in figure 2.23, suggested a competition between polymer-polymer and polymer particle interactions; such that the entanglement density created by the filler is reduced leading to lower stress. However, the possibility of colloidal interactions for well-exfoliated platelets cannot be eliminated. High extension rates geometrically bring clay platelets into close contact, as the cross section is reduced with the square of the elongation rate. The decrease in plate separation gives rise to increased surface-to-surface attractions creating larger flocculated clay stacks [101]. The larger stacks of clay have trapped intercalated chains of EVA between the clay sheets, which effectively reduce the number of possible polymer chain entanglements necessary to produce further strain hardening [101]. TEM results verified the agglomeration of stacks after deformation.

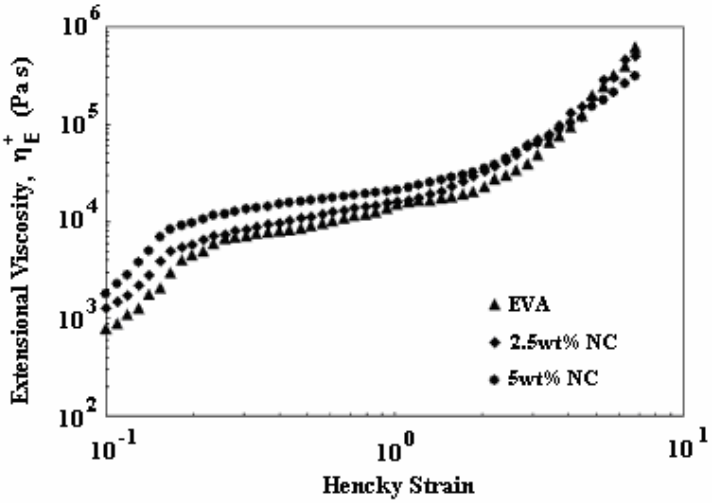

Figure 2.23. Extensional viscosity as function of Hencky strain and nanoclay loading for an alkyl ammonium modified clay melt blended with EVA [101].

2.1.5.2 *Rheology of CNT and CNF Polymer Nanocomposites*

To reap the rewards promised by increase electrical conductivity and increased elasticity in polymer-nanotube composites, the concentration of carbon nanotubes or nanofibers must exceed the percolation limit, which is exceptionally low compared to the silicates above. The critical volume fraction for the onset of percolation networking is inversely proportional to the cylinder aspect ratio for randomly dispersed particles [135]. As expected, enhancements of rheological properties occur at much lower concentrations of nanotubes than nanofibers because of the roughly order of magnitude difference in aspect ratios. However, these changes in rheological behavior depend on the polymer-nanocylinder network formation and not simple geometric confinement.

2.1.5.2.1 Dynamic Oscillatory Shear Measurements

Dispersions of CNTs in polycarbonate, polymethylmethacrylate, and polypropylene are among the few composites examined for rheological behavior. Despite the polymer matrix, increasing the concentration of nanotubes, either single or multi-walled, the complex viscosity increases. The degree of viscosity increase depends on the molecular weight of the polymer, the dispersion of the nanotubes, the isotropy of the tubes within the matrix, the nanotube aspect ratio distribution, and processing conditions. Therefore, the critical concentration for a percolated network structure depends on these factors as well.

A recent study examined the relationship of storage modulus to molecular weight of the polymer matrix at the same level of carbon nanotubes loading. For a 0.5 wt% CNT/PMMA nanocomposite, the higher molecular weight polymer showed a low frequency storage modulus plateau that was an order of magnitude greater than the lower molecular weight polymer, which deemed the rheological behavior as not dominated by the nanotube network [136]. The authors proposed the longer polymer chains restricted the motion of the tubes through the matrix, thus increasing storage modulus response and complex viscosity. The same authors reported the effect of nanotube dispersion or exfoliation within the polymer matrix. As the dispersion of the CNTs increased, the storage modulus curve shifted from terminal to non-terminal slopes and the low frequency modulus increased. Therefore, the percolation threshold for agglomerated systems increased to higher concentrations, which reflects the influence of aspect ratio. Agglomerated particles have smaller effective aspect ratios and, hence, the ability of these larger particles to percolate the matrix decreased. Figure 2.24 shows the rheological and electrical percolation threshold shown by the insulator-conductor transition as the

conductivity increases 8 orders of magnitude over a 0.01 volume fraction increase and the shift toward solid-like behavior in the development of a 5 order of magnitude increase and non-terminal slope in G' from dynamic measurements.

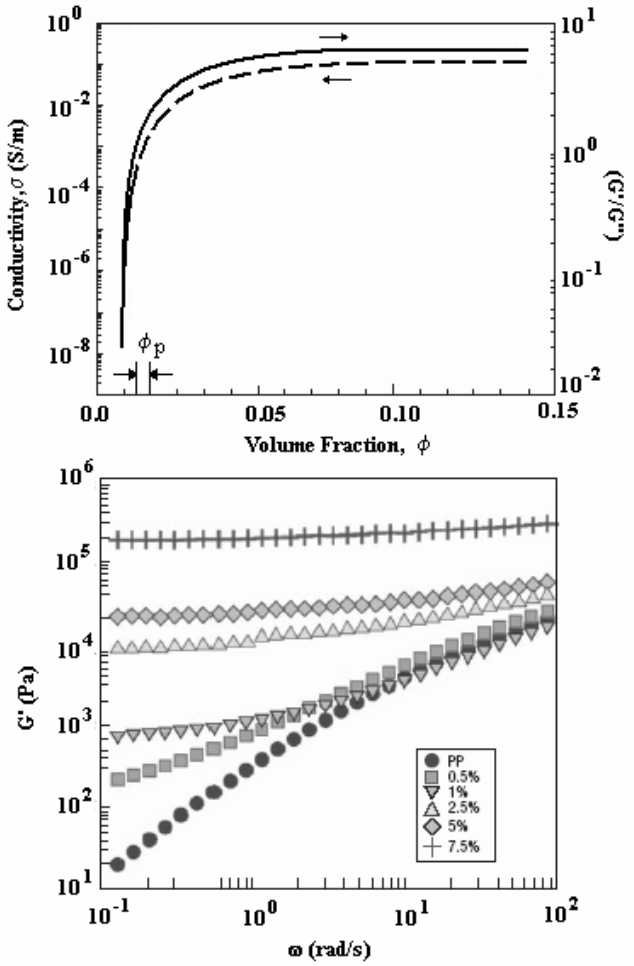

Figure 2.24. (Top) Electrical conductivity and inverse loss tangent, expressed as G'/G'', as a function of CNT volume fraction in a PP matrix. (Bottom) G' as a function of angular frequency and CNT loading (vol%) melt blended with PP [137].

Two studies indirectly showed the effect of longer processing time and higher temperature during processing. Potschke et al [138, 139] examined CNTs in different PC matrices. The authors observed a lower percolation threshold decrease to lower a concentration when the CNT and PC were allowed longer mixing time in a hotter extruder. Longer mixing time is traditionally believed to aid dispersion of particles, while the higher temperature could have stimulated chain motion to permeate and disperse the CNT domains.

Disentangled and agglomerated CNTs readily move with the matrix and diminish the shear thinning behavior of the suspensions. The observation that the onset of strong shear thinning of the complex viscosity with angular frequency as the concentration of nanotubes increases, denotes the percolation threshold. The material changes from liquid-like to solid-like in response. The shear thinning behavior of CNT/polypropylene composites was fitted to the Carreau model to quantify the degree of shear thinning with concentration [137]. Potschke et al. [139] concluded that the shear-thinning exponent decreased with CNT content and eventually became constant at higher loadings. However, at higher angular frequencies the rheological effects of nanotube concentration were weakened. Du et al. [136] suggested that the CNTs did not affect the polymer chain dynamics, which was exemplified by the invariance of glass transition temperature with nanotube loading.

Dynamic shear provides a valuable insight into the relationship between rheological and electrical percolation. Less dense nanotube networks are not effective conductors of electricity, yet on average only one third of nanotubes are metallic. Therefore, electrical percolation thresholds require slightly larger amounts of nanotubes than rheological

limits to ensure conductive contacts permeate [140]. Even though, for some matrices the electrical and rheological limits are nearly equivalent [137, 138].

The rheological attributes of CNF suspensions in polymer melts are essential by the same as CNT suspensions, except the phenomena indicating network formation occur at higher concentrations. Potschke et al. [139] reported a percolation concentration of CNT in a PC matrix an order of magnitude lower than the concentration required to form a network of CNFs in PP [141]. The rotations of short CNF were restricted by nearest neighbor interactions, because as the length of the fibers decrease the likelihood of fiber-fiber entanglements also declines [142]. Although solid-like behavior is observed in short and long CNF suspensions, the concentration for a critical network structure decreases with increasing length. The non-terminal slopes of storage modulus with angular frequency and the development of stronger shear thinning elucidate these observations expected from the close similarity to CNT suspensions.

Identification of the percolation limit is not always obvious from complex viscosity data, such as in cases where the matrix possesses an inherent microstructure. A comparison of complex and steady viscosities showed that the Cox-Merz rule is not applicable to system of thermotropic liquid crystalline polymer (TLCP) and CNF [143]. The isotropic ordering of liquid crystalline domains eliminated the low frequency Newtonian plateau, making the percolation threshold not as obvious from viscosity data alone. Therefore, the authors believed that the transition of the composite from originally viscously dominated, $G'' > G'$, liquid-like behavior to elastically dominated, $G'' < G'$, solid-like behavior with increasing concentration of CNFs marked a clearer network formation limit.

2.1.5.2.2 Normal Stress Difference and Elastic Effects

Studies of normal stress differences of CNT composites are rare, but the understanding is essential for processing applications. The sign of the primary normal stress difference appears to depend on the percolation concentration. From parallel plate steady shear experiments, Kharchenko et al. [137] determined the primary normal stress difference decreased with increasing nanotube loading shown in figure 2.25 (note this plot is $\Delta N = N_1\text{-}N_2$ vs. shear rate). Not only did N_1 decrease, it also became largely negative as the percolation concentration was exceeded. Typically, highly entangled polymer melts under shear exert a force against the plates that pushes them apart, creating a positive normal force. Cone and plate data revealed the primary normal stress difference was negative. The authors proposed that the large and negative N_1 was a consequence of the deformation of the percolated nanotube network by simultaneous stretching in the flow direction and compression in the direction normal to flow. These actions could be coupled to the elasticity of the nanotube cylinders, which may distort the flow streamlines similar to simulations of flexible fiber suspensions that were also shown to exert a negative normal stress difference [125].

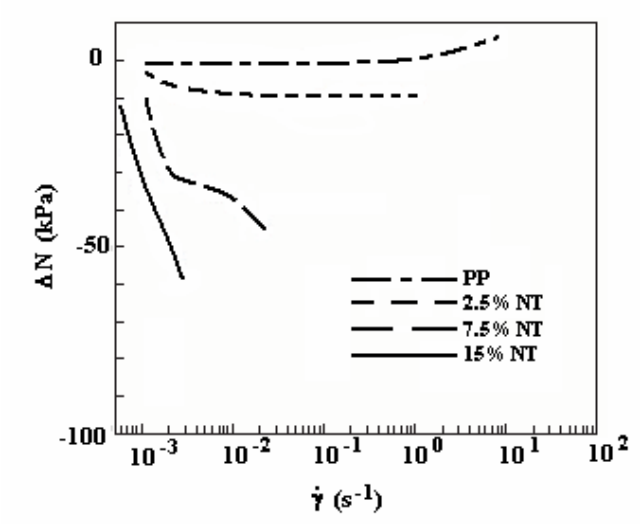

Figure 2.25. Negative normal stress difference from parallel plate rheometry ($\Delta N = N_1 - N_2$, where N_1 was deemed the more negative quantity) as a function of nanotube (NT) loading melt blended with PP [137].

A result of a negative normal stress difference may be the suppression of die swell behavior. Polyolefin melts, among others, show a post die expansion of the extrudate diameters that can range between 2-6 times the die diameter depending on molecular weight and extrusion rate. The addition of 2.5 vol % CNTs, a concentration above percolation, to a PP matrix showed a dramatic reduction in diameter compared to pure PP from the same die [137]. The authors also noted that CNT addition prevented shape distortion and the extrudate diameter was smaller than the die. The reduction of die swell has been observed for other systems such as polymer layered-silicate nanocomposites.

2.1.6 CONSTITUTIVE THEORIES FOR NANOPARTICLE FILLED POLYMER MELTS

2.1.6.1 *Rheology and Structure*

In this section we address whether fluids (primarily polymer melts) containing nano-particles require any special considerations concerning their rheology. Before one can model their rheology, it is necessary to have knowledge of their structure. We have seen that there is a plateau in G' at low frequencies similar to materials with yield stresses. We have also seen that peaks occur in the stress growth behavior and stress relaxation is retarded significantly. As we saw in section 2, dispersion or exfoliation of the individual platelets and particles is very difficult and, hence, the structural state of the system is unclear. As a result there are a number of questions which need to be answered. Is the rheology due to the effect of nano-size particles with high surface area? Is Brownian motion a significant factor in the process of relaxation? Is the structure possibly a percolated network in which recovery of structure is driven by thermodynamics? A knowledge of this structure is pertinent to not only developing constitutive equations but to understanding the state of the composite. In other words, the knowledge of the rheology may be an indicator of the state of the nano-composite (e.g. intercalated or exfoliated). In this section we review those rheological studies aimed at understanding what approach is required to model the rheology of nano-composites and studies concerned with modeling the rheology of these systems.

Solomon and coworkers [89] carried out an intensive rheological study involving both linear and non-linear shear behavior of polypropylene (PP) containing nano-clay particles. The particular system consisted of PP hybrid clay structures prepared using

amine surfactants to promote intercalation. Above a concentration of 1.3 wt%, G' and G'' exhibited plateaus at low frequencies indicative of a viscoleastic solid or viscoleastic fluid with a characteristic relaxation time > 10^2 s, as no terminal region was observed for $\omega < 0.01$ s^{-1}. This was attributed to either the existence of a percolated network or rotational relaxation of anisometric clay platelets or platelet domains. Time-temperature superposition could be used to shift data obtained over a range of temperatures from 165 to 210 ^oC to obtain a single master curve. The shift factor for the pure PP and composite were identical. This peculiar time-temperature superposition behavior was attributed to non-Brownian structure of the hybrid material [111].

To further explore the structure of these hybrids two additional non-linear rheological experiments were carried out by Solomon and coworkers [89]. Flow reversal experiments were carried out in which samples were sheared for 300 s at a shear rate of 0.1 s^{-1}. The flow was stopped and the sample was held quiescently for various times (0 to 2000 s) and then sheared in the reverse direction for 300 s and the same shear rate. The degree of stress overshoot was strongly dependent on the rest time which was believed by the authors to be a strong indication that the structure of the hybrid material evolved under quiescent conditions. The recovery could be due to either Brownian motion or strong thermodynamic interaction (i.e. aggregation). Reorganization due to Brownian motion can only be relevant if the characteristic dimension of the hybrid structure is sufficiently small. The crossover from Brownian to non-Brownian behavior in a flowing suspension is controlled by a rotational Peclet number (or Weissenberg number):

$$Pe = \frac{\dot{\gamma}}{D_r}, \qquad \text{.....(12)}$$

where D_r is the rotational diffusion coefficient for a circular disk given by:

$$D_r = \frac{3k_bT}{4\eta_s d^3} \quad , \qquad \text{.....(13)}$$

where η_s is the viscosity of the suspending medium. For the PP melt used by Solomon et al. (η_o = 2000 Pa s) it is estimated that d may be no larger than 300 nm for rotational relaxation to be due to Brownian motion. Individual clay particles are thought to have diameters in the range of 100 to 300 nm and, hence, if the particles were fully exfoliated and non-interacting, then Brownian motion could account for the recovery of structure.

The second set of experiments consisted of the stress growth behavior at the start up of shear flow. Solomon and coworkers [89] reported that the shear stresses scaled with strain. They interpreted this behavior to be characteristic of materials that possess no characteristic time scale such as thermotropic liquid crystalline polymers and non-Brownian suspensions of rods and disks [4]. However, for the scaling to be complete, the magnitude of the normalized stress must also scale with shear rate, and it did not as shown in figure 2.19. Entangled polymer melts also exhibit scaling of the peak stress with strain but not its magnitude [4]. Hence, it is unclear whether the interpretation of the results is correct.

From their work Solomon and coworkers [89] concluded that the structure most consistent with the experimental observations is one of non-Brownian particulate domains that are thermodynamically unstable and anisometric. The particulate domains were believed to consist of aggregates of multiple ordered platelets. Linear viscoelastic measurements alone could not be used to determine whether the platelet structure was networked or dispersed. Their interpretation was primarily based on their observation that

the stress overshoot scaled with strain, which we have argued is not complete scaling as the magnitude of the normalized stress should also scale with shear strain. The linear and non-linear rheological properties were consistent with a hybrid structure of a weakly agglomerated network of multi-platelet particulate domains that was ruptured and reformed under flow and quiescent conditions.

For a suspension of nanotubes in a viscous solvent, the composite structure was that of a percolated network that heavily depended on particle-particle interactions. Kharchenko et al. [137] made similar calculations on the rotary diffusion coefficient to determine the dominating forces under flow. For a semi-concentrated suspension of rod-like particles [144]:

$$D_r = \frac{\beta k_b T \ln(a_r)}{3\pi\eta L^3 (nL^3)^2} \qquad \text{.....(14)}$$

where β is unity (from Doi and Edwards [144]), a_r is the nanotube aspect ratio, n is the number density of nanotubes, and L is the length of the nanotube. Kharchenko and coworkers determined that the Peclet number was of the order $10^{14} - 10^{16}$ and due to the large viscosity of the melt phase and relatively long nanotube length. Thus, for suspensions of multi-walled CNTs in viscous fluids the contribution of Brownian motion was negligible. Therefore, the rheological response of the percolated network structure was due to frictional and hydrodynamic forces.

2.1.6.2 *Modeling the Rheology*

Based on the discussions above, the polymer-nano-particle mixtures most frequently consist of non-Brownian particulate aggregates and on occasion single isolated particles (exfoliated). Various approaches have been proposed for describing the

rheology of polymer-particle mixtures but with no specifications concerning particle size. Most of the models are based on network theory for the case of polymer-particle and polymer-polymer interactions but not for the agglomerated structures.

Ren and Krishnamoorti [111] proposed that the rheological behavior of polymer and clay nanocomposites at low shear rates resulted from the development of a three-dimensional percolated network meso-structure which is similar to the ideas of Solomon et al [89]. At higher shear rates the silicate layers align and steady state rheological properties approach those of the unfilled polymer [111]. Although it is unclear that the structure of polymer nano-clay composites would lead to rheological properties appropriately described by the K-BKZ constitutive equation, they evaluated the ability of this model to capture the rheological response of polystyrene-polyisoprene diblock copolymers and organically modified montmorillonite composites. They used step strain experiments to obtain the strain dependent relaxation modulus, $G(\gamma,t)$ as a function of time. They found that time-strain separability was valid for the composite materials but over a much smaller range of strain than that for the pure matrix. Furthermore, they found that a damping function of the form [145] (referred to as the PSM damping function):

$$h(\gamma) = \frac{1}{1 + \alpha\gamma^2} \qquad \text{.....(15)}$$

fit the nano-clay composite data well for clay concentrations from 0 to 9.5 wt%. The onset of strain for shear thinning decreased with increasing silicate loading for concentrations greater than 3.5 wt% and time-strain separability was valid only at much lower strains. They speculated that this behavior was due to the highly anisotropic silicate layers orienting when subjected to moderate and large strains. Furthermore, they speculated that this was the cause of shear thinning rather than confinement-induced

shear thinning [146] or shear-induced disaggregation of the tactoids. The disruption of the quiescent mesostructure at relatively modest strains was surmised to result in the premature failure of time-strain separability for the higher silicate content nanocomposites.

According to the interpretation of Solomon and coworkers [89], the nano-composite hybrid structure is one of a weakly agglomerated network of multi-platelet particulate domains that is ruptured and reformed under flow and quiescent conditions. When close-range filler interactions dominate, phenomenological models of filler cluster breakdown and re-agglomeration cluster networks have been proposed to describe some aspects of the resulting nonlinear viscoelastic behavior. These models were not aimed specifically at nano-sized particles nor was size a factor.

Leonov [147] proposed a continuum thermodynamic approach for the kinetics of floc evolution, which was successful in describing yielding, thixotropy, and frozen memory effects without using a yield criterion. Leonov proposed that the stress tensor was the sum of stresses due to matrix flow around flocs of particles and a stress in the flocs due to particle-particle interactions. The behavior of the matrix was modeled by the Leonov model [148]. A closed set of equations was obtained in terms of the deviatoric stress, strain rate, and Finger tensor. The particle mode was considered to be elastic leading to a general expression in terms of the configuration tensor and its invariants. Above a critical elastic energy stored in the flocs, or equivalently above a critical deformation of the flocs, the flocs started to rupture. The critical elastic energy was assumed to follow a Maxwell-type kinetic equation. Particle-particle interactions were considered in terms of attractive forces between particles leading to flocs behaving

elastically before their rupture. Leonov and Simhabhatla [149] more recently considered strong polymer-particle interactions. The models were proposed to simulate the transient, yield, and thixotropic behavior of mixtures.

In another approach the filled system is assumed to consist of two independent networks. Doremus and Piau [150] assumed the matrix network is due to the segments of polymer chains between the particles. The second network is due to the polymer chains strongly absorbed on the particle surfaces. The kinetics of each network was described by an evolution equation proposed by Jamamoto [151]. The rates of formation and destruction of networks were taken as functions of the second invariant of the rate of deformation tensor. The rate of change of the configuration of the network was assumed to be proportional to the rate of deformation tensor and to the velocity gradient adjusted with a slip parameter. This gave rise to an expression for the stress tensor of a Gaussian network. The model predicts a yield stress value but not the stresses in the transient start up of flow. Inn and Wang [152] also used a double Yamamoto network model but assumed the additivity of the stresses due to entanglements and absorbed bonds. The functions describing the creation of the network segments were taken to be dependent on the volume fraction and on the ratio of the length of the polymer chain in the network to the diameter of the particle. The functions governing the rates of destruction of the networks were considered to increase with the length of the polymer chain in the network. There were no indications as to the ability of this approach to model the transient rheology of the composite system.

Havet and Isayev [153] employed a double network model also in which the network was created by the entangled polymer matrix and the absorbed polymer. Both

networks were assumed to be described by the Giesekus constitutive relation [154]. They assumed that the total stress was the sum of contributions from the polymer and polymer-particle interactions but neglected the particle-particle interactions. The matrix rheology is assumed to be governed by the kinetics of creation and destruction of entanglements. The stress due to the polymer-filler interaction was considered to be due to the adsorption of the polymer onto the filler and to be proportional to the bridging density of the network created by the adsorbed polymer segments. During flow the polymer chains continuously absorb and desorb from the particle surfaces following an equilibrium process. The driving force for adsorption was expressed in terms of the Gibbs free energy which allowed one to calculate the rate constants for adsorption and desorption. Calculations for steady shear, stress growth, and stress relaxation were carried out as a function of relaxation time for the absorbed network and for various chain lengths between adsorbed sites. The predictions were qualitatively similar to the experimental behavior of polymers containing a well-dispersed filler.

In these analytical models, the dependence of the viscoelastic properties on filler size is not included. On the other hand, in many applications fillers with a size comparable to the characteristic length scale of the suspending medium (e.g. the radius of gyration of polymeric chains) are used. In such situations, additional physics may become important. The situation is complicated by the fact that in nanocomposites even at small filler volume fractions, a large surface area exists and most polymeric chains are close to the filler surface. Sarvestani and Picu [155] presented a conceptual model for the overall viscoelasticity of polymer nanocomposites with strong filler-polymer interactions. They considered non-agglomerated configurations in which rigid spherical nanoparticles with a

diameter comparable to the radius of gyration of the polymer molecules were homogeneously dispersed in the polymeric matrix.

The proposed molecular structure is shown in figure 2.26. Three types of segments were identified: a bridging segment; a dangling end; a loop. The junctions were assumed to be reversible and their time evolution was due primarily to the applied deformation. The internal structure had a transient topology and its dynamics was controlled by the rate of the attachment and detachment process and depends on the applied deformation. The stress was assumed to be the superposition of contributions of the bridging and dangling segments. Network theory was used to describe the stress in the bridging segments, and the elastic dumbbell model was assumed to describe the stress contributions from dangling segments. The configuration distribution for the bridging segments was modified to include the rate of generation and destruction of bridging segments per unit volume. The configuration distribution function for the dangling chains was represented by a dumbbell model and considered one end of the chain fixed while the other end interacted with the matrix through a frictional contact. In order to obtain the configuration distribution functions the attachment/detachment dynamics of the chains from the particle surfaces were estimated using the approach of Chernyak and Leonov [156]. Calculations of G' and G'' showed that at low frequencies a solid-like plateau was predicted when the filler-polymer interaction was strong.

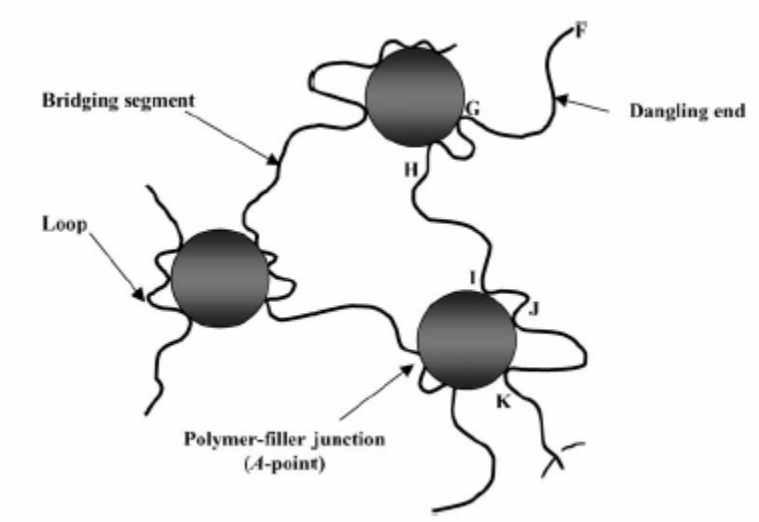

Figure 2.26. Schematic from Sarvestani and Picu [155]. The polymers bridge, loop, and dangle as they come in contact with and adsorb on to the nanoparticles.

Even though typically contributions to the stress are assumed to come from both the matrix, the matrix particle and particle-particle interactions, Ren and Krishnamoorti [111] applied the K-BKZ constitutive equation to polystyrene-polyisoprene diblock copolymers and organically modified montmorillonite composites. The time dependence of the linear stress relaxation modulus, $G(t)$, was fit well by a sum of exponentials for both the matrix and the nano-composites, even for sample containing 9.5 wt% clay in which a tail in $G(t)$ was observed. The strain dependent part of the memory function was fit by the PSM damping function. At low shear rates, less than 0.2 s^{-1}, the K-BKZ model fit the shear stress growth data behavior well but failed at higher shear rates for the nanocomposites. The model fit the shear stress growth well at all shear rates for the matrix. The predicted steady shear viscosity agreed well with experimental data for shear rates up to 2.0 s^{-1} for both the matrix and the composites but under predicted the viscosity for higher shear rates. At all shear rates the model under predicted the primary normal stress difference, N_1, for both the matrix and the composites. Hence, the K-BKZ model using the linear

$G(t)$ and the PSM damping function obtained from step strain experiments was inadequate for predicting the rheological data of the nano-composites as might be expected for fluids with potentially complex structure. The deviation of the model from the data was proposed to be due to the evolution of a mesoscale oriented structure at intermediate shear rates which was not covered by the damping function measurements. The failure of the K-BKZ model to predict N_1 suggested an inherent shortcoming of the model to describe the rheology of the nanocomposite system.

2.1.7 SUMMARY OF THE RHEOLOGY OF HIGH ASPECT RATIO NANO-PARTICLE FILLED LIQUIDS

In general, the addition of solid particles to low or high molecular weight liquids causes an increase in all viscoelastic parameters. As shown in this review, abnormalities such as strain thickening and large negative normal stress differences occur independently from liquid molecular weight. The tendency to compare nanocomposite to liquid crystalline polymers is cautioned, as such properties of stress scaling in start-up of steady shear flow do not apply. Other factors contribute against the general trend. Particle agglomeration or flocculation has the effect of artificially increasing particle concentration, and hence, the focus of most polymer nanocomposite literature lies on particle exfoliation. It is believed that exfoliated particles produce the largest increasing in mechanical properties, so that steric stabilizers, in the form of surface treatments, are added to reduce the van der Waals forces of attraction between platelets. One dimensional carbon nanotubes require the least amount of loading to reach a percolation threshold upon which the suspension possess characteristics more similar to a gel-like

solid. The reformation of the mesostructural network after shear induced alignment of the large aspect ratio particles strictly depends on the thermodynamics of the composite system. Yet, the actual physics of mesostructural deformation in the nanocomposite melt is not completely understood, and many authors have attempted to describe the flow behavior through constitutive equations.

2.2 FIBER SPINNING AND PROCESSING OF PET AND PET NANOCOMPOSITE FIBERS

The following section reviews the art of PET nanocomposite fiber formation from the melt phase and the secondary processing steps required to produce a suitable technical yarn for tire cord applications. The general concepts of nanocomposite synthesis by melt compounding and in-situ polycondensation are discussed and weighed with pros and cons for each method. The mechanism and variables of solid state polymerization of PET nanocomposites and the reaction's benefits to finished fiber properties is reviewed. Next, the methods of finishing fibers by second stage drawing and heat setting are reviewed in terms of the nanofillers effect on crystallinity and orientation of the continuous polyester phase. In addition, the use of super critical carbon dioxide as an exfoliant and as a drawing aid is discussed. Where information lacks for PET nanocomposite fibers comparisons and expectations are drawn from nylon nanocomposite fibers, since the latter has had more success as a composite material in general.

2.2.1 THE SYNTHESIS OF PET NANOCOMPOSITES

As stated earlier, PET is a semicrystalline polymer with excellent thermal and mechanical properties that are relatively easy to harness and produce on the commercial scale. The synthesis of pure PET typically requires two stages. The first step is the transesterification of dimethyl terephthalate (DMT) or terephthalic acid with ethylene glycol (EG) to form oligomers. Then the temperature of the reaction system is raised and the pressure lowered to melt the oligomers and increase mobility and reaction rate and to drive off the evolving EG and methanol, or water byproducts. The reaction is allowed to proceed until the specified molecular weight is reached by minimizing degradative by-products and the addition of termination agents. Melt phase polycondensation of PET usually produce a number average molecular weight in the range of 15,000 to 25,000. Higher molecular weights are only reached by solid state polymerization, a process described in section 2.2.1.4. For a detailed review of the processing equipment and polymerization conditions with different catalysts, the monograph by Fourné [157] possesses enough information to nearly replicate a commercial PET synthesis plant.

Yet, the review at hand is particularly interested in nanocomposite synthesis and fabrication. There are three common methods to producing a polymer layered silicate nanocomposite: in-situ polymerization of the polymer in the presence of the filler, solvent casting or mixing of the dissolved polymer and suspended filler, and melt compounding or intercalation of the filler particles into the molten polymer. These methods have been adequately reviewed by Ray and Okamoto [2] for a myriad of polymer systems other than PET. PET nanocomposites are not formed by solvent casting methods, because the alternatives are much more environmentally benign and much less expensive. In-situ and

melt intercalation methods are used instead. The polymerization reaction conditions of PET are relatively easy to reproduce and, therefore, the addition of a layered silicate at any stage to that medium is not laborious. Melt compounding is a favorable approach because some PET fiber plants receive their supplies of raw material from other sites and re-extrude to produce the final products. To melt compound a nanocomposite at these sites the pellets would only require an additional dry blending step to coat them in nanoparticles; no other additional equipment is required and no great capital expenditure is necessary.

Therefore the question remaining is what approach to PET nanocomposite synthesis gives the best thermal and mechanical properties, in-situ polymerization or melt compounding? The degree of exfoliation of the silicate layers in the PET matrix is the measurement for success of a particular method, because it is exfoliation or the even dispersion of platelets that leads to the greatest improvements to thermal and mechanical properties. In the next two sections this question is answered to relative satisfaction. In the penultimate and ultimate sections, the roles of nanoparticles with processing aids and on solid state polymerization are examined.

2.2.1.1 *In-situ Intercalative Polymerization Methods*

With the exception of polyamide based nanocomposites, the majority of successfully exfoliated nanoparticle morphologies have been achieved using in-situ addition polymerization reactions. Heinemann et al. [158] showed that in-situ polymerization of polyethylene nanocomposites were more intercalated (better dispersed) than those produced by melt compounding. The great advantage of in-situ polymerization

methods is the rapid diffusion of monomer units into the clay galleries that subsequently expand the interlayer spacing when the initiator or second monomer is introduced. However, for PET and its step growth polymerized nanocomposites, the claim of an exfoliated morphology is rare and in most cases can be disputed because of missing or contradictory data.

Chang et al. [159] produced PET nanocomposite fibers from synthetic fluoro-micas modified with triphenyl-long alkyl chain surfactants. The surface treated clay was dispersed in ethylene glycol and then vigorously mixed in dimethyl terephthalate with a titanium catalyst in a reaction tube. The synthetic fluoro-mica had been substituted with fluorine atoms for every hydroxyl group on the surface of the clay. Therefore, it was not expected that any PET should be bound to the silicate surface. However, a clay with a surface treatment containing no polar groups should not be expected to be fully dispersed in ethylene glycol, but should have been well-dispersed in dimethyl terephthalate. The details of the synthesis were not the focus of the paper and the polymerization stopping criteria was not reported. Therefore, the reported inherent viscosities of the formed nanocomposites have some unexplained variation. Morphologically, X-ray diffraction and transmission electron microscopy confirm the composites were not exfoliated. The fiber tensile modulus increased 31% for a 1wt% loading of silicate over the pure fibers of equal thermal history and higher inherent viscosity.

Imai and Saujanya and coworkers [160, 161] examined synthetic fluoro-micas treated with a functionalized triphenyl-phosphonium surfactant and in-situ polymerized in bis(2-hydroxyethyl) terephthalate (BHET) in the presence of an antimony oxide catalyst. Although the polar functional group on the clay surface treatment covalently

bonded to the backbone of the PET matrix, none of the nanocomposites were reported as exfoliated. The XRD peaks at best showed interlayer spacings of 1.9 nm, which was approximately double the interlayer spacing of unmodified mica. Yet, Imai [160] cited a 200% increase in flexural modulus for an 8wt% loading of modified fluoro-mica, which was excellent for an intercalated nanocomposite.

In the single study that claimed exfoliation of clay layers, Guan et al. [162] mixed 1.5 wt% poly(vinyl pyrrolidone) modified montmorillonite with dimethyl terephthalate, ethylene glycol, and a zinc catalyst to form an oligomeric suspension that was then catalyzed with an antimony oxide to build molecular weight. The authors synthesized their control pure PET under the same conditions, and the possible differences in molecular weight were ignored. The composites by XRD were deemed exfoliated, but were not checked by TEM. The XRD peaks shown were most likely caused by lamellar crystallites in the formed pellets and fibers, they appeared as very broad peaks in the range of interlayer spacings of 0.3 to 0.5 nm. The mechanical properties of the material showed a decrease in strength and heat shrinkage, which contradict the behavior of exfoliated nanocomposites.

2.2.1.2 *Melt Intercalation Methods*

The commercial scale manufacture of polymer layered silicate nanocomposites requirs a melt processing step through some type of extrusion device in the fabrication route. Because melt processing is essential to inexpensive and rapid production, synthesizing the polymer nanocomposite in this step is intuitive and nearly environmentally benign. The requirements for achieving an exfoliated morphology or a

morphology as dispersed as the in-situ polymerization method are to use either a single or twin screw extruder of relatively short residence time and high shear, as well as a surface treated clay that favorably interacts with PET and does not degrade the polymer phase at the melt processing temperature. Matayabas et al. [163] reported a very large decrease in inherent viscosity of Claytone APA (a commercially available nanoclay) melt blended with 1,4-cyclohexanedimethanol modified PET that decreased further with addition of clay. Davis et al. [164] reported that their dimethyl-dioctadecylammonium modified MMT when melt mixed with PET in their twin screw extruder produced a very brittle, black and completely degraded product. The degradation temperature of their long alkyl chain modified clay was about 250 °C and the melt processing was run at 285 °C. Other authors have observed enhanced melt phase degradation in the presence of nanomaterials in PET [84, 165, 166]. Nevertheless, in comparison to the in-situ method where 1 in the 5 available studies on PET nanocomposites claimed exfoliation, 6 out of 10 melt compounding studies claimed exfoliation of the silicate particles, and 8 of the 10 articles had the nanocomposites synthesized by twin screw extrusion.

The most relevant study to the review at hand came from a study by McConnell et al. [165] who examined the effect of fluoro-micas and montmorillonites on the tensile modulus of PET nanocomposite fibers. In a double pass, single screw extrusion experiment, the authors mixed the desired filler type and loading with an antioxidant at slow 15 rpm at 260°C, then reprocessed the pellets at 3 times greater shear to aid in the dispersement of individual silicate layers. The resulting nanocomposites had intrinsic viscosities all lower than the PET control. The morphology of the nanocomposites was intercalated in most cases except for a long-alkyl chain (tallow) modified fluoro-mica

which was deemed exfoliated by the authors' analysis of XRD data. No TEM images were taken to verify the absence of intercalated stacks. In addition the "exfoliated" nanocomposites showed lower tensile moduli than the pure PET in fiber form; the loss in modulus exceeded 50% in the "exfoliated" alkyl-modified fluoro-mica at 4wt%. However, at lower spinning speeds these nanocomposites showed improvements up to 80% for the 4wt% sample, even though the nanocomposite molecular weight had an average of 18 less mers per molecule than the pure PET.

In another single screw melt compounding experiment, Pegoretti et al. [167] examined nanocomposites formed directly from a dry blend of clay and polymer in an injection molding machine. By WAXD and TEM, the authors determined that some clay stacks were exfoliated into single layers but most were still stacked, in which the surface modified (long alkyl chain) nanoclay showed better intercalation. At any loading the tensile modulus increased, but the long alkyl-chain modified nanocomposite showed overall higher values than the unmodified filled system.

In melt compounding, a master-batch of a very high loading of nanoparticles mixed with polymer is formed and then in a second process step "diluted" with pure polymer to form the final nanocomposite of desired particle concentration. The basic premise relies on the master-batch having a poor to mild intercalated morphology, which upon subsequent compounding, the intercalated polymer chains favor the diffusion of polymer into the galleries or provides lubrication of the platelets so that separation under shear is relatively easier. For PET nanocomposites, the master-batch method by twin screw extrusion produced exfoliated morphologies of an hydroxyl-modified montmorillonite at only 1% by weight concentrations [166, 168]. The morphology in

these cases was checked by TEM and XRD and found very few stacks larger than two platelets and no diffraction peaks at a 1wt% loading. The basal or interlayer spacing decreased as clay loading increased. At 3 and 5wt% from the master-batch the basal spacing fell to 4.1 nm or roughly 4x the basal spacing of unmodified montmorillonite. No modulus values were reported.

Lee et al. [169] and Wang et al. [170] studied the effect of hydrotalcite on the mechanical properties of PET when melt blended by twin screw extrusion. In both studies the TEM images showed aggregates, regardless of the surfactant type on the hydrotalcite. In addition, no noticeable change in mechanical properties regardless of filler concentration or surfactant concentration was noted. The greatest improvement to modulus was only 7% for a sulfonated long-alkyl chain modified hydrotalcite [169].

Without a master-batch, Sanchez-Solis et al. [84, 171] examined the effect of long-alkyl chain length and compatibilizer concentration on the dispersion of montmorillonite in PET injection molded samples by twin screw extrusion. In their earlier efforts [84, 171], the authors found that no matter the maleic anhydride or pentaerythritol compatibilizer concentration all samples of dehydrogenatedtallow (65% of which had chains containing 18 carbons) modified montmorillonite were not exfoliated. The authors concluded that another screw geometry was necessary to achieve exfoliation. Even when intercalated, the modulus increases by 17% at a clay loading of 2wt%. In 2004, Sanchez-Solis and coworkers [84] showed that longer alkyl chains improve the basal spacing of the clay, but when melt compounded the longer carbon chains are too entangled to allow intercalation and prevent the full exfoliation of the clay stacks. The authors claimed that a 1wt% dodecylammomiun surface treated clay

produced the only exfoliated morphology determined by the absence of XRD peaks. No TEM images were reported to verify the complete dispersal of clay stacks. In comparing tensile modulus data for exfoliation, the authors reported a 36% increase in modulus of injection molded samples of 1 wt% dodecylammonium treated clay, but at 2wt% of the same clay the modulus decreased by 85% in some cases.

So far the majority of studies have focused on melt compounding PET with alkyl (or non-polar) modified nano-particles, with the exception of an hydroxyl (polar) modified study in which the inherent viscosity was observed to drop by 33%. Therefore, some authors sought to determine highly compatible PET-nanoclay systems that had stable interactions at melt processing temperatures. Barber et al. [172] studied the effect of ionomer concentration on the exfoliation of PET/nanoclay composites. Unmodified, phenyl-modified, and alkyl-modified montmorillonites (5wt%) were melt blended by twin screw extrusion with varying amounts of sulfonated PET ionomer concentrations. The XRD data showed no peaks, but TEM analysis showed that all samples were intercalated at best. The authors reported that the ionic concentration aids in the dispersion, though no concentration produced an exfoliated morphology. The phenyl modified clays showed the best dispersions and gave a 35% increase in tensile modulus with no ionomer content for injection molded samples. A 55% increase in tensile modulus was reported for the phenyl-modified clay with the highest ionomer content, and thus the best dispersion. Davis et al. [164] reported that their immidazolium triphenyl surfactant was stable at PET's melt temperature. Their shortest residence time (2min) in the twin screw extruder showed an exfoliated morphology by TEM in which no more

than two sheets of tactoids were observed. XRD showed a broad, short peak for this sample though, and unfortunately no property improvements were reported.

In terms of which method of nanocomposite synthesis gives the best dispersion of nanoparticles, the current literature for PET nanocomposites favors the melt intercalation methods. Although in controversial circumstances, in-situ polymerization can produce the exfoliated morphology. In addition each method has its disadvantages: the control of colloidal interactions of monomers and particles to form a dispersed phase in the in-situ polymerization method, and the control correct conditions of extruder residence time, melt temperature, polymer degradation, and twin screw component configuration in the melt compounding method. In the next section the use of plasticizing agents is discussed as a way to minimizing PET degradation in the melt phase with the presence of amine treated clay surfaces.

2.2.1.3 *The Effect of sc-CO_2 on Nanoparticle Dispersion in Thermoplastic Matrices*

The high viscosity of high molecular weight polymers is a major obstacle to efficiently and rapidly melt processing such systems. Typically the very large molecular weight polymers are not processable, degrade at sustained exposure to the melt temperature, or become severely distorted extrudates from gross melt fracture at lower shear rates. To overcome this problem, super-critical fluids may aid in plasticizing the polymer to lower the melt viscosity. In particular, super-critical carbon dioxide (sc-CO_2) has been used in many applications from the food and drug industries to the commercial plastics industry [173]. The benefits of sc-CO_2 over other super-critical fluids are its

relatively lower effect on the environment, lower toxicity, lower cost, and non-flammability [174-178]. Additionally, at ambient conditions the removal of sc-CO_2 from the polymer is relatively easy.

In terms of the study at hand, montmorillonite is an expandable material in polar solvents such as water (and when appropriately treated, it is expandable in non-polar solvents.) CO_2 at near critical conditions behaves like a polar organic solvent and is expected to able to expand the montmorillonite interlayer distances. Therefore, the application of sc-CO_2 to polymer layered silicate nanocomposites is obvious and has been reported by a few authors [179-181]. However, the successes of the current literature have not been convincing enough to assert that melt processing with sc-CO_2 is indeed overwhelmingly beneficial because of the absence of published mechanical properties. The more recent study by Lesser [179] and coworkers showed a 100% increase in inter-gallery spacing of the silicate layers when using sc-CO_2 to plasticize an HDPE melt mixed with alkyl-modified (Cloisite 15A) and unmodified (Cloisite Na^+) montmorillonite. The authors used a pressurized hopper filled with the dry mixed polymer and nano-filler and varied the soak time of the sc-CO_2, so that it seems that the pellets and silicate were foamed and then melt compounded. Lesser found that the particle surface treatment had no significant effect, from which they then concluded that the exfoliation was determined solely by the presence of sc-CO_2. In their earlier efforts, Lesser and coworkers [180] reported a 50% increase in modulus for a system of PMMA/nanoclay/sc-CO_2, at a clay loading of 40% by weight. However, these nanocomposites were formed by in-situ polymerization in the presence of sc-CO_2, then

melt compounded so that the possibility of some re-agglomeration or collapsing of silicate layers could have occurred.

2.2.1.4 *The Effect of Nanofiller on Solid State Polymerization*

Typical melt phase polymerization of PET is limited to creating number average molecular weights in the range of 15,000 to 25,000 g/mol. The molecular weight range obtained in melt phase polycondensation is adequate for several commercial products, such as staple fiber for textiles. Yet, the melt phase hosts several degrading side reactions which after long reaction times eclipse the esterification reaction and reduce polymer molecular weight. However, high performance applications of PET products, such as high modulus tire cord and soda bottles, require a much higher molecular weight that should exceed 30,000 g/mol. Therefore, to reach such high molecular weights, solid phase or solid state polymerization (SSP) processes provide a route to obtaining higher molecular weights by limiting degrading side reactions.

It has been shown that as the reaction temperature is lowered from 285 to 230°C the rate of polymerization drops but a factor of 6, but the rate of degradation is lowered by an order of magnitude to about a factor of $1/40^{th}$ the rate at 285°C [182]. In some cases [183-185] the side reactions in the solid state do not include, to any significance, the formation of diethylene glycol, which has been observed as highly sensitive to thermo-oxidative degradation and a leading cause of molecular weight loss during melt processing of dried pellets PET [186]. In the temperature range of 200-230°C, typical of most SSP conditions, the diffusion of water and acetaldehyde by-products is rapid enough to neglect any negative effects due to their formation.

From the comments above, one can infer that reaction temperature plays a significant role in the rate of SSP molecular weight build. Yet, some other variables in SSP of engineering interest are the choice of reaction medium (inert sweep gas such as N_2, CO_2, or Ar, inert liquid dispersant such as mixtures of alkanes, and/or applied vacuum), residual catalyst from PET pre-polymer formation, sample size and porosity to aid in the diffusion of ethylene glycol away from the reaction zone, the initial polymer molecular weight, and (seemingly more important) the morphology of the crystal structure and its associated thermal history. To this list one may add for the case of PET solid stated with intercalated nanoclay platelets: nanoclay type (montmorillonite, hectorite, etc.), the degree of nanoclay dispersion, nanoclay concentration or loading, and the functionality of the filler surface treatment.

Additionally, by no means are these factors completely separable and independent. In particular the available studies on nanocomposites in SSP and the recent pure PET SSP literature have been concerned mostly with the crystallinity of the polymer phase and its relation to the physical diffusion of ethylene glycol from the reaction zone and chemical diffusion of reactive chain ends in the amorphous phase. Small thin crystals leave more of the reactive end groups outside of the crystal structure thus increasing the reaction rate and aiding the chemical diffusion [187]. Yet, Gantillon et al. [187] suggest that a minimum chain length is needed to form regular small crystals, and subsequent molecular weight, and that the low viscosity of low molecular weight chains cause the formation of larger crystals with more trapped chain ends that inhibit SSP rates. This point has been discussed by other authors as well [184, 185]. Kim et al. [184] note a possible trade off between minimizing the crystal size and maximizing the diffusion of

ethylene glycol by-product by hinting at tortuousity. Nevertheless, the crystal structures and SSP rate is dependent upon reaction temperature and thermal history. The consensus on the conditions conducive to the fastest rate of solid state polymerization of PET are to begin with a high molecular weight sample that has small, regular crystallites with all chain defects outside the lamellae and apply high temperature and low pressure on relatively thin and/or porous samples.

So far the discussion has pertained to pure PET materials in SSP and particularly with the effects of crystallinity and to an extent initial molecular weight, and such discussion is relevant when melt intercalating nanoparticle into the PET matrix. From initial experiments, this author has noticed distinctly lower molecular weight behaviors in both I.V. and zero shear viscosity tests that reflect the nanoparticles and/or their surface treatments degrade PET during melt processing. Litchfield [188] has observed that the degradation is dependent on clay loading, in which molecular weight loss increases with higher loadings of nanoclay. Therefore, the discussions of initial molecular weight and nanoclays' effect on crystallinity are particularly useful for understanding the SSP rates when the chips are brought back to equal zero shear viscosities. In the literature to date, only 2 studies explicitly document the effect of nanoparticles on the solid stating kinetics of PET.

Yu et al. [189] investigated the effect of a 2.5wt% montmorillonite (MMT) with balance PET composite (that had been produced by either in-situ or melt compounding and may or may not have a surface treatment on the MMT) on the rate of SSP with an N_2 sweep at 230°C for up to 25 hours. Due to lack of published data on the initial conditions, it was assumed that their samples had equal by associated thermal histories

and the sizes were small enough to be ethylene glycol diffusion limited (>1mm) and, thus, dependent on crystal size. The molecular weight build-up is reported to be faster or accelerated in the nanocomposite over the neat PET, because the nano-platelets limit the crystal size but nucleates crystal growth, such that ethylene glycol diffusion occurs faster. The reasoning was based on the theory that optimal crystal size balances the amount of available chain ends for reaction and the tortuousity of gas diffusion, to produce the fastest rate of polymerization. The published intrinsic viscosity data was relatively weak evidence for the authors' claim, as the difference in relative rates did not monotonically rise with solid stating time.

Recently, Bikiaris et al.[190] observed the effect of fumed silica surface functionality on the melt strength of SSP PET/silica nanocomposites, and recorded the first literature documentation of an insoluble fraction post solid state reaction. The authors noted that increasing the concentration of nanoparticles reduced the rate of polymerization. They attributed the slower kinetics to increased tortuousity from the impermeable solid barrier of nanoparticles retarding ethylene glycol diffusion. More interestingly the authors analyzed an unexpected residue or insoluble component from their intrinsic viscosity measurements by FT-IR (Fourier transform infrared spectroscopy) and TGA/DSC. Thermal measurements showed no distinct melting event and upon auto-ignition the sample retained half its original mass. FT-IR showed the insoluble had both silica and PET character. In addition the melt strength dramatically increased with filler loading, even though IV and loadings were inversely proportional. The above phenomena led the authors to conclude that the surface silanol (i.e. hydroxyl groups attached to the silica surface) and PET end groups formed a cross-linked network

illustrated in figure 2.27 below. The ether linkages between polymer and surface groups may not withstand long periods of heat and shear and in a melt process may degrade the PET matrix. For PET/nanoclay composites, the available hydroxyls on the clay surface may induce the same response. Therefore, in the molten state, one would expect a lower viscosity from the constant attachment and detachment of PET chains from the silanol surface, but in the solid state, if the crosslinks form during cooling, one would expect an improve mechanical response.

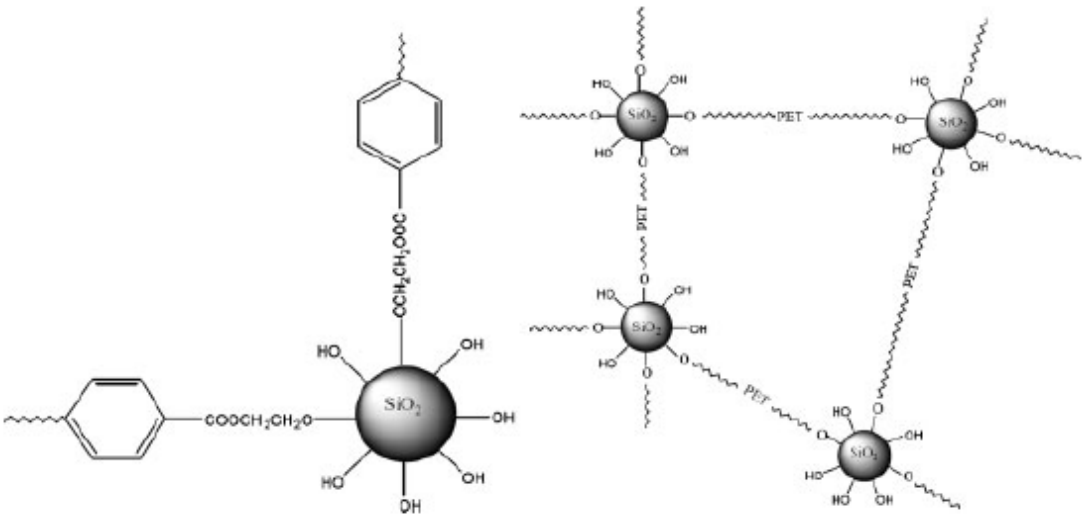

Figure 2.27. Schematic of crosslinking and possible branching reactions of PET to the silanol surface (hydroxyl groups) of nanosilicates [187, 190].

2.2.2 POST-PROCESSING OF PET-NANOCOMPOSITE FIBERS

The term post-processing refers to the steps take after the filament has solidified from melt phase spinning to produce a highly oriented, highly crystalline yarn. For purposes of brevity and scope, this section focuses only on the drawing process and its related process variables. In the first sub-section, the methods of drawing fiber, both traditional and experimental are discussed. Then the effects of drawing aids are reviewed with the majority of focus on super-critical CO_2. In the next sub-sections, the draw induced microstructures are examined, as well as strain-induced crystallization and nanoparticle induced crystallization. The section concludes with a brief discussion of the effect of nanoparticles on the glass transition temperature, T_g, of PET fibers. This section does not examine heat setting, twisting, texturing, dyeing, etc. because these treatments are more easily explored when the microstructure, dictated by the drawing process, is known.

2.2.2.1 *Fiber Drawing Methods for Increased Tensile Properties*

2.2.2.1.1 *Drawing Processes*

For approximately 70 years PET has been a commercially significant produced fiber. For half of those seventy years most PET fiber was produced at very low take-up speeds with little or no induced orientation and, therefore all fiber was drawn in a second step to produce the mechanical properties required. High speed spinning (>3000 m/min) did not take off industrially until advances in the electrical engineering of the winding motors were made. Researchers quickly found that melt spinning at high speeds

produces a significantly more molecularly oriented fiber. The tensile stresses created at these high speeds induced the formation of oriented crystallites, which were also induced by drawing. Therefore, winding speeds were increased in hopes of eliminating the drawing step. However, the orientation of molecules in the non-crystalline regions of the fiber was low and larger quantities of chain folding were present when compared to the orientation induced from drawing low speed spun fiber in a separate step. The end mechanical properties of high speed spun fibers were adequate for textile applications, but high performance and engineering fibers required a greater modulus manifested in a greater degree of orientation and crystallization, only achieved in drawing after spinning.

The techniques for drawing fiber or film in the laboratory and in the commercial setting are in most ways significantly different. Most laboratory tests are drawn on constant extension rate or constant strain rate tensile or universal testing machines that usually output stress as a function of draw ratio and/or draw temperature. In constant extension rate experiments the upper jaw of the tensile machine moves upward with constant speed such that the true strain rate is

$$\varepsilon(t)=(t + L_o/v)^{-1} \qquad \ldots\ldots(16)$$

The quantities t, L_o, and v are the draw time, sample gauge length, and crosshead speed or extension rate, respectively. In constant rate of strain experiments the upper jaw speed is continuously adjusted to maintain a constant rate of strain such that the true strain rate is [191]

$$\varepsilon(t) = (1/t)\ln\{L(t)/L_0\} \qquad \ldots\ldots(17)$$

where the quantity L(t) is the length of the sample at after draw time t and $L(t)/L_o$ is the draw ratio, λ. The "tenter process" for film drawing is the only constant rate of extension process used commercially [192].

Industry typically favors continuous methods; both constant rate of extension and constant rate of strain techniques are not feasible as continuous methods. In commercial drawing processes, the as-spun fiber is continuously supplied from a feed roll at constant velocity to another roll at a higher constant velocity. Here, the force applied to the fiber by the second roll is constant, and the strain-rate profile along the draw-line self-minimizes the force applied to reach the required draw ratio [191]. These constant force processes typically reach an order of magnitude higher strain rate than that obtained at the maximum extension rate of constant extension rate devices [191]. The general conclusion is that one cannot compare the information from constant rate of extension to that of constant force experiments because the great difference in applied strain can generate significantly different microstructures.

Nevertheless, because both methods have been investigated to such depths, both constant rate of extension and constant force methods are reviewed briefly. As stated earlier, the tensile or constant extension rate drawing process usually gives a stress-elongation curve that permits analysis of the deformation. A typical stress-elongation curve is shown in figure 2.28 for an amorphous un-oriented PET film at two strain rates above the polymer's T_g [193]. In the figure, the resistance of the entanglement network causes the initial increase in stress as significant molecular orientation is induced. The first inflection point E_1 reflects the onset of strain induced crystallization. The crystallinity and non-crystalline orientation increase rapidly between points E_1 and E_2

without a large increase in stress. At the point E_2 the characteristic level of crystallinity is reached, in which a crystallite network has formed. The developed network is independent of strain rate, but depends on drawing temperature. The rapid development of stress after this point is a result of the increased polymer viscosity, which is in turn caused by the connectivity of the crystal network structure [193].

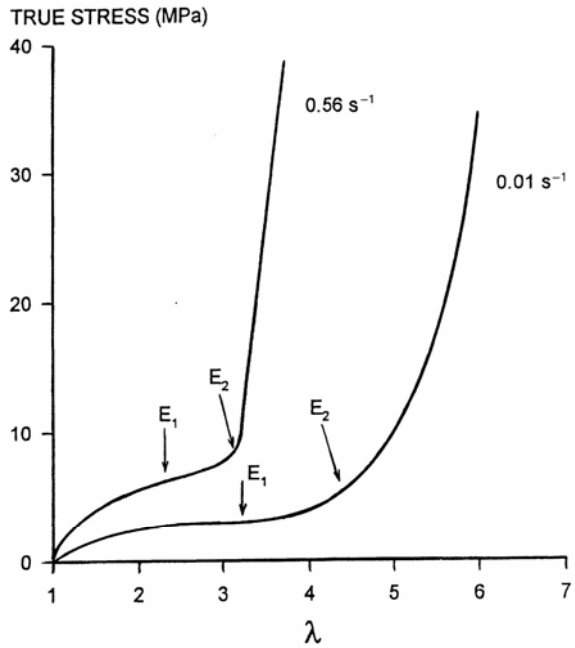

Figure 2.28. True stress as a function of draw ratio, λ, at two strain rates and draw temperature of 90 °C [193].

These observations have led to several proposed mechanisms for the development of microstructure in drawn PET in this high stress region. Figure 2.29 shows one authors' proposed mechanism two-dimensionally and radically simplified for crystal blocks tied together by the amorphous phase [194]. The polymer chains tend to fold into a regular structure, but the crystals are imperfect. Due to entanglements, some chain ends are folded into multiple crystallites to form ties for the network, or are left free and form

the slip planes depicted in the figure below. According to Hearle [195], longer chains make the organization into crystals more difficult, and it is more likely that different segments of the same chain have joined into different growing crystals making the microstructure more complicated, less regularly folded, and possessing more links between crystals. It should be emphasized that the schematic below is not the realistic representation of the true polymer morphology or topology. From the topological aspect, what is known is that drawing amorphous PET reduces the *gauche* content of glycol units and increases the *trans* content as the sample is oriented [196]. In addition, the *trans* glycol units and the benzene rings are highly oriented in the fiber-axis direction.

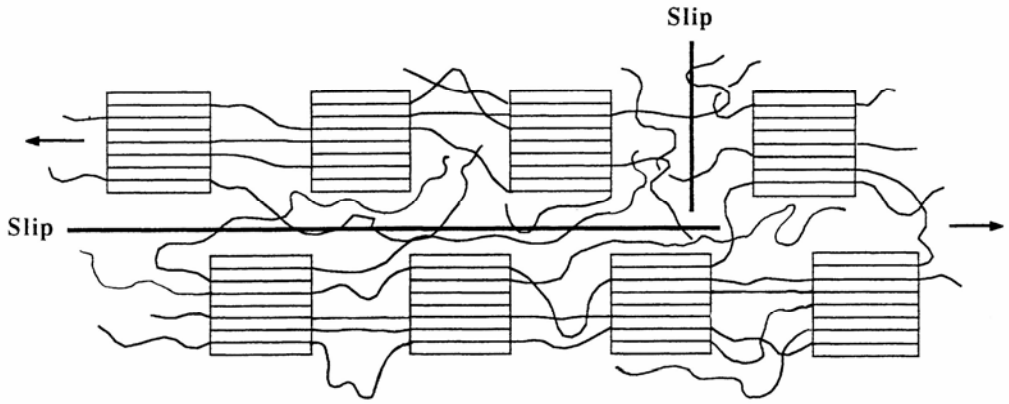

Figure 2.29. Schematic diagram of a proposed mechanism for the extension of PET under high stress [194].

Decreasing the draw temperature has a similar effect to increasing the strain rate, but the two variables are not mutually exclusive. Figure 2.30 shows the general trends of temperature, strain rate, and molecular weight found in the stress-strain curves for an amorphous polymer sample [191]. Increasing the temperature of the system above T_g increases the molecular mobility of the polymer chains and aids in molecular relaxation,

which yields a more ductile response. When drawing below T_g, the chains lack sufficient mobility for relaxation or chain slippage to occur, and the final upturn in stress is due to the increasing molecular orientation in the sample and not necessarily due to the physical crosslinking network structure of the crystals. As expected, longer molecules (i.e. higher molecular weight) require longer amounts of time for relaxation, and the effect of increasing molecular weight is similar to lowering the drawing temperature.

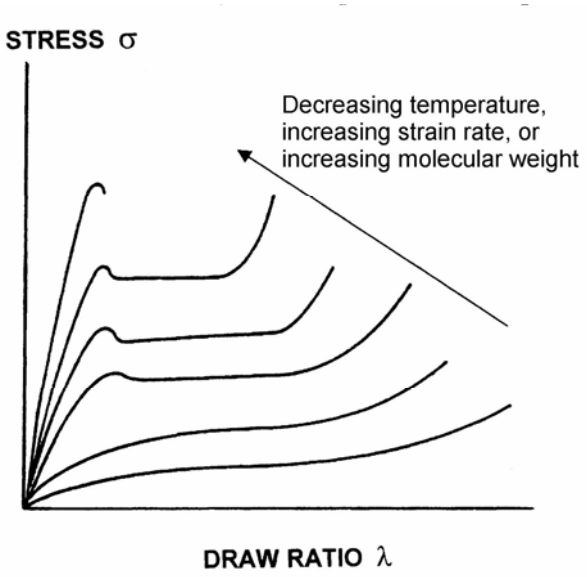

Figure 2.30. General stress as a function of draw ratio, strain, for an amorphous unoriented polymer [191]

Commercial processes apply continuous drawing methods that exert a constant force on the fiber and not constant extension, mainly because the fiber is more easily drawn between two rolls at different speeds that can handle hundreds of thousands of meters of fiber rather than at most 1 or 2 meters in constant extension drawing. The most general constant force draw technique is shown in figure 2.31. Here, the fiber is supplied from a feed bobbin to the first roll or godet, and then passes over or through a heated plate or chamber to a second godet, and finally taken-up to another bobbin by a

winder. The two rolls operate at different speeds; and raising or lowering the applied force (or the velocity differential between the two godets) adjusts the residence time for heat transfer over the heated region. In addition, the heated plate length, dx, can be shortened to a simple heated pin to apply controlled heat. If the fiber is passed through a heated chamber, the medium within that chamber that imparts heat transfer may vary. Some proprietary processes may use steam or heated air [197]. Longer residence times or higher temperature, at constant force, in the heated region create more crystalline microstructures. A commercial drawing technique referred to as the incremental drawing process continuously draws fiber or film in up to 100 zones, in which drawing temperatures and forces vary in small units through the draw line [198], and is particularly useful for investigating process-structure-property relationships.

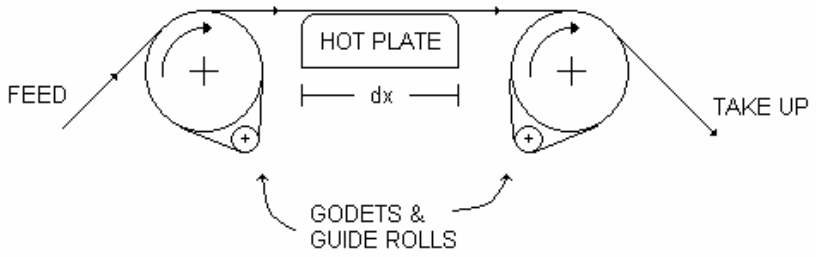

Schematic of Typical Fiber Cold or Hot Drawing Apparatus

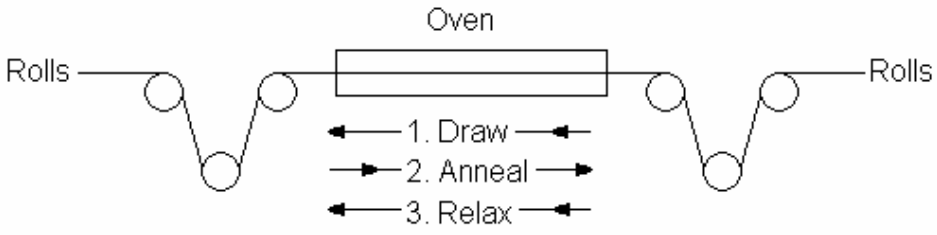

Figure 2.31. Schematic representations of commercially viable constant force drawing mechanisms. The bottom diagram shows a three step draw-annealing process with heat conduction to the fiber by a fluid medium.

When the applied force and the associated deformation are below a critical level, the molecules do not orient and "flow drawing" occurs. The sample will extend to failure because there is sufficient time for chain slippage, unless ample time for crystallization is allowed while preventing a decrease the molecular orientation [199]. Figure 2.32 shows the effect of applied load on the achieved draw ratio over time, similar to a creep experiment. Initially, the rate of deformation is low due to the resistance of the entanglement network. As the deformation continues, strain softening occurs from the slippage of chains to give a sharp increase in strain rate. Finally, a plateau draw ratio is reached at which the resistance of the polymer network equals the applied load. It has been noted [191] that increasing the load increases the plateau draw ratio, because the higher stress deforms the growing crystallite network more readily. From a figure of this sort, it is possible to deduce the drawing force associated with a given draw ratio when the residence time between rolls is known.

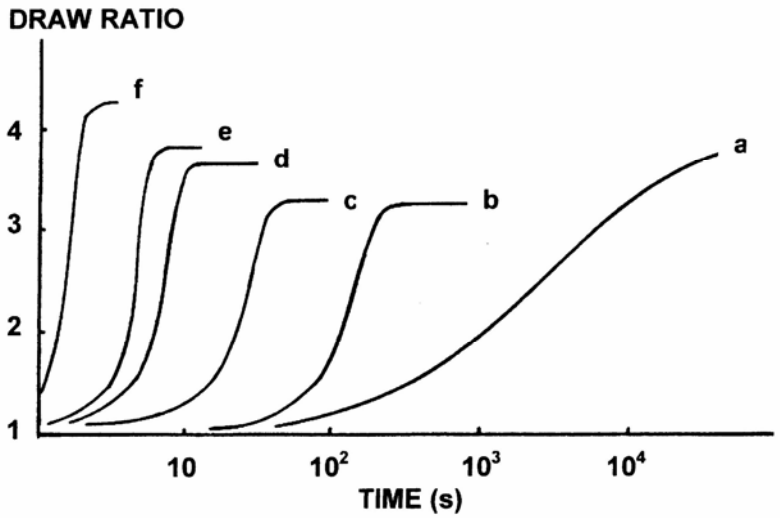

Figure 2.32. The effect of applied force on the rate of deformation of PET film drawn above the T_g (80 °C): (a) 1.5, (b) 3.8, (c) 5.0, (d) 6.3, (e) 7.5, (f) 10.5 MPa [200].

In terms of specific laboratory techniques, zone drawing and zone annealing and solid state co-extrusion methods are well-known for producing highly oriented fibers and films. Zone drawing and zone annealing techniques are variations on the well known hot and cold draw methods. Instead of the fiber moving over a stationary heated plate or pin, the zone drawing technique holds the fiber steady and moves a heater in a controlled fashion. Kunugi et al. [201] developed a combined zone draw and zone anneal system, in which a thin band heater attached to the crosshead of a tensile tester moved over a PET film under tension, as shown in figure 2.33 [202]. The focused heat prevents an overall deformation of the polymer film. The zone draw and zone anneal is carried out with the intention of arranging the molecular chains into fibrils while minimizing the chain back-folding crystallization behavior. The advantages cited by the authors are that zone draw/anneal prevents the generation of numerous crystal nuclei, eliminates the internal distortion of crystallites, prevents thermal degradation by reducing heating time, and produces fibers of very high dimensional stability. In a later study by Kunugi et al. [203] the zone draw and zone anneal method was applied multiple times to the same sample, where the applied tension was increased on each application of heat to achieve a higher tensile modulus. Some properties of the zone method for PET films are shown in table 2.2. The drawbacks to this method are the batch nature of samples being drawn and that the method is incomparable to constant force drawing in terms of the magnitude of applied strain.

Table 2.2. Tensile properties of zone drawn and zone annealed PET film.			
	Amorphous un-oriented → Amorphous oriented → Crystalline oriented		
	"As spun" →	"Drawn" →	"Annealed"
Modulus (GPa)	1.4	7.0	14.5
Strength (kg/mm)	-	26.0	86.9
Crystal %	1.8	21.4	45.5

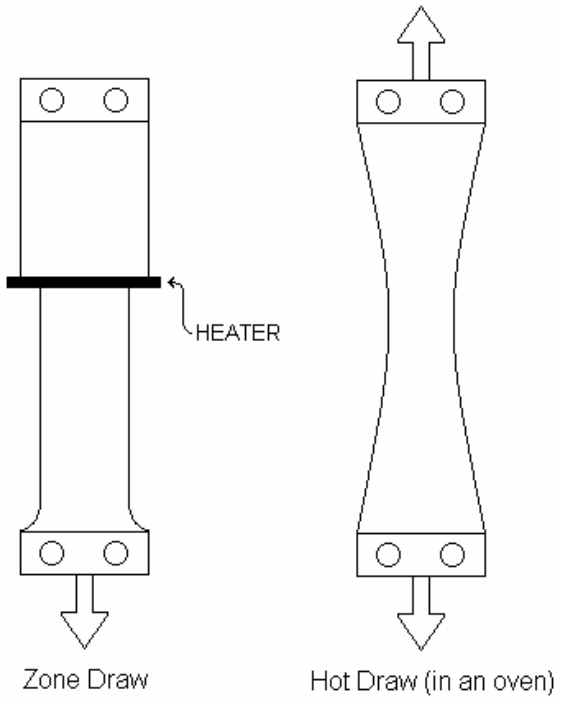

Adapted from: Kunugi et al. J. Appl. Polym. Sci. (1986) 31, 429-439

Figure 2.33. Schematic diagram of zone drawing/annealing deformation versus hot draw deformation of a polymer film.

Solid state extrusion methods of drawing semi-crystalline and amorphous polymers are based on old and well documented metallurgical techniques. These methods are not continuous, even though Griswold et al. [204] claimed the solid state co-extrusion is capable of producing large quantities of film. Essentially, a wafer (for film drawing) or a plug (for fiber drawing) is sandwiched or wrapped in a sheath to form a "split billet", see figure 2.34. Then the billet assembly is extruded through a conical die around the glass transition temperature of the amorphous wafer or plug or just below the melt temperature for semi-crystalline samples. The sheath is typically a more ductile material but may also be the same material as the wafer or plug. The conventional solid state extrusion method uses a solid homogenous billet. Griswold et al. [204] reported a tensile modulus of their HDPE solid state co-extruded films 450% greater than the conventional solid state method. The highest textile modulus and draw ratio obtained for HDPE were 70 GPa and 45, respectively [205, 206]. Although no tensile properties were reported, Sun et al. [207] concluded that solid state co-extrusion orients and orders PET segments gradually and continuously with increasing draw ratio. The orientation of the amorphous phase reaches a saturation after which it begins to be converted to imperfect PET crystallites. Ito et al. [208] compared tensile drawing to solid state co-extrusion. The authors reported a modulus of 29.5 GPa for samples drawn at their highest draw ratio in a tensile, constant rate of extension, apparatus. For samples drawn in solid state co-extrusion, at their maximum draw ratio, the reported modulus was 14 GPa. Thus, solid state co-extrusion is a novel and certainly practical drawing technique, but the inability to make the method continuous coupled with the fact that the achieved properties are lower than tensile drawing severely limit the justification of exploring this method further.

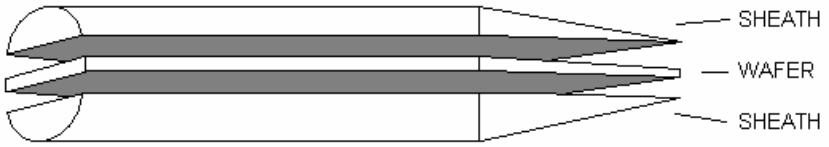

The Split Billet Assembly for Solid State Coextrusion of Films
Adapted from: Griswold et al. Polym. Eng. Sci. (1978) 18, 861-863.

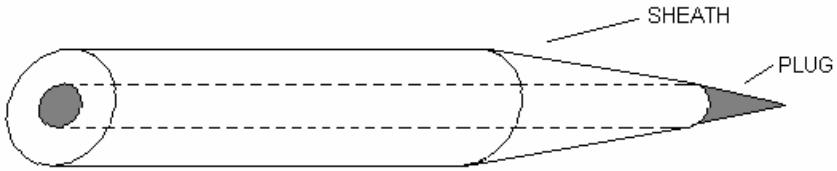

The Split Billet Assembly for Solid State Coextrusion of Fibers

Figure 2.34. The "split billet" assemblies for solid state co-extrusion of films (top) and fibers (bottom), note the required taper to fit the conical die.

The internal heating effects are a concern for tensile and roll drawing experiments when the deformation rate is high. The polymer can absorb a large amount of dissipated energy when the fiber sample is relatively thick and drawn below its T_g. For PET films of 30-μm thicknesses the internal temperature above T_g in constant force drawing increased by 2-3 °C at average strain rates of 15 s^{-1} [191]. Generally, low deformation rates prevent heat transfer between the system and surroundings. For internal heating to make an effect, the relative time-scales for heat transfer and deformation must be comparable and depend upon the properties of the material, such as latent heat of crystallization, heat capacity, etc. Pendse et al. [166] studied the temperature evolved during deformation of PET nanocomposites in bar-shaped samples. The authors found

that with increasing clay content the internal heating effects were progressively dampened out.

2.2.2.1.2 *Drawing Aids for Higher Orientation*

The final strength and modulus of a given PET filament depends upon the sample molecular weight and entanglement density and the load applied during drawing. Generally, extremely high molecular weight PET has a high melt viscosity that makes melt spinning and subsequent drawing difficult. Thus, low molecular weight PET is typically commercially spun into fibers of lower mechanical properties than their ultra-high counterparts.

To compromise without sacrificing the environmentally benign melt spinning process, research has focused on using drawing aids to reach very high draw ratios in ultra-high molecular weight PET. For example, Ito et al. [209] treated PET fibers with acetone or dimethylformamide (DMF)/water solutions that produced a 20% increase in tensile strength. The work of Lesser and co-workers has focused on the drawing process using super critical carbon dioxide (sc-CO_2) as the plasticizer, because of its cited two-order of magnitude higher diffusion rate than acetone or DMF. In the studies by Lesser [210-212], the fiber surfaces of air drawn and sc-CO_2 drawn fiber samples have equal surface smoothness and diameters for a given draw ratio. Yet, the authors have found that sc-CO_2 plays a major role in the morphological development. The presence of sc-CO_2 reduced the entanglement density, permitted chain slippage in the amorphous phase, and prevented strain-induced crystallization. The observed effect was a dramatically increased final draw ratio. Unfortunately, the increased drawability did not have a positive effect on the orientation of PET chains and the ultimate tensile modulus

improved by only 10% when drawn by a factor of 12 at 200°C [211]. Lesser claimed that drawing PET in sc-CO_2 below 130°C did not produce any improvement to fiber mechanical properties. In fact, the author stated this method worked better for nylon and ultra high molecular weight polyethylene; because the former typically required the presence a polar plasticizer to achieve high mechanical properties and the latter's dominating α-crystal relaxation process.

2.2.2.2 *The Effect of Nanoparticles on Crystallinity and Related Thermal Behaviors*

This section includes the discussion of crystallinity and the glass transition temperature and specifically how these thermodynamic properties influence the polyester fiber drawing process. To begin the discussion the general theory and observed effects of stress-induced crystallization are examined for the case of pure PET. The ultimate goal is to improve the tensile mechanical properties by nanoparticle addition, but to clearly understand why the property enhancement occurs requires a thorough grasp of the deformation process of the pure material during drawing. This section concludes with a discussion of the observed effects of nanoparticles on the crystallization kinetics, as well as crystallite size and shape, and the glass transition temperature of the polyester composite.

Crystallization rates in the oriented phase have been cited as several orders of magnitude greater than those in the isotropic un-oriented phase. From thermodynamics, the decrease in entropy from molecularly oriented chains causes an increase in the free energy of crystallization, which enhances the crystal nucleation rate. Many authors have attempted to interpret the theory of orientation-induced crystallization [213-219]. Most

of the derived relationships start from the classical isothermal crystallization theory and then modify it phenomenologically to include the effects from orientation, cooling rate, and crystallization temperature. Most equations for induced crystallinity are similar to the Avrami equation [220]:

$$\theta = 1 - \exp\left(-kt^{n}\right) \qquad \ldots\ldots(18)$$

Here, the variables θ, k, t, and n are the relative crystallinity, the crystallization rate constant, the time allowed for crystal growth, and the Avrami index exponent, respectively. For example, Nakamura et al. [221] derived the following equation with an "isokinetic approximation" for non-isothermal crystallization conditions:

$$\theta = 1 - \exp\left[-\left(\int_0^t K(T)dt'\right)^{n}\right] \qquad \ldots\ldots(19)$$

With K(T) defined as:

$$K(T) = \left[k(T)\right]^{1/n} \qquad \ldots\ldots(20)$$

In the differential form the integral is eliminated to give:

$$\frac{d\theta}{dt} = nK(T)(1-\theta)\left[\ln\left(\frac{1}{1-\theta}\right)\right]^{\frac{n-1}{n}} \qquad \ldots\ldots(21)$$

Until the mid 1990's, Patel and Spruiell [222] determined Nakamura's relationship was the best model available in the current literature.

In melt spinning, however, the effects of molecular orientation must be included, and are most conveniently combined in the K term such that K=K(T,f), where f is a measure of molecular orientation. Zaibicki [223] proposed a series expansion of K(T,f) and arrived at a simple phenomenological relationship:

$$K(T,f) = K(T,0)\exp\left(A(T)f^{2}\right) \qquad \ldots\ldots(22)$$

Here the function A(T) is an experimentally derived linear parameter obtained from data and is assumed as always positive. Thus, when A is large (>100, as is the case for PET), small changes in orientation lead to large increases in crystallinity. Yet other approaches to stress-induced crystallization exist. Katayama [224] and Kobayashi [225] begin with the theory of rubber elasticity and claim the crystallization rate depends on the thermodynamic effects from the distortion of the molecular entanglement network. Nevertheless the available theory is severely limited and is still at best, good for describing near-isothermal, low applied stress crystallization rates.

Because a substantial theory for describing the crystallization rates of un-oriented polymer chains under stress is lacking, correct interpretations of the data from tensile experiments are still required. And again, the type of drawing deformation (constant extension or constant force) will dictate the observed response. In constant rate of extension drawing, increasing the draw temperature (above T_g) increases the shift of the crystallization onset (point E_1 in figure 2.28) to higher draw ratios, as shown in figure 2.35 [191]. The greater thermal energy of the system lowers the entropic barrier to an ordered crystalline state. However, the temperature dependent shift in crystallization onset weakens as strain rate increases. At a given high strain rate, increasing temperature shifts the crystallization onset to lower draw ratios, because the higher temperature increases the rate of orientation relaxation as well as the rate of crystallization. When the time for relaxation is short, i.e. high strain rates, the available cystallizable material is that which is already highly oriented.

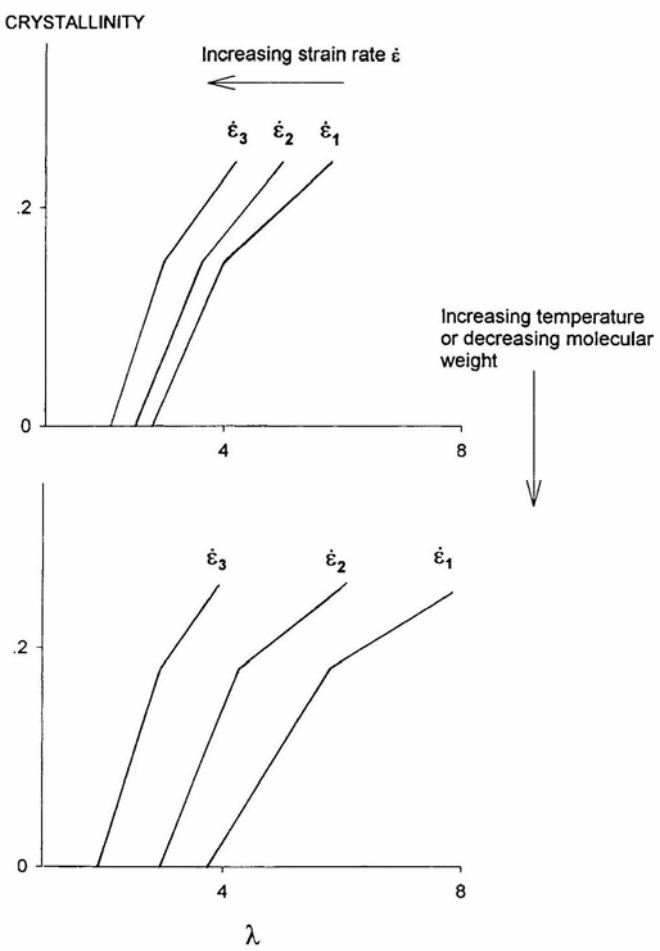

Figure 2.35. Schematic of the influence of strain-rate, temperature, or molecular weight on the crystalline content during a constant rate of extension draw of PET [191].

Some similarity can be drawn between constant rate of extension and constant force drawing crystallization phenomena. For example, similar temperature increases produce faster crystallization at a given level of non-crystalline orientation. In constant force drawing the imposed strain rates are much greater and the time for relaxation is much less than in constant extension rate draws, as such, an equivalent level of crystallinity could be expected to develop at lower draw ratios at a constant force. Yet figure 2.36 shows that within the draw ratios examined the constant force draws have a

lower level of crystallinity. Thus, the degree of crystallinity development in constant force drawing is heavily relaxation time dependent, where larger crystal contents are achieved with longer oven residence times or plate lengths (figure 2.31). It has been shown [226] that increasing the drawing temperature well over T_g (120-130°C) produces an increase in constant force draw ratio, which is characterized in terms of "flow drawing." The rate of relaxation is too rapid to allow orientation of the chains and the strain rate increases sharply as the entanglements slip and diminish the network. The end effect is a greater draw ratio, but, by speculation of the phenomena, the tensile modulus and strength are expected to be reduced.

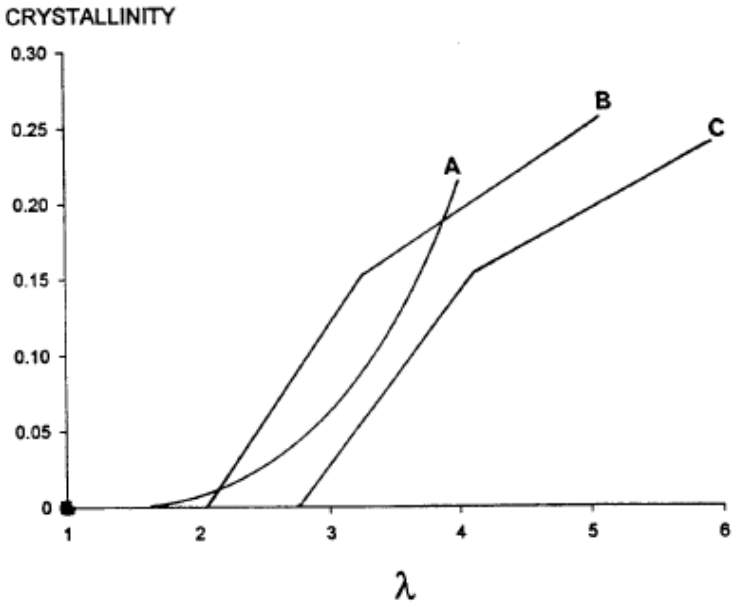

Figure 2.36. Volume fraction of crystal content as a function of draw ratio for PET film drawn at 90°C at constant force (A) with an average strain rate of 5 s^{-1}, at constant extension rate (B and C) with strain rates of 0.42 s^{-1} and 0.042 s^{-1} respectively.

For polymer layered silicate nanocomposites, the clay particles in a given polymer matrix always act as a heterogeneous nucleating agent for the generation of spherulites. The general effect of this nucleating agent is the significant reduction in crystallites size.

However, the enhanced nucleation effect is observed at low clay loading levels, typically between 1 and 5 wt% [227]. Outside the range, the higher concentrations of nanoclays provide larger steric or physical barriers. The increased physical hindrance at higher clay loading restricts the mobility of the chains and prevents the growth of well-developed lamellar crystals [228]. Except for the case of PEO and Na^+ MMT nanocomposites, the current literature cites a wide variety of polymer-clay systems that show enhanced crystallization. The matrices examined include: polyamides [229],[230], polypropylene [231],[232], polyethylene [233], poly(ethylene terephthalate) [234], poly(butylenes terephthalate) [235],[236], polystyrene [237], and poly(vinylidene fluoride) [238-240], among others. (To clarify the case of PEO, the Na^+ MMT surface promotes non-crystalline PEO chain conformations as the polymer readily forms strong coordination complexes with the surface cations [241].)

The case for nylon 6 and general polyamide layered silicate nanocomposites are reviewed because they are the only composites for which a crystal nucleation mechanism has been proposed. For some polymer nanocomposite systems, the nanoclay increases the polymorphic content, but for nylon 6 the γ-crystalline phase increases at the sacrifice of the α-crystalline phase[†]. From X-ray diffraction, data on nylon 6 show that the polymer almost exclusively crystallizes in the γ form [227]. Thus, one would expect that the amide-linkage of the nylon 6 backbone is hydrogen bonded with the surface of the silicate. Maiti and Okamoto [242] proposed a mechanism for the observed crystallization effect from TEM micrographs as the schematic shown in figure 2.37. From the diagram , the nylon chain hydrogen bonds in an orderly fashion to the clay surface (or surface

[†] Recall the γ form of polyamide molecules have hydrogen bonding between chains in a parallel arrangement

treatment, not shown), which in turn permits orderly hydrogen bonding of other nylon chains to that base. The hydrogen bonding continues until the structure becomes large an the amount of defects increases to create the amorphous phase of non-crystalline chain ends. The sandwiched type structure makes the system extremely rigid and significantly contributes to the improved mechanical properties. However, this system is specific to only polyamide layered silicate nanocomposites, and can not explain the enhanced crystallization of other polymer nanocomposite systems, such as the case of polypropylene. In addition, the two dimensional schematic is over-simplified because the chains are fully elongated, and the nanoclay is represented as a rod instead of a disk, leading the casual observer to assume the chains are hydrogen bonded one on top of another. Nevertheless, the proposed mechanism for crystal nucleation is one of very few available in the current literature.

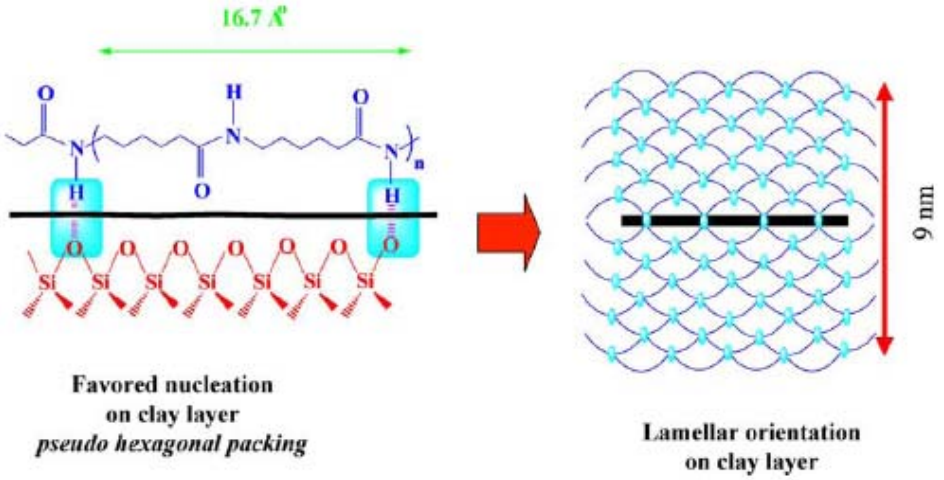

Figure 2.37. Schematic representation of the predominance of the γ-crystalline phase due to increased hydrogen bonding of the amide linkages to the silicate surface for nylon 6 nanocomposites depicting epitaxial crystallization, adapted from [242].

For PET nanocomposites, no such mechanisms have been proposed in the literature; yet a number of studies have reported the effect of nanoclay on both non- and isothermal crystallization kinetics. The majority of non-isothermal crystallization experiments have concluded that the nanoclay in PET lowers the cold crystallization temperature and raises the melt crystallization temperature compared to the neat PET, when the nanoclay loading is below 3 wt% [162, 168, 169]. Lee et al. [169] noted that the depth of the crystallization endotherm for the nanocomposite nearly equaled that of the pure material. The authors concluded from this observation that the nanoclay did not have any effect on the PET crystal size and shape, but rather only increased the crystal nucleation rate. However, Chang et al. [243] did not observe a change in cold or melt crystallization temperatures for triphenyl surface modified MMT in PET and concluded the nanoclay did not have a nucleation effect when the clay loading ranged from 0-3 wt%. At a 5 wt% loading of their organically modified clay, the authors [159] observed a decrease in melt crystallization temperature from 245°C to 227°C. Chang and coworkers concluded that because the 5wt% composite was not exfoliated the silicate layers could not provide an adequate "heat insulation effect" and caused the decrease in melt crystallization temperature.

Isothermal crystallization experiments have shown that nanoclays reduce crystallization half times of the Avrami analysis, and, therefore, accelerate the rate of crystal growth [168, 172, 234]. Ke et al. [234], in the perhaps the most widely cited PET nanocomposite crystallization paper, reported that the crystallization half times decreases with increasing clay loading from 0 to 5wt% of MMT. In fact the crystallization rate at 5wt% was 3 times faster than that of the pure material, even though the reported intrinsic

viscosities were 0.56 and 0.68 for the pure and 5wt% nanocomposite, respectively. The following was not concluded by Ke et al. [234], but aids in the discussion. A ratio between the calculated viscosity average molecular weight, M_v, (determined from the IV) and the molecular weight for entanglements is made to clarify the significant difference between the two IVs. The ratio of viscosity average molecular weight to the molecular weight for entanglements gives some idea into the degree of entanglement density and the rate of relaxation. For Ke and coworkers, the 5wt% composite is 20 to 30% more entangled that the pure material, which would signal a much slower, much more irregular crystallization mechanism. However the half time data clearly show that the 5wt% crystallizes faster, and leads to the speculation that the clay and PET synergistically produce crystalline structures regardless of the degree of entanglement. Barber et al. [172] observed a similar effect as Ke and coworkers, except that Barber et al. studied the effect of nanoclay on sulfonated PET ionomers. Barber observed that unmodified clay crystallized faster than an alkyl or phenyl modified clay. In addition, the authors noted that with increased exfoliation, the individual clay particles become less efficient at nucleating PET crystals. The conclusion reached was that "…the phenomena observed may be attributed to the presence of interactive surfaces that are capable of immobilizing chains in conformations that are more favorable for crystallization, as in epitaxial crystallization" [172]. No matter the complexity of the explanation, the authors found that intercalation of the nanoclay in PET aided crystallization.

The only study on the effects of drawing on the crystallization of PET nanocomposites fibers available, at this juncture, is the work of Xiao et al. [244]. The authors used a Barmag^{TM} drawing apparatus, assumed to be of the constant force type

discussed above. Unfortunately, the draw ratios were not reported, and the study mainly focused on the drawing temperature on the crystal size and volume fraction as a probe into the dimensional stability of the composite fiber (i.e. thermal shrinkage). The authors found that the nanocomposite fibers showed increased thermal shrinkage when compared to the pure PET at equal draw temperature [244]. The authors noted that PET/MMT fibers possessed overall lower crystal content and small had smaller crystal sizes. They concluded ultimately that the clay aids in nucleation but restricts the polymer chain motions, which were conclusions similar to those stated above.

A relatively small amount of research effort has focused on how nanoparticles effect the glass transition temperature, T_g, of PET [159, 245]. Recall that there are five factors that influence the T_g for a given polymer:

1. The free volume of the polymer; higher free volume gives lower T_g because there is more "room" for segmental motions.
2. The strength of the intermolecular forces between chains; stronger hydrogen bonding provides favorable interactions between segements and increases T_g.
3. The internal mobility of the chains and their freedom to rotate about their bonds; easier rotations lower the T_g.
4. The chain stiffness of the polymer backbone; benzene rings in the main chain typically make the backbone more rigid and increases the T_g.
5. The chain length of the polymer; from free volume and solid state properties the following equation can be derived to describe the relationship between T_g and chain length:

$$T_g = T_{g\infty} - \frac{K}{M_n} \qquad \text{……(23)}$$

In equation 23, the quantities $T_{g\infty}$, K, and M_n are the glass transition temperature at infinite chain length, a polymer dependent constant, and the number average molecular weight respectively. Therefore, from the five factors above only items 1 and 2 are the more likely factors that nanoclay fillers could influence. A surface modification to the clay could alter the molecular interactions and increase the free volume of the system. However, if there is a chemical reaction between the clay and polymer, such as in the cases of PET and PC (see the rheology section above and/or reference [84]), all five factors are likely to be influenced, particularly the chain length. As the clay induces degradation in the polymer, the chains become shorter and as equation 22 predicts, the T_g decreases rapidly. Chang et al. [159] observed a decrease in the glass transition temperature when the clay loading reached 5wt%. The IV of the 5wt% composite was slightly less than the lower clay concentrations, but the authors attributed the decrease in T_g as "due to clay agglomeration."

2.3 MECHANICAL PROPERTY IMPROVEMENTS OF PET AND RELATED STEP-GROWTH POLYMER NANOCOMPOSITES

After reviewing the literature on drawing PET fiber to a higher modulus, one would ask why not pursue perfecting the drawing process and inducing very high crystal contents and orientations to optimize the modulus, as opposed to filling the melt with nanoparticles? The answers are legion. For an example, the crystal modulus of PET has been calculated as 110-146 GPa [208, 246], but to date the largest moduli of highly-

drawn, solution-spun, high-molecular weight PET fibers range between 30-40% of the crystal modulus. With the considerable research effort spent toward producing the perfectly oriented, highly crystalline PET fiber, the effort and expense are becoming too great. On the other hand, fillers are used to improve the stiffness, rigidity, and heat distortion temperature of the polymer matrix. In addition, cheap fillers reduce the volume of polymer needed for a given application, which in turn reduces costs associated with expensive polymers.

The tensile (or Young's) modulus, breaking strength, toughness, and impact strength of filled polymer composites depends on particle size, aspect ratio, surface modification, concentration in the melt, and the degree of dispersion of the given concentration [6]. In particular, nanoparticles have been raised to the forefront of filler materials in polymers, whether thermoset or thermoplastic, at the expense of traditional micron sized particles. In the following sections, it will be shown that the higher aspect ratio and larger surface area of nanoparticle are the primary factors that bring the large improvements to mechanical properties such as the modulus (as much as a 30-70% increase) at very low weight percent loadings (<7 wt%). Due to the large surface areas, these particles can be modified with larger volumes of surfactants that interact favorably with the polymer matrices to further increase the mechanical properties. As well, nanoparticles are inherently favored as fillers in melt spinning processes, because the individual particles have dimensions up to 3 orders of magnitude smaller than macro-particles, which helps considerably in preventing cohesive fracture. A particle on the order of magnitude of the extruded fiber would induce melt instabilities just after the spinneret and would be nearly impossible to push through a proper PET spin-pack.

Therefore it is worthwhile to examine the mechanical properties of nano-particle filled PET composites and related polycondensate systems (i.e. nylon-6). This section begins with a review of the attempts at modeling the response of nanoparticle filled polymers. The bulk of work has examined the application of the Halpin-Tsai equations, but other models are discussed. Then the specific responses of some nanoparticle filled PET fibers and injection molded parts are compared. Where appropriate for discussion, nylon-6 nanocomposite fibers supplement the review.

2.3.1 PREDICTING THE MODULI OF POLYMER NANOCOMPOSITES BY COMPOSITE THEORY

The discussion of modeling the elasticity of semi-crystalline polymer composites will begin with the success of modeling the initial and full stress-strain curves of pure semi-crystalline PET. Melt spun PET fiber have the generally accepted microstructure consisting of crystalline micelles, fringed with amorphous free ends, stacked in a fibrillar manner [247]. Hearle et al. [247] used composite theory to develop a quantitative approach to examine this qualitative microstructure model. The authors noted two challenges to developing such a model; both amorphous and crystalline moduli of the polymer need to be extrapolated, and assumptions need to be made to simplify the complex fiber system. The authors neglected variations in crystal size and orientation and assumed an isotropic non-crystalline phase. Although the authors attempted to model the entire stress-strain curve, they reported mild success of predicting modulus values at low (>10%) strain values. The two models used were based on ideal

composites deformed at constant strain (parallel model with a fibrillar microstruture) and deformed at constant stress (series model with a lamellar microstructure). In the first case the authors applied a weighting factor, P, to average the simple rule of mixtures response to deformation.

The series rule of mixtures (Voight):

$$E_s = \left(X_c E_c^{-1} + (1 - X_c)E_a^{-1}\right) \qquad \ldots\ldots(24)$$

The parallel rule of mixtures (Reuess):

$$E_p = X_c E_c + (1 - X_c)E_a \qquad \ldots\ldots(25)$$

The weighted average E_s and E_p by factor P.

$$E_m = PE_p + (1 - P)E_s \qquad 0 \le P \le 1 \qquad \ldots\ldots(26)$$

Here the variables E_s, E_p, E_m, E_a, and E_c are the modulus of the series prediction, parallel prediction, weighted mean average, amorphous polymer phase, and crystalline polymer phase. The variable X_c is the volume fraction of crystalline content. Note that for P=0.5, the weighted average model describes the fringed micelle microstructure. Thus for the case of nanoparticle fillers in semi-crystalline polymers, the question arises as to whether an accurate prediction could stem from a further modification of equation 26, for example:

$$E'_m = X_n E_n + (1 - X_n)E_m \qquad \ldots\ldots(27)$$

where the parameters X_n and E_n are the nanoparticle volume fraction and elastic modulus.

A further examination of micro-composite theory is required. Typically, fillers are added as mass fractions or in weight ratios to the polymer matrix during composite synthesis, but all composite theories are based on volume fraction. Therefore, to convert between mass and volume the density of the clay and polymer must be accurately known.

Obviously, if the individual platelets are exfoliated in the matrix their density will differ from the bulk. The general calculation has been outlined by Chen and Evans [248], and was an adjustment of the bulk density with the volume of water and inter-gallery spacing removed.

$$\rho = \rho_{bulk}\left(1-\phi_{water}\right)\frac{d_{001}}{h_s} \qquad \ldots\ldots(28)$$

Where ρ_{bulk} is the volume fraction of water in the clay, d_{001} is the basal spacing of the silicate sheets from XRD, h_s is the platelet thickness, and, therefore, d_{001}/h_s is the fraction of void space or space to be filled with polymer between the two platelets. Chen and Evans [248] stated that the density could be calculated by the ideal crystal structure and chemical formula. But, they noted that the ideal structure does not account for impurities and defects, which are common in these clays.

From density estimates of the clay filler, the elastic modulus can be estimated by interpolation of other similar clay structures. Fornes and Paul [249] estimated the modulus of their montmorillonite clays as 178 GPa based on the structure of muscovite. Chen and Evans [248] proposed that the elastic modulus of montmorillonite type clay platelets was in the range of 178-265 GPa. These authors showed that, although the range was rather wide, there was relatively little error when using volume fractions below 30%. The low and high values cited in the literature were 49 [250] and 400 [251] GPa, which the low values could be taken as estimates of the bulk modulus, but the highest values are too unrealistic compared to similar clays. By the same reasoning, the Poisson's ratio of montmorillonite, 0.28, was based on literature values of mullite (0.28 [252]) and kaolinite (0.27 [253]).

The simplest composite theories relate or simplify to the rule of mixtures under certain conditions. Built on self-consistent field theories, Halpin and Tsai [254] developed a simple analytical composite theory that predicted the modulus of a uni-directional composite as a function of aspect ratio. The Halpin-Tsai equation is of the form:

$$\frac{E}{E_m} = \frac{1 + \zeta\eta\phi_f}{1 - \eta\phi_f} \qquad \ldots\ldots(27)$$

with:

$$\eta = \frac{E_f / E_m - 1}{E_f / E_m + \zeta} \qquad \ldots\ldots(28)$$

Where, E, E_f, and E_m are the moduli of the composite, filler, and matrix respectively; ζ is a shape factor or aspect ratio; ϕ_f is the filler volume fraction. The series and parallel rules of mixtures are obtained when the parameter $\zeta = 0$ and ∞ respectively. Thus, at infinitely long aspect ratio the resulting modulus is directly proportional to the sum of each weighted modulus. However, the utility of the Halpin-Tsai equation comes from its application to systems of discontinuous fibers and platelets fillers. The model assumes that the filler is perfectly aligned, asymmetric, and uniform in shape and size and that there is perfect adhesion between the filler and continuous phase.

Fornes and Paul [249] compared the Haplin-Tsai and Mori-Tanaka models and their success at predicting the modulus of nylon-6 montmorillonite nanocomposites. Although the Mori-Tanaka model was capable of predicting transverse and uniaxial moduli, the theory blurred the shape of the filler particle by making it ellipsoidal in geometry. The Halpin-Tsai equation predicted more accurate sample geometry, but

heavily depended on aspect ratio and did not include a Poisson's ratio for calculation of the transverse modulus. Even so, the Mori-Tanaka and Halpin-Tsai equations shed understanding of the effect of aspect ratio and exfoliation. Compared to the data, both models over predicted the modulus at the true platelet aspect ratio, and bulked properties were substituted to adequately fit the data.

Many authors have shown that the Halpin-Tsai equations over estimate the modulus of the nanocomposite [255-259]. In addition, as Fornes and Paul [249] reaveled, the number of platelets per stack, N, has the most significant effect on the composite modulus for $1 \leq N \leq 5$. Therefore, exfoliation of the clay particles has been reaffirmed as a necessary condition for optimal reinforcement. However, most polymer nanocomposites are intercalated to some extent, and the application of Halpin-Tsai theory, with N equal to an integer, can not accurately model the reinforcement. Some authors have modified the theory semi-empirically to account for varying degrees of intercalation. Brune and Bicerano [260] made perhaps the most mathematically involved attempt at Halpin-Tsai modification for the case of nanocomposites, but their success was not backed by any experimental data. Kinloch et al. [255] and Wu et al. [261] introduced simple pre-factors of 1/3 or 2/3 respectively to adjust the Halpin-Tsai predictions, but no justification was given, even though these could be adjustments for mis-orientation or imperfect bonding between filler and matrix.

A model established to ease the assumptions of perfect bonding and axial alignment was an extension of Takayanagi's 2-phase composite theory by Ji et al. [262]. The model by Ji and coworkers takes into account a third inter-facial phase in addition to the traditional two phases of filler and matrix present in polymer layered silicate

nanocomposites. The interfacial phase is hypothesized as the trapped polymer phase between two silicate sheets of small separation. Ji's model, shown below, makes no assumption as to the state of clay orientation in contrast to Halpin-Tsai.

$$\frac{1}{E}=\frac{1-\alpha}{E_m}+\frac{\alpha-\beta}{(1-\alpha)E_m+\frac{\alpha(k-1)E_m}{\ln k}}+\frac{\beta}{(1-\alpha)E_m+\frac{(\alpha-\beta)(k+1)E_m}{2}+E_f\beta} \quad \ldots(31)$$

with:

$$\alpha=\sqrt{\phi_f\left(2(\tau/t_c)+1\right)} \quad \ldots\ldots(32)$$

$$\beta=\sqrt{\phi_f} \quad \ldots\ldots(33)$$

$$k=\frac{E_f}{E_m} \quad \ldots\ldots(34)$$

Where the parameters E, E_f, and E_m are the moduli of the composite, filler, and matrix respectively; τ is the thickness of the interphase region taken to be the basal spacing from XRD; t_c is the thickness of a single MMT sheet ~ 1 nm; ϕ_f is the filler volume fraction. The dependence of equation 31 on the interfacial separation between clay platelets further generalizes the model by not making an assumption of the state of clay dispersion. Therefore, only basal spacing data are required to estimate the elastic modulus using this model; no TEM micrographs are required to discern aspect ratios. The α parameter is a form factor related to the particle geometry and changes its relationship for spherical or cylindrical fillers. The model is most sensitive to changes in particle shape and, thus, the form of α. The model predicts that spherical fillers produce the largest enhancement in modulus at a given volume fraction over disk- or rod-like fillers, which is in grave contradiction of Halpin-Tsai equations that clearly show higher aspect ratios produce

larger effects. In perhaps another inherent flaw, as the thickness of the interfacial region increases, so does the modulus without a plateau at extreme distances in which the interface has become the continuous phase of the pure matrix.

At low volume fraction the composite theories do not over estimate the modulus to an unrealistic extent, so perhaps a low volume fraction theory would provide better accuracy, such as that of Guth and Gold [263] for filled rubbers. A polymer above its Tg and under small strains with enough molecular weight for several entanglements can be approximated as a lightly crosslinked rubber. Under these conditions for a filled polymer, these systems are analogous to filled rubbers. Guth and Gold developed a theory to account for the interactions of rubber and spherical filler particles. Guth [264] later generalized the theory to account for the filler shape:

$$E = E_m\left(1 + 0.67\alpha\phi + 1.62(\alpha\phi)^2\right) \qquad \ldots\ldots(35)$$

The shape factor α can certainly be related to the filler aspect ratio. Wu et al. [261] tested the modulus of SBR filled with various volume fractions of disk-like nanoparticles. The authors found that the Halpin-Tsai equations without a modification poorly modeled the experimental moduli, while the Guth, equation 35, model accurately predicted the modulus up to the limit of Guth theory of 10 volume percent.

So far the discussion of the modifications to composite theory has focused on the influence of aspect ratio on modulus. However, some authors believed that the correct calculation of the true volume fraction has the same effects as aspect ratio included and therefore was the more substantial modification to composite theory. Chen and Evans [265] concluded that when the dimensions of the particle are on the order of magnitude of

the radius of gyration of the polymer, the physical properties of each phase change at the molecular level. These properties change significantly when the polymer phase was adsorbed on the silicate surface. The authors noted the polymer in the galleries was strongly adsorbed to the nearest platelets and was, therefore, likely to possess an elastic modulus larger than the bulk. The clay particles were very well known to cause the formation of a tie chain network and physical crosslinking by this adsorption. Vaia and Giannelis [266] underlined the changes in conformations and morphology caused by polymer-to-silicate adsorption and stated that much of the polymer was "interphase-like" instead of the distinct filler-polymer boundaries. Chen and Evans [265] accounted for this interphase-like region in the volume fraction, which could then be substituted into the traditional composite theories to obtain a more accurate prediction. In turn, the authors developed relationships to account for varying degrees of intercalation and exfoliation. Chen and Evans began with the traditional volume fraction for a composite:

$$\frac{1}{\phi_c} = 1 + \frac{\rho_c (1 - \mu_c)}{\rho_p \mu_c} \qquad \ldots\ldots(36)$$

The parameters ρ_c and ρ_p are the densities of the clay and polymer respectively; μ_c is the mass fraction of clay; ϕ_c is the volume fraction of clay. The authors then modified equation 34 based on the argument that the layer of polymer adsorbed on the surface of the particle is on the order of the radius of gyration, R_g [267-269], such that the effective clay volume fraction must become:

$$\phi_c^{\downarrow} = \phi_c \left(1 + k R_g A_p \rho_c\right) \qquad \ldots\ldots(37)$$

Where the variables A_p and k are the specific surface area of the particle and the fraction of the adsorbed layer acting as a solid respectively. Based on these simple arguments, Chen and Evans [265] derived a series of relationships for the effective volume fraction of intercalated untreated clay, intercalated organically modified clay, and a mixture of intercalated-exfoliated nanocomposites. For this last class of nanocomposites, the effective volume fraction of exfoliated clay particles is defined by equation 38 and intercalated particle by equation 39.

$$\phi_c^e = \frac{\rho\mu_c^{|}(1-f_i)\mu_c^o}{\rho_c^p} \qquad \ldots\ldots(38)$$

$$\phi_c^i = \frac{\rho\mu_c^{|}f_i\left[d_2(N-1)+h\right]}{\rho_c^{|}\left[d_1^{|}(N-1)+h\right]} \qquad \ldots\ldots(39)$$

Where ρ, ρ_c^p, ρ_c' are the densities of the composite, the clay platelet, and the organoclay respectively; μ_c'and μ_c^o are the mass fractions of organoclay and silicate platelets in the organoclay respectively; d_1' and d_2 are the basal spacings of the organoclay and the intercalated composite respectively; h is the thickness of the platelet; N is the number of platelets in the intercalated stack; f_i is the fraction of clay intercalated or not exfoliated. The authors compared the composite theory moduli, calculated from the effective volume fractions, to those obtained experimentally and found better agreement than those calculated from nominal volume fractions. Chen et al. [270] found good agreement between their data and the modulus values calculated from a Christensen composite model [271] using effective volume fractions.

Crystallinity in a polymer composite is a difficult feature to capture in a two phase composite theory, and numerically intense methods (finite elements, molecular

dynamics) are used to account for polymer crystallinity. Sheng et al. [257] examined the effect of crystallinity on the modulus enhancement of nylon-6 nanoclay composites by a finite element scheme. The authors found that the crystallinity of a matrix did not have a significant effect on the modulus, but that the nanoparticles provided the dominant reinforcement. The details of how crystal content was incorporated into the model were left unclear, but for PET with a crystal modulus of 147 GPa and a filler modulus of 178 GPa, it would be assumed that crystallinity has a noticeable effect in large quantities. Molecular dynamics simulations are alternatives to capturing effects of crystallinity among others. Buryachenko et al. [272], besides deriving their own numerically intense methods, reviewed molecular dynamic simulations in polymer nanocomposites. The authors found that the simulation of only spherical nano-fillers can give realistic results in relatively short computation times; otherwise most simulations have problems accounting for the large aspect ratio of the silicate filler with respect to the atom scale of the polymer chains.

From the above collage of composite theories the following conclusion can be made for the state of elastic modulus prediction in polymer nanocomposites. First, successful analysis requires accurate physical data such as the moduli of the respective components in the bulk and molecularly, volume fractions, densities, basal spacings, intercalated stack sizes, and correct determination of aspect ratio. It is apparent that all of these physical quantities are highly dependent on the degree of dispersion. Second, almost all theories assume perfect adhesion between polymer and particle, and because of this assumption almost all methods (Halpin-Tsai, Mori-Tanaka, Takayanagi, Chrsitensen, etc..) over-predict the modulus response at high loadings of clay (<5 vol%). The iterative

or more numerically intense models estimate the moduli to a better accuracy, but require longer computation times. At this juncture, it is concluded that modeling polymer nanocomposite for modulus response can at best give an order of magnitude estimate.

2.3.2 EXAMINATION OF THE FACTORS LEADING TO MODULUS AND TENACITY IMPROVEMENT IN PET NANOCOMPOSITES

The factors examined in this section include filler type, filler surface modification, filler loading or concentration, type of compatibilizing agent to improve adhesion between filler and polymer, and spinning speed, for the case of fibers. These are the five factors that have been studied in the current polyester nanocomposite literature to a significant extent. By no means are these the only factors that can effect the mechanical properties of the composites. For instance, the synthesis route by either in-situ polymerization or melt compounding has already been discussed, as well as the subsets of compounding by twin screw or single screw extrusion. Molecular weight is a significant factor that dictates not only the spinnability, or threshold viscosity for filament formation, by the degree of entanglements that ultimately affects the strength and modulus of the composite. Unfortunately, no authors in the current literature discuss the influence of matrix molecular weight, and, therefore, this factor is omitted. Additionally, the effect of polymer crystallinity is expected to have a major influence on end properties, but because the current literature lacks such data this subject is omitted from the list above. In fact, structure property relationships are currently lacking in the polyester nanocomposite literature, and for purposes of crude comparison the nylon-6 nanocomposite fiber literature is discussed. However, throughout this section, one should

bare in mind the non-mutual exclusivity of these factors and, for the basis of cross comparison with other authors, the assumption that the dispersion of particulates is relatively equal in each case.

2.3.2.1 *The Effect of Mineral Filler Type*

So far in this review the focus of filler type has been on montmorillonite (MMT) type layered silicates. However, other clays and minerals exist that are capable of nano-order dimensions and that possess high elasticity similar to MMT. Brucite is a magnesium hydroxide mineral that has a neutral charge so that no interaction persists between the layers. The chemical make up brucite-type clays are similar to the middle layer of the silicate sandwich found in MMT. Lee et al. [169] studied injection molded PET nanocomposites with brucites in the form of layered double-hydroxides that possessed an anionic charge between the galleries. The layers were formed by the substitution of trivalent aluminum for divalent magnesium to create a positive charge. For these authors, filler concentrations were limited to 2 wt% due to the brittleness of the composite above this loading level. Unfortunately no molecular weight documentation was made, but the shear viscosity decreased upon addition of larger quantities of brucite filler, which was a sign that the PET matrix was degrading in the presence of the filler. Nonetheless, the authors recorded the largest improvement of an 8% increase in tensile modulus and 16% increase in tensile strength for a 2wt% dodecylsulfate-modified brucite/PET nanocomposite, in which the improvements were relative to a pure PET sample [169]. Other results obtained were a 6.7% increase in modulus and 4.7% increase

strength for a 1 wt% dodecylbenzene sulfonate-modified brucite in PET [169]. In every case examined the elongations at break, when compare to the pure un-filled resin, were drastically reduced from 420% for the pure to 70-75% for the composites [169].

For injection molded samples containing MMT type minerals, Sanchez-Solis et al. [84] found that for a 1wt% dodecylamine-modified MMT the tensile modulus increased by 22% and the strength increased by 36% over the pure resin. The elongation at break for this sample was 2/3 of the magnitude of the pure material's response. These authors also showed qualitatively that the molecular weight of this composite was nearly equivalent to their pure sample, such that the MMT did not catalyze matrix degradation. Other notable results for these authors were a 30% increase in modulus and 15% increase in strength for a 2wt% octadecylamine-modified MMT/PET nanocomposite. Therefore, in comparing the two papers, MMT type minerals produce larger improvements in modulus and strength per mass loading than brucite-type layered double hydroxides when modified with long alkyl chain surfactants (in this case dodecylamine or dodecylsulfate) and injection molded with PET.

Chang and coworkers [159] investigated the case of the effect of clay type for PET nanocomposite fibers. In their earlier experiments [243], the authors treated MMT with a dodecyltriphenyl-phosphonium chloride surfactant and in-situ polymerized their PET nanocomposites. At a 2wt% loading of this clay and at their lowest take up speed (effects of take up speed are discussed later in this section) the authors reported a 50% increase in tensile modulus and 48% increase in tensile strength with a marginal effect on the strain at break [243]. Later experiments [159] by these authors were with a modified synthetic fluoro-mica treated with the same triphenyl-surfactant. A fluoro-mica has had

all of its surface hydroxyl groups replaced with fluorines, by which one hopes to eliminate the complexed surface water to reduce the possibility of matrix degradation. They synthesized a 2wt% nanocomposite of treated fluoro-mica and PET in a similar fashion as before and obtained an inherent viscosity (molecular weight) equal to that of their 2wt% MMT. However, at 2wt% of fluoro-mica, the modulus and strength increased by only 40% and 39%, respectively, with a decrease in strain at break relative to the same pure PET sample as before [159]. Therefore, for fibers as well as injection molded plaques, MMT gives the greater improvements to tensile properties per loading of filler than fluoro-mica or brucite.

2.3.2.2 *The Effect of Particle Concentration*

When increasing clay concentration from 0 to 5wt%, the general trend is that the tensile modulus increases monotonically with clay addition. In contrast, the tensile strength decreases with clay addition for injection molded composites. Fibers behave much the same in modulus, but the tenacity occasionally increases with clay loading. For instance, the two studies by Chang and coworkers [159],[243] showed conflicting trends in strength as a function of nano-filler loading that depends on the type of filler in the PET matrix. The study on MMT filled systems [243] showed that strength increases monotonically from an improvement of 26% over the pure at 1 wt% to 54% at 3 wt% (at take up speed equal to their extrusion speed and with no correlation with molecular weight). For the fluoro-mica study, the trend in strength as a function of filler loading showed the distinct reduction in strength as clay loading increases. Beyond the 5 wt%

range most mechanical properties did not improve, mainly because of the inability to fully disperse the individual particles and the gross reduction in matrix molecular weight from the interstitial water retained in the clay galleries.

2.3.2.3 *The Effect of Particle Surface Treatment*

The inherent incompatibility between an organic polymer phase and an inorganic mineral phase leads to the necessity of a particle surface treatment to produce better dispersion in nearly all cases of polymer nanocomposites. The combined studies of Pegoretti et al. and Barber et al. provide a base of comparison for determining the influence of MMT surfactants. For example, Barber and coworkers [172] showed that at a 5wt% loading of Cloisite 10A (a phenyl-modified clay) the increase in modulus was 19% greater than that produced from the addition of 5 wt% of unmodified clay to a PET matrix. The authors also showed an 8% greater increase in 5 wt% Cloisite 15A (a long alkyl chain-modified clay) than that produced from the unmodified nanoclay composite [172]. Pegoretti et al. [167] showed that a 5 wt% loading of Cloisite 25A (a shorter long alkyl chain modified clay than Cloisite 15A) produced an 18% greater increase modulus relative to a 5 wt% unmodified-MMT injection molded composite. However, one must keep in mind that the reported concentrations in both papers were nominal, such that the silicate concentration was not used as the basis for comparison. In fact, Cloisite 25A is 34% by weight surfactant and thus 66% silicate, which would put its comparison concentration with the unmodified clays closer to 3 wt% instead of 5 wt%. If this is the basis of comparison, then for Pegoretti at al. the Cloisite 25A surface modification

produced a 24% increase in modulus and a 180% increase in tensile strength. The dramatic increase in strength denotes the increased interfacial interaction between the clay and PET. Therefore, one can confirm the conclusion that a particle surface treatment is necessary to improve the tensile properties of injection molded PET nanocomposites.

McConnell and coworkers [165] examined three types of surfactants on synthetic fluoro-micas melt compounded to with PET to form nanocomposite fibers. The author's results were heavily dependent on spinning speed[‡], but at the lower spinning speeds a 4wt% polypropylene oxide modified fluoro-mica produced a 180% increase in modulus and 130% increase in strength [165]. The other two modifications were based on non-polar long-alkyl chains. A triple (double) long alkyl-chain amine modified fluoro-mica gave a 170% (82%) and 110% (24%) increase in modulus and tenacity, respectively. Therefore, it was suspected that the polar oxygen groups on the polypropylene oxide modified surface yielded the more favorable interactions with PET, than the non-polar alkyl-amines at low spinning speeds.

2.3.2.4 *The Effect of Compatibilizers*

PET is a polymer in which the dominant forces of molecular interactions are either due to hydrogen bonding by the carbonyl at the ester linkage or more likely due to van der Waals attractions at the benzene rings. In which case, polar surfactant groups on the filler surface may be incapable of producing the optimal interfacial attractions to retain or improve the composite strength. So too, one would not intuitively expect that

[‡] See section 2.3.2.5 for the effect of spinning speed and the effect of the degree of molecular orientation of the matrix chains on modulus and tenacity values.

non-polar long-alkyl chain surfactants would improve the mechanical properties to a greater extent than polar surfactants. Further, large phenyl rings or benzyl-type rings produce physical hindrances that possibly prevent a larger number of favorable van der Waals interactions. These considerations have led some authors to conclude that a compatibilizing or grafting agent may aid in boosting the necessary interactions between the polymer and surfactant to optimize the mechanical property response.

Sanchez-Solis and coworkers incorporated maliec anhydride and pentaerithritol compatibilizing agents into PET/unmodified MMT composites [84]. Except for a single odd case at 1wt% unmodified clay with pentaerithritol, the addition of either agent reduced the strength of the composite. In fact, the results using only unmodified MMT were greater than those that had a compatibilizer. However, the modulus values were larger when using the agents, but the sacrifice in strength defeats the purpose of using these agents. Retention of improvement of the composite's strength shows that the filler and polymer adhere well with each other, and because a compatibilizer is supposed to boost the degree of interaction, strength should increase. In most cases the strain at break for all the compatibilized composite in this study was extraordinarily reduced. For example, the pure PET sample had a strain at break of 150%, but for the compatibilized composites the strain at break was 2-3% [84]. Therefore, for PET/MMT composites, neither maliec anhydride nor pentaerithritol are effective compatibilizers.

Barber et al. [172] studied the effect of grafted ionomer concentration onto the PET backbone on the modulus of injection molded polyester nanocomposites. The authors showed that a phenyl-modified (Cloisite 10A) nanoclay filler at 5 wt% gave the greatest improvement in modulus to a pure un-grafted PET resin. When the amount of

ionomer was increased, in which the authors expected the ionomer to interact favorably with the particle surface, the improvement to the tensile modulus was not more than an additional 3.5% at the highest ionomer content. For the case of un-modified clay filled systems, in which the entire surface is open to sodium ion displacement by the ionomer, the additional improvement to modulus was not more than 2% at the highest ionomer concentration. Thus, grafting sulfonated ionomers onto the PET backbone produces only a marginal increase in mechanical response in injection-molded samples.

2.3.2.5 *The Effect of Spinning Speed*

The spinning process produces several forces that act on the freshly extruded filament. The winding device or take-up machine, in most cases, applies the dominant force to the filament. Therefore, as the take-up speed increases, the other forces involved must balance out and often results in the reduction of the filament diameter. As the diameter reduces, the molecules are pulled into alignment with each other to produce an anisotropic orientation in the take-up direction. As discussed earlier, orientation aids in the development of crystallites, which generally improve modulus and strength.

For the case of PET nanocomposite fibers, increasing the take-up speed decreases the modulus and tenacity of the fibers [159], [165]. Such an observation is interesting to the discussion of nanocomposite orientation. At first glance, these results seem contrary to the stance of current nanocomposite reinforcement, which is of the opinion that total nanoparticle alignment to the direction of deformation gives the optimal mechanical property response [2],[88],[273]. One would expect higher spinning speeds to increase

the orientation of the particles and, thus, improve the modulus of the composite, if one believes that there *is* a significant interaction between the polymer and clay surface.

Those, that believe there is an interaction rightfully conclude so from the large quantity of data on injection molded nanocomposites. These authors then follow suit in their conclusions on nanocomposite fibers. For example, McConnell et al. [165] suggested from the SEM images that the larger surface irregularities in the higher speed spun nanocomposite fibers led to the reduction in modulus. However, the authors did not correlate the relationship between filler type and the degree of surface irregularity to the obtained modulus data. The conclusion was reached by comparing the composites as a whole against the smooth pure PET fibers. Furthermore, in some cases, the authors found an increase in tenacity with increasing take-up speed relative to the pure material. A composite with an irregular surface would not intuitively lead to the conclusion that it would have greater strength over a smoother sample. Perhaps another mechanism was at play; the answer may pertain to molecular orientations.

Chang et al. [159, 243, 274, 275] attributed the decline in modulus with spinning speed to "debonding" and the presence of voids in the nanocomposite samples. More explicitly, the authors were quoted as stating [159]:

> "…hydrostatic elongation during [extrusion] resulted in debonding of the polymer chain itself and void formation around the polymer-clay interface...[poor adhesion between polymer and filler] leads to yielding or debonding, or both, to occur at or near the interface."

Then, Chang et al. [159] cited papers that have reported an imperfect polymer-filler interface and lower Young's modulus improvements than expected. Cavitation around the filler surface under applied tension is a well documented observation. In fiber

analysis, the presence of voids will lead to cavitations and affect the drawability as well as the modulus and tenacity. However, one would expect that an increase in filler concentration, not spinning speed, would create a larger amount of voids in the fiber, if void numbers are proportional to particle surface area. Yet, Chang et al. [159, 243, 274, 275] reported an increase in exfoliation with increasing spinning speed, such that the larger amounts of exfoliated platelets could produce the larger number of voids[§]. Additionally, the authors' definition of the cryptic term "debonding" is unclear. In the first part of the statement above, it seems as though the authors were implying that the PET chains degrade during melt processing. Certainly under extremely high shear rates molecular weight degradation may occur in some polyesters. Unfortunately, Chang et al. [159] did not report the associated extrusion speed or take-up speeds, rather the authors took the ratio of the two and reported the draw down ratio. Indeed, if this was the intent of "debonding's" definition then the authors should have kept records of molecular weight data. In the second part of the statement by Chang and coworkers, "debonding" seems to refer to a short-lived strong interaction between the polymer and clay that now because of the increased spinning speed, has lost most of its strength. The authors did not offer an explanation as to why the polymer and clay "debond."

However, it may be conjectured from the following logic that the increased molecular orientation from higher spinning speeds reduces polymer-particle interactions. If a void is considered a defect, then to an extent a clay particle may be considered a defect as well, because the platelet creates the extra void or defect space. In fiber samples, defects act as area of stress concentration, such that the exfoliated clay platelets

[§] Recall, increasing the exfoliation of a nanoparticle increases the volume fraction of platelets and exposed surface area.

may be considered as more effective stress concentrators and larger defects than the intercalated stacks. A stress concentrator makes the local material more compliant or more readily deformable than the surrounding material. So, when spinning speed is increased, exfoliation is increased and the amount of stress concentration or defects per volume is increased producing a softer, less stiff composite. Now, the question remains as to why the material surrounding the nanoparticle is more compliant when the composite is in fiber form as opposed to a thicker injection molded form. In which case, the question arises as to why the higher degree of molecular orientation imparted during fiber spinning change the strength of interactions from polymer-particle dominated to polymer-polymer dominated as orientation increases. Then this raises the issue of whether the polymer and filler interact at all in a fully polymer chain oriented PET nanocomposite.

As discussed in previous sections, high speed spinning and second step drawing, after initial spinning, are two methods that improve the molecular orientation of polymer chains and are used to achieve appropriate levels of modulus and tenacity for required applications. For PET nanocomposites although at low spinning speeds (1-1000 m/min), the modulus may decrease with an increase in spinning speed, the scenario becomes slightly different when high spinning speeds are examined in nylon-6 nanocomposites. It must be noted that the following discussion pertains to nylon-6-clay nanocomposite fibers and that to extrapolate the following conclusions to the discussion of PET nanocomposite fibers should be done with extreme caution if at all. Nonetheless, because relatively little has been published on PET composite fibers, the following gives a valuable perspective.

Giza et al. [276] studied the effects of high spinning speeds on the structure property relationships of clay filled nylon-6 nanocomposite fibers. The speeds used were in the 1000-5000 m/min range to produce partially oriented yarns and to observe the effect that clay filler had on the onset of stress induced crystallization. The general finding was that increased spinning speeds created an increase in modulus concomitantly with increasing clay content at a given birefringence or rather at a roughly equal degree of molecular orientation. However, the authors found that spinning pure nylon-6 at a higher speed (in the range of 6000-7000 m/min) produced an equivalent modulus to the nanocomposites spun at lower speeds (in the range of 2000-3000 m/min). Yet, the strength of the unfilled material spun at higher speeds was much greater than the nanocomposite's strength when spun at lower speeds, possibly because of the lower degree of amorphous orientation in the nanocomposites. The increase in modulus with spinning speed for the composites was partially attributed to the larger amount of γ-crystalline phase content nucleated by the MMT filler, which grew at the sacrifice of α-form crystalline content[**]. Giza et al. [276] did not specifically focus on the rise in modulus with spinning speed, but focused on the effects of clay concentration. The authors affirmed a conclusion made by Usuki et al. [277] that the nylon-6 backbone ionically bonded to the clay particles to stiffen the un-oriented non-crystalline phase, which explained the increase in modulus with clay content, but did not explain the increase with spinning speed. Rather, the conclusion can be made that although the clay particles aided in strengthening the amorphous phase and allowed for higher drawability such that a higher degree of molecular orientation could be achieved at a lower spinning

[**] Recall from the discussion on drawing that larger amounts of γ-form crystallites improve the ductility and drawability of a polyamide material, because of the lower density of these crystals as opposed to the tightly packed hydrogen bonded α-forms.

speed, the modulus will increase, but the loss in stronger, denser α-form hydrogen bonded crystals inhibits significant improvements in strength or tenacity. Unfortunately, for PET fibers the main intermolecular interaction is not through hydrogen bonding of the carbonyls, such that the above conclusion does not apply per se.

A mechanism that could apply to PET-clay nanocomposite fibers from the nylon-6 nanocomposite fiber literature was proposed by Ibanes and coworkers [278, 279]. Essentially, the authors stated that the lack of reinforcement by the clay filler was due to the discrepancy in microfibril to nanoparticle length scales. Microfibrils or fibrils are the bundled constituents of filaments; a fibril diameter is roughly 1-10 nm and depends on the polymer compared to the filament diameter of melt spun fibers on the order of several microns. In drawn samples, the fibril length scales determined by small angle x-ray scattering, SAXS, was on the order of several microns, which greatly exceeded the dimensions of the clay platelets oriented in the fiber's long axis [280, 281]. Therefore upon deformation the majority of applied stress is absorbed by the fibrils and the parallel coupling between particle and polymer modulus does not occur. In addition, it can be concluded that there is no specific interaction between polymer and clay. Rather, the clay particles improve properties by aiding the molecular orientation of the polymer chains during deformation by physically blocking and inhibiting molecular entanglements. The authors reached this conclusion from the radically greater achieved draw ratios and associated tenacities of the nylon-6-clay nanocomposite fibers relative to the unfilled samples [278]. Ibanes and coworkers [278] deduced from their SAXS data that the MMT platelets do not fit in the amorphous regions between fibrils, because the length of the platelets exceeds that of the fibril long period (the long period of a fibril is the

characteristic measure of the variation between crystalline and amorphous phases along the fibril axis, such that the length of one crystalline phase and the sequential amorphous phase equals one long period). Thus an increase in void space around the nanoparticle may occur, because the platelets do not exactly fit. Indeed, Ibanes and coworkers [279] showed that the fibril radius of gyration of the clay filled nylon-6 composites is much larger than that of the unfilled fiber fibrils, and the authors showed that the clay filled fibers have a greater propensity to cavitate under strain than the unfilled. Thus, to discern between the effects of different processing operations, Ibanes and coworkers [279] stated that in injection-molded nanocomposites, the nucleated crystallinity caused by the presence of MMT in nylon-6 aided in producing a stiff three-dimensional network that was not necessarily present in the nylon-6 nanocomposite fibers.

The conclusions of Ibanes et al. [278, 279] are not particularly confined to nylon-6 nanocomposite fibers. Similar conclusions could explain the behavior of the PET composites of McConnell [165] and Chang [159, 243, 274, 275] and their coworkers. One can progress the theory to include the effects of clay concentration. If the fibril lengths are a function of clay loading, then one may conclude that an increase in clay loading will decrease fibril length and orientation, because of the increased tortuous path a fibril would follow around more particles. Then upon applying stress the load is prescribed more evenly between polymer and clay to give a greater overall response. This same phenomenon occurs when adjusting the spinning speed. At low speeds the fibrils are short, un-oriented and ill-formed to allow a greater particle contribution to the modulus, but at higher speeds the fibrils become longer, more defined, and oriented in the fiber axis to give a greater polymer contribution to the composite's modulus. However,

the key to reinforcement still lies in creating and maintaining a strong interaction between the polymer and clay, even when the polymer chains are oriented. For example, if the polymer is chemically bonded to the filler particle, the interaction between polymer and clay will persist despite the very highest spinning speeds.

2.3.2.6 *Conclusions on Modulus and Tenacity Improvement*

In sum, the exact nature of the PET-nanoparticle interface and the inter-molecular structure are uncertain, the five factors discussed above influence the mechanical properties of the composite. Of immediate conclusion, the use of maleic anhydride and pentaerythritol 'compatibilizing' agents should be avoided. Melt blending by either twin screw extrusion or by a double pass in a single-screw extruder yield better initial particle dispersion. In addition the filler concentration should not exceed 5 wt%, but loading level depends heavily on surface treatment and filler type. Thus far, non-polar surfactants on the nanoparticle surface produce the greatest improvements in modulus and tenacity, which is presumably because the non-polar surfactant repel interstitial water molecules and contributes to better matrix molecular weight retention. The nature of the filler particle, montmorillonites vs. talcites vs. fluoro-micas, influences modulus and tenacity properties as well. The literature shows that montmorillonites produce the better property improvements better mass. Of course, the reasons why are quite complex. Nevertheless, the presence of nanoparticles leads to the achievement of greater draw ratios. The particles physically block entanglements, therefore, allowing for greater quantities of non-crystalline orientation. However, nanoparticles in this role reduce the

number of tie chains between crystallites to limit the improvement in strength. Yet, nanoparticles have been cited as influencing molecular weight and the increase in drawability could occur as a result of an increased polydispersity of matrix polymer chains. Finally, the initial draw down ratio and spinning speed heavily affect the as-spun properties of PET-nanocomposites. The authors of nylon-6 nanocomposite fiber studies concluded that the decrease in as-spun modulus with increasing spinning speed was a result of the inability of the nanoparticle to efficiently fit into the growing microfibril microstructure. In terms of structure property relationships in PET nanocomposite fibers, much is still unknown. The barrier to expanding knowledge rests on overcoming the difficulty in probing the particle-matrix interface.

2.4 REFERENCES

1. van Olphen, H., *Clay Colloid Chemistry*. 1977, New York: Wiley & Sons.
2. Ray, S.S. and M. Okamoto, *Polymer/layered silicate nanocomposites: areview from preparation to processing.* Prog. Polym. Sci., 2003. **28**: p. 1539-1641.
3. Solomon, M.J. and Q. Lu, *Rheology and dynamics of particles in viscoelastic media.* Curr. Opin. Colloid & Inter. Sci., 2001. **6**: p. 430-437.
4. Larson, R.G., *The Structure and Rheology of Complex Fluids*. 1999, New York: Oxford University Press.
5. Luckham, P.F. and S. Rossi, *The colloidal and rheological properties of bentonite suspensions.* Adv. Colloid & Interface Sci., 1999. **82**: p. 43-92.
6. Shenoy, A.V., *Rheology of Filled Polymer Systems*. 1999, London: Kluwer Academic.
7. Barnes, H.A., *Review of the rheology of filled viscoelastic systems.* Rheology Reviews, The British Society of Rheology, 2003.
8. Metzner, A.B., *Rheology of suspensions in polymeric liquids.* J. Rheology, 1985. **29**: p. 739-775.
9. Krishnamoorti, R., R.A. Vaia, and E.P. Giannelis, *Structure and dynamics of polymer-layered silicate nanocomposite.* Chem. Mater., 1996. **8**: p. 1728-1734.
10. Krishnamoorti, R. and K. Yurekli, *Rheology of polymer layered silicate nanocomposites.* Curr. Opin. Colloid & Inter. Sci., 2001. **6**: p. 464-470.
11. Ray, S.S., K. Okamoto, and M. Okamoto, *Structure-property relationship in biodegradable poly(butylene succinate)/layered silicate nanocomposites.* Macromolecules, 2003. **36**: p. 2355-2367.
12. Lim, Y. and O.O. Park, *Phase morphology and rheological behavior of polymer/layered silicate nanocomposites.* Rheol. Acta, 2001. **40**: p. 220-229.
13. Kaneto, K., et al., *Electrical conductivities of multi-wall carbon nanotubes.* Synthetic Met., 1999. **103**: p. 2543-2546.
14. Krishnan, A., et al., *Young's modulus of single-walled nanotubes.* Phys. Rev. B, 1998. **58**: p. 14013-14019.
15. Hilding, J., et al., *Dispersion of carbon nanotubes in liquids.* J. Dispersion Sci. & Tech., 2003. **24**: p. 1-41.
16. Pan, Z.W., et al., *Very long carbon nanotubes.* Nature (London), 1998. **394**(6694): p. 631-632.
17. Iijima, S., *Helical microtubes of graphitic carbon.* Nature (London), 1991. **354**(6348): p. 56-58.
18. Li, Y.L., Y.D. Yu, and Y.A. Liang, *A novel method for synthesis of carbon nanotubes: Low temp. solid pyrolysis.* J. Mater. Res., 1997. **12**: p. 1678-1680.
19. Lee, B.O., et al., *EMI shielding properties of carbon nanofiber filled poly(vinylodene fluoride) coating materials.* J. Ind. & Eng. Chem. (Korea), 2001. **7**(5): p. 305-309.
20. Xu, J., et al., *Rheology of polystyrene/carbon nanofiber composites.* Ann. Tech. Conf. Society of Plastic Engineers, Technical Papers, 2005: p. 1950.
21. Blumstein, A., *Polymerization of adsorbed monolayers: II. Thermal degradation of the inserted polymers.* J. Polym. Sci., A, 1965. **3**: p. 2665-2673.
22. Theng, B.K.G., *Formation and properties of clay-polymer complexes*. 1979, Amsterdam: Elsevier.
23. Islam, M.F., et al., *High weight fraction surfactant solubilization of single-wall carbon nanotubes in water.* Nano Letters, 2003. **3**: p. 269-273.
24. Lozana, K., A. Gaspar-Rosas, and E.V. Barrera, *Rheological examination of C60 in low density solutions.* Carbon, 2002. **40**: p. 271-276.
25. Hirsch, A., U. Sagman, and S.R. Wilson, *Patent Appl. Pub. US serial 367646: Use of buckysome or carbon nanotubes for drug delivery*. 2004.
26. Venkatesan, N., et al., *Liquid filled nanoparticles as a drug delivery tool for protein therapeutics.* Biomaterials, 2005. **26**: p. 7154-7163.
27. Hu, J.J. and J.S. Zabinski, *Nanotribology and lubrication mechanisms of inorganic fullerene-like MoS2 nanoparticles investigated using lateral force microscopy (LFM).* Tribology Letters, 2005. **18**: p. 173-180.
28. Ginzburg, B.M., et al., *Thermal and tribological properties of fullerene-containing composite systems: Part 1. Thermal stability of fullerene-polymer systems.* J. Macromolecular Science, Physics, B, 2004. **43**: p. 1193-1230.

29. Rapoport, L., et al., *Polymer nanocomposites with fullerene-like solid lubricant.* Advanced Engineering Materials, 2004. **6**: p. 44-48.
30. Harth, E., et al., *A facile approach to architecturally defined nanoparticles via intramolecular chain collapse.* J. Amer. Chem. Soc., 2002. **124**: p. 8653-8660.
31. Tenne, R., *Inorganic nanotubes and fullerene-like materials.* Chem. Eur. J., 2002. **8**: p. 5296-5304.
32. Einstein, A., *On the theory of brownian movement.* Ann. Phys. (Leipz.), 1906. **19**: p. 371-381.
33. Batchelor, G.K., *The stress generated in a non-dilute suspension of elongated particles by pure straining motion.* J. Fluid Mech., 1971. **46**: p. 813-829.
34. Baker, F., *The viscosity of cellulose nitrate solutions.* J. Chem. Soc. Trans., 1913. **103**: p. 1653-1675.
35. Krieger, I.M. and T.J. Dougherty, *A mechanism for non-Newtonian flow in suspensions of rigid spheres.* Trans. Soc. Rheol., 1959. **3**: p. 137-152.
36. Tsai, S.C., D. Botts, and J. Plouff, *Effects of particle properties on the rheology of concentrated non-colloidal suspensions.* J. Rheology, 1992. **36**: p. 1291-1305.
37. Quemada, D., *Rheology of concentrated disperse systems and minimum energy dissipation principle: I. Viscosity-concentration relationship.* Rheol. Acta, 1977. **16**: p. 82-94.
38. Barnes, H.A., J.F. Hutton, and K. Walters, *An Introduction to Rheology*. 1989, Amsterdam: Elsevier.
39. Xu, J., et al., *Shear and extensional rheology of carbon nanofiber suspensions.* Rheol. Acta, 2005. **44**: p. 537-562.
40. Kislenko, V.N. and R.M. Verlinskaya, *Rheological behavior of kaolin and montmorillonite suspensions at low concentrations.* J. Colloid Interface Sci., 2001: p. 405-409.
41. Norrish, K., *The swelling of montmorillonite.* Discuss. Faraday Soc., 1954. **19**: p. 120-134.
42. Swartzen-Allen, S.L. and E. Matijevic, *Surface and colloid chemistry of clays.* Chem. Rev., 1974. **74**: p. 385-400.
43. Hunter, R.J., *Foundations of Colloid Science, vol. 1*. 1986, New York: Oxford Univ. Press.
44. Keren, R., I. Shainberg, and E. Klein, *Settling and flocculation value of sodium-montmorillonite particles in aqueous media.* Soil Sci. Soc. Am. J., 1988. **56**: p. 76.
45. Zhong, Y. and S.Q. Wang, *Exfoliation and yield behavior in nanodispersions of organically modified montmorillonite clay.* J. Rheology, 2003. **47**: p. 483-495.
46. Heller, H. and R. Keren, *Rheology of Na-rich montmorillonite suspension as affected by electrolyte concentration and shear rate.* Clay & Clay Minerals, 2001. **49**: p. 286-291.
47. Bekkour, K., et al., *Time-dependent rheological behavior of bentonite suspensions: An experimental study.* J. Rheology, 2005. **49**: p. 1329-1345.
48. Miano, F. and M.R. Rabaioli, *Rheological scaling of montmorillonite suspensions: the effect of electrolytes and polyelectrolytes.* Colloids Surf. A., 1994. **84**: p. 229.
49. Rand, B., et al., *Investigation into the existence of edge—face coagulated structures in Na-montmorillonite suspensions.* J. Chem. Soc. Faraday Trans, 1980. **76**: p. 225.
50. Pignon, F., A. Magnin, and J.-M. Piau, *Thixotropic behavior of clay dispersions: Combinations of scattering and rheometric techniques.* J. Rheology, 1998. **42**: p. 1349-1373.
51. De Groot, J., et al., *Flow induced anisotropic SALS in silica filled PDMS liquids.* J. Colloid Interface Sci., 1994. **166**: p. 404-413.
52. Potanin, A.A., *On the mechanism of aggregation in the shear flow of suspensions.* J. Colloid Interface Sci., 1991. **145**: p. 140-157.
53. Potanin, A.A., *On the computer simulation of the deformation and break-up of colloidal aggregates in shear flow.* J. Colloid Interface Sci., 1993. **153**: p. 399-410.
54. Schott, H., *Deflocculation of swelling clays by nonionic and anionic detergents.* J. Colloid Interface Sci., 1968. **26**: p. 133-139.
55. Zamam, A.A. and N. Delorme, *Effect of polymer bridging on rheological properties of dispersions of charged silica particles in the presence of low-molecular-weight physically adsorbed pol(ethylene oxide).* Rheologica Acta, 2002. **41**: p. 408-417.
56. Heath, D. and T.F. Tadros, *Influence of pH, electrolyte, and poly(vinyl alcohol) addition on the rheological characteristics of aqueous dispersions of sodium montmorillonite.* J. Colloid & Inter. Sci., 1983. **93**: p. 307-319.

57. Brown, J.M., D. Curliss, and R.A. Vaia, *Thermoset-layered silicate nanocomposites: Quaternary ammonium montmorillonite with primary diamine cured epoxies.* Chem. Mater., 2000. **12**: p. 3376-3384.
58. Dean, D., et al., *Chemorheology and properties of epoxy/layered silicate nanocomposites.* Polymer, 2005. **46**: p. 3014-3021.
59. Le Pluart, L., et al., *Rheological properties of organoclay suspensions in epoxy network precursors.* Applied Clay Science, 2004. **25**: p. 207-219.
60. Moraru, V.N., *Structure formation of alkylammonium montmorillonites in organic media.* Applied Clay Science, 2001. **19**: p. 11-26.
61. Hough, L.A., et al., *Viscoelasticity of single wall carbon nanotube suspensions.* Physical Rev. Lett., 2004. **93**: p. 168102-1-4.
62. Advani, S.G. and F. Zhihang, *Effect of dispersion state on the rheology of multi-walled carbon nanotube suspensions in shear flow.* AIP Conference Proceedings, 2004. **712**: p. 1619-1623.
63. Gardel, M.L., et al., *Elastic behavior of cross-linked and bundled actin networks.* Science, 2004. **304**: p. 1301-1305.
64. Doi, M. and S.F. Edwards, *The Theory of Polymer Dynamics*. 1992, Oxford: Clarendon.
65. Girifalco, L.A., M. Hodak, and R.S. Lee, *Carbon nanotubes, buckyballs, ropes, and a universal graphitic potential,.* Phys. Rev. B: Cond. Matter & Mater. Phys., 2000. **62**: p. 13104-13110.
66. Davis, V.A., et al., *Phase Behavior and Rheology of SWNTs in Superacids.* Macromolecules, 2004. **37**: p. 154-160.
67. Marrucci, G. and P.L. Maffetone, *Description of the liquid-crystalline phase of rodlike polymers at high shear rates.* Macromolecules, 1989. **22**: p. 4076-4082.
68. Larson, R.G., *Arrested tumbling in shearing flows of liquid-crystal polymers.* Macromolecules, 1990. **23**: p. 3983-3992.
69. Larson, R.G. and M. Doi, *Mesoscopic domain theory for textured liquid crystalline polymers.* J. Rheology, 1991. **35**: p. 539-563.
70. Marrucci, G., *Liquid crystallinity in polymers*. 1991, New York: VCH Publishers.
71. Sierou, A. and J.F. Brady, *Rheology and microstructure in concentrated noncolloidal suspensions.* J. Rheology, 2002. **46**: p. 1031-1056.
72. Brenner, H., *Rheology of a dilute suspension of brownian particles.* Int. J. Multiphase Flow, 1974. **1**: p. 195-341.
73. Krishnamoorti, R. and E.P. Giannelis, *Rheology of end-tethered polymer layered silicate nanocomposites.* Macromolecules, 1997. **30**: p. 4097-4102.
74. Krishnamoorti, R. and E.P. Giannelis, *Strain hardening in model polymer brushes under shear.* Lagmuir, 2001. **17**: p. 1448-1452.
75. Cho, J.W. and D.R. Paul, *Nylon 6 nanocomposites by melt compounding.* Polymer, 2001. **42**: p. 1083-1094.
76. Fornes, T.D., et al., *Nylon 6 nanocomposites: The effect of matrix molecular weight,.* Polymer, 2001. **42**: p. 9929-9940.
77. Incarnato, L., et al., *Rheological behavior of new melt compounded copolyamide nanocomposites.* Polymer, 2004. **45**: p. 3487-3496.
78. Aubry, T., T. Razafinimaro, and P. Mederic, *Rheological investigation of the melt state elastic and yield properties of a poly-amide-12 layered silicate nanocomposite.* J. Rheology, 2005. **49**: p. 425-440.
79. Tung, J., et al., *Rheological and mechanical comparative study of in situ polymerized and melt blended nylon 6 nanocomposites.* Polymer, 2005. **46**: p. 10405-10418.
80. Lee, K.M. and C.D. Han, *Effect of hydrogen bonding on the rheology of polycarbonate/organoclay nanocomposites.* Polymer, 2003. **44**: p. 4573-4588.
81. Yoon, P.J., D.L. Hunter, and D.R. Paul, *Polycarbonate nanocomposites. Part 2: Degradation and color formation.* Polymer, 2003. **44**: p. 5341-5354
82. Hsieh, A.J., et al., *Mechanical response and rheological properties of polycarbonate layered silicate nanocomposites.* Polym. Eng. & Sci., 2004. **44**: p. 825-837.
83. Wagener, R. and T.J.G. Reisinger, *A rheological method to compare the degree of exfoliation of nanocomposites.* Polymer, 2003. **44**: p. 7513-7518.

84. Sanchez-Solis, A., et al., *Mechanical and Rheological Studies on Polyethylene Terephthalate-Montmorillonite Nanocomposites.* Polym. Eng. & Sci., 2004. **44**: p. 1094-1102.
85. Wu, D., et al., *Effect of flocculated structure on rheology of poly(butylenes terephthalate)/clay nanocomposites.* J. Polym. Sci, Part B: Polym. Phys., 2005. **43**: p. 2807-2818.
86. Scarfato, P., et al., *Effect of the Organoclay structure on morphology and rheological response of PBT nanocomposites.* Macromol. Symp., 2005. **228**: p. 125-137.
87. Galgali, G., C. Ramesh, and A. Lele, *A rheological study on the kinetics of hybrid formation in polypropylene nanocomposites.* Macromolecules, 2001. **34**: p. 852-858.
88. Okamoto, M., et al., *A house of cards structure in polypropylene/clay nanocomposites under elongational flow.* Nano Letters, 2001. **1**: p. 295-298.
89. Solomon, M.J., et al., *Rheology of polypropylene/clay hybrid materials.* Macromolecules, 2001. **34**: p. 1864-1872.
90. Li, J., et al., *Study on rheological behavior of polypropylene/clay nanocomposites.* J. Appl. Polym. Sci., 2003. **89**: p. 3609-3617.
91. Pavlikova, S., et al., *Fiber spinning from poly(propylene)-organoclay nanocomposite.* J. Appl. Polym. Sci., 2003. **89**: p. 604-611.
92. Koo, C.M., et al., *Mechanical and rheological properties of maleated polyproylene-layered silicate nanocomposites with different morphology.* J. Appl. Polym. Sci., 2003. **88**: p. 1526-1535.
93. Gu, S.Y., J. Ren, and Q.F. Wang, *Rheology of poly(propylene)/clay nanocomposites.* J. Appl. Polym. Sci., 2004. **91**: p. 2427-2434.
94. Koo, C.M., et al., *Melt-extensional properties and orientation behaviors of polypropylene-layered silicate nanocomposites.* J. Polym Sci. Part B: Polym. Phys., 2005. **43**: p. 158-167.
95. Lertwimolnun, W. and B. Vergens, *Influence of compatibilizer and processing conditions on the dispersion of nanoclay in a polypropylene matrix.* Polymer, 2005. **46**: p. 3462-3471.
96. Lee, J.A., et al., *Time and shear dependent rheology of maleated polyethylene and its nanocomposites.* Polymer, 2005. **45**: p. 6595-6600.
97. Hatzikiriakos, S.G., N. Rathod, and E.B. Muliawan, *The effect of nanoclays on the processibility of polyolefins.* Polym. Eng. Sci., 2005. **45**: p. 1098.
98. Sternstein, S.S. and A.J. Zhu, *Reinforcement mechanism of nanofilled polymer melts as elucidated by nonlinear viscoelastic behavior.* Macromolecules, 2002. **35**: p. 7262-7273.
99. Gelfer, M., et al., *Manipulating the microstructure and rheology in polymer-organoclay composites.* Polym. Eng. Sci., 2002. **42**: p. 1841-1851.
100. Pasanovi-Zujo, V., R.K. Gupta, and S.N. Bhattacharya, *A constitutive analysis of extensional flow of EVA nanocomposites.* Intern. Polym. Processing XIX, 2004. **4**: p. 388-394.
101. Gupta, R.K., V. Pasanovi-Zujo, and S.N. Bhattacharya, *Shear and extensional rheology of EVA/layered silicate nanocomposites.* J. Non-Newt. Fluid Mech., 2005. **128**: p. 116-125.
102. Gelfer, M.Y., et al., *Relationships between structure and rheology in model nanocomposites of ethylene-vinyl-based copolymers and organoclays.* Macromolecules, 2005. **38**: p. 3765-3775.
103. Kotsilkova, R., *Rheology-structure relationship of polymer/layered silicate hybrids.* Mech. Time-Dependent Mater., 2002. **6**: p. 283-300.
104. Wang, M., A.J. Hsieh, and G.C. Rutledge, *Electrospinning of poly(MMA-co-MAA) copolymers and their layered silicate nanocomposites for improved thermal properties.* Polymer, 2005. **46**: p. 3407-3418.
105. Hoffman, B., et al., *Morphology and rheology of polystyrene nanocomposites based upon organoclay.* Macomol. Rapid Commun., 2000. **21**: p. 57-61.
106. Lim, Y.T. and O.O. Park, *Rheological evidence for the microstructure of intercalated polymer/layered silicate nanocomposites.* Macomol. Rapid Commun., 2000. **21**: p. 231-235.
107. Zhong, Y., Z. Zhu, and S.Q. Wang, *Synthesis and rheological properties of polystyrene/layered silicate nanocomposite.* Polymer, 2005. **46**: p. 3006-3013.
108. Ren, J., A.S. Silva, and R. Krishnamoorti, *Linear viscoelasticity of disorder polystyrene-polyisoprene block copolymer based layered-silicate nanocomposites.* Macromolecules, 2000. **33**: p. 3739-3746.
109. Krishnamoorti, R., J. Ren, and A.S. Silva, *Shear response of layered silicate nanocomposites.* J. Chem. Phys., 2001. **114**: p. 4968-4973.
110. Mitchell, C.A. and R. Krishnamoorti, *Rheological properties of diblock copolymer/layered-silicate nanocomposites.* J. Polym Sci. Part B: Polym. Phys., 2002. **40**: p. 1343-1443.

111. Ren, J. and R. Krishnamoorti, *Nonlinear viscoelastic properties of layered-silicate-based intercalated nanocomposites.* Macromolecules, 2003. **36**: p. 4443-4451.
112. Lee, M.W., et al., *PP/LCP composites: effects of shear flwo, extensional flow, and nanofillers.* Compos. Sci. & Tech., 2003. **63**: p. 1921-1929.
113. Haung, W. and C.D. Han, *Dispersion characteristics and rheology of organoclay nanocomposites based on a segmented main-chain liquid crystalline polymer having pendent pyridyl group.* Macromolecules, 2006: p. 257-267.
114. Jeon, H.S., J.K. Rameshwaram, and G. Kim, *Structure-property relationships in exfoliated polyisoprene/clay nanocomposites.* J. Polym. Sci. Part B: Polym. Phys., 2004. **42**: p. 1000-1009.
115. Sadhu, S. and A.K. Bhowmick, *Unique rheological behavior of rubber based nanocomposites.* J. Polym. Sci. Part B: Polym. Phys., 2005. **43**: p. 1854-1864.
116. Lee, K.M. and C.D. Han, *Linear dynamic viscoelastic properties of functionalized block copolymer/organoclay nanocomposites.* Macromolecules, 2003. **36**: p. 804-815.
117. Chow, W.S., Z.A. Hohd Ishak, and J. Karger-Koscis, *Morphological and rheological properties of polyamide 6/poly(propylene)/organoclay nanocomposites.* Macromol. Mater. & Eng., 2005. **290**: p. 122-127.
118. Di, Y., et al., *Poly(lactic acid)/organoclay nanocomposites: Thermal rheological properties and foam processing,.* J. Polym. Sci.: Part B Polym. Phys., 2005. **43**: p. 689-698.
119. Hyun, Y.H., et al., *Rheology of poly(ethylene oxide)/organoclay nanocomposites.* Macromolecules, 2001. **34**: p. 8084-8093.
120. Lim, Y.T., J.H. Park, and O.O. Park, *Improved electrorheological effect in polyaniline nanocomposite suspensions.* J. Colloid & Interface Sci., 2002. **245**: p. 198-203.
121. Choi, H.J., et al., *Synthesis and electrorheology of emulsion intercalated PANI-clay nanocomposite.* Synthetic Met., 2001. **121**: p. 1325-1326.
122. Bonn, D., et al., *Laponite: What is the Difference between a Gel and a Glass?* Lagmuir, 1999. **15**: p. 7534-7536.
123. Ho, R.M., et al., *Functionalization of polypropylene via melt mixing.* Polymer, 1993. **34**: p. 3264-3269.
124. Payne, A.R.J., *The dynamic properties of carbon black-loaded natural rubber vulcanizates, Part I.* J. Appl. Polym. Sci., 1962. **6**: p. 57-63.
125. Becker, L.E., M.J. Shelley, and P.R.L. , 87 (2001) 198301., *Instability of elastic filaments in shear flow yields first-normal stress differences.* Phys. Rev. Lett, 2001. **87**: p. 198301.
126. Cates, M.E., et al., *Jamming, force chains, and fragile matter.* Physical Rev. Lett., 1998. **81**: p. 1841-1844.
127. Barnes, H.A., *The yield stress—a review or 'παντα ρι'—everything flows?* J. Non-Newt. Fluid Mech., 1999. **81**: p. 133-178.
128. Mackay, M.E., et al., *Nanoscale effects leading to non-Einstien-like decrease in viscosity.* Nature Materials, 2003. **2**: p. 762-766.
129. Karin, T., et al., *Molecular-dynamics simulation of model polymer nanocomposite rheology and comparison with experiment.* J. Chem. Phys., 2005. **123**: p. 194905.
130. Ferry, J.D., *Viscoelastic Properties of Polymers*. 1980, New York: Wiley.
131. Tanaka, H. and W.J. L., *Experimental investigations of shear and elongational flow properties of polystyrene melts reinforced with calcium carbonate, titanium dioxide, and carbon black.* Polym. Eng Sci., 1980. **20**: p. 949.
132. Han, C.D., *Multiphase Flow in Polymer Processing*. 1981, New York: Academic.
133. Bortner, M.J., P.J. Doerpinghaus, and D.G. Baird, *Effects of sparse long chain branching on the spinning stability of LLDPEs.* Int. Polym. Processing, 2004. **19**: p. 236-243.
134. Fong, H., et al., *Generation of electrospun fibers of nylon 6 and nylon 6-montmorillonite nanocomposite.* Polymer, 2002. **43**: p. 775-780.
135. Balberg, I., *Recent developments in continuum percolation.* Phil. Mag. B, 1987. **56**: p. 991-1003.
136. Du, F., et al., *Nanotube networks in polymer nanocomposites: Rheology and electrical conductivity.* MAcromolecules, 2004. **37**: p. 9048-9055.
137. Kharchenko, S.B., et al., *Flow-induced properties of nanotube-filled polymer materials.* Nature Materials, 2004. **3**: p. 564-568.
138. Abel-Goad, M. and P. Potschke, *Rheological characterization of melt processed polycarbonate-multiwalled carbon nanotube composites.* J. Non-Newt. Fluid Mech., 2005. **128**: p. 2-6.

139. Potschke, P., T.D. Fornes, and D.R. Paul, *Rheological behavior of mutiwalled carbon nanotube/polycarbonate composites.* Polymer, 2002. **43**: p. 3247-3255.
140. Powell, R.L., *Rheology of suspensions of rod-like particles.* J. Stat. Phys. , 1991. **62**: p. 1073-1094.
141. Loazano, K., J. Bonilla-Rios, and E.V. Barrera, *A study on nanofiber-reinforced thermoplastic composites (II): Investigation of the mixing rheology and conduction properties.* J. Appl. Polym. Sci., 2001. **80**: p. 1162-1172.
142. Xu, J., et al., *Rheology of polystyrene/carbon nanofiber composites.* Ann. Tech. Conf. Society of Plastic Engineers, Technical Papers, 2005: p. 1950-1954.
143. Lee, S., M.S. Kim, and A.A. Ogale, *Rheology of carbon nanofiber-modified thermotropic liquid crystalline polymers.* Ann. Tech. Conf. Society of Plastic Engineers, Technical Papers, 2005: p. 1955-1957.
144. Doi, M. and S.F. Edwards, *The Theory of Polymer Dynamics*. 1986, New York: Oxford University Press.
145. Papanastasiou, A.C., L.E. Scriven, and C.W. Macoscko, *An integral constitutive equation for mixed flows: Viscoelastic characterization.* J. Rheology, 1983. **27**: p. 387-410.
146. Manias, E., et al., *On the nature of shear thinning in nanoscopically confined films.* Europhys. Lett., 1996. **33**: p. 371-376.
147. Leonov, A.I., *On the rheology of filled polymers.* J. Rheology, 1990. **34**: p. 1039-1068.
148. Leonov, A.I., *On equilibrium thermodynamics and rheology of viscoelastic polymer media.* Rheol. Acta, 1976. **29**: p. 85-96.
149. Leonov, A.I. and M. Simhambhatla, *On the rheological modeling of filled polymers with particle-matrix interactions.* Rheol. Acta, 1995. **34**: p. 329-338.
150. Doremus, P. and J.-M. Piau, *Yield stress fluid: Structural model and transient shear flow behavior.* J. Non-Newt. Fluid Mech., 1991. **39**: p. 335-352.
151. Jamamoto, M., *The viscolelastic properties of network structure. I. General formalism.* J. Phys. Soc. Jap., 1956. **11**: p. 413-421.
152. Inn, Y.W. and S.Q. Wang, *Transient network model for a multiphase polymeric fluid.* Rheol. Acta, 1993. **32**: p. 581-588.
153. Havet, G. and A.I. Isayev, *A thermodynamic approach to the rheology of highly interactive filler-polymer mixtures: Part I – Theory.* Rheol. Acta, 2001. **40**: p. 570-581.
154. Giesekus, H., *A simple constitutive equation for polymer fluids based on the concept of deformation dependent tensorial mobility.* J. Non-Newt. Fluid Mech., 1982. **11**: p. 69-109.
155. Sarvestani, A.S. and C.R. Picu, *Network model for the viscoelastic behavior of polymer nanocomposites.* Polymer, 2004. **45**: p. 7779-7790.
156. Chernyak, Y.B. and A.I. Leonov, *On the theory of the adhesive friction of elastomers.* Wear, 1986. **108**: p. 105-138.
157. Fourne, F., *Synthetische Fasern*. 1999, Munich: Hanser Publishers
158. Heinemann, J., et al., *Polyolefin nanocomposites formed by melt compounding and transition metal catalyzed homo- and copolymerization in the presence of layered silicates.* Macromol. Rapid Commun., 1999. **20**: p. 423-430.
159. Chang, J.H., M.K. Mun, and I.C. Lee, *Poly(ethylene terephthalate) Nanocomposite Fibers by In Situ Polymerization: The Thermomechanical Properties and Morphology.* J. Appl. Polym. Sci., 2005. **98**: p. 2009-2016.
160. Imai, Y., et al., *High Modulus Poly(ethylene terephthalate)/Expandable Mica Nanocomposites with a Novel Recative Compatibilizer.* Chem. Mater., 2002. **14**: p. 477-479.
161. Saujanya, C., Y. Imai, and H. Tateyama, *Structure and thermal properties of compatibilized PET/expandable fluorine mica nanocomposites.* Polymer Bulletin, 2002. **49**: p. 69-76.
162. Guan, G.-H., C.-C. Li, and D. Zhang, *Spinning and Properties of Poly(ethylene terephthalate)/Organomontmorillonite Nanocomposite Fibers.* J. Appl. Polym. Sci., 2005. **95**: p. 1443-1447.
163. Matayabas, J.C., et al., *Patent US6084019: High inherent viscosity polyester compositions containing platelet particles*. 2000: United States of America.
164. Davis, C.H., et al., *Effects of Melt-Processing Conditions on the Quality of Poly(ethylene terephthalate) Montmorillonite Clay Nanocomposites.* J. Polym. Sci.: Part B. Polym. Phys., 2002. **40**: p. 2661-2666.

165. McConnell, D.C., et al., *Structure Property Relationships in PET Nanocomposite Fibres.* Ann. Tech. Conf. Society of Plastic Engineers, Technical Papers, 2006: p. 387-392.
166. Pendse, S., N. D'Souza, and J.A. Ratto, *Deformation of PET Nanocomposites.* Ann. Tech. Conf. Society of Plastic Engineers, Technical Papers, 2005: p. 3492-3496.
167. Pegoretti, A., et al., *Recycled poly(ethylene terephthalate)/layered silicate nanocomposites: morphology and tensile mechanical properties.* Polymer, 2004. **45**: p. 2751-2759.
168. Pendse, S., et al., *Effect of Montmorillonite Layered Silicate (MLS) on Crystallization growth Rate in Semi-Crystalline PET Nanocomposites.* Ann. Tech. Conf. Society of Plastic Engineers, Technical Papers, 2004: p. 2343-2347.
169. Lee, W.D., et al., *Preparation and properties of layered double hydroxide/poly(ethylene terephthalate) nanocomposites by direct melt compounding.* Polymer, 2006. **47**: p. 1364-1371.
170. Wang, M., M. Zhu, and B. Sun, *A New Nano-Strcutured Flame-Retardant Poly(ethylene terephthalate).* J. Macromole. Sci. PArt A: Pure & Appl. Chem., 2006. **43**: p. 1986-1875.
171. Sanchez-Solis, A., A. Garcia-Rejon, and O. Manero, *Production of Nanocomposites of PET-Montmorillonite Clay by an Extrusion Process.* Macromol. Symp., 2003. **192**: p. 281-292.
172. Barber, G.B., B.H. Calhoun, and R.B. Moore, *Poly(ethylene terephthalate) ionomer based clay nanocomposites produced via melt extrusion.* Polymer, 2005. **46**: p. 6706-6714.
173. Eckert, C.A., B.L. Knutson, and P.G. Debenedetti, *Supercritical fluids as solvents for chemical and materials processing.* Nature (London), 1996. **383**: p. 313-318.
174. Tomasko, D.L., et al., *A review of CO2 Applications in the Processing of Polymers.* Ind. Eng. Chem. Res, 2003. **42**: p. 6431-6456.
175. Chiou, J.S., J.W. Barlow, and D.R. Paul, *Plasticization of glassy polymers by CO2.* J. Appl. Polym. Sci., 1985. **30**: p. 2633.
176. Garg, A., E. Gulari, and C.W. Manke, *Thermodynamics of Polymer Melts Swollen with Supercritical Gases.* Macromolecules, 1994. **27**: p. 5643-5653.
177. Lee, M.H., C. Tzoganakis, and C.B. Par, Adv. in Polym. Tech., 2000. **19**: p. 300.
178. Berens, A.R. and G.S. Huvard, *Interaction of Polymers with Near-Critical Carbon Dioxide*. Super Critical Fluid Science and Technology, ed. K.P. Johnston and J.M. Penninger. 1989, Washington DC: American Chemical Society. 208.
179. Lesser, A.J. and G.L. Manuel, *Polymer Clay Nanocomposites Prepared in Supercritical Carbon Dioxide.* Ann. Tech. Conf. Society of Plastic Engineers, Technical Papers, 2004: p. 1528-1532.
180. Zerda, A.S., T.C. Caskey, and A.J. Lesser, *Highly Concentrated, Intercalated Silicate Nanocomposites: Synthesis and Characterization.* Macromolecules, 2003. **36**: p. 1603-1608.
181. Wingert, M.J., et al., *Rheological Changes in CO2 Impregnated Polystyrene Reinforced with Nanoclays.* Ann. Tech. Conf. Society of Plastic Engineers, Technical Papers, 2003: p. 986-990.
182. Ravindranath, K. and R.A. Mashelkar, *Modeling of poly(ethylene terephthalate) reactors. IX. Solid state polycondensation process.* J. Appl. Polym. Sci., 1990. **39**: p. 1325-1345.
183. Gantillon, B., R. Spitz, and T.F. McKenna, *The Solid State Postcondensation of PET, 1: A Review of the Physical and Chemical Processes Taking Place in the Solid State.* Macromole. Mater. & Eng., 2004. **289**: p. 88-105.
184. Kim, T.Y., E.A. Lofgren, and S.A. Jabarin, *Solid-State Polymerization of Poly(ethylene terephthalate). I. Experimental Study of the Reaction Kinetics and Properties.* J. Appl. Polym. Sci., 2003. **89**: p. 197-212.
185. Ma, Y., et al., *Solid-state polymerization of PET: influence of nitrogen sweep and high vacuum.* Polymer, 2003. **44**: p. 4085-4096.
186. MacDonald, W.A., *New advances in poly(ethylene terephthalate) polymerization and degradation.* Polymer Intern., 2002. **51**: p. 923-930.
187. Gantillon, B., R. Spitz, and T.F. McKenna, *The Solid State Postcondensation of PET, 4: Solid State Polycondensation in Gas and Slurry Directly From Prepolymers.* Macromole. Mater. & Eng., 2004. **289**: p. 119-130.
188. Litchfield, *unpublished data*. 2006.
189. Yu, H., K. Han, and M. Yu, *The Rate Acceleration in Solid-State Polycondensation of PET by Nanomaterials.* J. Appl. Polym. Sci., 2004. **94**: p. 971-976.
190. Bikiaris, D., V. Karavelidis, and G. Karayannidis, *A New Approach to Prepare Poly(theylene terephthalate)/Silica Nanocomposites with Increased Molecular Weight and Fully Adjustable Branching or Crosslinking by SSP.* Macromole. Rapid Comm., 2006. **27**: p. 1199-1205.

191. Salem, D.R., *Draw-Induced Structure Development in Flexible-Chain Polymers: in "Structure Formation in Polymeric Fibers"*, ed. D.R. Salem. 2001, Munich: Hanser.
192. Okubo, K., et al., *Patent JP19970047254 19970214: Biaxially drawn resin films and their manufacture.* 1997: Japan.
193. Clauss, B. and D.R. Salem, *A Chain-Intrinsic Fluorescence Study of Orientation-Strain Behavior in Uniaxially Drawn Poly(ethylene terephthalate) Film* Macromolecules, 1995. **28**: p. 8328-8333.
194. Clauss, B. and D.R. Salem, *Characterization of the non-crystalline phase of oriented poly(ethylene terephthalate) by chain-intrinsic fluorescence.* Polymer, 1992. **33**: p. 3193-3202.
195. Hearle, J.W.S., *Fiber Formation and the Science of Complexity: in "Structure Formation in Polymeric Fibers"*, ed. D.R. Salem. 2001, Munich: Hanser.
196. Pearce, R., et al., *Studies of post drawing relaxation phenomena in poly(ethylene terephthalate) by infrared spectroscopy.* Polym. Eng Sci., 1997. **37**: p. 1795-1800.
197. Rim, P., *Private Communications*. 2006.
198. Sussman, M.V., *US Patent Numbers 3,978,192 (1976); 4,891,872 (1990); 4,980,957 (1991).*
199. Desai, P. and A.S. Abhiraman, *Fundamental aspects of stress, deformation, and phase transitions in crystallizable polymers: Experiments with poly(ethylene terephthalate) in uniaxial stress fields.* J. Polym Sci. Part B: Polym. Phys., 1988. **26**: p. 1657-1675.
200. Le Bourvellec, G., J. Beautemps, and J.P. Jarry, *Fundamental aspects of stress, deformation, and phase transitions in crystallizable polymers: Experiments with poly(ethylene terephthalate) in uniaxial stress fields.* J. Polym. Sci. Part B: Polym. Phys., 1988. **26**: p. 1657-1675.
201. Kunugi, T., A. Suzuki, and M. Hashimoto, *Preparation of High-Modulus and High-Strength Poly(ethylene terephthalate) fiber by Zone Annealing.* J. Appl. Polym. Sci., 1981. **26**: p. 213-221.
202. Kunugi, T., C. Ichinose, and A. Suzuki, *Preparation of High-Modulus and High-Strength Poly(ethylene terephthalate) Film by Zone Annealing Method.* J. Appl. Polym. Sci., 1986. **31**: p. 429-439.
203. Kunugi, T., et al., *Preparation of ultra-high-strength nylon-6 fibre by a multi-step zone annealing method.* Polymer, 1982. **23**: p. 1983-1987.
204. Griswold, P.D., A.E. Zachariades, and R.S. Porter, *Solid State Co-Extrusion: A New Techniques for Ultradrawing Thermoplastics Illustrated with High Density Polyethylene.* Polym. Eng Sci., 1978. **18**: p. 861-863.
205. Zachariades, A.E., W.T. Mead, and R.S. Porter, *Recent developments in ultraorientation of polyethylene by solid-state extrusion.* Chem. Rev., 1980. **80**: p. 351.
206. Wang, L.H., S. Ottani, and R.S. Porter, *Two-stage drawing of high-molecular-weight polyethylene reactor powder.* Polymer, 1991. **32**: p. 1776-1781.
207. Sun, T., C.R. Desper, and R.S. Porter, *Orientation in poly(ethylene terephthalate) drawn by solid state co-extrusion.* J. Mater. Sci., 1986. **21**: p. 803-809.
208. Ito, M., K. Takahashi, and K. Kanamoto, *Effects of sample geometry and draw conditions on the mechanical properties of drawn poly(ethylene terephthalate).* Polymer, 1990. **31**: p. 58-63.
209. Ito, M., K. Takahashi, and K. Kanamoto, *Preparation of high-modulus and high-strength fibers from high-molecular-weight poly(ethylene terephthalate).* J. Appl. Polym. Sci., 1990. **40**: p. 1257-1263.
210. Hobbs, T. and A.J. Lesser, *In Situ Drawing of High Molecular Weight Poly(ethylene terephthalate) in Subcritical and Supercritical CO2.* J. Polym Sci. Part B: Polym. Phys., 1999. **37**: p. 1881-1891.
211. Hobbs, T. and A.J. Lesser, *Preparation of high performance poly(ethylene terephthalate) fibers: two-stage drawing using high pressure CO2.* Polymer, 2000. **41**: p. 6223-6230.
212. Hobbs, T. and A.J. Lesser, *Drawing in High Pressure CO2 - A New Route to High Performance FIbers.* Polym. Eng Sci., 2001. **41**: p. 135-144.
213. Flory, P.J., *Thermodynamics of Crystallization in High Polymers. I. Crystallization Induced by Stretching* J. Chem. Phys., 1947. **15**: p. 397-408.
214. Krigbaum, W.R. and R.J. Roe, J. Polym. Sci. Part A, 1964. **2**: p. 4391.
215. Gaylord, R.J., J. Polym. Sci. Polym. Phys. Ed., 1976. **14**: p. 1827.
216. Ziabicki, A., *Theoretical analysis of oriented and non isothermal crystallization* Colloid Polym. Sci., 1974. **252**: p. 207-221.
217. Ziabicki, A., *Generalized theory of nucleation kinetics. III. Nucleation in dilute systems and/or in systems with a limited number of effective single elements* J. Chem. Phys., 1977. **66**: p. 1638-1643.

218. Jarecki, L. and A. Ziabicki, *Thermodynamically controlled crystal orientation in stressed polymers: 1. Effects of strain energy of crystals embedded in an uncrosslinked amorphous matrix and hydrodynamic potential.* Polymer, 1977. **18**: p. 1015-1021.
219. Jarecki, L., *Thermodynamics of deformation of an isolated polymer chain* Colloid Polym. Sci., 1979. **257**: p. 711-719.
220. Avrami, M., *Kinetics of Phase Change. I General Theory.* J. Chem. Phys., 1939. **12**: p. 1103-1112.
221. Nakamura, K., et al., *Some aspects of nonisothermal crystallization of polymers. I. Relationship between crystallization temperature, crystallinity, and cooling conditions.* J. Appl. Polym. Sci., 1972. **16**: p. 1077-1091.
222. Patel, R.M. and J.E. Spruiell, *Crystallization kinetics during polymer processing - Analysis of available approaches for process modeling.* Polym. Eng Sci., 1991. **31**: p. 730-738.
223. Ziabicki, A., *Fundamentals of Fibre Formation*. 1976, London: Wiley.
224. Katayama, K. and M. Yoon, *in High Speed Fiber Spinning - Science and Engineering Aspects, p 207*, ed. A. Ziabicki and H. Kawai. 1985, New York: Wiley.
225. Kobayashi, K. and T. Nagasawa, J. Macromol. Sci., 1970. **4**: p. 331.
226. Salem, D.R., *Orientation and Crystallization in Poly(ethylene terephthalate) During Drawing at High Temperatures and Strain Rates.* Polym. Eng Sci., 1999. **39**: p. 2419-2430.
227. Tjong, S.C., *Structural and mechanical properties of polymer nanocomposites.* Mater. Sci. and Eng. Rev., 2006. **53**: p. 73-197.
228. Di Maio, E., et al., *Isothermal crystallization in PCL/clay nanocomposites investigated with thermal and rheometric methods* Polymer, 2004. **45**(8893-8900).
229. Fornes, T.D. and D.R. Paul, *Crystallization behavior of nylon 6 nanocomposites* Polymer, 2003. **44**: p. 3945-3961.
230. Lincoln, D.M., R.A. Vaia, and R. Krishnamoorti, *Isothermal Crystallization of Nylon-6/Montmorillonite Nanocomposites* Macromolecules, 2004. **37**: p. 4554.
231. Hambir, S., N. Bulakh, and J.P. Jog, *Polypropylene/Clay nanocomposites: Effect of compatibilizer on the thermal, crystallization and dynamic mechanical behavior.* Polym. Eng Sci., 2002. **42**: p. 1800-1807.
232. Maiti, P., et al., *The effect of crystallization on the structure and morphology of polypropylene/clay nanocomposites.* Polym. Eng Sci., 2002. **42**: p. 1864-1871.
233. Gopakumar, T.G., et al., *Influence of clay exfoliation on the physical properties of montmorillonite/polyethylene composites* Polymer, 2002. **43**: p. 5483-5491.
234. Ke, Y., C. Long, and Z. Qi, *Crystallization, Properties, and Crystal and Nanoscale Morphology of PET-Clay Nanocomposites.* J. Appl. Polym. Sci., 1999. **71**: p. 1139-1146.
235. Chisholm, B.J., et al., *Nanocomposites Derived from Sulfonated Poly(butylene terephthalate).* Macromolecules, 2002. **35**: p. 5508-5516.
236. Wu, D., et al., *Nonisothermal crystallization kinetics of poly(butylene terephthalate)/montmorillonite nanocomposites.* J. Appl. Polym. Sci., 2006. **99**: p. 3257-3265.
237. Wu, H.-D., C.-R. Tseng, and F.-C. Chang, *Chain Conformation and Crystallization Behavior of the Syndiotactic Polystyrene Nanocomposites Studied Using Fourier Transform Infrared Analysis* Macromolecules, 2001. **41**: p. 2992-2999.
238. Dillon, D.R., et al., *On the structure and morphology of polyvinylidene fluoride–nanoclay nanocomposites* Polymer, 2006. **47**: p. 1678-1688.
239. Priya, L. and J.P. Jog, *Poly(vinylidene fluoride)/clay nanocomposites prepared by melt intercalation: Crystallization and dynamic mechanical behavior studies.* J. Polym Sci. Part B: Polym. Phys., 2002. **40**: p. 1682-1689.
240. Shah, D., et al., *Dramatic Enhancements in Toughness of Polyvinylidene Fluoride Nanocomposites via Nanoclay-Directed Crystal Structure and Morphology.* Adv. Mater., 2004. **16**: p. 1173-1177.
241. Strawhecker, K.E. and E. Manias, *Crystallization Behavior of Poly(ethylene oxide) in the Presence of Na+ Montmorillonite Fillers.* Chem. Mater., 2003. **15**: p. 844-849.
242. Maiti, P. and M. Okamoto, *Crystallization controlled by silicate surfaces in nylon 6 - clay nanocomposites.* Macromol. Mater. & Eng., 2003. **288**: p. 203-208.
243. Chang, J.H., et al., *Poly(ethylene terephthalate) nanocomposites by insitu interlayer polymerization: the thermo-mechanical properties and morphology of the hybrid fibers.* Polymer, 2004. **45**: p. 919-926.

244. Xiao, W., et al., *Study on PET iber Modified by Nanomaterials: Improvement of Dimensional Thermal Stability of PEt Fiber by Forming PET/MMT Nanocomposites.* J. Appl. Polym. Sci., 2005. **96**: p. 2247-2252.
245. Phang, I.Y., et al., *Crystallization and melting behavior of polyester/clay nanocomposites.* Polymer International, 2004. **53**: p. 1282-1289.
246. Lyons, W.J., Appl. Phys., 1958. **29**: p. 1729.
247. Hearle, J.W.S., R. Prakash, and M.A. Wilding, *Prediction of mechanical properties of nylon and polyester fibres as composites.* Polymer, 1987. **28**: p. 441-448.
248. Chen, B. and J.R.G. Evans, *Elastic Moduli of clay platelets.* Scripta Materialia, 2006. **54**: p. 1581-1585.
249. Fornes, T.D. and D.R. Paul, *Modeling properties of nylon 6/clay nanocomposites using composite theories.* Polymer, 2003. **44**: p. 4993-5013.
250. Pawley, A.R., S.M. Clarks, and N.J. Cheinnery, *Equation of state measurements of chlorite, pyrophyllite, and talc* American Mineralogist, 2002. **87**: p. 1172-1182.
251. Manevitch, O.L. and G.C. Rutledge, *Elastic Properties of a Single Lamella of Montmorillonite by Molecular Dynamics Simulation* J. Phys. Chem. B., 2004. **108**: p. 1428-1435.
252. Hildmann, B., et al., *Structural Control of Elastic Constants of Mullite in Comparison to Sillimanite.* J. Amer. Ceramics Soc., 2001. **84**: p. 2409-2414.
253. Vanorio, T., M. Prasad, and A. Nur, *Elastic properties of dry clay mineral aggregates, suspensions and sandstones* Geophysical J. Inter., 2003. **155**: p. 319-326.
254. Halpin, J.C. and J.L. Kardos, *The Halpin-Tsai equations: A review.* Polym. Eng Sci., 1976. **16**: p. 344-352.
255. Kinloch, A.J. and A.C. Taylor, *Mechanical and fracture properties of epoxy/inorganic micro- and nano-composites.* J. Mater. Sci. Lett., 2003. **22**: p. 1439-1441.
256. Lielens, G., et al., *Prediction of thermo-mechanical properties for compression moulded composites.* Composites A., 1997. **29**: p. 63-70.
257. Sheng, N., et al., *Multiscale micromechanical modeling of polymer/clay nanocomposites and the effective clay particle.* Polymer, 2004. **45**: p. 487-506.
258. Zhu, L. and K.A. Narh, *Numerical simulation of the tensile modulus of nanoclay-filled polymer composites.* J. Polym. Sci., Part B: Polym. Phys., 2004. **42**: p. 2391-2406.
259. Ramakrishna, S., et al., *Modified Halpin-Tsai equation for Clay-Reinforced Polymer Nanofiber.* Mech. Advanced Mater. & Struct., 2006. **13**: p. 77-81.
260. Brune, D.A. and J. Bicerano, *Micromechanics of nanocomposites: comparison of tensile and compressive elastic moduli and prediction of effects of incomplete exfoliation and imperfect alignment on modulus.* Polymer, 2002. **43**: p. 369-387.
261. Wu, Y.-P., et al., *Modeling Young's modulus of rubber-clay nanocomposites using composite theories.* Polymer Testing, 2004. **23**: p. 903-909.
262. Ji, X.L., et al., *Tensile Modulus of Polymer Nanocomposites.* Polym. Eng Sci., 2002. **42**: p. 983-993.
263. Guth, E. and O. Gold, *Hydrodynamical theory of the viscosity of suspensions.* Phys. Rev., 1938. **53**: p. 322.
264. Guth, E., J. Appl. Phys., 1945. **16**: p. 20.
265. Chen, B. and J.R.G. Evans, *Nominal and Effective Volume Fractions in Polymer-Clay Nanocomposites.* Macromolecules, 2006. **39**: p. 1790-1796.
266. Vaia, R. and E.P. Giannelis, *Polymer Nanocomposites: Status and Opportunities.* MRS Bulletin, 2001: p. 394-401.
267. Granick, S. and H.W. Hu, *Nanorheology of Confined Polymer Melts. 1. Linear Shear Response at Strongly Adsorbing Surfaces.* Langmuir, 1994. **10**: p. 3857-3866.
268. Peanasky, J., et al., Lagmuir, 1994. **10**: p. 3874-3879.
269. Sens, P., C.M. Marques, and J.F. Joanny, Macromolecules, 1994. **27**(3812-3820).
270. Chen, B., et al., *Morphology and Elastic Modulus of Novel Poly[oligo(ethylene glycol) diacrylate]-Montmorillonite Nanocomposites.* J. Polym Sci. Part B: Polym. Phys., 2005. **43**: p. 1785-1793.
271. Christensen, R.M., *Mechanics of Composite Materials*. 1979, New York: John Wiley & Sons.
272. Buryachenko, V.A., et al., *Multi-scale mechanics of nanocomposites including interface: Experimental and numerical investigation.* Compos. Sci. & Tech., 2005. **65**: p. 2435-2465.

273. Galgali, G., S. Agarwal, and A. Lele, *Effect of orientation on the tensile modulus of polypropylene-nanoclay composites.* Polymer, 2004. **45**: p. 6059-6069.
274. Chang, J.H., et al., *Poly(butylene terephthalate)/organoclay nanocomposites prepared by in situ interlayer polymerization and its fiber (II).* Polymer, 2003. **44**: p. 5655-5661.
275. Chang, J.H. and S.J. Kim, *Polyester nanocomposite fibers: comparison of their properties with poly(ethylene terephthalate) and poly(trimethylene terephthalate) (II).* Poymer Bulletin, 2004. **52**: p. 289-296.
276. Giza, E., et al., *Fiber Structure Formation in High-Speed Melt Spinning of Polyamide 6/Clay Hybrid Nanocomposites.* J. Macromol. Sci. - Phys, 2000. **B39**: p. 545-559.
277. Usuki, A., et al., J. Mater. Res., 1993. **8**: p. 1179.
278. Ibanes, C., et al., *Structure and Mechanical Behavior of Nylon-6 Fibers Filled with Organic and Mineral Nanoparticles. I. Microstructure of Spun and Drawn Fibers.* J. Polym. Sci. Part B: Polym. Phys., 2004. **42**: p. 3876-3892.
279. Ibanes, C., et al., *Structure and Mechanical Behavior of Nylon-6 Fibers Filled with Organic and Mineral Nanoparticles. II. In-Situ Study of Deformation Mechanisms.* J. Polym. Sci, Part B: Polym. Phys., 2004. **42**: p. 2633-2648.
280. Murthy, N.S., et al., J. Polym Sci. Part B: Polym. Phys., 1996. **34**: p. 821-835.
281. Prevorsek, D.C. and H.B. Chin, Intern. J. Polym. Mater., 1994. **25**: p. 161-184.

3.0 Improved Mechanical Properties of PET Nanocomposite Fibers

David W. Litchfield[a], Donald G. Baird[a], Peter B. Rim[b]

[a] Department of Chemical Engineering, Virginia Polytechnic Institute and State University, Blacksburg, Virginia 24061

[b] Performance Fibers Inc, Richmond, Virginia 23219

ABSTRACT

Improvements in Young's modulus and strength (tenacity) of poly(ethylene terephthalate) (PET) fibers were obtained by drawing un-oriented nanocomposite filaments containing low concentrations (< 3 wt%) of various organically modified montmorillonites (MMTs) in a second step at temperatures above the glass transition. Prior to melt-spinning, solid state polymerization (SSP) was used to rebuild lost molecular weight (MW), due to MMT induced degradation, to a level suitable for producing high strength fibers. Greater improvements in mechanical properties occurred when the MMT stacks were intercalated with PET. A nominal 1 wt% loading of dimethyl-dehydrogenated tallow quaternary ammonium surface modified MMT in drawn PET fiber showed a 28% and 63% increase in Young's modulus and strength, respectively. Relative to an un-filled PET fiber, these results surpassed the upper-bound of the rule of mixtures estimate and suggested that both the type of surface modification and concentration of MMT affect the degree of PET orientation and crystallinity. Furthermore, drawability above T_g and elongation-at-break increased upon the addition of organically modified MMT to un-oriented PET fibers, which was a key distinction of this work from others examining similar systems.

3.1 INTRODUCTION

Poly(ethylene terephthalate), PET, is an industrially significant polymer with a variety of commercial and engineering applications from fibers and films to bottles and packaging. The demand for PET fiber in the US alone is estimated at nearly 800 million lbs/year [1]. Among other features, PET has a low crystallization rate and excellent spinnability that aids in the development of oriented polymer chains for filaments with high modulus and strength, which is important to the tire cord industry, for example. Only recently has the attention of polymer nanocomposite research extended to the development of nanoparticle filled fibers for improvements to dimensional stability, initial modulus, and strength [2-7]. Yet, authors examining PET nanocomposite fibers have not produced oriented fibers with sufficient modulus and strength for use in tire cord applications nor have they examined the effect of drawing on mechanical properties [6, 7].

Over a decade of research has shown the potential of polymer nanocomposites to become one of the more significant engineering materials with a number of immediate applications [8, 9]. In particular, polymer layered silicate nanocomposites have shown significant improvements in their physical, chemical, and mechanical properties at lower filler loading levels than conventionally filled composites [9, 10]. While conventional fillers with particle sizes in micron range have shown similar effects, the greater filler concentrations and larger particle dimensions have been problematic, making the production of reinforced melt-spun polymer fibers infeasible. On the other hand, the use of disk-shaped layered-silicates or nanoclays with initial moduli of 178 GPa [11] and nano-meter dimensions (3-4 orders of magnitude smaller than the diameter of the melt spun

filament) permit such nano-structured composites to be formed continuously without major irregularities and interruptions in the spin line. Continuous filaments with <100 μm diameters of nanocomposite material have been formed using nylon [3] and polypropylene [2, 12] in un-oriented and drawn form, and PET [6, 7] in an un-oriented state only.

In addition to the relatively high modulus, nanoclays possess other interesting properties that make them attractive as filler particles for polymer matrices. Among these, nanoclays have large aspect ratios ranging from cited values of 50-300 [8]. This high aspect ratio leads to a greater surface area for interaction with the intercalating polymer backbone or side groups. The combination of high modulus, aspect ratio, and abundant surface area leads to the conclusion by micromechanical arguments that very low volume fractions of nanoclay are required to produce significant improvements in physical properties. However, these particles typically exist as aggregates (i.e. as stacks of silicate sheets) due to van der Waals forces. Particle aggregation decreases the effective particle aspect ratio and limits surface area, which in turn prevents the attainment of theoretical predictions.

A current problem in polymer nanocomposites is the achievement of completely exfoliated nanoparticle morphology within the polymer matrix [13]. Regardless of the method used to prepare the polymer layered-silicate nanocomposites, the primary step toward exfoliation is the organic modification of the inorganic particle surface. Through a cation exchange reaction the naturally present alkali cations (Na^+, Ca^{2+}, etc) within the silicate sheets are displaced by quaternary alkylammonium surfactants. Thus, the inherently hydrophilic nanoclay surface has been rendered hydrophobic by the organic

modification and now promotes more favorable interactions with the hydrophobic polymer chains. The choice of surfactant depends upon polymer characteristics such as polarity.

The next step in effective nanoparticle dispersion is the combination of polymer and nano-filler by a synthesis method. Nguyen and Baird [13] recently reviewed "in-situ" polymerization, solution, or melt-intercalation methods and proposed a novel approach using super-critical fluids that shows promise in obtaining exfoliated nanoparticle morphologies. The conventional methods for producing PET nanocomposites focus on either intercalation of nanoparticles by a suitable monomer and subsequent in-situ polymerization [14-18] or melt compounding by single screw [6, 19] or twin screw [20-29] extrusion. Several of these authors [17, 18, 22, 26] have claimed exfoliation of their PET nanocomposites, and it seems at this point that neither method presents itself as being a significantly more effective technique at dispersing nanoclays in PET than the other.

Regardless of the synthesis route of forming PET nanocomposites, rapid and efficient manufacturing of usable products most likely requires a melt processing step, in which thermal instabilities of the polymer and/or nanoclay could induce polymer and/or surfactant degradation. The solid state polycondensation of PET nanocomposites is a viable route to removing these unfavorable by-products from the system while building back lost molecular weight [30]. In the nanocomposite literature, the presence of nanoclay in PET has been shown to create smaller crystallites in the melt-phase heterogeneous nucleation [31]. Yu et al. [32] demonstrated that solid state polymerization (SSP) of PET in the presence of montmorillonite type nanoclays is feasible and is shown to accelerate the solid state polycondensation reaction relative to pure PET. However, the effects of

nanoclay dispersion or concentration were not discussed. Based on conjecture of other observed phenomena with nanoparticles, it is suggested that the improved barrier properties by the addition of large amounts of dispersed nanoclay or by the addition of higher concentrations of nanoclay that ethylene glycol diffusion will become limited and the solid state reaction will progress at a slower rate. Therefore, it is considered best to solid state intercalated PET nanocomposites and then exfoliate the nanoparticles in a subsequent second or third processing step.

Increasing the molecular weight of the PET phase by SSP also contributes to enhanced mechanical performance. Higher molecular weight resins can accommodate significantly larger physical network deformations than lower molecular weight resins before fracture. This is due to the longer chain's ability to redistribute and relieve stress more effectively because of a larger concentration of chain entanglements per volume than shorter molecular chains. Reviews of the rheological [33] and mechanical [10] behaviors of other polymer nanocomposite systems have shown that nanoparticles alter the entanglement structure of the intercalating polymer molecules. This effect has yet to be exploited for the enhancement of PET nanocomposite fiber properties by drawing at temperatures above the glass transition. Drawing PET, at temperatures where its relaxation times are long but molecular orientation occurs readily, could be enhanced by the presence of nanoparticles and lead to significantly improved mechanical properties. To date, drawing has not been studied with PET nanocomposite fibers spun with low or high take-up speeds. Although the mechanical properties of un-oriented PET nanocomposites spun at various speeds have been examined, these fibers do not show adequate strength and modulus for use in tire cord applications [6, 7].

The purpose of this article is to determine whether low loading levels of nanoclay in un-oriented PET fibers produce improved mechanical properties relative to an unfilled PET subjected to an equal processing history. A series of montmorillonite nanoclay concentrations and surfactant types is examined to deduce the appropriate choice of nanoclay properties for optimal improvement in fiber mechanical properties. In addition, this work uses SSP to rebuild lost molecular weight of degraded melt-compounded PET nanocomposites proving this method's value in reversing the effects of surfactant instabilities. Furthermore, the authors are unaware of any study examining drawn PET nanocomposite fibers on an equi-molecular weight basis.

3.2 EXPERIMENTAL

3.2.1 Materials

Poly(ethylene terephthalate) of intrinsic viscosity of 0.96 dl/g was donated by Performance Fibers Inc. (Richmond, VA) and was used as received. Surface modified montmorillonites Cloisite 20A and Cloisite 30B and un-treated Cloisite Na^+ were obtained from Southern Clay Products Inc (Gonzalez, TX) and used without further modification. The surface modified clays are produced commercially by the substitution of interlayer sodium cations by dimethyl, dehydrogenated tallow or methyl, tallow, bis-2-hydroxyethyl quaternary ammonium cations for Cloisite 20A and 30B respectively. In this commercial process, free surfactant not confined to the particle surface can account for up to 35% of the total organic modification [34]. Phenol and 1,1,2,2 tetrachloroethane

were purchased from Sigma-Aldrich and used without additional purification for the determination of intrinsic viscosity.

3.2.2 Melt Compounding

Before melt compounding, PET and clay were mechanically mixed and dried together at 120 °C for at least 24 hours under vacuum to remove excess moisture from the PET and nanoclays. PET nanocomposite chips were prepared by direct melt compounding using a single screw extruder (Killion KL-100) to form intercalated dispersions of nanoclay and PET. A nitrogen feed was used through the hopper to prevent contact with atmospheric moisture and air. The nanocomposite chips were extruded using a screw speed of 20 rpm and an ascending temperature profile beginning at 250 °C at the solids conveying zone and progressing to 280 °C at the circular die. The single screw was of constant channel width and pitch angle design, consisted of no additional mixing features, and had a diameter of 2.54 cm and an L/D of 20:1. The nanocomposite extrudate was quenched using a cold water bath at 20 °C and pelletized into approximately 1 cm long by 0.2 cm diameter pellets.

3.2.3 Solid State Polymerization, SSP

Melt compounded PET and PET nanocomposite chips were checked for molecular weight loss by rheological methods detailed later. The reduced PET molecular weight was rebuilt (to a M_w ~60,000 g/mol) by SSP in a Fisher Scientific Isotemp Oven,

Model 282A, at 210 °C under vacuum (<0.05 in Hg) for a pre-determined amount of time usually on the order of 1 day. A nitrogen purge was used to open the oven. Chips were stirred every two hours until crystallization was complete, which was designated as the point after which the chips were no longer tacky.

3.2.4 Fiber Spinning

The solid-state polymerized, melt-compounded PET nanocomposite pellets were formed into filaments using a Killion 100 single screw extruder with a screw geometry of 2.54 cm diameter and 24:1 L/D, a Zenith precision gear pump to regulate the mass flow rate through a spin-pack. A 10 hole spinneret consisting of holes of circular cross section of 0.508 mm diameter was used. The filtration part of the spin-pack consisted of 80 g of 5 mm glass beads and 2 stainless steel wire mesh filters with openings of 60 μm to remove large particulate matter. The pressure above the spin-pack was measured by means of a Dynisco Instruments transducer model PT462E (0-5000 psig). The filaments were cooled using ambient quench air down a 2 meter vertical spin-line and taken up by a Leesona Model 966 winder at 550 m/min. Five bobbins of ten filaments from each nanocomposite sample were collected and then creeled to a single roll of fifty filaments in order to improve the accuracy of the tensile measurements and facilitate second step draw. Before melt spinning the nanocomposite pellets were dried for a minimum of 24 hours at 120 °C under vacuum. At the hopper, a nitrogen bleed was used to prevent contact of outside moist air with the pellets before metering and subsequent melting in the extruder.

3.2.5 Fiber Drawing

The as-spun filaments were attenuated to oriented morphologies by a second step drawing process at a temperature of 83 °C, which was above the glass transition. This step was completely separate from the melt spinning process. It is important to note that the melt spinning and fiber drawing steps did not occur in the same line of operation. Yet, both processes are continuous to the extent that several kilometers of fiber can be handled. The un-oriented yarns were drawn within 8 hours of melt spinning to avoid possible complications from physical aging. The fiber drawing line (Randcastle Extrusion Systems) consisted of two sets of three cold godets. The fiber was wrapped around and fed through the first set of godets to the second set, which rotated at a greater linear velocity than the first. Between the sets of godets there was a hot air oven that by combined radiative and convective heat transfer from the elements and heated air increased the temperature of the filaments to facilitate hot draw and the evolution of an oriented-semicrystalline PET morphology. The drawn fiber was then taken-up at an average speed of 10 m/min onto another bobbin. All fibers were drawn to nearly 95% of their maximum extent. Maximum draw ratios were verified by tensile measurements of elongation at break at room temperature.

3.2.6 Characterization

The tensile properties of the nanocomposite fibers were determined using an Instron 4204 Universal Testing Machine at room temperature and humidity. A crosshead speed of 30 cm/min was used for testing the drawn fibers at a gauge length of 25.4 cm. For the un-oriented fibers, gauge lengths of 7.62 cm and crosshead speeds of 9.0 cm/min were used. Reported values are averages of 8 samples with uncertainties corresponding to 95% confidence limits. To track the development of applied load with draw ratio, hot drawing experiments were conducted in constant extension rate mode within a convection air oven (Russell Technical Products) mounted on the Instron UTM. The fiber sample gauge length was 1.27 cm, and the extension rate was 30 cm/min at 85 °C.

Rheological measurements were performed using a Rheometrics Mechanical Spectrometer Model 800 (RMS-800). Samples were dried for 24 hours under vacuum at 120 °C and pressed within the rheometer at the melt temperature to circumvent compression molding into performs and causing further processing induced degradation of the PET matrix. Dynamic frequency sweep experiments were performed under a continuous nitrogen atmosphere using 25-mm cone and plate fixtures at 285 °C in the linear viscoelastic region of the materials in the frequency range of 0.1-100 rad/s. The linear viscoelastic limit was determined using strain sweeps at a frequency of 10 rad/s and equivalent environmental conditions. Time sweeps were performed to test the stability of the PET matrix in the presence of surface-modified and un-modified nanoclay at 285 °C, a frequency of 1 rad/s, and strain of 5%.

The intrinsic viscosity of the un-oriented nanocomposite fibers was evaluated to check the final molecular weight of the PET matrix by an Ostwald type viscometer. The polymer solutions were prepared by dissolving the PET nanocomposite fiber in 1:1 by

weight phenol/1,1,2,2 tetrachloroethane. The intrinsic viscosity [η] in dl/g was determined by use of Eq. 1 from the concentration of polymer, c, and flow time measurements at 25 °C to calculate a relative viscosity (η_{rel}) term[35]. The viscosity average molecular weight can then be calculated by a Mark-Houwink relationship [36].

$$[\eta] = \left(\frac{1}{c}\right)\left[2(\eta_{rel} - 1) - 2\ln(\eta_{rel})\right]^{1/2} \qquad (1)$$

The true clay content of the nanocomposite fibers was checked by a burn-off technique in an ashing oven at 600 °C for 1 hour. The clay concentrations are reported as an average of three burn-off samples and are reported to include 100% of the organic modifier.

The morphology of the nanoclay within the PET nanocomposites was determined using wide angle X-ray diffraction (XRD). XRD patterns were obtained using a Scintag XDS 2000 diffractometer with Cu K radiation at a wavelength of 1.54 Å with a scan rate of 0.5°/min from 1.5 to 10°. This study was not immediately focused on complete exfoliation of the nanoparticles, and thus transmission electron images of the nanocomposite were not taken for the specimens showing little to no peak in the XRD pattern.

3.3 RESULTS AND DISCUSSION

3.3.1 General Features of Solid State Polymerization of PET Nanocomposites

The loss in PET molecular weight with the addition of organically-modified nanoclay is shown in Fig. 3.1 in terms of complex viscosity, |η*|, versus frequency, ω, for four PET nanocomposite melts compounded with 0, 1, 3, and 5 wt% of Cloisite 30B. The observed reduction in viscosity values is correlated with molecular weight by the equation of Fox and Berry[37]

$$\eta_0(T, M_w) = k(T)(cM_w)^{3.4} \qquad (2)$$

where η_0 is the zero shear viscosity, k(T) is a constant dependent on temperature (for examples see Van Krevelen [38]) c is the polymer concentration, and M_w is the weight average molecular weight. The zero shear viscosity is determined by fitting the Bird-Carreau model to the |η*| vs. ω curve in the range of 1-100 rad/s. The curve is fit only in the 1-100 rad/s range, because obtaining data points at low frequencies requires longer experimental times and can lead to additional degradation of the sample. Based on time sweep experiments, shown later, to assess the stability of |η*| over time at a constant ω, the PET nanocomposites have approached their equilibrium molecular weights at the time required (360 s) to obtain the viscosity at 1 rad/s. Therefore, the slight upturn in the complex viscosity curve at low frequencies is most likely not due to the development of yield behavior created by networked arrangements of nanoparticles as some authors have observed with other polymer nanocomposite systems [39]. Degradation to this degree has been observed by other authors examining the rheology of PET nanocomposites [22]. Alternative theories have attributed slip between the smooth filler and polymer during shear flow as a cause for the reduced viscosity [22]. For Cloisite 30B, in which functional hydroxyl groups on the surfactant are available to bond with PET, slip is considered negligible, and, thus, the drop in viscosity is attributed to chain scission. Table 3.1 shows

M_w values calculated from |η*| vs. ω curves for the melt-compounded long alkyl chain modified, Cloisite 20A and un-modified Cloisite Na^+ nanoclays. Molecular weight is shown to decrease with increasing filler concentration with these nanoclays as well, although the degree of degradation is not as severe as that of Cloisite 30B. These results show that the presence of nanoclay promotes degradation of PET, but the addition of an alkyl quaternary ammonium surfactant further encourages chain scission when melt-compounded with PET at 280 °C.

The melt processing temperature of PET in the range of 275-285 °C is greater than the onset of thermal degradation for some commercially available nanoclay surfactants [34]. Matayabas et al. [20] and Davis et al. [21] have observed severe PET degradation post-melt compounding with thermally unstable organically modified nanoclays. Others have observed enhanced PET molecular weight loss with organo-nanoclay when melt compounding to form injection molded [22, 28] and continuous fibers [6]. A mechanism for this enhanced PET degradation induced by the presence of thermally unstable organo-nanoclay could be extrapolated from a study by Bellucci et al. [34]. Long alkyl chain (tallow) and hydroxyl-tallow quaternary ammonium surfactants were shown to decompose to volatile vinyl compounds, polyenes, ammonia, and acetaldehyde with the production of an H^+ proton (capable of promoting acid hydrolysis in PET)[34]. The enhanced gas barrier properties of the dispersed silicate layers can limit the diffusion of these decomposed surfactants from the PET melt, making it more likely that these by-products will react and sever polymer chains. In addition, quaternary ammonium hydroxides have been known to cause chain scission by alkyline hydrolysis in PET

recycling and textile texturing [40, 41]. Thus, the presence of free surfactant not bound to the nanoclay surface could contribute to PET molecular weight loss.

As mentioned in the background section of this article, SSP can be used to rebuild lost molecular weight and remove harmful by-products created from PET degradation. Fig. 3.2 shows the build of molecular weight over time up to 50 hours for a representative 3 wt% loading of the different types of nanoclays compared to an un-filled sample. The points on Fig. 3.2 represent data accumulated from frequency sweeps at each 10 hour period of SSP. The lines represent best fits to the data in order to empirically determine the time required to carry out SSP of the nanocomposites to a specific molecular weight.

SSP is used in this work as a tool to overcome the detrimental effects of melt-compounding with nanoclays before melt-spinning. The determination of the mechanism and reaction kinetics to describe the condensation of polymer chains is considered beyond the scope of this work. Although the complexity of the reaction is recognized, Fig. 3.2 shows that longer reaction times are required for SSP of the nanocomposite resins. These longer reaction times are most likely due to both the larger loss in molecular weight and the slower diffusion of ethylene glycol caused by an increased path tortuousity from intercalated silicate layers from the chips.

The melt stability of the solid stated PET nanocomposite chips was checked at 280 °C by a time sweep tracking the relative complex viscosity ($|\eta^*|(t)/|\eta^*|(t=0)$) with time. Shown in figs. 3.3 and 3.4 are the matrix stabilities of 1 wt% and 5 wt% loadings of Cloisite 30B and Cloisite 20A before and after SSP. For both nanoclay surfactants the benefits to stability are most clearly seen in the 5 wt% loadings after SSP. This is most likely due to the formation of a significantly larger amount of low molecular weight

compounds during melt-compounding at 5 wt% vs. 1 wt% loadings, which are subsequently removed or condensed to show greater stability improvement. Therefore, the relatively insignificant change in behavior at 1 wt% of either clay surfactant is indicative of the presence of nanoclay and interstitial water within the clay galleries in the de-polymerization PET chains. Cloisite 20A exhibits a less deleterious effect on PET molecular weight than Cloisite 30B due to the absence of surface hydroxyls, which promote transesterification, and a slightly higher thermal decomposition temperature, which is estimated as 300 °C vs. 280°C for Cloisite 30B [34].

After solid-state polymerizing all materials to an equivalent molecular weight, the shear rheology as determined by means of dynamic oscillatory measurements on the pure PET is nearly equivalent to that of the nanocomposites of various clay types and loadings. Figs. 3.5 and 3.6 show the values of $|\eta^*|$ vs. ω and G' vs. ω respectively for the solid stated nanocomposites of Cloisite 30B. The observed "plateau" in G' in Fig. 3.6 and "yield-like" behavior in viscosity in Fig. 3.5 at low frequencies are due to matrix degradation. In these figures the experimental time elapsed at the determination of the viscosity data points is displayed on the right hand axis. Again, the solid-like behavior of exfoliated or percolated nanoparticles in PET is not displayed at these nanoclay concentrations, which were melt-compounded by single screw extrusion.

3.3.2 Morphological Characterization of Nanoparticle Dispersion

Rheological measurements hint that solid state polymerization does not improve the degree of nanoparticle dispersion, and wide angle X-ray diffraction patterns confirm

this observation. Fig. 3.7 shows the diffraction pattern of a 5wt% loading of Cloisite 20A in PET and solid state polymerized for various times. The inset in Fig. 3.7 shows the pattern of pure Cloisite 20A as a reference for peaks at 3.7° of 2θ, corresponding to the inter-particle distance of organically modified clay, d_{001} or the "d-spacing", and 7.3° of 2θ, corresponding to a secondary peak, d_{002} [42]. In melt-compounding PET with 3 wt% of Cloisite 20A by single-screw extrusion, some intercalation of PET occurs shown by the shift in the peak maximum to lower angles of 2θ. However, Fig. 3.7 shows no shift to lower angles with reaction time, which suggests that end-groups polymerize out-side of the intercalated stacks during solid state polymerization time and do not diffuse into the clay galleries. In addition, there appears to be no trend in peak height or area under the curve with reaction time. The number fraction of intercalated stacks of particles has been shown to directly correlate with the area under the peak [43]. Therefore, SSP of PET intercalated within the nanoclay layers does not have any discernable trend on particle disorder.

For the case of nanocomposite fibers, Fig. 3.8 shows X-ray diffraction patterns of the as-spun low orientation nanocomposite fibers at concentrations of 1 and 3 wt% in order to compare surface treatments. The Cloisite 20A nanocomposite fibers show the greatest inter-particle separation as well as successful intercalation of the PET chains into the nanoclay layers. The peak for the Cloisite 20A fibers is shifted to lower angles than the peak of pure 20A shown in the inset of Fig. 3.7, which demonstrates that some degree of intercalation took place. Cloisite 30B nanocomposite fibers do not show PET intercalation. Rather, these nanocomposites show a collapse in inter-particle distance by a shift to higher angles, which is believed to occur from surfactant degradation during

melt processing in fiber spinning. Cloisite Na^+ nanocomposite fibers show no evidence of the intercalation of PET, as expected. In terms of concentration effects, the Cloisite 20A fibers show a shift in peak position to higher angles as concentration is increased with an increase in area under that peak. Therefore, as the concentration of 20A is increased the degree of exfoliation is reduced and the number of larger agglomerates increases. For the nanocomposite fibers of Cloisite 30B and Na^+, no change in intercalation is observed with concentration, but the number of nanoparticle agglomerates increases with nanoparticle addition.

Fig. 3.9 shows the nanoparticle morphologies in the drawn fiber for various concentrations of Cloisite 20A, which were shown to possess intercalated PET chains. Comparing the un-oriented and oriented fibers at 1 and 3 wt%, the peak positions have been shifted to slightly higher angles. This indicates that drawing the nanoparticle fibers leads to a collapse in inter-particle distance. This collapse is suspected to be due to the reorganization of amorphous, curled polymer chains to oriented, extended chain crystallites. Although, it appears that the particle spacings have collapsed, the number of stacked particles as agglomerates in the drawn nanocomposite fibers decreased dramatically compared to the as-spun fibers. Thus, it is perceived that drawing has increased the aspect ratio of the nanoparticles and sheared the stacked agglomerates like a deck of playing cards, such that the overlap of silicate layers has been reduced. In terms of fiber drawing and concentration effects on nanoparticle dispersion, Fig. 3.9 shows that the 1 wt% Cloisite 20A fiber undergoes the largest amount of collapse (~0.6 nm) compared to the 0.5, 1.5, and 3 wt% fibers after drawing. The number of agglomerated overlapping stacks increases monotonically with nanoclay concentration up to 3 wt%.

Transmission electron microscopy, TEM, imaging was deemed unnecessary to describe to dispersion of the nanocomposite systems because Cloisite 20A shows a peak in its X-ray pattern at all concentrations, while Cloisite 30B and Na^+ show no signs of intercalation of PET. Therefore, the nanocomposite fibers formed in this work are not of an exfoliated morphology. However, the mechanical properties of the PET nanocomposite fibers were observed to increase despite only achieving intercalation.

3.3.3 Mechanical Properties of Solid Stated PET Nanocomposite Melt-Spun Fibers

Table 3.1 shows the nanoclay concentrations in which fiber spinning was undertaken in this study. The original series of nanoclay concentrations used for this study were 0 (un-filled PET), 1, 3, and 5 wt% loadings of each nanoclay type. However, continuous melt spinning of 5 wt% loadings of Cloisite 20A, 30B, and Na^+ proved difficult due to the frequent amount of line breaks occurring in the thread-line during take-up at 550 m/min. Similar observations have been observed for PET spinning, at 800 m/min, with un-solid stated nanocomposites at 4 wt% by McConnell et al. [6] and for polypropylene nanocomposite fiber spinning by Houphouet-Boigny et al. [12] for nanoclay loadings up to 5 wt%. However, 3 wt% nanoclay fibers showed good spinnability with zero line breaks during 1 hr of melt spinning. Therefore, for the Cloisite 20A and 30B nanoclays, which showed improvements in drawn mechanical properties, refinements to nanoclay concentrations in 0.5 wt%'s were made to establish the optimum loading of nanoclay.

Table 3.2 shows the true organo-nanoclay content and the as-spun (un-oriented) mechanical properties of the PET and PET/MMT nanocomposite fibers tested at room temperature and humidity. Processing the nanocomposite using two melt-compounding steps leads to some filtration of agglomerated silicate from the system and volatilization of the thermally unstable organic surfactant. Thus, a reduced true clay content relative to the original concentration is expected.

Regardless of nanoclay surfactant or concentration (with a single exception), the un-oriented nanocomposite fibers have lower Young's moduli and maximum strengths than the pure PET standard spun at equivalent conditions. These results are similar to those of other reports of as-spun PET/MMT nanocomposite fibers [6]. Yet, the striking difference between the pure and nanocomposite fibers in their un-oriented states is the greatly increased toughness and concomitantly increased elongation at break of the organically modified nanocomposite fibers, which to date has not been reported for PET fibers containing montmorillonite nanoparticles in PET fibers [7].

Cited increases in nanocomposite toughness using layered silicates are rare and have been observed to occur only in exfoliated systems in which the individual silicate layers prevent micro-crack propagation [44, 45]. However, the majority of systems examined with polymer layered-silicate nanocomposites have been for injection molded materials, where a long range three dimensional micro- or meso-structure may dictate the mechanical response [46, 47]. The situation is different for melt-spun fibers, which have diameter dimensions on the 10 μm scale. The deformation of the networked polymer chains progresses primarily by chain extension into microfibrils (i.e. 2-D or ideally 1-D microstucture) with limited lamella formation. Nevertheless, if the inorganic phase is

well distributed in the PET matrix to alter the chain dynamics of the polymer by either increased entanglements or chemical "tetherment" of the polymer to the particle surface, then it could be suggested that toughness can increase with the addition of an elastic phase by the enhancement of stress redistribution. Thus, as a result of the as-spun data, it is clear that the organically modified nanoclays, Cloisite 20A and Cloisite 30B, show more interaction with PET than the unmodified Cloisite Na^+.

Table 3.2 also displays the molecular weight data for the pure PET and PET nanocomposite fibers obtained by intrinsic viscosity measurements and converted to molecular weight by equations 1 and 2 discussed above. Molecular weight loss due to the presence of clay is inevitable but recoverable. It is clear that SSP is a useful tool to produce and compare nanocomposite fibers with nearly equal PET molecular weights. By comparing these on an equal molecular weight basis, a more accurate determination of the effect of organically-modified nanoclay on the chain dynamics can be made. In the comparison of degraded samples of lower molecular weight, the number of entanglement points as physical crosslinks is reduced in relation to the standard unfilled matrix. Under hot drawing conditions, just above the glass transition, nanocomposite fibers of lower molecular weight possess shorter relaxation times and are suspected to crystallize more readily under deformation. This prevents the development of a highly oriented phase.

The mechanical properties of the PET nanocomposite fibers subjected to an additional drawing step are shown in Table 3.3. After hot drawing the PET nanocomposite fibers to their maximum draw ratios, the modulus is observed to increase and show improvement over un-filled PET at organically-modified nanoclay concentrations below 3 wt%. The strength improvement is shown to depend on the type

of nanoclay surfactant as well as concentration. Fibers containing Cloisite 20A at low loadings (<3 wt%) show significant strength improvements (63% at 1 wt%) relative to pure PET when drawn. As expected from the as-spun toughness results, the maximum draw ratios of the organically modified Cloisite 20A and 30B nanocomposites increased relative to pure PET. The fibers containing un-modified Cloisite Na^+ fibers fractured before reaching the maximum draw ratio of unfilled-PET. However, the drawn nanocomposite fiber toughness values are lower than those of the pure PET fiber. The formation of an oriented, crystalline PET phase may not interact as favorably with the nanoparticle surfaces as the amorphous phase did in the as-spun fibers. In addition, the 20A and 30B nanocomposite fibers reach finer deniers than the pure PET, but final denier and maximum draw ratio are interestingly independent of nanoclay loading with this type of continuous low speed drawing.

Tensile stiffness and maximum strength of the drawn fibers are shown to have a greater dependency on both nanoclay loading and choice of nanoclay surfactant. Figs. 3.10 and 3.11 illustrate the dependency of Young's modulus and strength, respectively, on Cloisite 20A, 30B, and Na^+ concentration. In both modulus and strength, fibers filled with Cloisite 20A show enhancements, which reach a maximum at a nanoclay loading of 1 wt%. Beyond this optimal concentration the properties begin to decrease with concentration, possibly due to reduced polymer orientation or the increased variation in fiber cross section from the presence of large agglomerates of nanoclay. At high agglomerate levels premature failure of the filament under tension is due to cavitation and void formation as the stress on the polymer chains concentrates around the agglomerate. At loadings of nanoclay below 1 wt%, the polymer chains are observed not

to exhibit as much molecular orientation during drawing as the case of 1 wt%, and the resulting modulus and strength values are below optimum.

The modulus improvement is compared to a rule of mixtures upper-bound, Eq. 3, under the assumption that the pure PET and nanocomposite fibers possess equal polymer morphologies, where E_{comp} is the modulus of the composite, ϕ_c is the volume fraction of organoclay, E_c is the modulus of the nanoclay estimated as 178 GPa, and E_p is the modulus of the polymer taken as 9.9 GPa in this case.

$$E_{comp} = \phi_c E_c + (1 - \phi_c) E_p \qquad (3)$$

The volume fractions of nanoclay is estimated by conversion of the mass fraction according to

$$\phi_c = \left(\frac{\rho_{NC} \times x_c}{\rho_c} \right) \qquad (4)$$

with

$$\rho_{NC} = \phi_c \rho_c + (1 - \phi_c) \rho_{PET} \qquad (5)$$

where ρ_{NC} and ρ_c are the densities of the nanocomposite and nanoclay, respectively. The densities of the nanoclays are given by the supplier; x_c is the true mass fraction of nanoclay used in the composite given in table 3.2; and ρ_{PET} is taken as 1.38 g/cm^3, which is the density of a 35% crystalline PET fiber [48]. The rule of mixtures (the dashed line in Fig. 3.10) is shown to *under* estimate property improvements in 0.5 wt% and 1 wt% loadings of Cloisite 20A and 0.5 wt% loadings of Cloisite 30B. Therefore, the assumption of equivalent PET morphologies between the unfilled and nanocomposite drawn fibers is incorrect. By the degree of underestimation from the rule of mixtures at

1wt% of Cloisite 20A, the presence of low concentrations of nanoclay is suggested to greatly enhance the orientation and/or crystallinity of the PET phase.

The mechanism behind this trend in mechanical properties with Cloisite 20A nanoclay concentration will be addressed in a future article. Yet, it is apparent by simple mechanical modeling as well as by comparison of the X-ray diffraction patterns of the un-oriented and drawn nanocomposite fibers of Cloisite 20A that the increased dispersion of nanoparticles by drawing does not fully account for the dramatic improvement in mechanical properties. The particles are assumed to be well oriented in the fiber direction in the as-spun state [12, 47] and the effect of drawing the fibers only increases the effective nanoparticle aspect ratio.

Fig. 3.12 shows the improved stress-strain behavior when hot drawing the 1 wt% Cloisite 20A nanocomposite fiber at constant extension rate. Although the stress-strain response for drawing in this manner is inherently different than in continuous drawing [49], the delayed stress at break of the nanocomposite compared to the pure fiber suggests that the nanoparticles improve the molecular orientation of the PET chains and do not have a significant effect on the onset of strain induced crystallization. The responses of the pure PET and 1 wt% Cloisite 20A fiber are nearly identical up to the maximum draw ratio of pure PET. Therefore, the nanocomposites and pure PET resins have nearly identical shear rheology as melts, but the extensional rheology in the rubbery region varies only by the achievement of enhanced drawability. The enhanced drawability could be attributed to the physical blockage of PET chain entanglements on either of the silicate sheets. Further analysis will be provided in a future publication.

3.4 CONCLUSIONS

In terms of the degree of intercalation and thermal stability of the PET matrix, Cloisite 20A seems to be the more favorable nanoclay surfactant than Cloisite 30B. XRD shows that 20A intercalates between the silicate galleries, whereas 30B shows a collapse in inter-particle spacing after fiber spinning due to volatilization of the surface treatment. The hydroxyl-tallow type surface modification has a potential for transesterification of the PET ester linkages to form a tethered PET-nanoclay structure. However, this surfactant readily degrades at the melt processing temperature. Thus, the mechanical properties of hydroxyl-modified nanoclay filled PET fibers do not show significant property improvements.

The solid state reaction for nanocomposites is found to progress at a slower rate than the unfilled PET polymer, because of the cited improved gas-barrier effect that this type nanoparticle has in polymers. In addition, the reaction rate depends upon the functionality of the nanoclay surfactant. The hydroxyl-tallow modified nanoclay system shows a significantly reduced molecular weight build rate at long times, which is most likely due to the increased number of –OH groups. During the SSP reaction, the degree of dispersion of nanoparticles is not enhanced, mainly because molecular diffusion of the PET chains is severely limited by the high crystallinity of the system.

The result of second step drawing generally improves the mechanical properties of the nanocomposite fibers, but this depends upon the type of nanoclay surfactant and the amount of clay intercalated in the system. At the higher loadings of nanoclay (~3 wt%), the nanocomposites are spinnable, but the increased presence of large

agglomerates along the fiber length most likely induces premature fiber failure during tensile loading because of stress concentration and subsequent micro-void formation. Therefore, at intercalated loadings of 1 wt% of organically modified clay, the number of large agglomerates is small enough to delay stress concentration around the particle to higher mechanical loads. At small loadings of clay (~0.5 wt%), molecular orientation of the PET chains may be less than optimum. Thus, the degree of property improvement is increased relative to pure PET, but not optimized with nanoclay concentration.

The presence of organically modified nanoclay facilitates the ability to draw PET to higher levels than possible with just pure PET. The higher degree of draw obtained most likely creates an enhanced morphological structure in the PET phase, which improves mechanical properties. Whether, this enhanced structure is due to higher amorphous orientation, degree of crystallinity, and/or connectivity of amorphous and crystalline chains is the subject of another publication. However, it is clear that the obtained mechanical property improvements are not due solely to the greater dispersion of nanoparticles created when drawing, because the obtained improvements are well beyond the estimates by the upper-bound of the rule of mixtures.

ACKNOWLEDGEMENTS

The authors would like to acknowledge the support of Performance Fibers Inc for the donation of PET resins and technical contributions on solid-state polymerization. In addition, we thank Southern Clay Products for donating the MMT nanoclays and Joseph Samaniuk for performing the XRD work presented in this article.

3.5 REFERENCES

1. Fiber Organon: 2008; pp 1-17.
2. Pavlikova, S.; Thomann, R.; Reichert, P.; Mulhaupt, R.; Marcincin, A.; Borsig, E., Fiber spinning from poly(propylene)-organoclay nanocomposite. *J. Appl. Polym. Sci.* **2003,** 89, 604-611.
3. Giza, E.; Ito, H.; Kikutani, T.; Okui, N., Fiber Structure Formation in High-Speed Melt Spinning of Polyamide 6/Clay Hybrid Nanocomposites. *J. Macromol. Sci. - Phys* **2000,** B39, 545-559.
4. Chang, J. H.; An, Y. U.; Kim, S. J.; Im, S., Poly(butylene terephthalate)/organoclay nanocomposites prepared by in situ interlayer polymerization and its fiber (II). *Polymer* **2003,** 44, 5655-5661.
5. Chang, J. H.; Kim, S. J., Polyester nanocomposite fibers: comparison of their properties with poly(ethylene terephthalate) and poly(trimethylene terephthalate) (II). *Poymer Bulletin* **2004,** 52, 289-296.
6. McConnell, D. C.; Hornsby, P. R.; Lew, C. Y.; Qua, E. H., Structure Property Relationships in PET Nanocomposite Fibres. *Ann. Tech. Conf. Society of Plastic Engineers, Technical Papers* **2006**, 387-392.
7. Chang, J. H.; Kim, S. J.; Joo, Y. L.; Im, S., Poly(ethylene terephthalate) nanocomposites by insitu interlayer polymerization: the thermo-mechanical properties and morphology of the hybrid fibers. *Polymer* **2004,** 45, 919-926.
8. Pinnavaia, T. J.; Beall, G., *Polymer-Clay Nanocomposites*. Wiley: New York, 2000.
9. Ray, S. S.; Okamoto, M., Polymer/layered silicate nanocomposites: a review from preparation to processing. *Prog. Polym. Sci.* **2003,** 28, 1539-1641.
10. Tjong, S. C., Structural and mechanical properties of polymer nanocomposites. *Mater. Sci. and Eng. Rev.* **2006,** 53, 73-197.
11. Fornes, T. D.; Paul, D. R., Modeling properties of nylon 6/clay nanocomposites using composite theories. *Polymer* **2003,** 44, 4993-5013.
12. Houphouet-Boigny, C.; Plummer, C. J. G.; Wakeman, M. D.; Manson, J.-A. E., Towards textile-based fiber-reinforced thermoplastic nanocomposites: melt-spun polypropylene montmorillonite nanocomposite fibers. *Polym. Eng Sci.* **2007,** 47, 1122-1132.
13. Nguyen, Q. T.; Baird, D. G., Preparation of polymer-clay nanocomposite and their properties. *Adv. Polymer Techn.* **2006,** 25, 270-285.
14. Chang, J. H.; Mun, M. K.; Lee, I. C., Poly(ethylene terephthalate) Nanocomposite Fibers by In Situ Polymerization: The Thermomechanical Properties and Morphology. *J. Appl. Polym. Sci.* **2005,** 98, 2009-2016.
15. Imai, Y.; Nishimura, S.; Abe, E.; Tateyama, H.; Abiko, A.; Yamaguchi, A.; Aoyama, T.; Taguchi, H., High Modulus Poly(ethylene terephthalate)/Expandable Mica Nanocomposites with a Novel Recative Compatibilizer. *Chem. Mater.* **2002,** 14, 477-479.
16. Saujanya, C.; Imai, Y.; Tateyama, H., Structure and thermal properties of compatibilized PET/expandable fluorine mica nanocomposites. *Polymer Bulletin* **2002,** 49, 69-76.
17. Guan, G.-H.; Li, C.-C.; Zhang, D., Spinning and Properties of Poly(ethylene terephthalate)/Organomontmorillonite Nanocomposite Fibers. *J. Appl. Polym. Sci.* **2005,** 95, 1443-1447.
18. Jung, M.-H.; Chang, J.-H.; Kim, J.-C., Polyethylene terephthalate nanocomposite fibers with new organomica via in situ polymerization. *Polym. Eng. Sci.* **2007,** 47, 1820-1826.
19. Pegoretti, A.; Kolarik, J.; Peroni, C.; Migliaresi, C., Recycled poly(ethylene terephthalate)/layered silicate nanocomposites: morphology and tensile mechanical properties. *Polymer* **2004,** 45, 2751-2759.
20. Matayabas, J. C.; Turner, S. R.; Sublett, B. J.; Connell, G. W.; Gilmer, J. W.; Barbee, R. B. Patent US6084019: High inherent viscosity polyester compositions containing platelet particles. 2000.

21. Davis, C. H.; Mathias, L. J.; Gilman, J. W.; Schiraldi, D. A.; Shields, J. R.; Trulove, P.; Sutto, T. E.; Delong, H. C., Effects of Melt-Processing Conditions on the Quality of Poly(ethylene terephthalate) Montmorillonite Clay Nanocomposites. *J. Polym. Sci.: Part B. Polym. Phys.* **2002,** 40, 2661-2666.
22. Sanchez-Solis, A.; Romero-Ibarra, I.; Estrada, M. R.; Calderas, F.; Manero, O., Mechanical and Rheological Studies on Polyethylene Terephthalate-Montmorillonite Nanocomposites. *Polym. Eng. & Sci.* **2004,** 44, 1094-1102.
23. Pendse, S.; Ranade, A.; D'Souza, N.; Ratto, J. A., Effect of Montmorillonite Layered Silicate (MLS) on Crystallization growth Rate in Semi-Crystalline PET Nanocomposites. *Ann. Tech. Conf. Society of Plastic Engineers, Technical Papers* **2004**, 2343-2347.
24. Pendse, S.; D'Souza, N.; Ratto, J. A., Deformation of PET Nanocomposites. *Ann. Tech. Conf. Society of Plastic Engineers, Technical Papers* **2005**, 3492-3496.
25. Wang, M.; Zhu, M.; Sun, B., A New Nano-Strcutured Flame-Retardant Poly(ethylene terephthalate). *J. Macromole. Sci. PArt A: Pure & Appl. Chem.* **2006,** 43, 1986-1875.
26. Sanchez-Solis, A.; Garcia-Rejon, A.; Manero, O., Production of Nanocomposites of PET-Montmorillonite Clay by an Extrusion Process. *Macromol. Symp.* **2003,** 192, 281-292.
27. Lee, W. D.; Im, S. S.; Lim, H.-M.; Kim, K.-J., Preparation and properties of layered double hydroxide/poly(ethylene terephthalate) nanocomposites by direct melt compounding. *Polymer* **2006,** 47, 1364-1371.
28. Todorov, L. V.; Viana, J. C., Characterization of PET nanocomposites produced by different melt based production methods. *J. Appl. Polym. Sci.* **2007,** 106, 1659-1669.
29. Bizarria, M. T. M.; Giraldi, A. L. F. d. M.; de Carvalho, C. M.; Velasco, J. I.; d'Avila, M. A.; Mei, L. H. I., Morphology and thermomechanical properties of recycled PET-organoclay nanocomposites. *J. Appl. Polym. Sci.* **2007,** 104, 1839-1844.
30. Gantillon, B.; Spitz, R.; McKenna, T. F., The Solid State Postcondensation of PET, 1: A Review of the Physical and Chemical Processes Taking Place in the Solid State. *Macromole. Mater. & Eng.* **2004,** 289, 88-105.
31. Jog, J. P., Crystallization in polymer nanocomposites. *Mater. Sci. and Techn.* **2006,** 22, 797-806.
32. Yu, H.; Han, K.; Yu, M., The Rate Acceleration in Solid-State Polycondensation of PET by Nanomaterials. *J. Appl. Polym. Sci.* **2004,** 94, 971-976.
33. Litchfield, D. W.; Baird, D. G., The rheology of high aspect ratio nano-particle filled liquids. *Rheology Reviews* **2006**, 1-60.
34. Bellucci, F.; Camino, G.; Frache, A.; Sarra, A., Catalytic charring - volatilization competition in organoclay nanocomposites. *Polymer Degradation & Stability* **2007,** 92, 425-436.
35. Ma, Y.; Agarwal, U. S.; Sikkema, D. J.; Lemstra, P. J., Solid-state polymerization of PET: influence of nitrogen sweep and high vacuum. *Polymer* **2003,** 44, 4085-4096.
36. Brandrup, J., *Polymer Handbook*. Wiley: New York, 1999.
37. Berry, G. C.; Fox, T. G., The viscosity of polymers and their concentrated solutions *Adv. Polym. Sci* **1967,** 5, 261-357.
38. van Krevelen, D. W., *Properties of polymers*. Elsevier: New York, 1990.
39. Nguyen, Q. T.; Baird, D. G., An improved technique for exfoliating and dispersing nanoclay particles in polymer matrices using super-critical carbon dioxide. *Polymer* **2007,** 48, 6923-6933.
40. Kao, C.-Y.; Chen, W.-H.; Wan, B.-Z., Investigation of alkaline hydrolysis of polyethylene terephthalate by differential scanning calorimetry and thermogravimetric analysis. *J. Appl. Polym. Sci.* **1998,** 70, 1939-1945.
41. Karger-Koscis, J., Recycling opertaions for post-consumer PET and PET containing wastes by melt blending. In *Handbook of Thermoplastic Polyesters*, Fakirov, S., Ed. Wiley-VCH: Weinheim, 2002; Vol. 2.
42. Southern-Clay-Products *Cloisite 20A: Typical Physical Properties Bulletin*; 2008.
43. Brindley, G. W., Order-Disorder in Clay Mineral Structures. In *Crystal Structures of Clay Minerals and their X-ray Indentification*, Brindley, G. W.; Brown, G., Eds. Mineralogical Society: London, 1980.

44. Qu, X.; Guan, T.; Liu, G.; She, Q.; Zhang, L., Preparation, structural characterization, and properties of poly(methyl methacrylate)/montmorillonite nanocomposites by bulk polymerization. *J. Appl. Polym. Sci.* **2005,** 97, 348-357.
45. Wang, K.; Chen, L.; Wu, J.; Toh, M. L.; He, C.; Yee, A. F., Epoxy Nanocomposites with Highly Exfoliated Clay: Mechanical Properties and Fracture Mechanisms. *Macromolecules* **2005,** 38, 788-800.
46. Varnot, K.; Reynaud, E.; Kloppfer, M.-H.; Vigier, G.; Varlet, J., Clay-reinforced polyamide: Preferential orientation of the montmorillonite sheets and the polyamide crystalline lamellae. *J. Polym Sci. Part B: Polym. Phys.* **2001,** 39, 1360-1370.
47. Ibanes, C.; David, L.; De Boissieu, M.; Seguela, R.; Epicier, T.; Robert, G., Structure and Mechanical Behavior of Nylon-6 Fibers Filled with Organic and Mineral Nanoparticles. I. Microstructure of Spun and Drawn Fibers. *J. Polym. Sci. Part B: Polym. Phys.* **2004,** 42, 3876-3892.
48. Litchfield, D. W. The Manufacture and Mechanical Properties of PET Fibers Filled with Organically Modified MMT. Virginia Tech, Blacksburg VA, 2008.
49. Salem, D. R., *Draw-Induced Structure Development in Flexible-Chain Polymers: in "Structure Formation in Polymeric Fibers"*. Hanser: Munich, 2001.

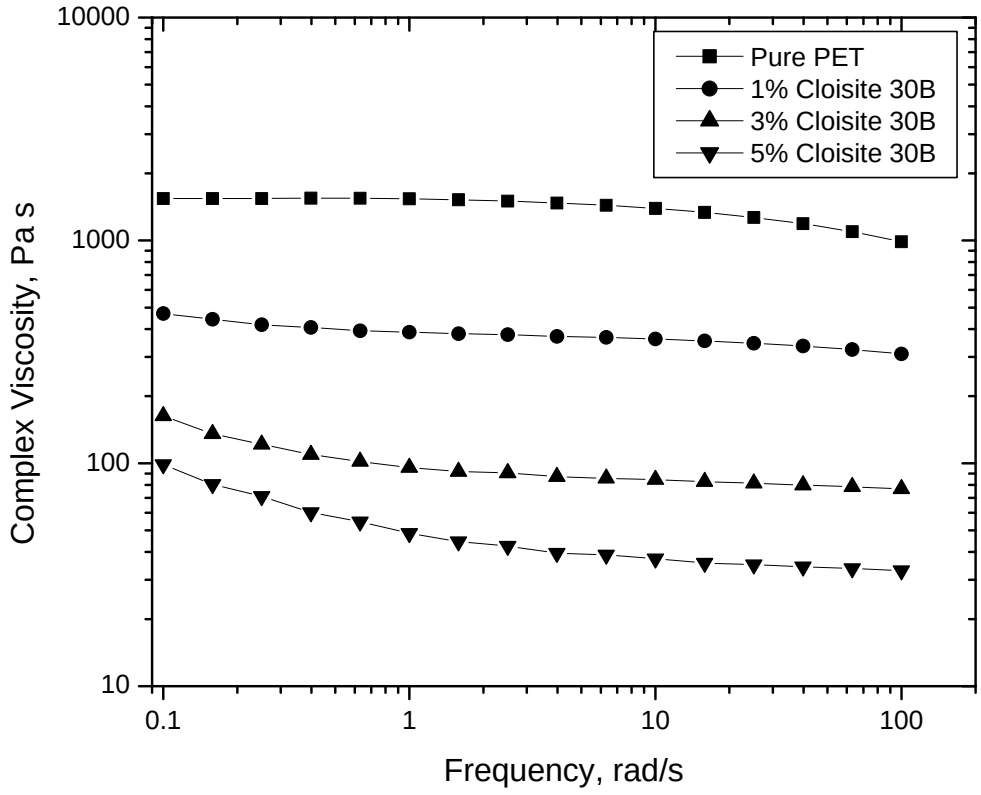

Fig. 3.1. Complex viscosity, |η*| vs. frequency, ω for the melt-compounded Cloisite 30B nanocomposites before SSP.

Table 3.1. Zero shear viscosity reduction of the PET matrix as a function of nanoclay surfactant and particle concentration.

Sample	Nominal Nanoclay Loading	Zero shear viscosity	M_w	Change in M_w
	wt%	Pa s	g/mol	%
Pure PET	0	1340	53400	0
Cloisite 20A	1	760	45400	-15.0
	3	610	42900	-19.7
	5	585	42700	-20.0
Cloisite 30B	1	610	42400	-20.6
	3	280	34400	-35.6
	5	190	30700	-42.5
Cloisite Na^+	1	1090	50500	-5.43
	3	970	49200	-7.86
	5	810	47100	-11.8

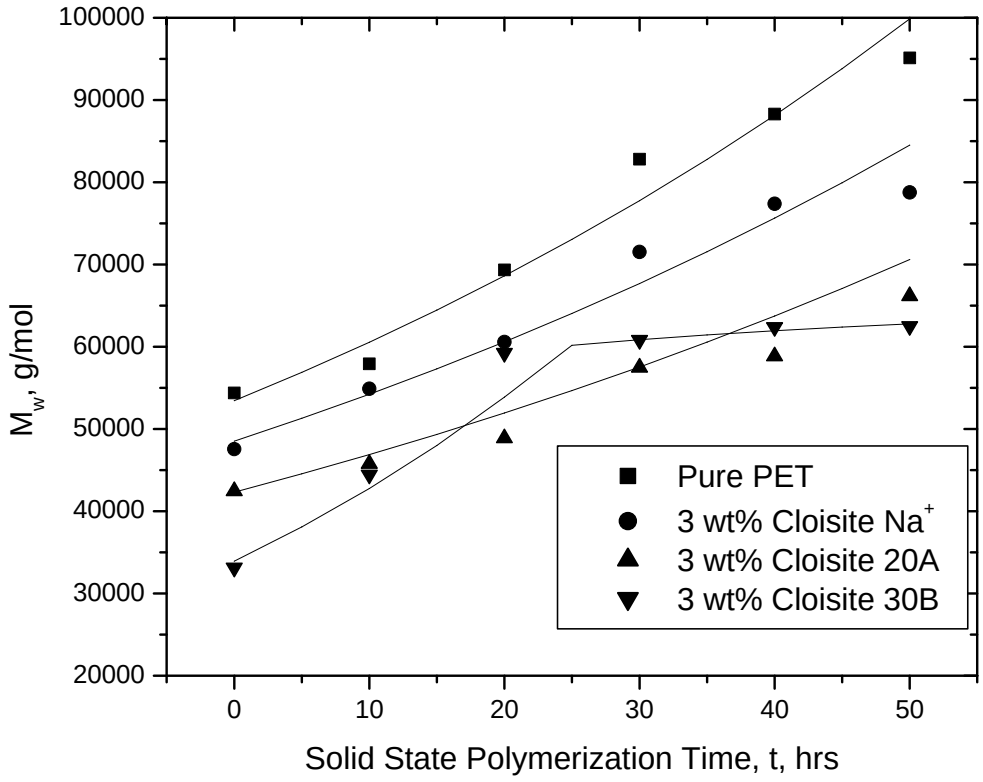

Fig. 3.2. Molecular weight as a function of solid state polymerization time for a nominal loading 3 wt% of various nanoclays.

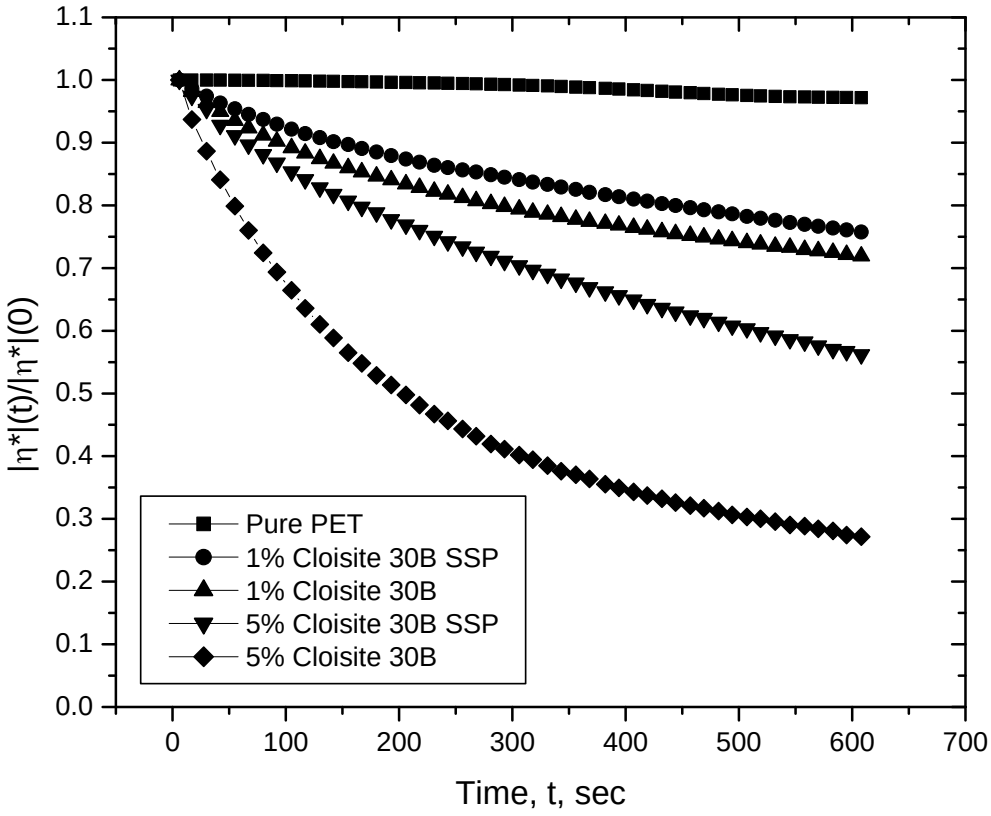

Fig. 3.3. Relative complex viscosity loss as a function of time for the Cloisite 30B series of nanocomposites with and without SSP.

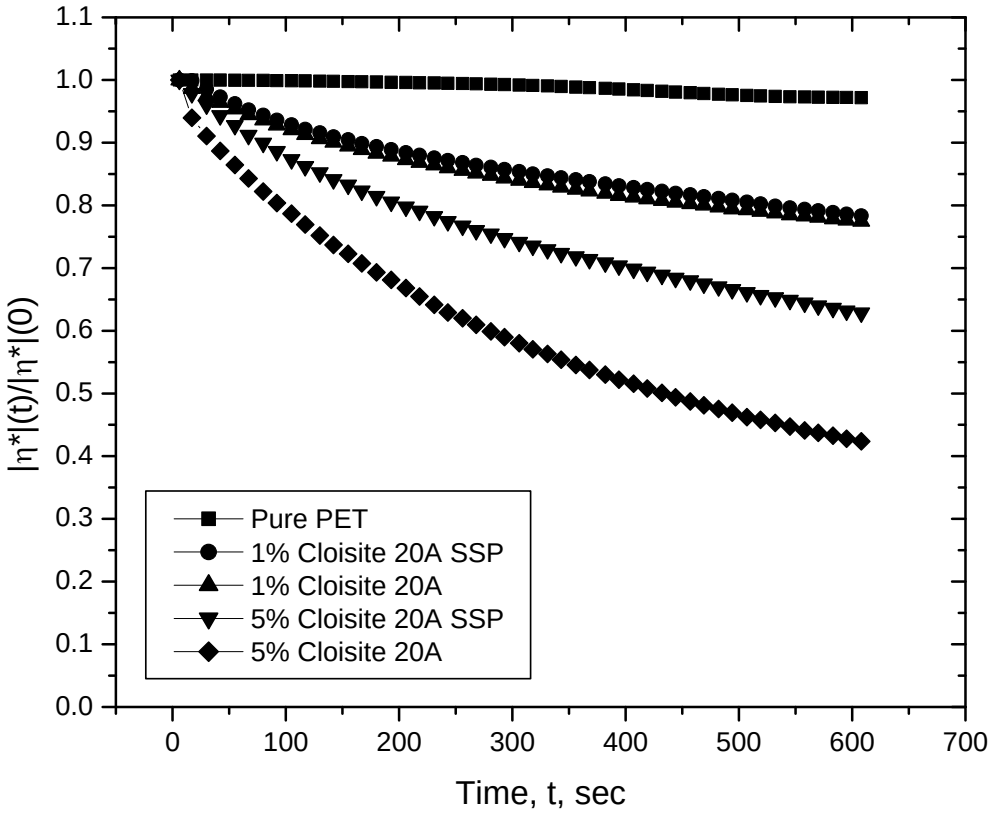

Fig. 3.4. Relative complex viscosity loss as a function of time for the Cloisite 20A series of nanocomposites with and without SSP.

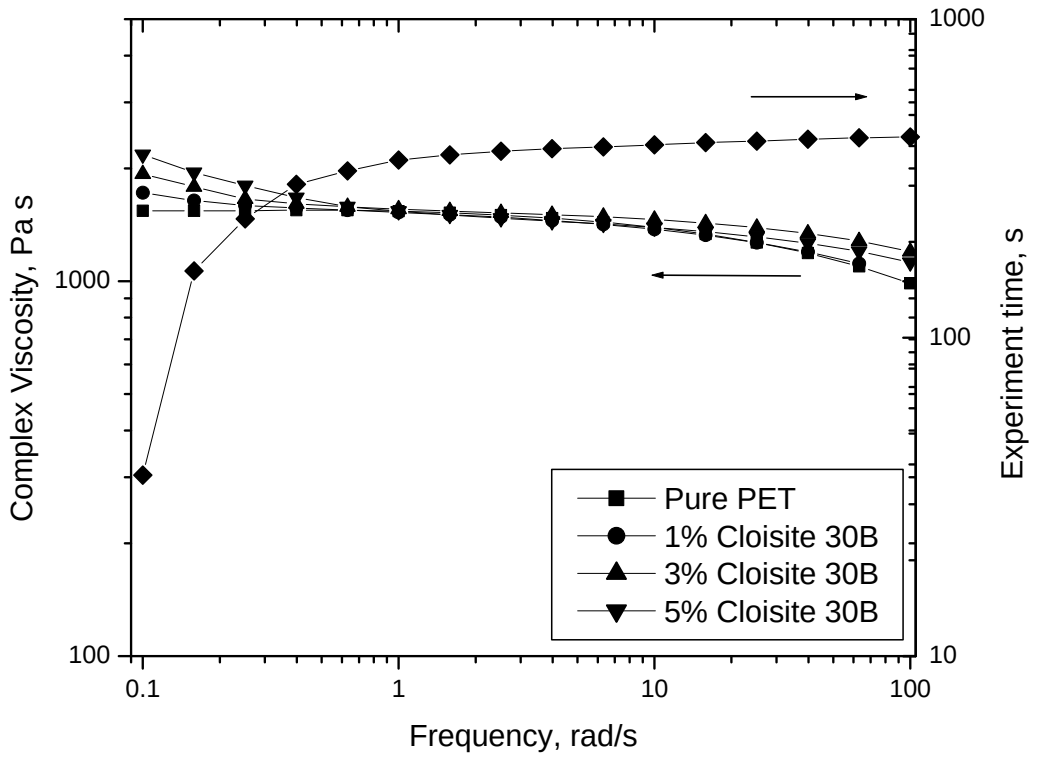

Fig. 3.5. (Left axis) complex viscosity, |η*| vs. frequency, ω for the melt-compounded Cloisite 30B nanocomposites after SSP and (right axis) experiment time elapsed for measurement of the respective data points.

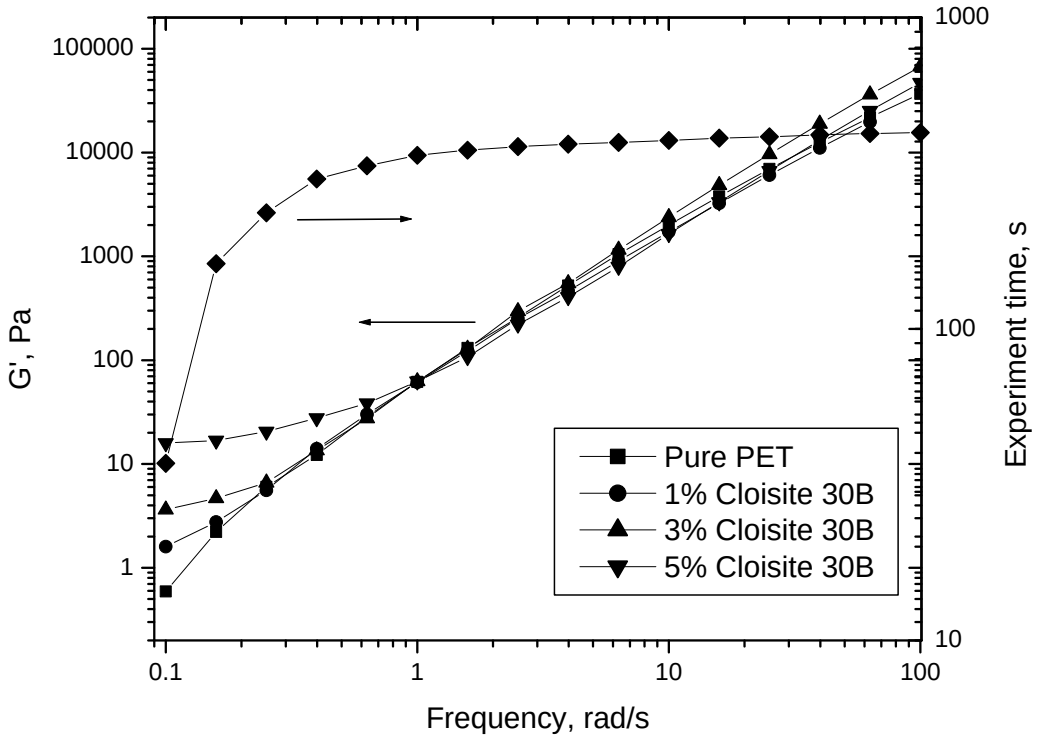

Fig. 3.6. (Left axis) storage modulus, G' vs. frequency, ω for the melt-compounded Cloisite 30B nanocomposites after SSP and (right axis) experiment time elapsed for measurement of the respective data points.

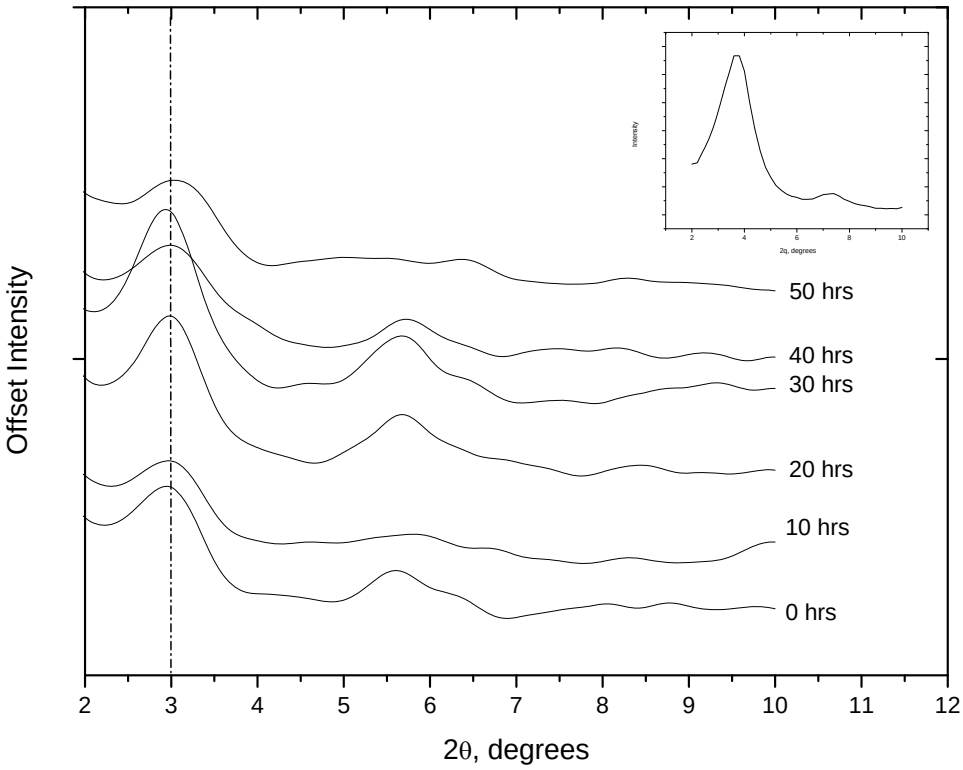

Fig. 3.7. X-ray diffraction spectra for a representative 3 wt% loading of Cloisite 20A in PET as a function of SSP time, scaled for clarity. Inset: XRD spectra of pure Cloisite 20A.

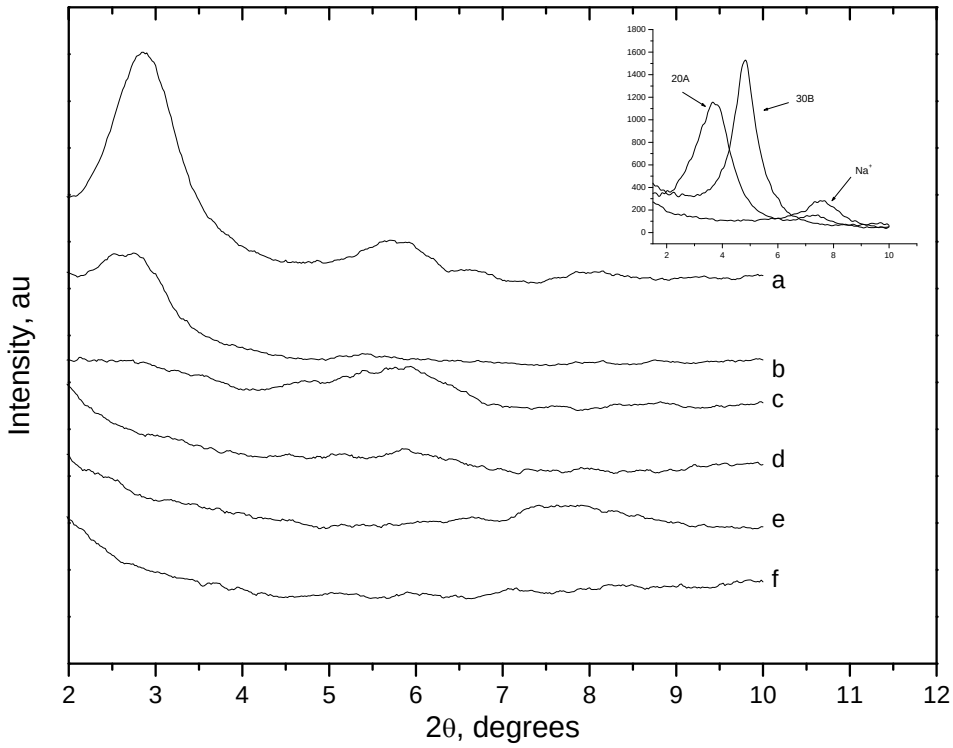

Fig. 3.8. XRD patterns for the as-spun, un-oriented nanocomposite fibers at 1 and 3 wt% loadings of various nanoclays, scaled for clarity. (a) 3wt% 20A, (b) 1 wt% 20A, (c) 3 wt% 30B, (d) 1 wt% 30B, (e) 3 wt% Na^+, (f) 1 wt% Na^+. Inset: XRD spectra of the pure nanoclays Cloisite 30B, 20A, and Na^+ as references for determining intercalation.

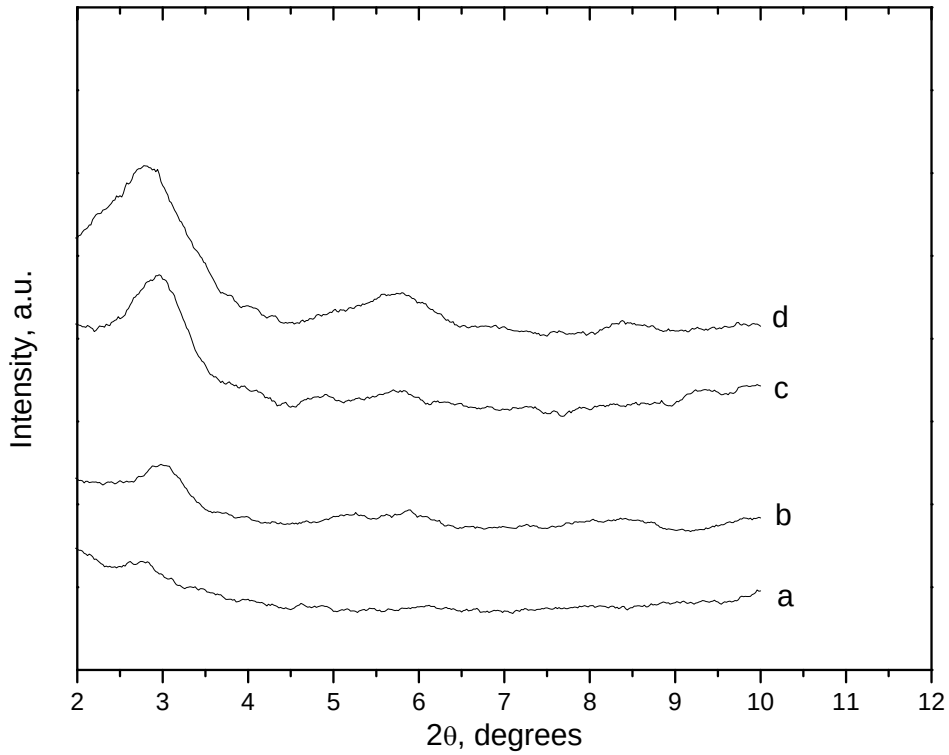

Fig. 3.9. XRD patterns for the drawn nanocomposite fibers at various loadings of Cloisite 20A, scaled for clarity. (a) Pure PET, (b) 0.5 wt% 20A, (c) 1 wt% 20A, (d) 3 wt% 20A.

Table 3.2. Tensile properties of as-spun (un-oriented) PET/MMT nanocomposite fibers with true clay content and molecular weight by intrinsic viscosity.

Clay Type	Nominal Loading	True Clay Content	M_w	Young's Modulus	Maximum Tenacity	Toughness	Elongation at Break
	wt%	wt%	g/mol	GPa	MPa	MPa	%
Pure PET	0.0	0.0	45800	2.00 ± 0.16	132 ± 5.4	197 ± 6.8	191 ± 8.9
Cloisite 20A	0.5	0.35	45800	1.48 ± 0.30	122 ± 2.7	262 ± 15	284 ± 5.9
	1.0	0.85	44900	1.65 ± 0.11	145 ± 5.4	277 ± 18	300 ± 3.1
	1.5	1.32	43200	1.81 ± 0.17	132 ± 2.7	235 ± 5.4	279 ± 10
	3.0	2.78	38800	1.47 ± 0.27	75.6 ± 5.4	190 ± 12	298 ± 19
Cloisite 30B	0.5	0.41	37900	1.57 ± 0.16	72.9 ± 4.1	269 ± 9.5	287 ± 12
	1.0	0.82	39700	1.66 ± 0.23	127 ± 2.2	236 ± 21	323 ± 26
	3.0	2.74	31400	1.51 ± 0.17	59.4 ± 1.4	170 ± 8.1	224 ± 14
Cloisite Na^+	1.0	0.81	50500	1.89 ± 0.15	77.0 ± 6.8	108 ± 12	154 ± 10
	3.0	2.69	49500	1.84 ± 0.15	101 ± 2.7	150 ± 5.4	51.4 ± 3.2

Table 3.3. Tensile properties of oriented PET/MMT nanocomposite fibers drawn in a second step above Tg.

Clay Type	Nominal Loading	Max. Draw Ratio	Denier per filament	Young's Modulus	Maximum Tenacity	Toughness	Elongation at Break
	wt%	A_o/A	dpf	GPa	MPa	MPa	%
Pure PET	0.0	2.5	6.3	9.92 ± 0.79	410 ± 18	36.4 ± 2.8	6 ± 0.5
Cloisite 20A	0.5	3.7	4.9	11.8 ± 0.45	590 ± 27	30.8 ± 2.8	5.6 ± 0.2
	1.0	3.5	5.2	12.7 ± 0.51	670 ± 20	29.4 ± 1.4	5.5 ± 0.2
	1.5	3.5	5.3	10.8 ± 0.67	539 ± 15	21.0 ± 1.4	5.1 ± 0.3
	3.0	3.6	4.7	9.32 ± 0.76	389 ± 10	18.2 ± 1.4	4.7 ± 0.3
Cloisite 30B	0.5	3.7	4.7	11.0 ± 1.0	327 ± 28	21.0 ± 1.4	4.6 ± 0.2
	1.0	3.2	5.2	10.3 ± 0.42	530 ± 21	32.0 ± 1.4	5.5 ± 0.1
	3.0	3.4	5.2	8.60 ± 1.0	262 ± 11	25.2 ± 2.8	4.6 ± 0.3
Cloisite Na^+	1.0	1.9	9.0	8.38 ± 0.35	251 ± 20	15.4 ± 5.6	5.1 ± 2.3
	3.0	2.2	7.6	8.54 ± 0.78	302 ± 14	19.6 ± 1.4	5.5 ± 0.7

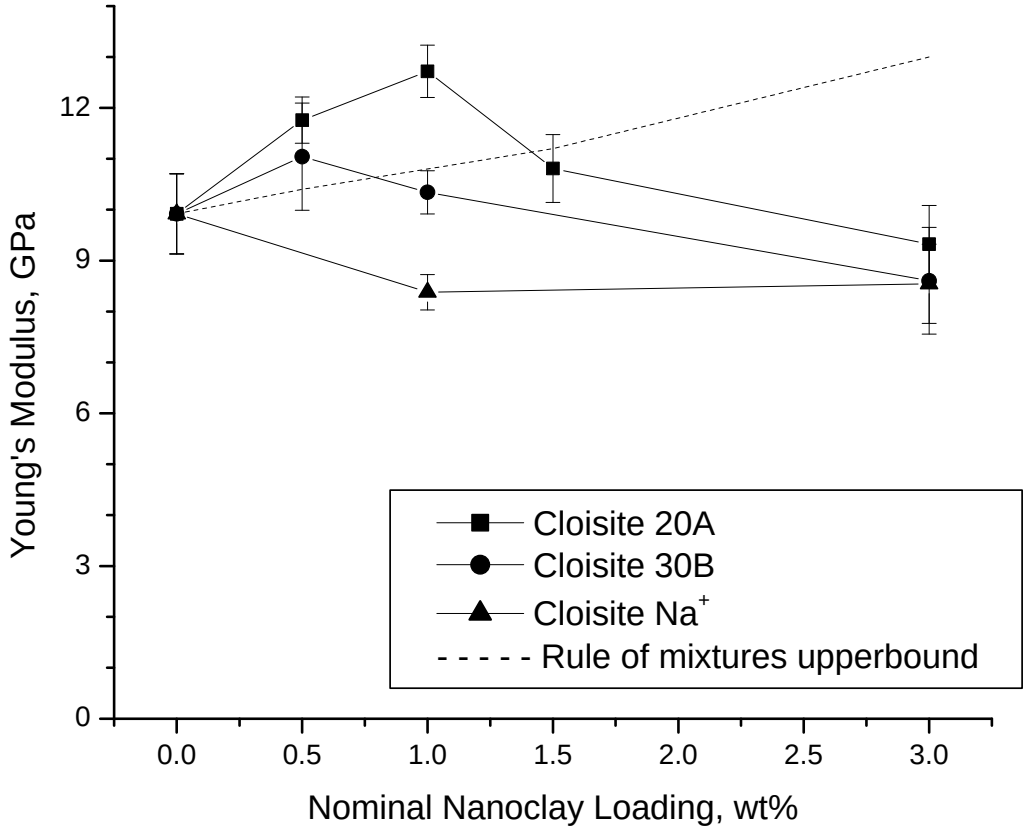

Fig. 3.10. Young's modulus of the drawn nanocomposite fibers as a function of nanoclay loading weight % for the different nanoclay surface treatments compared to a simple rule of mixtures estimate.

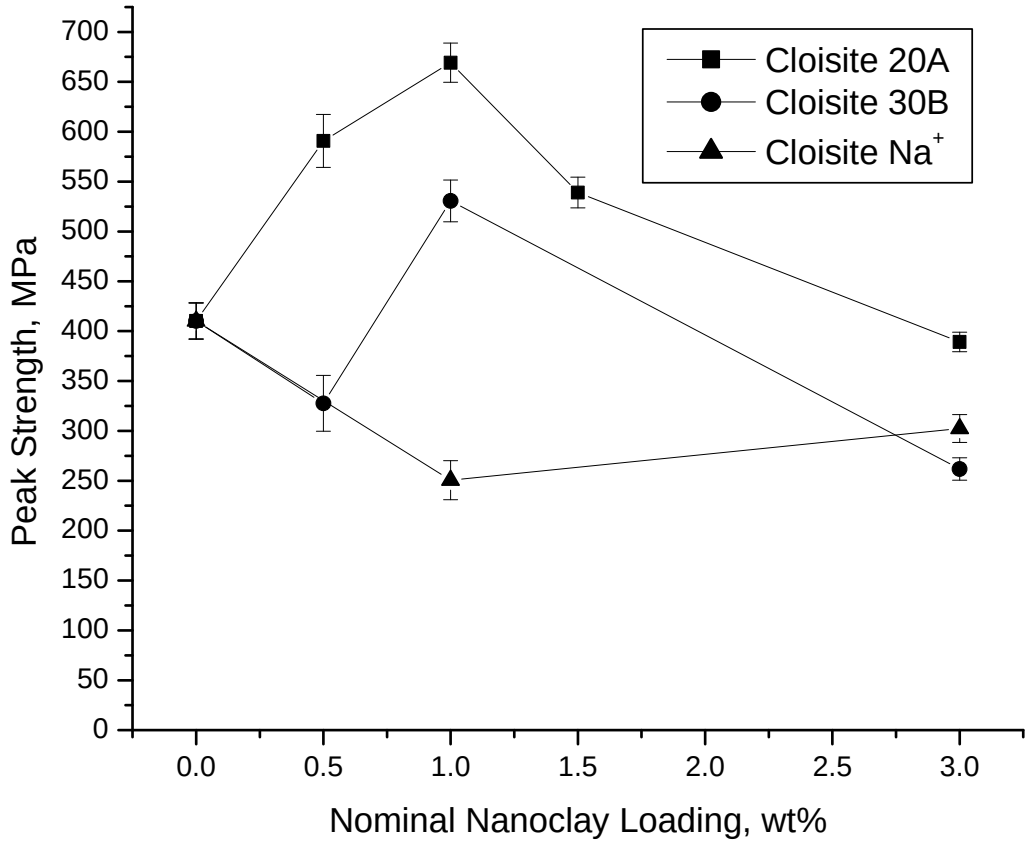

Fig. 3.11. Drawn fiber strength at maximum load versus nanoclay concentration in weight % for the various nanoclay surface treatments.

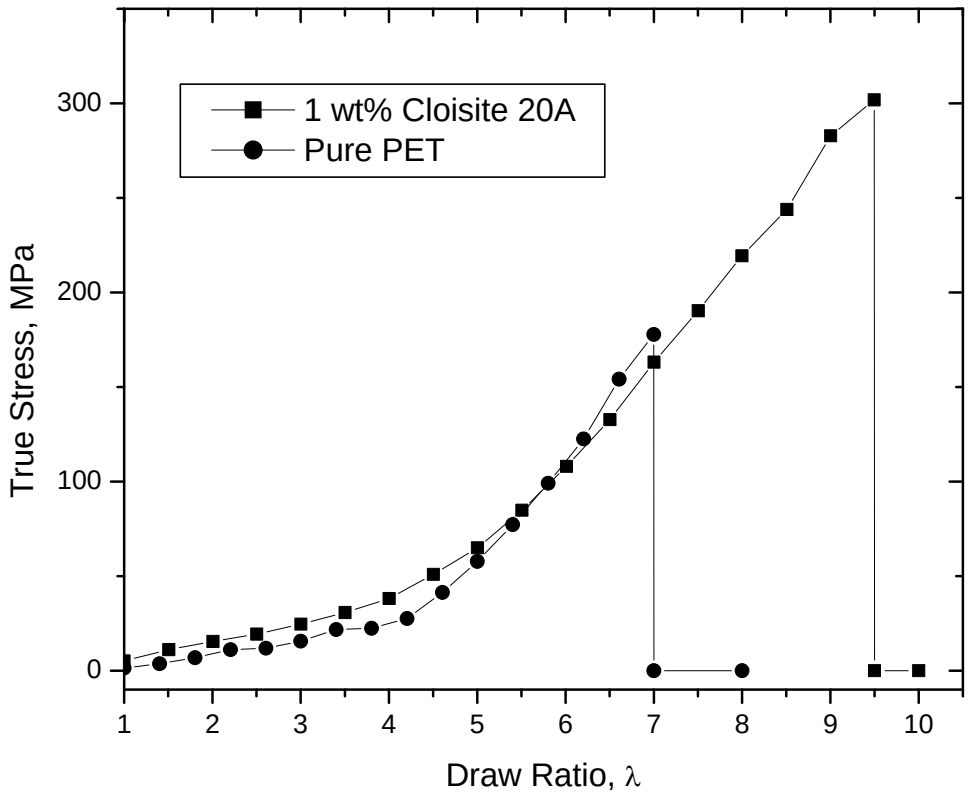

Fig. 3.12. True stress versus draw ratio of pure PET and a 1 wt% loading of Cloisite 20A at a draw temperature of 85 °C.

4.0 The Role of Nano-clay in the Generation of Poly(ethylene terephthalate) Fibers with Improved Modulus and Tenacity

David W. Litchfield and Donald G. Baird
Department of Chemical Engineering, Virginia Polytechnic Institute and State University, Blacksburg, Virginia 24061

ABSTRACT

The effect of nanoclay concentration on the molecular orientation and drawability of poly(ethylene terephthalate) PET was examined using thermal and vibrational spectroscopic analysis. Although drawability at 83 °C in hot air increased by the addition of nanoclay, the maximum draw ratio was independent of nanoclay concentration. The average molecular orientation of the PET chain was found to mimic the trend in mechanical property improvements found earlier. Both Young's modulus and tenacity (i.e. strength) showed the maximum improvement at a 1 wt% loading of clay, which was shown to coincide with the maximum amount of molecular orientation. Nanoclay was shown to intercalate with PET and enhance amorphous orientation that led to modulus and strength improvements. However, at higher concentrations of nanoclay the presence of large agglomerates prevented efficient orientation along the fiber axis and acted as stress concentrators to aid in cavitation and failure during testing. Raman spectroscopy showed that the as-spun unfilled PET fibers possessed significantly more trans conformer content of the ethylene glycol moiety than the nanocomposite fibers. The greater gauche content of the nanocomposite fibers delayed crystalline development as observed during non-isothermal DSC scans to higher temperatures and this delay in crystallization was believed to be associated with the increased drawability during fiber processing.

4.1 INTRODUCTION

The benefits of using layered silicate nanoparticles "nanoclays" for improving the physical, chemical, and mechanical properties of homogenous polymers have been shown by many studies [1-6] and reviewed by several authors [7-12]. These disk-shaped nanoparticles present a distinct advantage because significantly lower volume fractions are required to produce equal bulk property improvements when compared to conventional fillers (i.e. glass fibers, talc, etc.) [13]. The high specific surface area of nanoclay, due to its nanometer size and high aspect ratio, provides an increased number of polymer-particle and particle-particle interactions relative to conventional fillers. Maximum property improvements are believed to be obtained when the nanoparticles are uniformly dispersed into their individual sheets within the polymer matrix. Improvements in mechanical properties, for instance, have been widely cited for a number of polymer-nanoclay injection molded and, more recently, melt-spun fiber systems [9].

Several authors have reported the spinnability and mechanical properties of melt-spun nanocomposite fibers from polymer matrices of polypropylene [14, 15], polyamide [16, 17], and aromatic polyesters [18-24]. Nanocomposite fibers spun from isotactic polypropylene showed a significant reduction in tensile strength with increasing nanoclay concentration [14, 15]. Using microscopy and thermal shrinkage measurements, the decrease in tensile strength was attributed to a loss of in molecular orientation caused by crystallite growth perpendicular to the fiber axis during drawing [14, 15]. Giza et al. [16] and Ibanes et al.[17] examined the effect of nanoclay on mechanical properties of polyamide-6 fibers with

spinning speed and draw ratio, respectively. Values of modulus and tenacity were shown to increase with nanoclay concentration and spinning speed up to the onset of stress-induced crystallization [16]. Increasing the spinning speed beyond the point of stress induced crystallization produced nanocomposite fibers with enhanced modulus but with reduced tenacity compared to unfilled polyamide-6 [16].

Ibanes et al. [17] showed that a 1 wt% loading of nanoclay in polyamide-6 fiber, spun to an un-oriented state and subsequently drawn above the glass transition, produced nanocomposite fibers with improved drawability. The tenacity and crystal orientation of the nanocomposite fibers were significantly increased relative to unfilled polyamide-6 fibers when drawn to their maximum draw ratios [17]. These authors showed little improvement in nanocomposite fiber modulus and concluded that the nanoclay used did not interact favorably and couple with the oriented polyamide matrix. In addition, Ibanes et al. [17] did not examine the effect of nanoclay concentration on the degree of drawability or mechanical property improvement.

Until recently [24] research on polyester nanocomposite fibers focused on modulus and tenacity improvements with spinning speed [18] or spinning speeds in the form of draw down ratios [19-23] and not on the effect of second step draw. McConnell et al. [18] showed that increasing the spinning speed enhanced both modulus and tenacity of poly(ethylene terephthalate) (PET) fibers at a given nanoclay loading and with a specific surfactant type. Chang et al. [19-23] examined several polyester nanocomposite systems at various draw down ratios from the spinneret. PET fibers filled with organically modified montmorillonite showed a decrease in modulus and tenacity with increasing draw down ratio, but the fiber properties improved overall with nanoclay addition at constant draw

down [21]. In a more recent study, Chang et al. [23] found that modulus and tenacity were optimal at a 1 wt% addition of organically modified mica, but these properties were nearly independent of draw down ratio. The as-spun nanocomposite and pure PET fibers showed very low elongations at break (~3%) during loading at room temperature. In addition, the current literature [18, 21, 23] focusing on as-spun polyester nanocomposite fibers has shown modulus and tenacity values insufficient for industrial applications.

In our previous work [24], we reported good spinnability of nanocomposite fibers with alkyl surface-modified montmorillonite nanoclay concentrations below 5 wt%. Furthermore, significant increases were observed at low loadings of nanoclay in the modulus and tenacity of the nanocomposite fibers after drawing in a second step [24]. Table 4.1 summarizes the mechanical property improvements obtained from our previous study. For nanoclay loadings up to 1 wt%, the modulus improvement of the drawn nanocomposite fibers was observed to be much greater than a rule of mixtures prediction, which has not been reported in the prior nanocomposite fiber literature. As well, the tenacity of the nanocomposite fibers reached a maximum at the 1 wt% loading and was 66% greater than the tenacity of the unfilled PET fiber. Therefore, it was concluded that the PET phases in the neat and nanoparticle filled fibers possessed different morphologies. Additionally, the nanocomposite fibers showed increased drawability over the pure PET fiber. These observations were considerably different from those of previous authors examining PET nanocomposite fibers [18, 21, 23]. We concluded that solid state polymerization of the melt-compounded PET nanocomposites provides a means of keeping the molecular weight high enough to sustain axial loading over a higher degree

of strain. Therefore, in the nanoclay filled fibers the orientation of the polymer chains was believed to be enhanced relative to unfilled PET.

The current literature on PET nanocomposite fibers has not fully explained the microstructure of these systems. Several authors [18, 25-29] have cited that nanoclays act as nucleating agents in PET, and those examining PET fibers have shown that nanoclay addition increases the degree of crystallinity of as-spun filaments [18]. Although some authors have reported property improvements, no studies of PET nanocomposite fibers have reported the effect of nanoclay on molecular orientation [18, 21, 23]. It is well known that increases in fiber tenacity depend upon the degree of orientation of the polymer chains, while the modulus of the fiber relies upon the degree of crystallinity and amorphous orientation [30]. Therefore, a complete understanding of the mechanism behind the property improvements attained with nanoclays requires knowledge of the inter-play between the four phases involved: the rigid nanoclays and the three phases of PET (crystalline, oriented-amorphous, and purely amorphous).

This work evaluates the role of nanoclay in creating property improvements in PET nanocomposite fibers after drawing in a second step above the glass transition temperature. In particular, this work examines how the presence of nanoclay leads to greater drawability and molecular orientation of the PET phase, and then correlates these observations to the improvements in mechanical properties. Wide angle X-ray (XRD) measurements were made to discern the effect of nanoclay dispersion on final nanocomposite properties. Thermal analysis by differential scanning calorimetry (DSC) and thermal shrinkage measurements was used to probe the effects of nanoclay on crystallinity and amorphous orientation, respectively. Raman spectroscopy was used to

examine the changes in molecular conformations (i.e. gauche-trans isomerism) and also to study the changes in orientation of the PET backbone as a function of draw.

4.2 EXPERIMENTAL

4.2.1 Materials

The poly(ethylene terephthalate) used in this study had an intrinsic viscosity of 0.96 dl/g and was suitable for tire-cord applications. Surface modified montmorillonite nanoclay Cloisite 20A was obtained from Southern Clay Products Inc (Gonzalez, TX) and used without further modification. The surface modified clays are produced commercially by the substitution of interlayer sodium cations by dimethyl, dehydrogenated tallow quaternary ammonium cations.

4.2.2 Melt-Compounding, Fiber Spinning, and Fiber Drawing

The production of the PET nanocomposite fibers was described in our previous work [24, 31]. It is important to reiterate that the fiber spinning and drawing steps were performed separately in this work, but within a reasonable time frame to avoid complexity with physical aging. The draw oven was set to raise the temperature of the filaments to 83 °C, just above the glass transition temperature of PET. Maximum draw ratios were determined by increasing the speed ratio of the godets and observing the onset

of fiber fraying (i.e. filament mechanical failure), upon which the speed was reduced slightly.

4.2.3 Characterization

The tensile properties of the nanocomposite fibers were determined using an Instron 4204 Universal Testing Machine at room temperature and humidity. A crosshead speed of 30 cm/min was used for testing the drawn fibers at a gauge length of 25.4 cm. For the un-oriented fibers, gauge lengths of 7.62 cm and crosshead speeds of 9.0 cm/min were used. Reported values are averages of 8 samples with uncertainties corresponding to 95% confidence limits.

The morphology of the nanoclay within the PET nanocomposites was determined using wide angle X-ray diffraction (XRD) and scanning electron microscopy (SEM). XRD patterns were obtained using a Scintag XDS 2000 diffractometer with Cu K radiation at a wavelength of 1.54 Å with a scan rate of 0.5°/min from 1.5 to 10°. This study was not immediately focused on complete exfoliation of the nanoparticles, and thus transmission electron images of the nanocomposite were not taken for the specimens showing little to no peak in the XRD pattern. SEM images were taken using a LEO (Zeiss) 1550 high-performance Schottky field-emission SEM

The crystallization and melting behaviors were determined by rheology using a Rheometric Mechanical Spectrometer (RMS-800) and by differential scanning calorimetry (DSC) using a TA Instruments Q1000 thermal analyzer, respectively. Rheological “cooling curves” were obtained by reducing the temperature of the

nanocomposite melt at a rate of 40 °C/min and recording the storage modulus, G'. A 25 mm cone and plate geometry was used with an inert atmosphere. Samples were dried for 24 hrs at 120 °C prior to testing. The DSC was calibrated using sapphire and indium standards. Test specimens of about 10 mg were cut and sealed in hermetic aluminum pans. All tests were carried out under a nitrogen atmosphere. Samples were heated from 40 °C to 290 °C, equilibrated for 5 minutes and cooled back to 40 °C, and then reheated to 290 °C. The heating and cooling rates were set at 20 °C/min. The degree of crystallinity was calculated under the assumption that the heat of fusion is proportional to the crystalline content, as shown in Eq. 1

$$\chi = \frac{\Delta H_f}{\Delta H_f^o \left(1 - w_{clay}\right)} \qquad \text{(Eq. 1)}$$

where ΔH_f is the enthalpy of fusion of the sample, ΔH_f^o is the enthalpy of fusion of a completely crystalline sample and taken in this work as 140 J/g [32], and w_{clay} is the weight fraction of nanoclay in the nanocomposite fiber.

Thermal shrinkage measurements of the drawn nanocomposite fibers were obtained according to ASTM D4974-04 at 177 °C using 0.009 grams per filament tex. The reported values are an average of 8 tests with uncertainties corresponding to 95% confidence limits.

Polarized Raman spectra were collected from a JY Horiba LabRam HR spectrometer, with 600 groves/mm gratings and a slit width of 80 μm. Excitation was provided by a 632.8 nm Laser Physics 100S-632 Ne laser. The laser was focused through

a 40x objective on single filaments glued across the openings of 3/8 inch steel washers. Less than 10 mW of laser light was focused on the filaments. The detector was an electronically cooled open electrode CCD. Spectra were obtained from the samples in different geometrical arrangements using a rotating stage. In order to calculate the molecular orientation parameters, similar procedures of Lesko et al. [33] were followed. The detailed theory behind the determination of the molecular orientation parameters using polarized Raman spectroscopy is described elsewhere [33-37]. For the comparison of conformational isomers (*gauche* and *trans* content), the spectral bands were analyzed with the polarized light and fiber length arranged in parallel. Data analysis and peak fitting was done by using OriginPro v.8 (OriginLab) with embedded Gauss-Lorentz functions to deconvolute multiple peak bands and to determine the band full-width at half maximum (fwhm), peak center, and area. Accordingly, the area under the band was taken as the band intensity [35].

4.3 RESULTS AND DISCUSSION

4.3.1 Nanoparticle Morphology

The wide angle X-ray diffraction (XRD) spectra of the series of as-spun PET nanocomposite fibers are shown in Fig. 4.1. The inset in Fig. 4.1 shows the pattern of pure Cloisite 20A as a reference for peaks 2θ of 3.7°, corresponding to the inter-particle distance of organically modified clay, d_{001} or the "d-spacing", and 2θ of 7.3°, corresponding to a secondary peak, d_{002} [38]. The d-spacing from Bragg's law ($d_{001}=\lambda/2 \sin$

θ), which corresponds to the interparticle distance, was shown to be 2.42 nm for the pure 20A nanoclay. For the as-spun fiber with various loadings of nanoclay, the peak height is very weak at low loadings. The peak position is shifted to slightly lower angles indicating that intercalation of PET into the nanoclay layers has occurred and the inter-particle distance has increased. For nanoclay loadings below 3 wt%, the as-spun peak height is significantly suppressed, which implies that the number of agglomerates in the system is low. At 3 wt%, the large peak shows a pronounced number of aggregated nanoparticles in this fiber.

Fig. 4.2 shows the nanoparticle morphologies in the drawn fiber for various concentrations of 20A. Comparing the un-oriented and oriented fibers, the peak positions have been shifted to slightly higher angles and peak heights have been reduced. This indicates that drawing the nanoparticle fibers leads to a collapse in inter-particle distance. This collapse is suspected to be due to the reorganization of amorphous, coiled polymer chains to oriented, extended chain crystallites. Although it appears that the particle spacings have collapsed, the number of stacked particles as agglomerates in the drawn nanocomposite fibers has decreased compared to the as-spun fibers. Thus, drawing has increased the aspect ratio of the stacks of nanoparticles and sheared the stacked agglomerates, so that the overlap of silicate layers has been reduced. Fig. 4.2 shows that the 1 wt% Cloisite 20A fiber undergoes the largest amount of collapse (~0.6 nm) compared to the 0.5, 1.5, and 3 wt% fibers after drawing. The number of agglomerated overlapping stacks increases monotonically with nanoclay concentration up to 3 wt%.

Scanning electron images of individual filament surfaces at the 3 wt% loading in the as-spun and drawn states are shown in Fig. 4.3a and 4.3b respectively. Although the

majority of the filament surface looks relatively smooth, as shown in Fig. 4.3c, distortions in the filament surface are observed every meter or so in the as-spun fiber at high loadings of nanoclay, and these are believed to be large agglomerates of nanoparticles. Interestingly, both operations of fiber spinning from the melt and fiber drawing in the solid state are not significantly disrupted by the presence of these distortions. Comparing Fig. 4.3a to 4.3b, it appears that drawing may elongate the agglomerates giving further support to the conclusions deduced from the XRD studies. However, from the standpoint of mechanical reinforcement, these elongated large agglomerates of nanoclay, seen only at the higher concentrations, are believed to act as points of stress concentration and may lead to premature failure of the PET fiber. Yet, this does not explain for the increased drawability of these nanocomposites and a further examination into the morphology of the PET microstructure is given below.

4.3.2 Thermal Behavior

The ability to draw PET nanocomposites may depend upon the degree of crystallinity among other factors. DSC and rheological measurements were carried out to understand the role of 20A concentration on the crystallization process. Fig. 4.4 shows the DSC cooling behavior of PET nanocomposite melts at 20 °C/min. The 1.5 wt% sample has been omitted for clarity. Similar to other reports on the crystallization of PET nanocomposites [26, 28, 29], the presence of nanoclay increases the temperature for the onset of crystallization and peak crystallization temperature relative to pure PET. However, it is clear that the addition of nanoclay has a limited effect. The onset of crystallization

from the melt is increased by 3 °C at 0.5 wt% and by of 5 °C at 1 wt% 20A, but at 3 wt% the shift in temperature has been reduced to 2 °C.

A similar but more significant trend is observed in the rheological cooling of the PET nanocomposite chips. Fig. 4.5 shows the build in complex viscosity, η^*, with temperature as the melt is cooled from the equilibrium melt temperature. The difference in the temperatures for the onset of crystallization is accentuated compared to the DSC measurement on the same nanocomposites. The onset of solidification is shifted 20 °C higher for the 1 wt% sample than the solidification temperatures of the other nanocomposites. It then appears by the rise in viscosity that the nanoparticles are immobilizing the polymer chains in the melt at higher temperatures. The nanoparticles themselves may also act as nucleating agents as cited by many authors [18, 25-29].

Crystallization rates of two materials are typically compared by their time to reach 50% of the relative crystallinity, $t_{1/2}$ [39]. From non-isothermal measurements, such as those by DSC, the relative rate of crystallization may be determined by using Eq. 2 to define the relative degree of crystallinity, X, with temperature and by converting to the time domain through the cooling rate [40].

$$X = \int_{T_0}^{T} q dT \Big/ \int_{T_0}^{T_\infty} q dT \qquad \text{(Eq. 2)}$$

where T_0 and T_∞ are the onset and end of crystallization temperatures, respectively, and q is the heat flow at temperature T. Fig. 4.6 shows the difference in crystallization rates during non-isothermal cooling for the PET and PET nanocomposites. Interestingly, although the onset temperatures depend on the concentration of nanoparticles, the

crystallization half times of the nanocomposites are independent of nanoclay loading. Additionally, the rate of crystallization is shown to improve when compared to the pure PET. Therefore, in terms of forming PET nanocomposites through non-isothermal processing operations, the degree of crystallinity in the nanocomposite samples is expected to be greater.

In our crystallization studies from the glassy state, e.g. when using the as-spun fiber, nanoparticles are not shown to induce crystallinity. In fact, Fig. 4.7 shows that the presence of nanoclay raises the non-isothermal crystallization of PET to higher temperatures. The onset of cold crystallization is shifted to higher temperatures in the nanocomposites. In the case of 0.5 and 3 wt% 20A the onset is 18 °C higher and at 1 wt% the onset temperature is 15 °C greater than that of the pure as-spun fiber. Although, the spinning speed for every sample was 550 m/min, it is believed that the pure fibers have some greater degree of pre-orientation or crystallinity that would nucleate cold crystallization at much lower temperatures than the nanocomposite samples. Yet, the non-isothermal crystallization rate, shown in Fig. 4.8, from the glassy state depends on the concentration of nanoclay. In the cases of the nanoclay filled materials, cold crystallization progresses faster than the pure PET sample. Therefore, the crystal growth rate is accelerated by the presence of nanoclay and shifted to higher temperatures. The melting behavior of the as-spun nanocomposites and pure PET fibers are nearly equivalent with a slight shift (+2 °C) of the melting peak with the presence of nanoclay. In addition, within error the addition of nanoclay shows no significant effect on the glass transition, T_g, temperatures of PET, shown in Fig. 4.7 as 75 °C.

In the case of the drawn nanocomposite fibers, the thermal behavior during melting differs in the initial heat and repeated heating scans. Shown in Fig. 4.9 is the representative behavior during melting of the drawn pure PET, 1 wt%, and 3 wt% nanocomposite fibers. In the initial heating scan, the melting endotherms display shoulders at lower and higher temperature than the peak melting temperature reflecting a distribution of polymorphic crystalline structures in the fibers. The difference between the melting peaks of the 1st and 2nd heating scans decreases with increasing nanoclay concentration, possibly reflecting the reduced extended chain crystalline morphology as nanoparticle concentration increases. PET crystallites at high loadings of nanoclay have a more chain folded structure, although DSC measurements alone cannot confirm this.

By comparison of the melting enthalpy to the cold crystallization enthalpy in the drawn and as-spun cases, the degree of crystallinity, x_c, can be determined with nanoclay concentration. Table 4.2 shows that indeed the nanocomposite fibers have lower degrees of crystallinity than the pure PET fiber in the as-spun and drawn states. During melt spinning, the presence of the nanoclays alter the chain conformation of the PET chains either through particle-matrix interactions or through winding speed suppression due to the nanoclays ability to dissipate some of the deformational energy in the spin-line. From the melt, the nanoclay particles form a temporary network structure with the PET chains preventing the development of crystalline order and amorphous orientation. The result of this type of interaction would also postpone stress-induced crystallization permitting the achievement of greater drawability.

In terms of mechanical property improvements, the degree of crystallinity of the nanocomposites, as well as filler content, contribute to the level of stiffness. Table 4.2

shows that the drawn nanocomposite fibers have lower crystalline contents than the drawn pure PET fiber. Therefore, the observed improvement in Young's modulus as a function of nanoclay loading cannot be determined from crystallization data alone.

Thermal shrinkage experiments provide qualitative information on the degree of amorphous orientation in the PET and nanocomposite fibers [30]. The degree of thermal shrinkage expressed as the percent change in length of the filament after heating to 177 °C is shown in Fig. 4.10 for the drawn fibers. The addition of very low concentrations of nanoclay increases the degree of thermal shrinkage by 5% when the fibers have been drawn in a second step. Further addition of nanoclay has less of an effect, and at high loadings the degree of shrinkage is equivalent to that of pure PET fiber. Fiber strength and tenacity are dependent on the degree of molecular orientation [30], and the improvements observed here are qualitatively linked to the increased amorphous orientation (i.e. greater thermal shrinkage).

4.3.3 Molecular Orientation and Mechanical Property Improvement

Vibrational spectroscopic techniques are widely used non-destructive methods for the chemical and physical analysis of polymer molecules. Scattering methods, such as polarized Raman Spectroscopy, are powerful methods useful for determining molecular conformations, type and concentration of covalent bonding, and molecular orientation of the polymer chain [41]. In brief, Raman scattering is the inelastic scattering of infrared light by a molecule upon returning to its lower energy level after an excitation. As the frequency of light is changed, various Raman active groups within the polymer sample

vibrate and scatter light to produce bands of various intensity. When the light is polarized to a preferred direction of the electric field, an induced dipole moment in the molecule can occur. The interference of the scatter light with the incident polarized beam is analyzed to collect information on the orientation of these groups, for example with respect to the fiber axis. The theory of vibrational spectroscopy of PET has been outlined in more detail by Bower [41] and others [33-35], and the advantages of using polarized Raman spectroscopy versus alternatives such as infrared, x-ray, and birefringence has been summarized by Tanaka and Young [36].

The Raman spectra of the as-spun PET nanocomposite fibers at 0, 1, and 3 wt% of alkyl modified nanoclay are shown in Fig. 4.11 for the range of 250-3250 cm^{-1}. The filaments are arranged parallel to the polarized light in this figure. Raman bands of interest for orientation or molecular conformation in as-spun and oriented pure PET are located at 998, 1095, 1130, 1180, 1281, 1310, 1616, and 1730 cm^{-1}. These bands and others have been assigned by Stokr [42] and others [43] and are summarized in Table 4.3. As well, montmorillonite, MMT, has its own vibrational spectrum [44]. Characteristic bands for Na^{+} MMT are mainly those related to Si–O vibrations and are located at 450, 710, 1100 cm^{-1} [44]. In Fig. 4.11b and c the bands at 1100 and 450 cm^{-1} are not present in the nanocomposite samples, and both the MMT SiO_4 tetrahedron and the PET C–C ring stretch contribute to the 700-710 cm^{-1} band. Yet, the number of scatterering elements in Raman spectroscopy is linearly proportional to the intensity of the band [41]. At the low weight fractions of nanoclay used in this study ($\leq$ 3%), the contribution of montmorillonite to the observed spectrum can be considered insignificant. Furthermore,

Frost and Rintoul [44] observed that Raman spectra of MMT are difficult to obtain if the layers are dispersed or randomized in their spacing.

Nevertheless, the molecular conformations and orientation of the PET phase can be determined. Fig. 4.12 shows, by observation of the 1616 cm^{-1} band (phenylene ring stretch) in parallel and perpendicular arrangements to the polarized light, the absence of anisotropy from the as-spun 1 wt% 20A nanocomposite fibers and the presence of significant anisotropy in the drawn state of the same fiber. The drawn fibers thus show molecular orientation of the PET backbone along the fiber axis. The 1616 cm^{-1} band has been shown to be much less sensitive to changes in chain conformation (i.e. crystallinity), making it ideal for studying molecular deformation [43]. In addition when comparing Fig 4.12a to b, the *trans* conformation of the ethylene glycol segments at 998 cm^{-1} shows anisotropy, indicating there is some preferred crystalline orientation [35]. Discussed below, ideal crystallization converts gauche isomers to the all-trans conformation of the ethylene glycol moieties of the PET backbone [35]. The all-trans conformation of both the ethylene glycol and terephthalate units has been linked with the fully extended chain morphology that is desirable for high performance PET fibers.

The molecular orientation coefficients determined from the second order Legendre polynomial (i.e. Hermans orientation function [36]), f_{1616} and f_{998}, of the system average backbone and ethylene glycol units, respectively, are shown in Fig. 4.13 for the as-spun and drawn nanocomposite fibers. f_{1616} and f_{998} are determined directly from the solution of the coupled non-linear algebraic equations outlined by Lesko et al. [33] and Yang and Michielsen [35] using 5 geometrical arrangements of the sample with respect to the incident polarized light. In the as-spun state, the average molecular orientation of the

PET backbone is low, which is expected considering the relatively low winding speeds used during melt spinning. The nanocomposites do not possess a significant band at 998 cm^{-1} in the as-spun state and orientation coefficients calculated had large errors due to poor signal to noise resolution in our best spectra and is not displayed in Fig. 4.13. The drawn fiber backbone orientation coefficients show significant dependence on concentration of nanoclay. Both measures of orientation for the drawn fibers follow the trends in modulus and tenacity improvement with a maximum at 1 wt% of nanoclay. Beyond this loading, the orientation of the backbone and the crystalline units decreases with increasing nanoclay concentration. Yet, the reduction in crystal orientation is not as significant as that of the backbone. Therefore, low loadings of nanoclay may aid in the development of ordered polymer structures parallel to the fiber axis. High loadings of may disrupt the long-range order because the polymer chains must organize themselves around a larger number of rigid particles. At low concentrations of nanoclay, the full benefit to orientation is not realized, as less nanoclay is available. Above the optimum nanoclay concentration, the reduced molecular orientation combined with the increased number of agglomerates that contribute to stress concentration reduces the fiber modulus and tenacity.

The orientation parameters observed in this study are relatively low compared to high performance PET fibers and are most likely due to the low drawing speeds (~10 m/min). At low speeds, stress on the fiber is low and the development of stress induced crystallization is delayed or absent. However, DSC measurements show the degree of crystallinity in the drawn fibers to be relatively high ~40%. Yet, DSC overestimates the degree of crystallinity because the oriented amorphous chains act as a precursor to

thermal crystallization, as evidenced by the observation of thermal shrinkage. Through Raman spectroscopy, the carbonyl stretching band at 1727 cm^{-1} has been associated with sample density and crystallinity [33, 45]. Fig. 4.14 shows that after drawing the full width at half maximum, fwhm, (i.e. the fiber density) changes relatively little with respect to the as-spun fibers. Higher densities are associated with lower fwhm values and a corresponding shift in the peak to lower frequencies [45]. The 1727 cm^{-1} band has been regarded to provide insight into the conformation of the terephthalate group from gauche (at high fwhm) to trans (at low fwhm) [33]. Although the ethylene glycol units readily convert from gauche to trans, the terephthalate unit conformations remain relatively unaffected by drawing under these conditions. Thus, the *average* crystal and backbone orientations, which are the determined parameters via Raman spectroscopy, are low and the observed tenacity values are low compared to industry standards. However, compared to the current literature on PET nanocomposite fibers, the degree of mechanical property improvements listed in Table 4.1 has not been observed by others, particularly with regard to tenacity improvement. The effect of increasing drawing speed and stress induced crystallinity is the subject of our on-going research.

4.3.4 Molecular Conformation and Drawability Improvement

Interestingly, the nanocomposite fibers are capable of reaching higher draw ratios than the pure PET fiber. This is attributed to the effect nanoparticles have on the initial molecular conformation of the PET phase. As noted above, the trans conformation of the PET backbone is associated with extended chains, while the gauche conformation has

been assigned to characterize chain folding and irregularity found in the amorphous phase. Fig. 4.15 b-e shows the Raman spectra of the as-spun, low-orientation, PET nanocomposites in the range of 720 – 1550 cm^{-1} in comparison to the spectrum for pure PET (a) with the nanoclay filled fibers. The convoluted band in the range of 790 – 900 cm^{-1} is composed of four single bands at 795, 830, 858, and 886 cm^{-1}. As noted by others [46], the band intensity at 886 cm^{-1} can be compared with the 998 cm^{-1} band to determine the relative amounts of trans and gauche isomerism of the ethylene glycol units of the PET backbone. By visual inspection of Fig 4.15a with b – e, it is clear than the pure PET sample has a larger content of the trans conformation than the nanoclay filled systems. Further evidence is provided by inspection of the 1050 – 1200 cm^{-1} range. A convoluted band near 1125 cm^{-1} is clearly split into two bands for the pure PET sample. The first peak at 1097 cm^{-1} has been assigned to the *trans* conformation of the amorphous or crystalline phase, while the second peak at 1130 cm^{-1} corresponds to the *gauche* isomerism of these phases. The nanoclay filled systems show only a shoulder at 1097 cm^{-1}, which reflects less *trans* content than the pure PET.

Ibanes et al. [17] examined the drawability and orientation of only a 1 wt% loading of montmorillonite in polyamide-6. They found that nanoclay, indeed, increased drawability relative to unfilled polyamide, but did not lead to significantly enhanced molecular orientation when drawn to its maximum extent [17]. The authors deduced from small and wide angle X-ray measurements on the crystalline structure that the large impenetrable surfaces of the nanoclay block the development of inter-crystal tie chains, thereby reducing the entanglement density of the polyamide chain network [17].

For the PET nanocomposite fibers examined in this study a similar conclusion can be made for the increased extensibility of the polyester network. However, the effect of nanoclay concentration is considered here, as point of departure from the study of Ibanes et al. [17]. In Table 4.1 the maximum draw ratio is nearly independent of nanoclay loading. As nanoclay concentration is increased, the degree of agglomeration is increased as shown by the XRD peaks in Fig. 4.1. Therefore, the number of surfaces blocking entanglements remains relatively unchanged, because at higher concentrations the platelets are more likely to be stacked together into aggregates. If the platelets were exfoliated then perhaps higher draw ratios could be obtained as more entanglements are prevented with increased nanoclay concentrations up to a percolation limit. Additionally for the PET nanocomposite fibers, the nanocomposite samples have a less ordered structure after initial melt spinning than the pure PET. Therefore, the absence of crystallites, which have been shown to act as cross-link points between polymer chains, and lack of pre-orientation of the chains into their *trans* conformations permits the accomplishment of higher draw ratios with nanoclay filled PET fibers. The reduction in *trans* content is suggested to be the result of a combined effect of a favorable PET chain interaction with the silicate surface and the dissipation of deformational energy by the nanoclay during melt-spinning.

To interpret the cause of the increased drawability and origin of the greater gauche content of the nanocomposite fibers a few of scenarios are worth considering. Similar trends with enhanced amorphous phase content in fibers have been observed for the melt-spinning of polymer blends [47, 48]. These authors concluded that because the primary phase produces a shear field around the filler phase, the elongational viscosity of

the system is reduced, and the overall extension and orientation of chains is suppressed [47, 48]. Polymer molecules tend to un-coil and then orient more readily under stronger extensional flow. If the applied stress from the winding device is split between orienting the polymer molecules and the nanoparticles to the fiber axis, then the extensional flow can be considered weaker than if the whole stress was focused on the polymer chains alone.

An alternative explanation for the presence of an enhanced gauche content can be linked to PET-nanoclay surface bonding or "tetherment." From the intercalation data shown in Figs. 4.2 and 4.3 and from the modulus data of the drawn nanocomposites, some type of favorable coupling interaction is inferred between PET and the alkyl modified nanoclay. However, additional or abnormal bands in the Raman spectra of the nanocomposite fibers are not observed to any significance that would signify PET bonding with the surface of the nanoparticle or the surface treatment. For instance, surface hydroxyl groups on the montmorillonite nanoclay could bond with the ethylene glycol units on the PET chain, which would give rise to some change in the bands of O–C stretching. A bonded PET-nanofiller structure has been observed by Bikaris et al. [49] for silica filled PET, and a branched PET structure has been shown to lower the degree of crystallinity as well as broaden the melting endotherm in DSC experiments [50]. Although the nanocomposite degrees of crystallinity are reduced in the as-spun and drawn states relative to unfilled PET, the filled fiber have significantly increased drawability. Ibanes et al. [17] examined the drawability of polyamide-6 with hyperbranched fillers and a 1 wt% addition of montmorillonite. The hyperbranched additives significantly reduced drawability of PET by cross-linking the chains and restricting orientation development [17].

Therefore the rapid rise in complex viscosity of the nanocomposite resins, shown in Fig. 4.5, is probably not due to tetherment bonding of the PET and nanoparticles. Instead it is more likely due to a combined effect of heterogeneous nucleation at the surface of the silicate and homogenous nucleation by the immobilization of polymer chains by the silicate layers. Both of these effects are dependent on the concentration and degree of dispersion of nanoclay. Therefore, the interaction between PET and alkyl modified nanoclay is considered favorable but rather weak, such that a well-connected PET-nanoclay network is not formed with these organically modified montmorillonites.

4.4 CONCLUSIONS

The role of alkyl-modified montmorillonite in the improvement of PET fiber mechanical properties was discussed in terms of PET and nanoparticle morphology. When drawn to their maximum extents, modulus and tenacity improvement reached a maximum at a 1 wt% addition of nanoclay. Average molecular orientation of the phenylene rings and ethylene glycol groups reached a maximum with nanoclay concentration at 1 wt% as well. From thermal shrinkage measurements, the presence of nanoclay promoted the development of amorphous orientation. In addition, X-ray diffraction showed nanoparticle intercalation with PET, which suggested that favorable interaction existed between the polymer and nanoclay. At a 1 wt% loading of nanoclay, the degree of physical interaction with the polymer matrix yielded the optimal molecular orientation for the greatest amount of mechanical property improvement. For concentrations below 1 wt%, the loading of nanoclay was not high enough to develop

significant interactions with PET and alter the extent of molecular orientation. The degree of parallel coupling of PET and nanoclay was below optimum due to the low concentration. Therefore, the modulus improvement was not as great as that with the 1 wt% loading. At concentrations above the optimum, the degree of nanoclay agglomeration increased, and we believe the molecular orientation was disrupted by the inability of the polymer chains to efficiently rearrange around the larger stacks of particles parallel to the fiber axis. In addition, the larger agglomerates and the increased presence of nanoclay aided in the dissipation of some of the deformation from the PET chains to the silicate stacks. Furthermore, at high concentrations the large agglomerates appear to act as stress concentrators. The combination of the above led to reduced mechanical properties at high nanoclay loadings.

The ability to obtain higher degrees of molecular orientation was linked to the increased drawability of the nanocomposite fibers relative to pure PET. Nanocomposite yarns can be drawn to a greater extent because of the larger gauche content of the ethylene glycol units that delay the orientation and subsequent crystallization of the PET chains to higher draw ratios. In the as-spun state for pure PET fiber, the degree of trans content may reflect pre-ordering of the polymer chains. The degree of trans content may also impart physical cross links between ordered crystalline domains and serve as a nucleator for further crystallization. An increased amount of gauche content is due a favorable, although weak, interaction with the silicate surface, such that the polymer chains remain in a predominantly coiled amorphous state. In addition, the nanoparticles themselves are able to dissipate some of the deformational energy from the spinning process. Therefore, there may be a suppression of effective winding speed, such that the

polymer chains in the nanocomposite do not have the same as-spun ordering as the pure PET fibers at an equal spinning speed.

4.5 REFERENCES

1. Kojima, Y.; Usuki, A.; Kawasumi, M.; Okada, A.; Kurauchi, T.; Kamigaito, O., Synthesis of nylon 6-clay hybrid montmorillonite intercalated with caprolactam. *J. Appl. Polym. Sci., Part A: Polymer Chemistry* **1993,** 31, (4), 983-986.
2. Messersmith, P. B.; Giannelis, E. P., Synthesis and barrier properties of poly(caprolactone)-layered silicate nanocomposites. *J. Appl. Polym. Sci., Part A: Polym. Chem.* **1995,** 33, (7), 1047-1057.
3. Gilman, J. W., Flammability and thermal stability studies of polymer layered-silicate (clay) nanocomposites. *Applied Clay Science* **1999,** 15, 31-49.
4. Fornes, T. D.; Yoon, P. J.; Keskkula, H.; Paul, D. R., Nylon 6 nanocomposites: The effect of matrix molecular weight,. *Polymer* **2001,** 42, 9929-9940.
5. Chu, D.; Nguyen, Q. T.; Baird, D. G., Effect of matrix molecular weight on the dispersion of nanoclay in unmodified high density polyethylene. *Polymer Composites* **2007,** 28, 499-511.
6. Nguyen, Q. T.; Baird, D. G., An improved technique for exfoliating and dispersing nanoclay particles in polymer matrices using super-critical carbon dioxide. *Polymer* **2007,** 48, 6923-6933.
7. Nguyen, Q. T.; Baird, D. G., Preparation of polymer-clay nanocomposite and their properties. *Adv. Polymer Techn.* **2006,** 25, 270-285.
8. Ray, S. S.; Okamoto, M., Polymer/layered silicate nanocomposites: a review from preparation to processing. *Prog. Polym. Sci.* **2003,** 28, 1539-1641.
9. Tjong, S. C., Structural and mechanical properties of polymer nanocomposites. *Mater. Sci. and Eng. Rev.* **2006,** 53, 73-197.
10. Giannelis, E. P., Polymer layered silicate nanocomposites. *Advanced Materials* **1996,** 8, (1), 29-35.
11. Litchfield, D. W.; Baird, D. G., The rheology of high aspect ratio nano-particle filled liquids. *Rheology Reviews* **2006**, 1-60.
12. Okada, A.; Usuki, A., Twenty years of polymer-clay nanocomposites. *Macromol. Mater. & Eng.* **2006,** 291, 1449-1476.
13. Fornes, T. D.; Paul, D. R., Modeling properties of nylon 6/clay nanocomposites using composite theories. *Polymer* **2003,** 44, 4993-5013.
14. Houphouet-Boigny, C.; Plummer, C. J. G.; Wakeman, M. D.; Manson, J.-A. E., Towards textile-based fiber-reinforced thermoplastic nanocomposites: melt-spun polypropylene montmorillonite nanocomposite fibers. *Polym. Eng Sci.* **2007,** 47, 1122-1132.
15. Pavlikova, S.; Thomann, R.; Reichert, P.; Mulhaupt, R.; Marcincin, A.; Borsig, E., Fiber spinning from poly(propylene)-organoclay nanocomposite. *J. Appl. Polym. Sci.* **2003,** 89, 604-611.
16. Giza, E.; Ito, H.; Kikutani, T.; Okui, N., Fiber Structure Formation in High-Speed Melt Spinning of Polyamide 6/Clay Hybrid Nanocomposites. *J. Macromol. Sci. - Phys* **2000,** B39, 545-559.
17. Ibanes, C.; David, L.; De Boissieu, M.; Seguela, R.; Epicier, T.; Robert, G., Structure and Mechanical Behavior of Nylon-6 Fibers Filled with Organic and Mineral Nanoparticles. I. Microstructure of Spun and Drawn Fibers. *J. Polym. Sci. Part B: Polym. Phys.* **2004,** 42, 3876-3892.
18. McConnell, D. C.; Hornsby, P. R.; Lew, C. Y.; Qua, E. H., Structure Property Relationships in PET Nanocomposite Fibres. *Ann. Tech. Conf. Society of Plastic Engineers, Technical Papers* **2006**, 387-392.
19. Chang, J. H.; An, Y. U.; Kim, S. J.; Im, S., Poly(butylene terephthalate)/organoclay nanocomposites prepared by in situ interlayer polymerization and its fiber (II). *Polymer* **2003,** 44, 5655-5661.
20. Chang, J. H.; Kim, S. J., Polyester nanocomposite fibers: comparison of their properties with poly(ethylene terephthalate) and poly(trimethylene terephthalate) (II). *Poymer Bulletin* **2004,** 52, 289-296.

21. Chang, J. H.; Kim, S. J.; Joo, Y. L.; Im, S., Poly(ethylene terephthalate) nanocomposites by insitu interlayer polymerization: the thermo-mechanical properties and morphology of the hybrid fibers. *Polymer* **2004,** 45, 919-926.
22. Chang, J. H.; Mun, M. K.; Lee, I. C., Poly(ethylene terephthalate) Nanocomposite Fibers by In Situ Polymerization: The Thermomechanical Properties and Morphology. *J. Appl. Polym. Sci.* **2005,** 98, 2009-2016.
23. Jung, M.-H.; Chang, J.-H.; Kim, J.-C., Polyethylene terephthalate nanocomposite fibers with new organomica via in situ polymerization. *Polym. Eng. Sci.* **2007,** 47, 1820-1826.
24. Litchfield, D. W. The Manufacture and Mechanical Properties of PET Fibers Filled with Organically Modified MMT. Virginia Tech, Blacksburg VA, 2008.
25. Ke, Y.; Long, C.; Qi, Z., Crystallization, Properties, and Crystal and Nanoscale Morphology of PET-Clay Nanocomposites. *J. Appl. Polym. Sci.* **1999,** 71, 1139-1146.
26. Phang, I. Y.; Pramoda, K.; Liu, T.; He, C., Crystallization and melting behavior of polyester/clay nanocomposites. *Polymer International* **2004,** 53, 1282-1289.
27. Wang, Y.; Shen, C.; Li, H.; Li, Q.; Chen, J., Nonisothermal melt crystallization kinetics of poly(ethylene terephthalate)/clay nanocomposites. *J. Appl. Polym. Sci.* **2004,** 91, 308-314.
28. Wang, Y.; Gao, J.; Ma, Y.; Agarwal, U. S., Study on mechanical properties, thermal stability and crystallization behavior of PET/MMT nanocomposites. *Composites: Part B* **2006,** 37, 399-407.
29. Calcagno, C. I. W.; Mariani, C. M.; Teixeira, S. R.; Mauler, R. S., The effect of organic modifier of the clay on morphology and crystallization properties of PET. *Polymer* **2007,** 48, 966-974.
30. Salem, D. R., *Draw-Induced Structure Development in Flexible-Chain Polymers: in "Structure Formation in Polymeric Fibers"*. Hanser: Munich, 2001.
31. Baird, D. G.; Litchfield, D. W.; Rim, P. B., Method of Improving the Modulus and Strength of Polymeric Fibers by the Addition of Nanoparticles. *US patent appl. 60/991550* **2007**.
32. Mehta, A.; Gaur, U.; Wunderlich, B., Equilibrium melting parameters of poly(ethylene terephthalate). *J. Polym. Sci., Polym. Phys. Ed.* **1978,** 16, 289-296.
33. Lesko, C. C. C.; Rabolt, J. F.; Ikeda, R. M.; Chase, B.; Kennnedy, A., Experimental determination of the fiber orientation parameters and Raman tensor of the 1614 cm band of poly(ethylene terephthalate). *J. Molecular Structure* **2000,** 521, 127-136.
34. Citra, M. J.; Chase, D. B.; Ikeda, R. M.; Gardner, K. H., Molecular orientation of highe density polyethylene fibers characterized by polarized Raman spectroscopy. *Macromolecules* **1995,** 28, 4007-4012.
35. Yang, S.; Michielsen, S., Determination of the orientation parameters and Raman tensor of the 998 cm band of poly(ethylene terephthalate). *Macromolecules* **2002,** 35, 10108-10113.
36. Tanaka, M.; Young, R. J., Polarised Raman spectroscopy for the study of molecular orientation distributions in polymers. *J. Mater. Sci.* **2006,** 41, 963-991.
37. Bower, D. I., Orientation distribution functions for uniaxially oriented polymers. *J. Polym Sci.: Polym. Phys. Ed.* **1981,** 19, 93-107.
38. Southern-Clay-Products *Cloisite 20A: Typical Physical Properties Bulletin*; 2008.
39. van Krevelen, D. W., *Properties of polymers*. Elsevier: New York, 1990.
40. Jeziorny, A., Parameters characterizing the kinetics of non-isothermal crsytallization of PET by DSC. *Polymer* **1978,** 19, 1142.
41. Bower, D. I.; Maddams, W. F., *The vibrational spectroscopy of polymers*. Cambridge University Press: Cambridge, 1989.
42. Stokr, J.; Schneider, B.; Doskocilova, D.; Lovy, J.; Sedlacek, P., Conformational structure of poly(ethylene terephthalate). Infra-red, Raman, and n.m.r spectra. *Polymer* **1982,** 23, 714-721.
43. Yeh, W.-Y.; Young, R. J., Deformation processes in polyethylene terephthalate fibers. *J. Macromol. Sci. - Phys* **1998,** 37, 83-118.
44. Frost, R. L.; Rintoul, L., Lattice vibration of montmorillonite: an FT Raman and X-ray diffraction study. *Appl. Clay Sci.* **1996,** 11, 171-183.
45. Melveger, A. J., *J. Polym Sci. Part A-2* **1972,** 10, (317).
46. Rodriguez-Cabello, J. C.; Merino, J. C.; Quintanilla, L.; Pastor, J. M., Deformation-induced conformational changes in stretched samples of amorphous poly(ethylene terephthalate). *J. Appl. Polym. Sci.* **1996,** 62, 1953-1964.

47. Brody, H., Orientation Suppresion in Fibers Spun from Polymer Melt Blends. *J. Appl. Polym. Sci.* **1986,** 31, 2753-2768.
48. Miles, I. S., The reduction of orientation in fibers spun from 2-phase polymer blends via the introduction of shear into elongational flow by the presence of a second phase. *J. Appl. Polym. Sci.* **1987,** 34, 2793-2807.
49. Bikiaris, D.; Karavelidis, V.; Karayannidis, G., A New Approach to Prepare Poly(theylene terephthalate)/Silica Nanocomposites with Increased Molecular Weight and Fully Adjustable Branching or Crosslinking by SSP. *Macromole. Rapid Comm.* **2006,** 27, 1199-1205.
50. McKee, M. G.; Unal, S.; Wilkes, G.; Long, T. E., Branched polyesters: recent advances in synthesis and performance. *Prog. Polym. Sci.* **2005,** 30, 507-539.

Table 4.1. Tensile properties of as-spun (un-oriented) PET/MMT nanocomposite fibers with true clay content and molecular weight by intrinsic viscosity.

Clay Type	Nominal Loading	Draw Ratio	M_w	Young's Modulus	Maximum Tenacity	Toughness	Elongation at Break
	wt%		g/mol	GPa	MPa	MPa	%
Pure PET As-spun	0.0	-	45800	2.00 ± 0.16	132 ± 5.4	197 ± 6.8	191 ± 8.9
Cloisite 20A As-spun	0.5	-	45800	1.48 ± 0.30	122 ± 2.7	262 ± 15	284 ± 5.9
	1.0	-	44900	1.65 ± 0.11	145 ± 5.4	277 ± 18	300 ± 3.1
	1.5	-	43200	1.81 ± 0.17	132 ± 2.7	235 ± 5.4	279 ± 10
	3.0	-	38800	1.47 ± 0.27	75.6 ± 5.4	190 ± 12	298 ± 19
Pure PET Drawn	0.0	2.5	45800	9.92 ± 0.79	410 ± 18	36.4 ± 2.8	6 ± 0.5
Cloisite 20A Drawn	0.5	3.7	45800	11.8 ± 0.45	590 ± 27	30.8 ± 2.8	5.6 ± 0.2
	1.0	3.5	44900	12.7 ± 0.51	670 ± 20	29.4 ± 1.4	5.5 ± 0.2
	1.5	3.5	43200	10.8 ± 0.67	539 ± 15	21.0 ± 1.4	5.1 ± 0.3
	3.0	3.6	38800	9.32 ± 0.76	389 ± 10	18.2 ± 1.4	4.7 ± 0.3

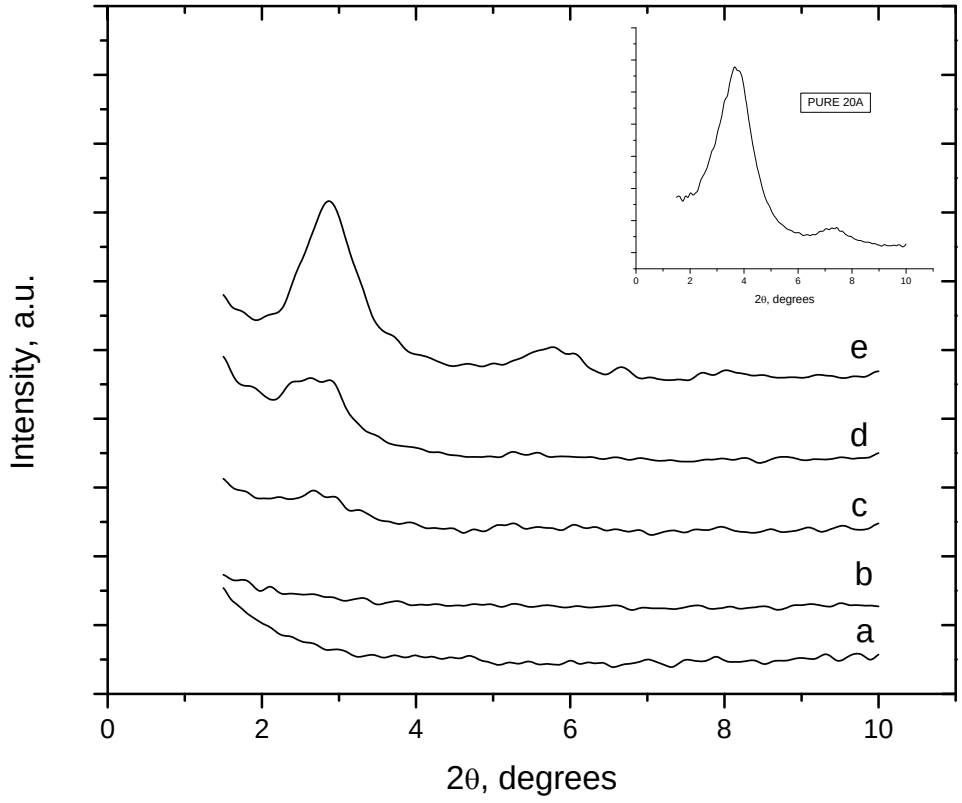

Fig. 4.1 XRD for the as-spun nanocomposite fibers (a) pure PET, (b) 0.5 wt% 20A, (c) 1 wt% 20A, (d) 1.5 wt% 20A, (e) 3 wt% 20A. Inset – pure Cloisite 20A nanoclay.

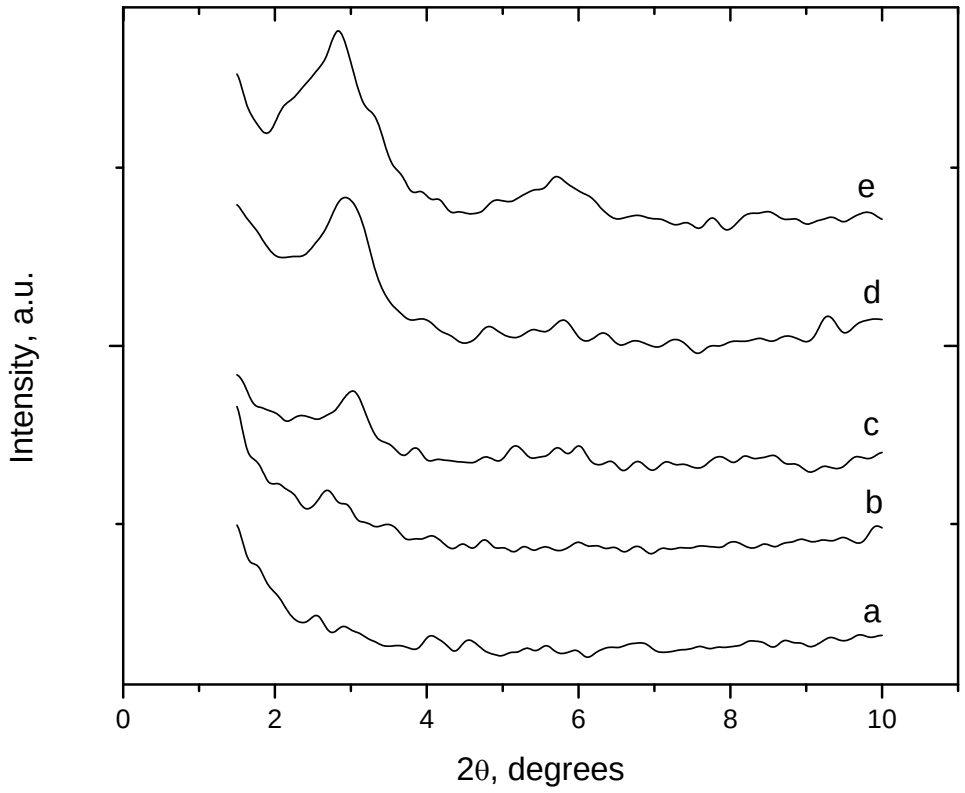

Fig. 4.2. XRD for the drawn nanocomposite fibers (a) pure PET, (b) 0.5 wt% 20A, (c) 1 wt% 20A, (d) 1.5 wt% 20A, (e) 3 wt% 20A.

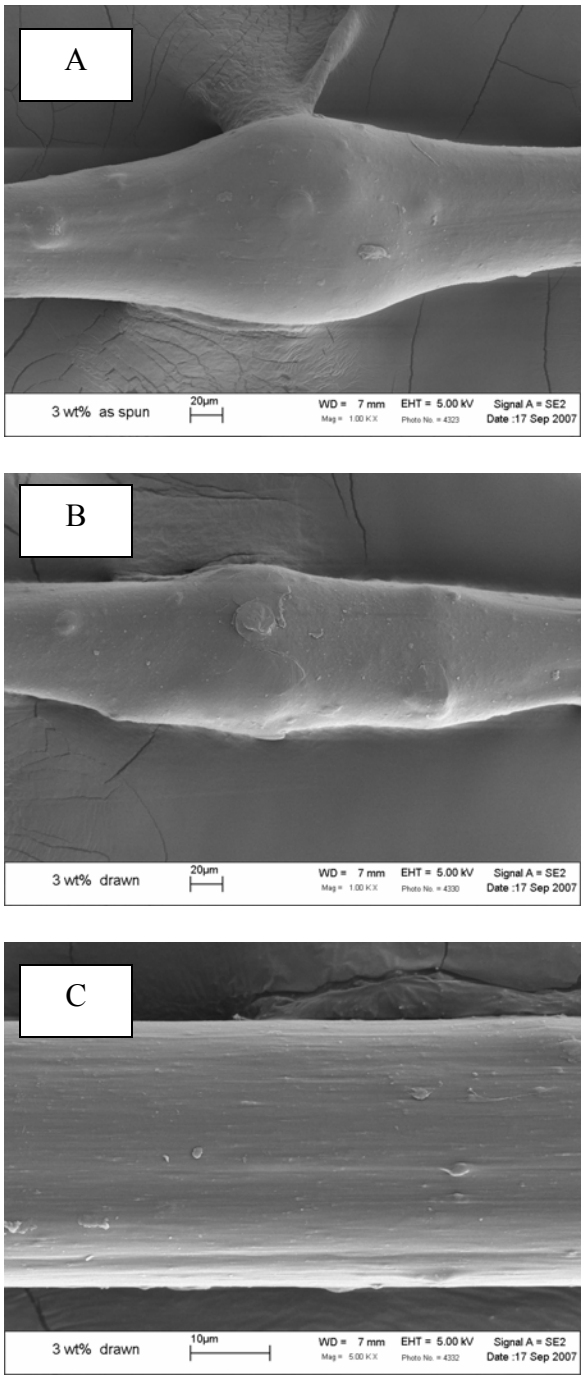

Fig. 4.3. SEM images of large agglomerates in the as-spun (a) and drawn (b) 3 wt% 20A nanocomposite fiber and a smooth section (c) of the drawn fiber.

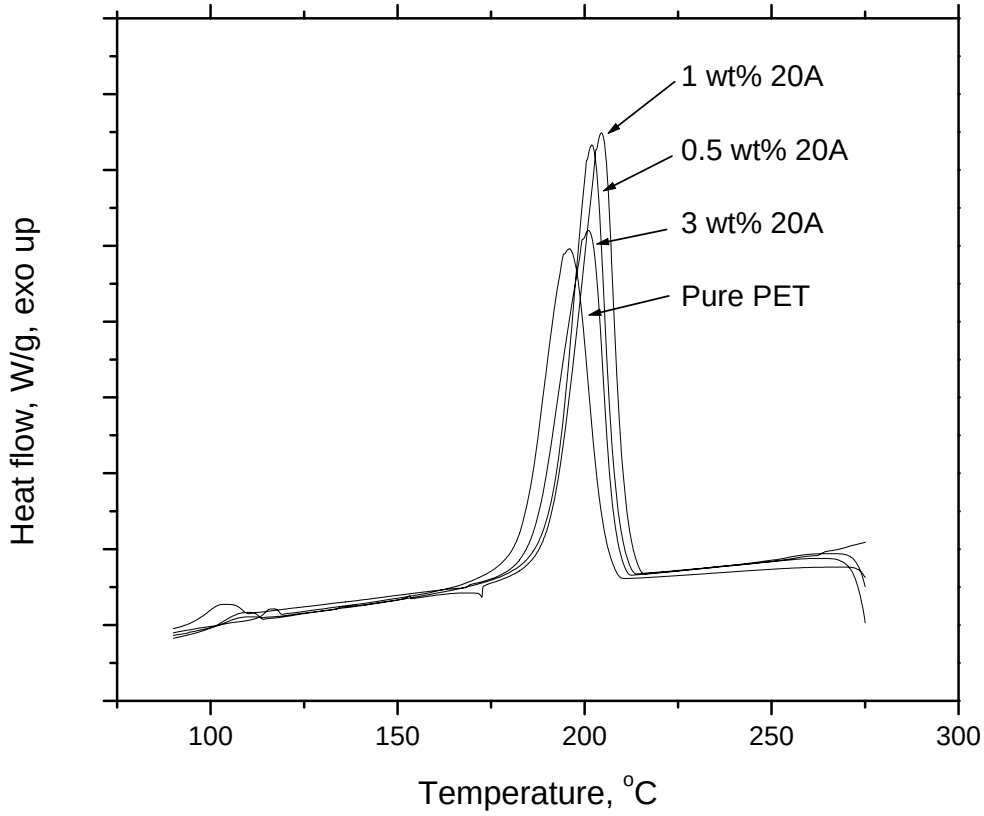

Fig. 4.4. Cooling from the melt at 20 °C/min, heat flow as a function of temperature for various nanoclay concentrations.

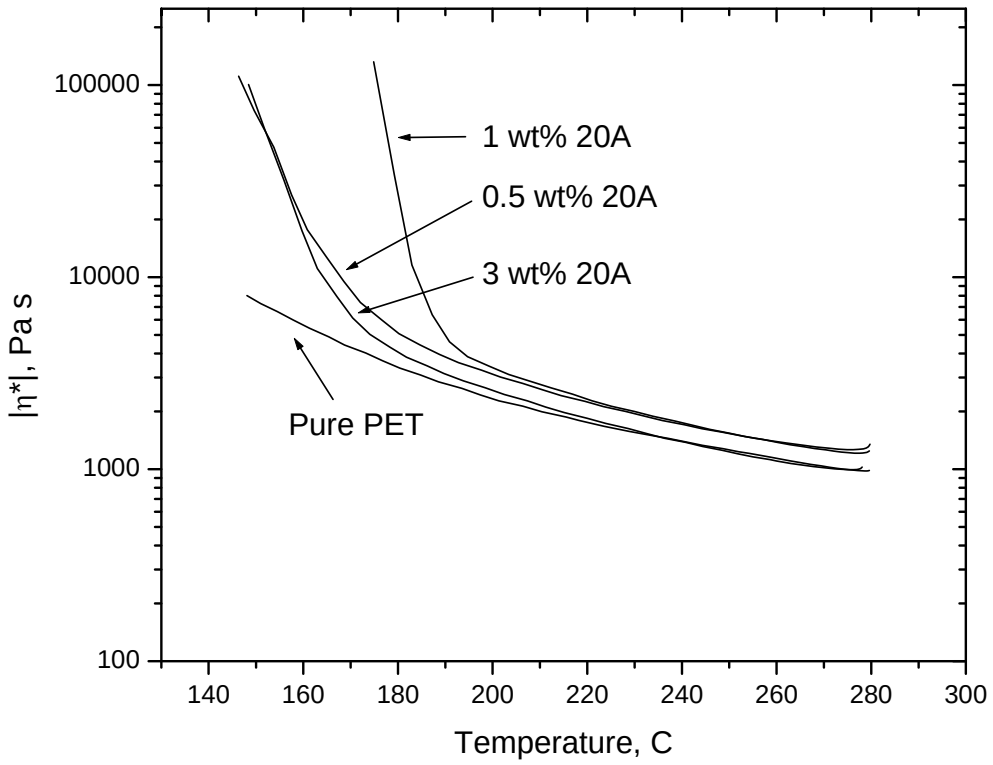

Fig. 4.5. Complex viscosity as a function of temperature for the PET nanocomposite chips cooled at 40 °C/min, 100 rad/s, under nitrogen.

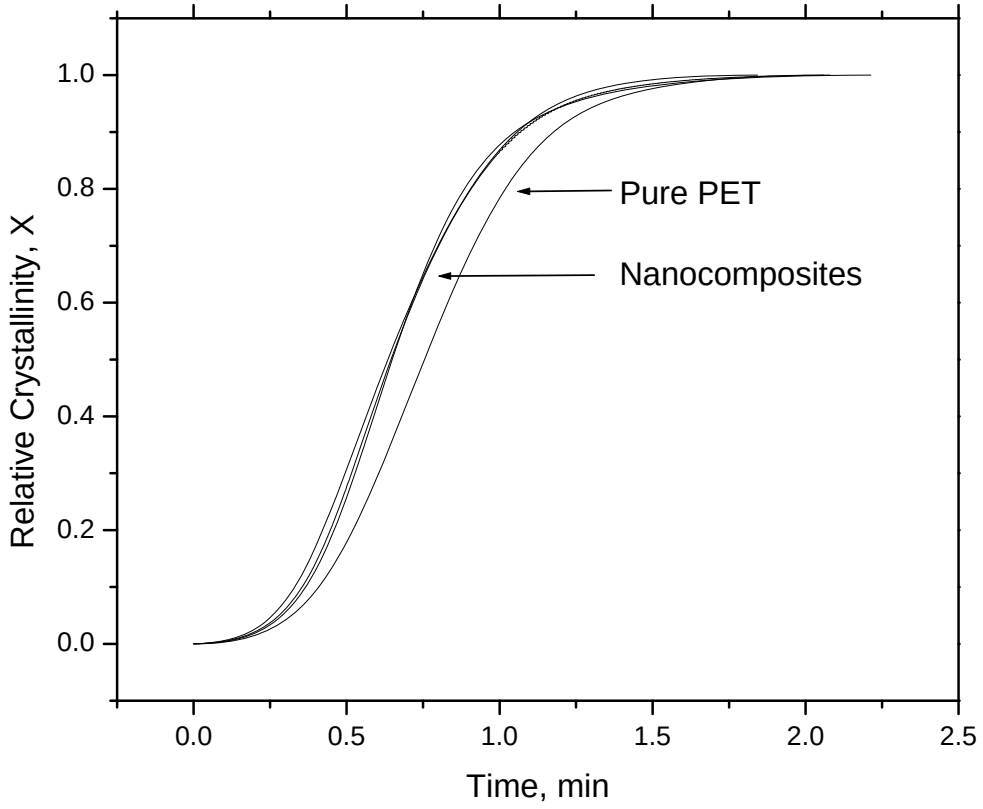

Fig. 4.6. Cooling from the melt at 20° C/min, non-isothermal crystallization, X, as a function of time for various nanoclay loadings.

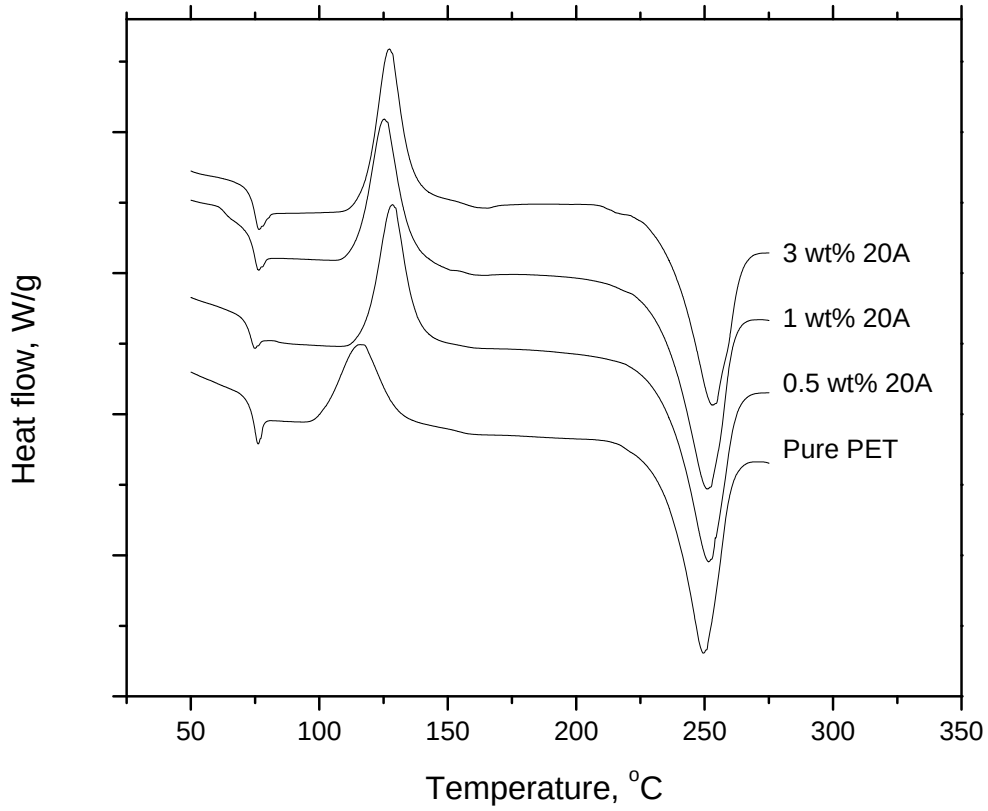

Fig. 4.7. 1st Heating of the as-spun nanocomposite fibers at 20 °C/min, heat flow as a function of temperature for various nanoclay loadings (scaled for clarity).

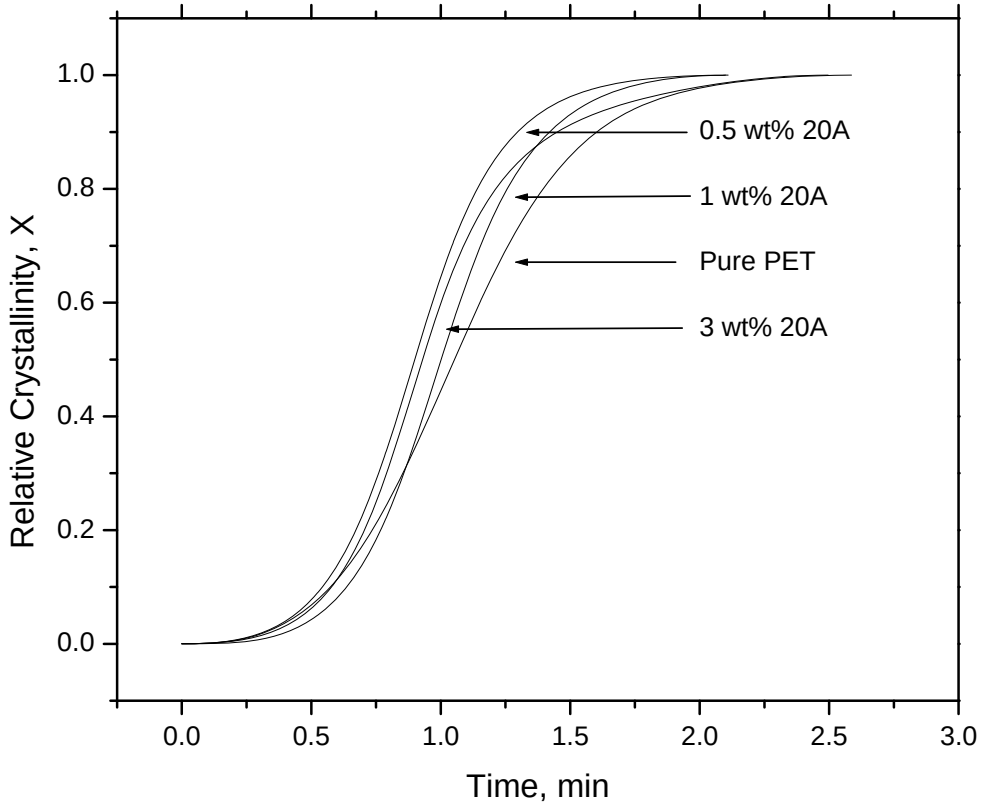

Fig. 4.8. 1st Heating of the as-spun nanocomposite fibers at 20 °C/min, non-isothermal crystallization, X, as a function of time for various nanoclay loadings.

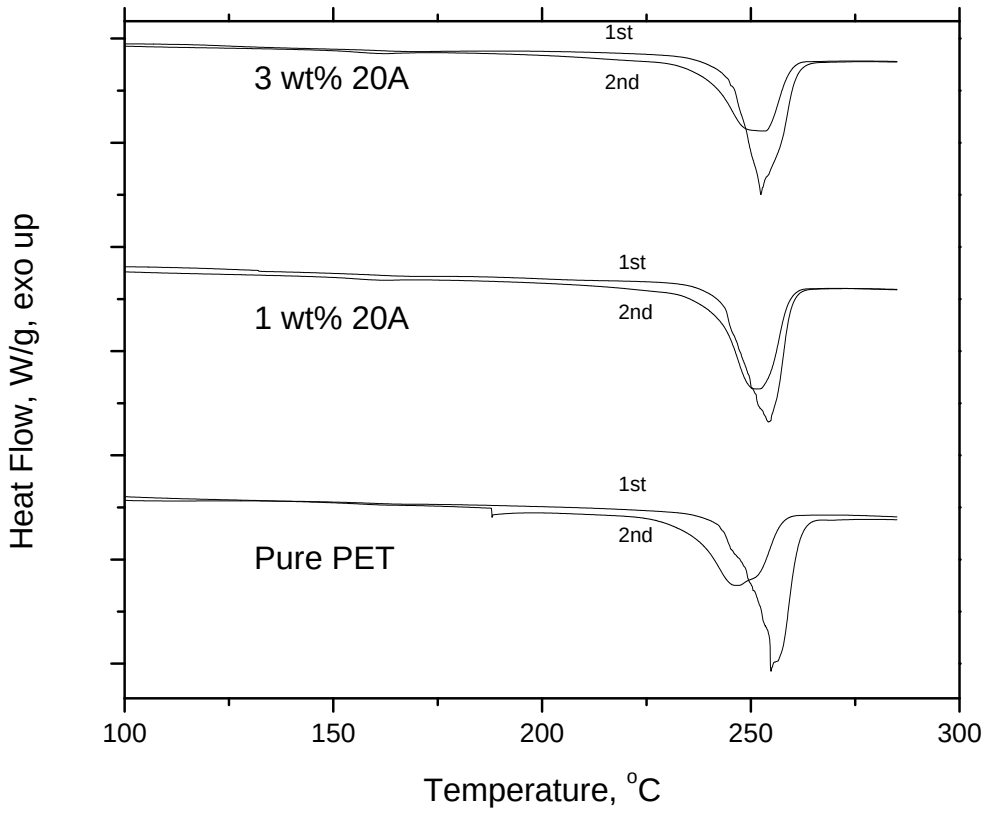

Fig. 4.9. 1st and 2nd Heating of the as-spun nanocomposite fibers at 20 °C/min, heat flow as a function of temperature for various nanoclay concentrations.

Table 4.2. PET nanocomposite fiber crystallinity, X_c, from DSC heating scans at 20 °C/min.

Sample	X_c (%)
Pure PET as-spun	14.5
0.5 wt% 20A as-spun	10.1
1 wt% 20A as-spun	10.2
1.5 wt% 20A as-spun	9.7
3 wt% 20A as-spun	6.5
Pure PET drawn	37.4
0.5 wt% 20A drawn	36.6
1 wt% 20A drawn	35.5
1.5 wt% 20A drawn	34.2
3 wt% 20A drawn	32.2

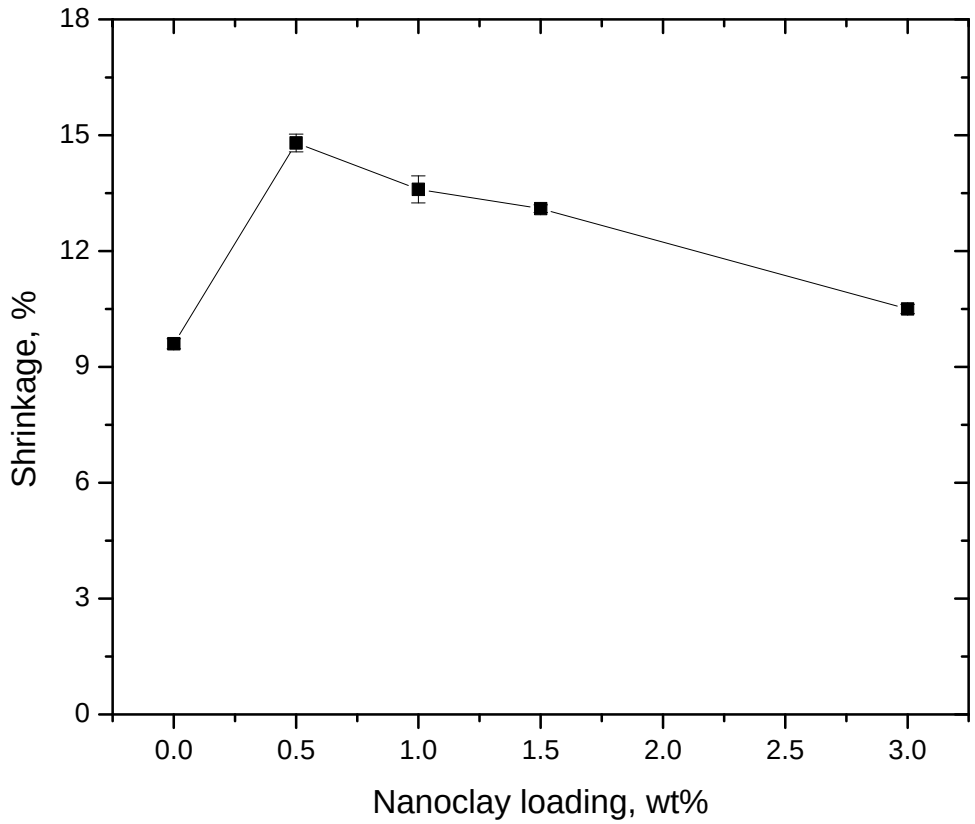

Fig. 4.10. Thermal shrinkage in % of the drawn nanocomposite fibers at 177 °C.

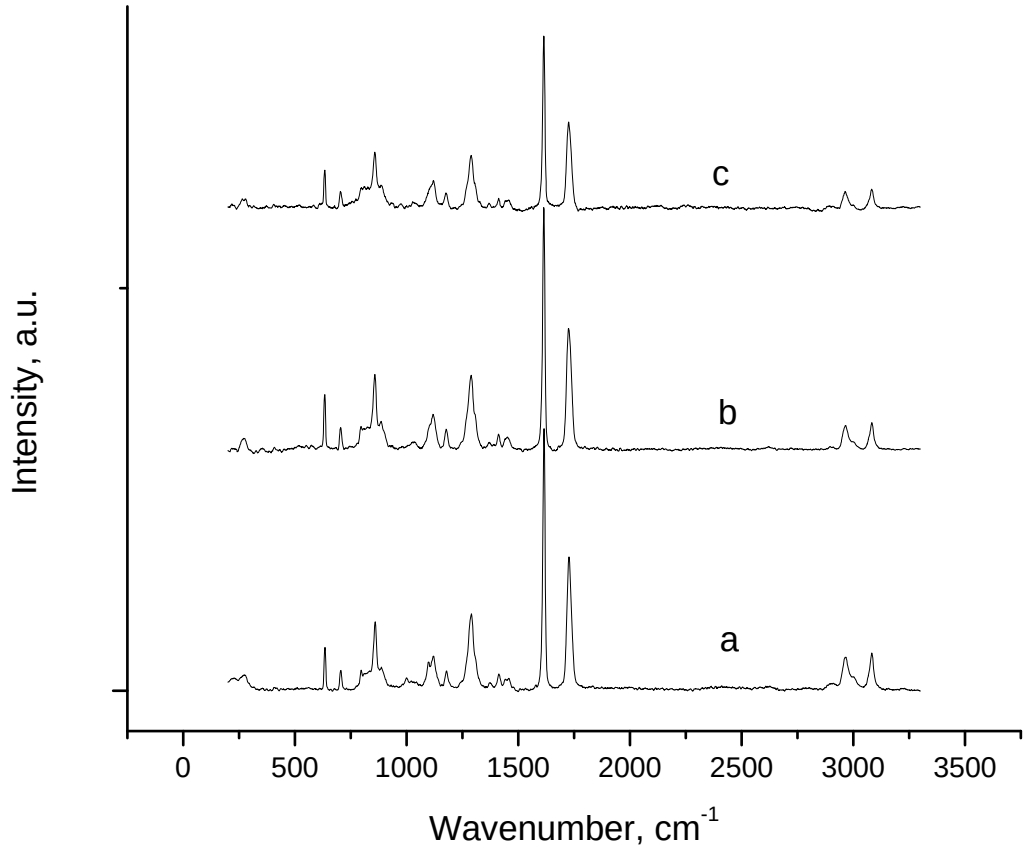

Fig. 4.11. Raman spectra of as-spun fibers of Pure PET (a), 1 wt% 20A (b), and 3wt% 20A (c) with the fiber samples parallel to the vector of polarized light.

Table 4.3. Raman Bands of Interest for Semicrystalline PET and Montmorillonite.

Wavenumber	Vibrational Mode
450	SiO_4 stretching (MMT)
710	Ring C–C stretching SiO_4 stretching (MMT)
795	Ring torsion and C=O stretching
858	Ring C–C, ester CO–C
886	$O–CH_2$ and C–C stretch of the *gauche* ethylene glycol unit
998	$O–CH_2$ and C–C stretch of the *trans* ethylene glycol unit
1095	Ethylene glycol C–O and C–C stretching, C–O–C bending
1125	Ester CO–O and ethylene glycol C–C stretching
1180	Ring C–C stretching
1281	CO–C stretching
1310	Ring C–C stretching
1616	Ring C_1–C_4 stretching
1730	C=O stretching

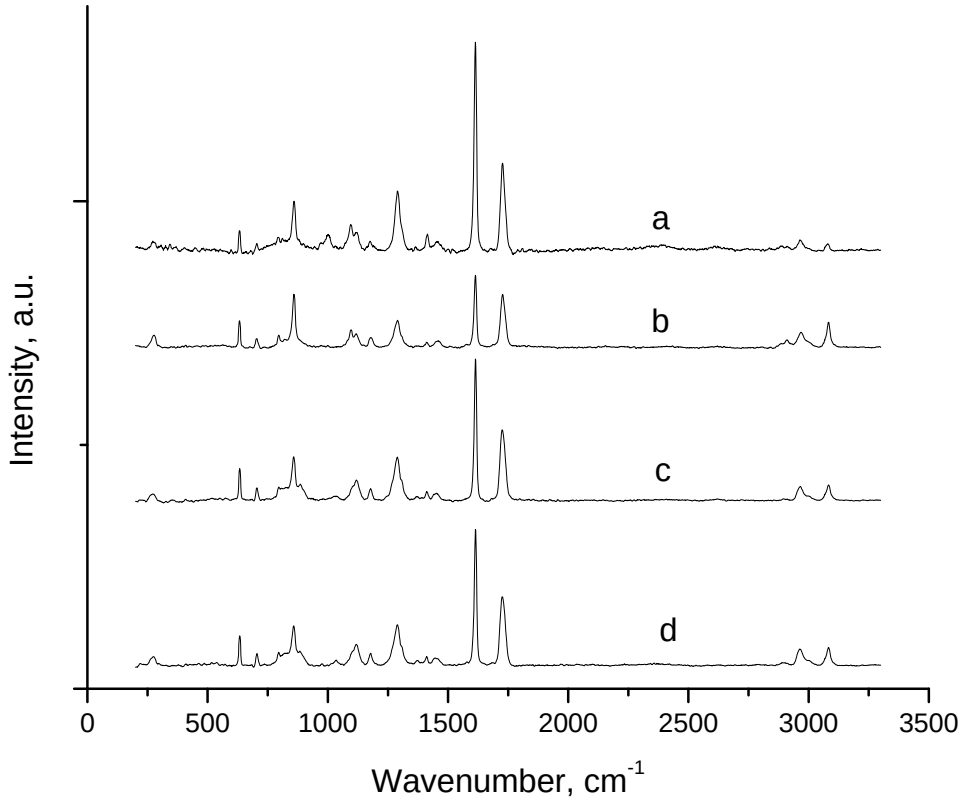

Fig. 4.12. Raman Spectra of parallel and perpendicular arrangements of the wt% 20A as-spun and drawn fibers (a) parallel spectra of drawn 1 wt% 20A, (b) perpendicular spectrum of drawn 1 wt% 20A, (c) parallel spectra of as-spun 1 wt% 20A, (d) perpendicular spectrum of as-spun 1 wt% 20A.

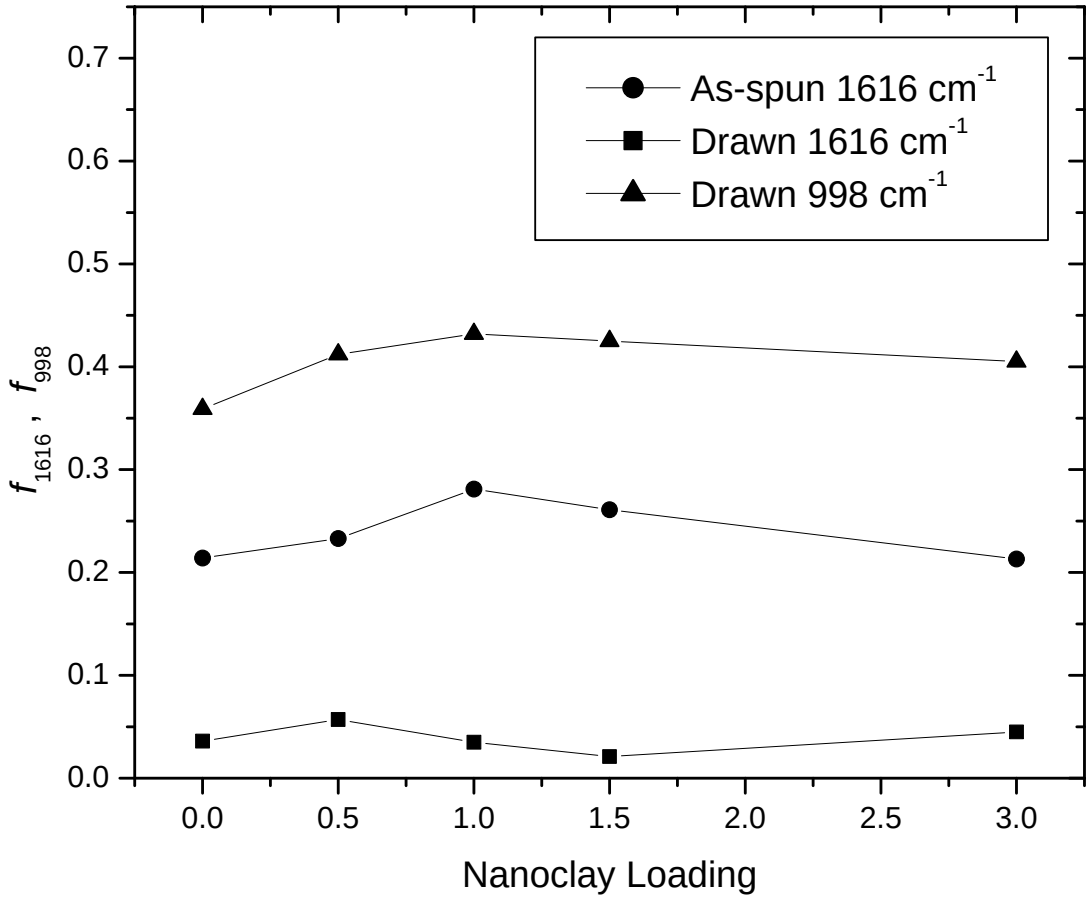

Fig. 4.13. Molecular orientation factor of the PET backbone (–C–C– stretch at 1616 cm^{-1}), f_{1616}, for the as-spun and drawn nanocomposite fibers and the orientation of the ethylene glycol units (stretch at 998 cm^{-1}), f_{998} for the drawn case only.

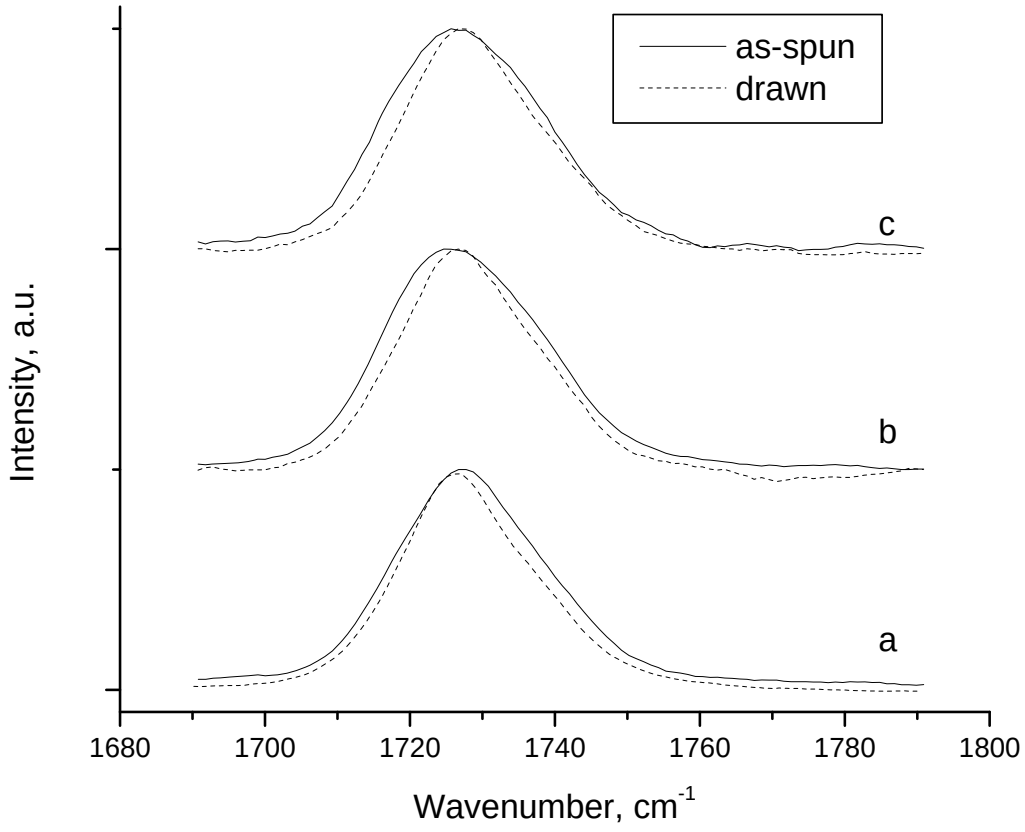

Fig. 4.14. 1727 cm^{-1} band as a function of nanoclay loading in the as-spun and drawn states, (a) Pure PET, (b) 1 wt% 20A, (c) 3 wt% 20A.

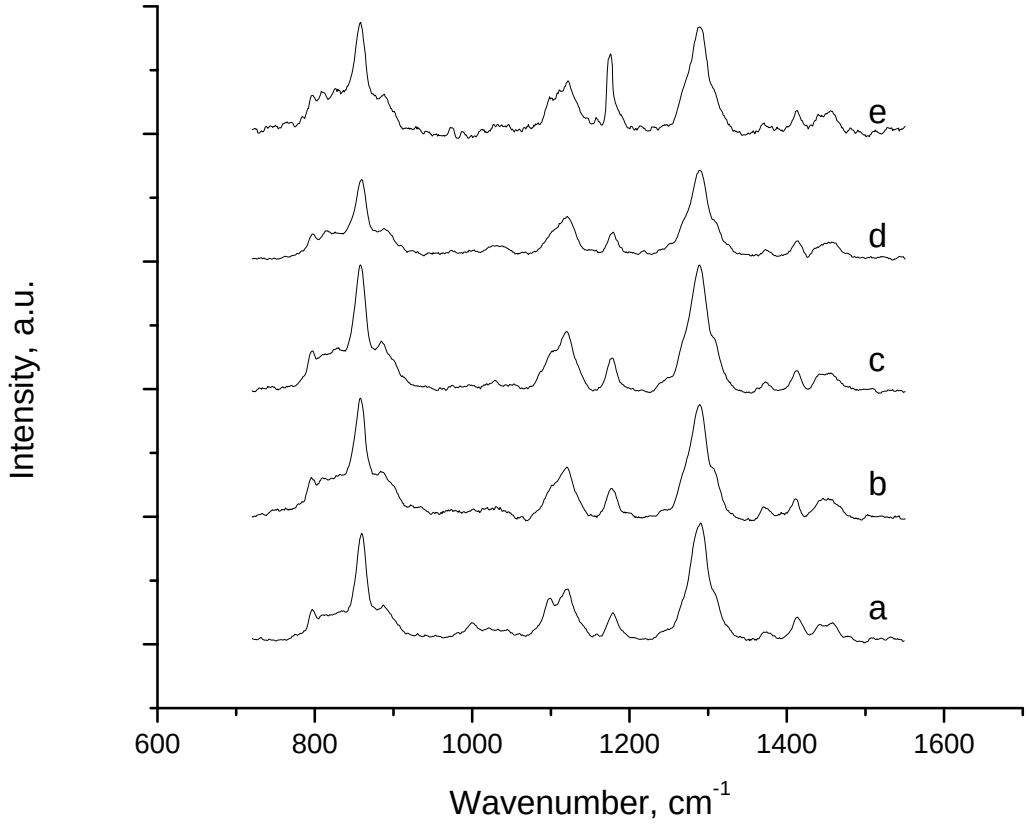

Fig. 4.15. Raman spectrum from 720-1550 cm^{-1} for the as-spun nanocomposite fibers, (a) pure PET, (b) 0.5 wt% 20A, (c) 1 wt% 20A, (d) 1.5 wt% 20A, (e) 3 wt% 20A.

5.0 Recommendations

5.1 The use of dispersion agents such as super-critical carbon dioxide to improve the degree of nanoclay exfoliation in the PET matrix.

Dispersing the nanoclay to its single sheet exfoliated structure and hence producing the uniform filament cross section along its length has proven to be the quintessential challenge of nanocomposite synthesis. The “traditional” methods used to synthesize layered silicate nanocomposites are intercalative. These methods are of three genres, in-situ polymerization of dispersed nanoclay in a suitable monomer reacted with a second monomer, intercalation of polymer and nanoparticle in solution, and melt compounding of molten polymer and clay. The overall degree of dispersion by any of the above methods depends on the filler concentration and filler organic modification. To date, the general conclusion on the success of the above methods at producing exfoliated structures of clay in polymers is isolated to a few cases.

Not only will exfoliation of the naturally intercalated stacks of nanoclay lead to improved product appearance, exfoliation will maximize the property improvements per filler addition. For example, the polymer packaging and films industry is looking for higher degrees of dispersion to retain optical clarity of their packaging as well as achieve the increased oxygen barrier properties to extend product lifetime before spoilage. The automotive industry is requires high degrees of dispersion to cut back on filler costs while improving product mechanical properties, such as strength and initial modulus. Yet, the conventional methods, mentioned above, used to produce these polymer nanocomposite structures are far from ideal in dispersion reliability and repeatability.

The most effective method for producing polymer nanocomposite structures is the method that is the easiest to facilitate, which is a melt compounding method. Melt intercalation has become mainstream for producing polymer layered silicate nanocomposites. Yet, the method of melt compounding includes several types of mixing methods, from extrusion using single or twin-screw extruders to batch mixing in high shear systems. A survey of the literature by Nguyen and Baird [1] discussed the intricacies of melt compounding machinery, processing conditions, and organic modification of the silicate clay on the degree of dispersion. The highest degrees of dispersion were obtained with thermally stable nanoclay surfactants that matched the hydrophilicity of the polymer molecules and that were compounded under controlled shear rate and residence times in a twin-screw extruder. In terms of the mechanical properties obtained from these nanocomposites, the degree of improvement of initial modulus plateaued with clay concentration at about 4 wt% clay (7 wt% clay for nylon 6). In tandem with the leveling off in mechanical properties, the degree of dispersion begins to collapse toward intercalated morphologies of nanoclay.

For the case of PET, a shear sensitive polymer, the available options for producing a melt compounded nanocomposite require tight processing conditions to avoid significant matrix degradation. Pet as a homopolymer is susceptible to several degradation reactions during processing. The most important degradation reaction is oxidation of the ester linkage to produce diethylene glycol a comonomer that has significant effects on final properties. As well shear heating and oxidation lead to the formation of acetalaldehyde, AA. AA is an undesirable byproduct of the chain scission of PET and is responsible for the discoloration after processing. AA is also responsible

for the “off” fruity taste in PET packaging. Therefore melt compounding techniques involving twin screw extrusion with a high degree of shear mixing may not be the optimal method for nanoparticle dispersion with retention of matrix molecular weight.

Several authors have reported severe degradation of PET as a result of twin screw melt compounding with montmorillonite nanoparticles [2, 3]. Yet some of these same studies have reported property improvements or at least successful intercalation of montmorillonite in PET. Often the degree of success depends on both the correct choice of surfactant on the particle (i.e. one that is thermally stable at the melt temperature of PET) and the optimization of processing conditions (i.e. low shear, cycle time, processing temp). However, reducing the shear contradicts the suggestions of Fornes et al. [4] and Chu et al. [5]. In these studies, higher molecular weights and high shear environments were shown to produce higher degree of nanoparticle exfoliation. As stated above, this is not acceptable for PET systems. Therefore, an alternative approach is highly desirable to avoid the degradation of PET and promote nanoparticle dispersion.

One possible alternative that will avoid PET matrix degradation during melt compounding is to use a plasticization agent such as sc-CO_2 to lower the processing temperature. In the super-critical state, CO_2 is known to have similar solubility characteristics to those of organic solvents and is known to not only plasticize a number of polymers, but to also reversibly plasticize them, such that CO_2 removal is facile under depressurization. Montmorillonite is a swellable mineral, due to its inherently large capacity for interlayer cations capable of forming complexes with polar solvents. In these polar solvents, the interlayer spacing between silicate sheets swells and expands to disperse the silicate sheets into their single individual layers.

Some authors have applied this concept to the fabrication of polymer layered silicate nanocomposites [1]. In particular, Nguyen and Baird [6] developed a method to increase the degree of dispersion to an exfoliated morphology by the addition of a mixture of sc-CO_2 and a given concentration of nanoclay to a stream of molten polypropylene in a single screw extruder. Nguyen and Baird compared this technique with other more conventional methods, such as single and twin-screw extrusion. The results of the study showed by x-ray diffraction and microscopy that higher degrees of dispersion are obtained, through which the mechanical properties are improved to a greater extent than by using twin-screw extrusion. By the sc-CO_2 method a 54% in initial modulus was recorded for a 6.6 wt% loading of nanoclay as opposed only a 35% increase in modulus for a twin-screw extruded 6.5 wt% addition of nanoclay.

The diffusion of sc-CO_2 in PET is well known in the dye technology literature, and PET is expected to be readily plasticized by sc-CO_2. Some authors have examined the effect of sc-CO_2 on the drawability of PET fibers. In the studies by Lesser [7], the fiber surfaces of air drawn and sc-CO_2 drawn fiber samples have equal surface smoothness and diameters for a given draw ratio. The presence of sc-CO_2 reduced the entanglement density, permitted chain slippage in the amorphous phase, and prevented strain-induced crystallization. The observed effect was a dramatically increased final draw ratio. The increased drawability did not have a positive effect on the orientation of PET chains and the ultimate tensile modulus improved by only 10% when drawn by a factor of 12 at 200°C.

Some preliminary results have been outlined by the method of Nguyen and Baird and applied to PET-nanoclay composites in injection molded form. The results show for

a 3 wt% addition of Cloisite 20A and 30B that an increase results in modulus and toughness compared to direct melt compounding. As well the degree of dispersion by XRD shows improvement when using sc-CO_2.

It is believed that the increased degree of dispersion will have two main effects in fiber spinning. One the degree of mechanical property improvement will improve at the optimum nanoclay concentration with the optimal nanoclay surfactant. Additionally, the optimum clay concentration will shift to lower loadings of clay as polymer relaxation time increases with the degree of dispersion with favorably interacting clay. Therefore when dispersion is optimized, high loadings of nanoclay will increase relaxation times, in turn raising the Deborah number during melt-spinning. High Deborah number melts are difficult to melt-spin due to the enhanced viscoelastic failure and filament breakages in the spin line during winding. Yet the benefit to mechanical properties without sacrifice to filament uniformity will be highly desirable at significantly reduced weight additions of nanoclay.

The recommendation is to spin filaments from the sc-CO_2 melt-compounded PET nanocomposites in a two step process. The pellets for fiber spinning are made by following the technique of Nguyen and Baird [6] and then spun under the conditions used in this study. At this point, one-step direct melt spinning with sc-CO_2 injection requires additional equipment to prevent foaming at the spinneret. The details of such high pressure equipment have been outlined elsewhere for the spinning of polyacrylonitrile by Baird and others [8].

5.2 The use of rod-like carbon nanofibers and nanotubes in replacement of disk-shaped layered silicate nanoclays.

Perhaps the reinforcement of polymeric fibers would be better accomplished by using a nanoparticle whose dimensions more closely resemble the filament geometry (i.e. an infinitely long rod). A 2-D disk shaped particle orients well with the fiber long axis, but the particle face is directed normal to this axis. This type of geometry and orientation of the particle can lead to non-uniform cross section issues in the thin polymer filaments. The diameter of the filament is on the order of 10 μm and the diameter of the platelets reaches nearly 1 μm. Unless the particles are well dispersed and ordered properly and evenly through out the filament, bulging of the filament can occur due to the inability of the particle platelets to pack efficiently. The underlying hope in using a rod-like filler particle is the development of a nematic microstructure with an even filament cross-section because the rods are aligned along the fiber and can pack more effectively. Therefore, greater degrees of property improvements can be obtained.

Carbon nanotubes are quickly becoming the most sought after filler materials. The tensile modulus of a single walled CNT has been estimated in the terepascal range. In addition the combination of CNT low density and high aspect ratio make these particle excellent candidates for use in polymer composites. Yet as it was discussed in the literature review section of this work, the full use of CNT can not be realized without overcoming the exceptional difficulty of dispersing them into a polymer matrix.

Fornes et al [9] looked at the morphology and mechanical properties of CNT dispersions in polycarbonate fibers. The authors found that the high mechanical property

improvements obtained with the addition of multi-walled and single-walled CNTs fell short of micromechanical estimates for fully aligned, exfoliated particles. The authors concluded based on efficiency predictions that the nanotubes should be kept short (~300 nm) in length to avoid the "nesting" or entanglement of long nanotubes. The nesting of CNTs makes them difficult to disperse in the polymer matrix. Additionally, it was unclear how the polycarbonate interacted with the nanotubes, an some deviation between the calculations and observed results was placed on imperfect adhesion of polymer to filler.

Lee et al. [10] has examined the dispersion of multi-walled CNTs in PET, but no mechanical properties of the formed articles were reported. From SEM images of the pelletized, thick strand and film cast samples, the authors noted that un-modified MWNTs are significantly agglomerated in PET. The authors used phosphoric acid to add terephthalic acid functional groups to the particle surfaces. Then, they polymerized ethylene glycol and terephthalic acid to build the PET matrix in the presence of the nanotubes. The dispersion of MWNTs in PET was much improved by the surface modification. Therefore it is suspected that there should be some considerable mechanical property improvement with the addition of CNTs in PET by either the direct coupling of polymer and particle of the enhanced degree of crystallinity in the particle filled samples.

CNTs have been widely explored as filler particles by academics, but the prohibitively high price of CNTs has limited industrial application. The alternative is to select carbon nanofibers, CNFs, which are considerably lower in price but not as cheap as layered silicates. CNFs have a similar geometry to CNTs, but larger diameter (~100-500

nm.) Furthermore, CNFs are not single molecule particles like CNTs, and therefore the property improvement is theoretically not as great.

The recommendation is to replace the layered-silicate nanoparticles with rod-like carbon nanofibers as fillers for PET fibers. The procedure for producing and testing the PET nanocomposite fibers would follow that detailed in this work for nanoclays. Successful attempts with CNFs would warrant studies with CNTs.

5.3 Simulation of the melt spinning dynamics of nanoparticle filled viscous poly-condensate polymers.

A benefit of modeling polymer processing operations such as melt spinning is the ability to predict structure and properties with out repetitive experimentation. Melt spinning is usually modeled as a 1-D radially uniform process by the thin filament approximation using a Newtonian or viscoelastic constitutive equation. Typically, these models decouple stress and deformation from crystallization and force the solidification point of the melt in the spin line at the glass transition temperature. As shown in this thesis nanoparticles significantly affect the crystallization behavior of PET. A suitable model, then, must include the effects of crystallization. Furthermore, nanoclays influence the chain conformations of PET and entanglement density. A second requirement for a suitable model is the appropriate treatment of the nanofiller particles into a constitutive equation for the relation of stress and deformation.

The modeling efforts of non-isothermal unfilled polymer melt spinning is reviewed continually in the literature, with each new attempt coming closer to predicting real results but increasing in complexity. Simple Newtonian fluid models cannot account for non-linear viscoelastic behavior such as the propagation of neck-like deformation at high spinning speeds. Additionally, Newtonian models lack a molecular basis such that orientation and crystallinity can not be predicted at high speeds. Several studies have examined fiber spinning with various viscoelastic models (i.e. Maxwell, White-Metzner, Leonov, Phan Thien Tanner, etc.) Yet, as observed by Doufas and McHugh [11], each has

their own faults, namely the inability to successfully handle stress of "flow" induced crystallization with increasing spinning speed.

Doufas and McHugh [11] applied previously developed stress induced crystallization microstructural modeling [12] to melt spinning of polymeric fibers. Their model claims to capture the effects of non-homogeneous, non-isothermal flow incorporating viscoelasticity, crystallization, air drag, inertia, and surface tension. Below the onset of crystallization temperature, the constitutive behavior results from the amorphous and crystalline phases and the rate of crystallization. The authors stated that the two phases act in parallel, such that the velocity gradient is the same for both phases and the system stress is the addition of the individual phase extra stresses. The results of their simulation using a Giesekus fluid model for the amorphous polymer agreed well with data provide from polyamide 6 spinning.

In terms of polymer nanocomposite systems, the rheological constitutive equation must account for the presence of the filler particles as well as capture accurate behavior during elongational flow (an attribute not represented in every rheological constitutive model). Previous modeling efforts of nanocomposite melts were reviewed earlier in this work with the general opinion that much is not understood of how nanoparticles and polymer interact. However, recent efforts by Baird and Eberle [13] have shown that the rheology and orientation of short glass fibers can be accurately predicted using Doi theory. Progression of this theory to nanoparticle systems shows promise to model the rheological phenomena in fiber spinning. The general scheme of Doufas and McHugh could be followed with the replacement of the Giesekus model with that of Doi and the arguments made by Baird and Eberle.

Nanoclays are well known to influence to crystallization of semicrystalline polymers. The general approach modeling non-isothermal crystallization behavior is through differential form of the Nakamura equation described earlier in the literature review section of this work. There is not any immediate reason to assume the crystallization behavior of polymers in the presence of nanoclay could not be modeled by use of the Nakamura equation. Indeed, isothermal crystallization studies with nanoclays in PET have shown good agreement with Avrami theory, which is the basis of Nakamura's derivation. The work of Doufas and McHugh links degree of crystallinity, x, to stress, $\underline{\underline{\tau}}$, through a substantial derivative as follows:

$$\frac{Dx}{Dt} = mK_{av}(T)\left[-\ln(1-x)\right]^{(m-1/m)}(1-x)\exp\left(\xi\frac{tr\,\underline{\underline{\tau}}}{G}\right)$$

where m and $K_{av}(T)$ are the Avrami exponent and constant respectively, ξ and G are a model parameter and the shear modulus respectively. For fiber spinning at high speeds the crystallization is assumed rod-like in nature, which make m equal to unity and simplifies the dimensionality of the model. Therefore $K_{av}(T)$ is the term of interest that can vary with particle physical and chemical properties including particle dispersion.

Logically, model validation is required to assess the applicability to real systems. Attempts at high speed spinning of PET nanocomposite fibers need to be made with varying nanoclay types, dispersions, etc. A study following the highly regarded work of Haberkorn et al. [14] is recommended with nanoparticles. The spinning of polyamide 66 and polyamide 6 was examined by in-line measurements of orientation and crystallinity through laser light scattering, infrared radiation, and wide angle x-ray scattering.

5.4 References

1. Nguyen, Q. T.; Baird, D. G., Preparation of polymer-clay nanocomposite and their properties. *Adv. Polymer Techn.* **2006,** 25, 270-285.
2. Davis, C. H.; Mathias, L. J.; Gilman, J. W.; Schiraldi, D. A.; Shields, J. R.; Trulove, P.; Sutto, T. E.; Delong, H. C., Effects of Melt-Processing Conditions on the Quality of Poly(ethylene terephthalate) Montmorillonite Clay Nanocomposites. *J. Polym. Sci.: Part B. Polym. Phys.* **2002,** 40, 2661-2666.
3. Sanchez-Solis, A.; Romero-Ibarra, I.; Estrada, M. R.; Calderas, F.; Manero, O., Mechanical and Rheological Studies on Polyethylene Terephthalate-Montmorillonite Nanocomposites. *Polym. Eng. & Sci.* **2004,** 44, 1094-1102.
4. Fornes, T. D.; Yoon, P. J.; Keskkula, H.; Paul, D. R., Nylon 6 nanocomposites: The effect of matrix molecular weight,. *Polymer* **2001,** 42, 9929-9940.
5. Chu, D.; Nguyen, Q. T.; Baird, D. G., Effect of matrix molecular weight on the dispersion of nanoclay in unmodified high density polyethylene. *Polymer Composites* **2007,** 28, 499-511.
6. Nguyen, Q. T.; Baird, D. G., An improved technique for exfoliating and dispersing nanoclay particles in polymer matrices using super-critical carbon dioxide. *Polymer* **2007,** 48, 6923-6933.
7. Lesser, A. J.; Manuel, G. L., Polymer Clay Nanocomposites Prepared in Supercritical Carbon Dioxide. *Ann. Tech. Conf. Society of Plastic Engineers, Technical Papers* **2004**, 1528-1532.
8. Bortner, M. J. Melt Processing of Metastable Acrylic Copolymer Carbon Precursors. Virginia Tech, Blacksburg, 2003.
9. Fornes, T. D.; Baur, J. W.; Sabba, Y.; Thomas, E. L., Morphology and properties of melt spun polycarbonate fibers containing single- and multi-walled carbon nanotubes. *Polymer* **2006,** 47, 1704-1714.
10. Lee, W.-J.; Oh, S.-J.; Choi, J.-Y.; Kim, J. W.; Han, J.; Tan, L.-S.; Baek, J.-B., In situ synthesis of PET in ethylene glycol containing terephthalic acid and functionalized multiwalled carbon nanotubes as an approach to MWNT/PET nanocomposites. *Chem. Mater.* **2005,** 17, 5057-5064.
11. Doufas, A. K.; McHugh, A. J.; Miller, C., Simulation of melt spinning including flow-induced crystallization Part 1. Model development and predictions. *J. Non-Newt. Fluid Mech.* **2000,** 92, 27-66.
12. McHugh, A. J., Mechanisms of flow induced crystallization. *Polym. Eng Sci.* **1982,** 22, 15-26.
13. Eberle, A. P. R.; Baird, D. G.; Wapperom, P. In *Modeling the rheology and orientation distribution of short glass fibers suspended in polymeric fluids: simple shear flow.*, Annual Technical Conference - Society of Plastics Engineers, Cincinnati, 2007; Cincinnati, 2007; pp 2823-2827.
14. Haberkorn, H.; Hahn, K.; Breuer, H.; Dorrer, H.-D.; Matthies, P., On the necklike deformation in high speed spun polyamides. *J. Appl. Polym. Sci.* **1993,** 47, 1551-1579.

APPENDIX A. MATERIALS AND METHODS SUMMARY.

A.1 Materials Summary

The three types of PET studied are listed in Table A.1. Listed next to the polyesters are their respective molecular weight averages in alternate forms, e.g. intrinsic viscosity (~ viscosity average molecular weight) and zero shear viscosity (~ weight average molecular weight.) Some of the associated physical properties of PET are listed in Table A.2.

All results disclosed earlier were obtained by using PF-601. Any reference to "pure PET" is PF-601 grade PET.

Table 3.1. Three grades of PET examined in this work and their related molecular weight averages.

Designation and Origin of Pellet	Appearance and crystallinity	Intrinsic Viscosity (g/dL)	Zero shear viscosity at 285 °C (Pa s)	M_n (g/mol)
PF-601 (Performance Fibers, USA)	green, amorphous	0.96	1550	30,000
WB-low (World Bright, China)	clear, amorphous	0.60	340	16,500
WB-high (World Bright, China	white opaque, crystalline	1.02	2750	32,000

Table A.2. Some physical properties of PET

Glass Transition Temperature, T_g	67-75 °C
Peak Crystallization Temperature, T_c	180-190 °C
Melting Temperature, T_m	250-260 °C
Entanglement Molecular Weight, M_e	3300 g/mol

The three types of nanoclay used in this study are listed in table A.3 with their respective modifier chemical formulas and nanoclay physical properties. The first nanoclay in table A.3 is the unmodified filler, in which no organic modifier has been used. From this type of clay, compared to a modified one such as entry 2, one may discern whether an organic modifier on the clay surface is necessary for exfoliation when melt blended with PET. The property of a charge exchange capacity or cation exchange capacity (CEC) is a measure of the amount of displaceable interstitial or interlayer cations in the form of alkaline metals or quaternary ammonium salts within the clay and serves as measure of surfactant concentration.

Table A.3. Montmorillonite nanoclays used in this study and their related properties

Clay Designation	Surfactant	CEC (meq/100g)	Interlayer Spacing (nm)	Bulk Density (g/mL)
Cloisite Na^+	none	92.6	1.17	2.86
Cloisite 30B	$CH_3 - N^+ - T$ (T = CH_2CH_2OH, CH_2CH_2OH) Where T is Tallow (~65% C18; ~30% C16; ~5% C14) *Anion: Chloride*	90	1.85	1.98
Cloisite 20A	$CH_3 - N^+ - HT$ (HT, CH_3) Where HT is Hydrogenated Tallow (~65% C18; ~30% C16; ~5% C14) *Anion: Chloride*	95	2.42	1.77

The surfactants in entries 2 and 3 of table A.3 offer different possibilities for intermolecular interactions with the PET polymer chain. Both surfactants are quaternary alkyl ammonium salts with low decomposition temperatures, but as shown in the table

both types of surfactant modified clay increase the interlayer spacing of the gallery, in which to ease the thermodynamic and geometric restrictions on the intercalation of polymer chains. The surfactant on entry 2 has dual hydroxyl groups that on a physical perspective could offer potential hydrogen bonding with the PET carbonyl group. The surfactant in entry 3 is a double long alkyl chain that can interact with the PET chain by van der Waals forces with the non-polar phenyl ring or ethylene glycol group. It is therefore presupposed that on the basis of physical phenomena that the hydroxyl modified clay should offer the stronger interactions with PET and thus lead to greater property improvements. However, chemically, the hydroxyl groups create matrix stability issues during the several processing steps required to form a nanocomposite fiber.

A.2 Methods Summary: US Patent application #60/991550 2007 by Baird, Litchfield, and Rim

Our technique of producing high strength and modulus polymer nanocomposite fibers uniquely combines existing methods in polymer nanocomposite generation (i.e. melt-intercalation) and fiber spinning and formation. But, it is found unexpectedly that an optimum concentration of 1 weight % of nanoparticles the strength of the fiber increased by 70% and the Young's modulus increased by 30%. For a schematic representation of the procedure described here, see figure 1. Our method begins with the selection of appropriately surfaced treated, high aspect-ratio (length or width >> thickness) nanoparticles that are then dry-blended with a preferably high molecular

weight polymer matrix.* This process coats the polymer chips with clay in the desired mass ratio of nanoparticles. This mixture is then dried for up to 24 hrs to remove all moisture from the nanoparticles and polymer, which is a key step to maintain a minimum of molecular weight loss of the polymer phase during melt-processing. The dried mixture is then blanketed with an inert atmosphere and is fed to an extruder (i.e. single or twin screw) that compounds the mixture at an elevated temperature, typically above the melting point of the polymer but below the degradation temperature of the nanoparticle. This extrusion melt-compounding or melt-intercalation process mixes the molten polymer and nanoparticles together to form the nanocomposite material, which is cooled and pelletized. This extrusion process is described in its most basic form in Giannelis et al. [Advanced Materials 1996, vol 8, p. 29.] However, the extrusion method of this technique can be done by single-screw or twin-screw extruders or melt-mixed by other "static" methods such as by Brabender mixers, and etc. The use of dispersion aids or "exfoliation" aids that help in creating the greatest dispersion of nanoparticles within this matrix can be used in this step of the technique. For examples of such agents and how they are used see US patent application 2006252871.

After the initial polymer nanocomposite pellets have been formed by a given melt-compounding method, the chips are analyzed for alterations to polymer molecular weight. The changes in molecular weight may arise from thermo-oxidative degradation or hydrolysis if the polymer is moisture sensitive, for example poly(ethylene terephthalate). The molecular weight is analyzed by appropriate methods known in the art, for instance by viscometry or shear rheology. Any lost molecular weight is then built

* To achieve high degrees of dispersion, it is best to treat the nanoparticles with an organic surfactant that will interact favorably with the polymer matrix. For example, a polar surfactant may be used with a polymer capable of hydrogen bonding to take advantage of this strong intermolecular force.

back into the polymer through re-polymerization. Solid state polymerization reactions are commonly employed to re-build lost molecular weight in recycled plastic products. In this invented technique, a solid state polymerization reaction is employed to rebuild appropriate molecular weight back into the polymer nanocomposite such that the comparison of mechanical properties of pure and filled materials is on an equal polymer basis. In addition, a solid state polymerization reaction requires system temperatures just below the melting point of the polycondensate polymer at which low molecular weight impurities, such as cyclic-oligomer compounds, are removed and an overall more stable nanocomposite chip is formed.

The re-polymerized polymer nanocomposite chips are then dried and immersed in an inert atmosphere and used in a melt-spinning process. In this step the polymer nanocomposite fibers are formed. The pellets are conveyed and melted under shear stresses imparted by an extruder. The molten polymer nanocomposite then passes through a spinning pack to produce thin filaments.[†] The extruded filaments are cooled as they descend from the die exit. The cooled filaments are then wound around a bobbin or tube that rotates under the power of an electric motor. The winding device is capable of taking-up polymer nanocomposite fiber from 1-1500 m/min, but larger winding devices can be employed to reach higher take-up speeds. Higher take-up speeds create larger amounts of aerodynamic drag on the filaments which in-turn leads to higher degrees of orientation and at a critical velocity induces crystallization of the polymer phase. These

[†] The components of a typical spinning pack are the filter media, filter media support, and spinneret. The filtering components remove debris and large particulate agglomerates from the melt (filtering media we used for pure and nanocomposite samples were glass beads of 5-2 mm diameter and stainless steel support meshes with at least 60 μm wide openings.) The spinneret used was a 10 hole die of 508 μm diameter. The molten polymer is pushed through the spinneret to form the fine filaments. Larger spinnerets with greater numbers of holes and different filter components can be applied in our method, such that the nanoparticles are not filtered from the melt.

factors improve the mechanical integrity of polymeric fibers; although it has been shown in the current literature that these factors do not improve properties in nanocomposite fibers. Thus, it is un-expected that uniaxially orienting and crystallizing these nanocomposite fibers under strain will lead to a mechanical property improvement.

Contrary to this expectation, the final step in our invention is to draw or to deform the nanocomposite fiber into a more oriented form. The bobbins of polymer nanocomposite fiber are transferred from the melt-spinning process to continuous drawing process. The drawing process used here is well known in the art and consists of two sets of rollers with a heater located between the sets in which the fibers pass over or through. The first set of rollers, which transfer fiber from the feed bobbin, operates at a slower rotational velocity than the second set of rollers, which are located after the oven, which stretch and attenuate the fiber and cause the orientation of the polymer molecules. Above the polymer's glass transition temperature and at high stretching or drawing rates, strain-induced crystallization progresses to create a network-type structure that percolates the fiber. Therefore, the polymer nanocomposite fibers manufactured by this technique are drawn to their maximum extents to reap the benefits of high orientation and dense crystalline networks.

The drawn polymer nanocomposite fibers are then evaluated to assess their mechanical properties by appropriate methods known in the art. It has been shown that the nanocomposite fibers produced by this sequence of methods show improvements in mechanical properties such as strength (70% at 1 wt%) and modulus (30% at 1 wt%) with little change to elongation at break and thermal shrinkage. Therefore, this method is

unique, and this method is an improvement over the current methods available for polymer nanocomposite fiber manufacturing.

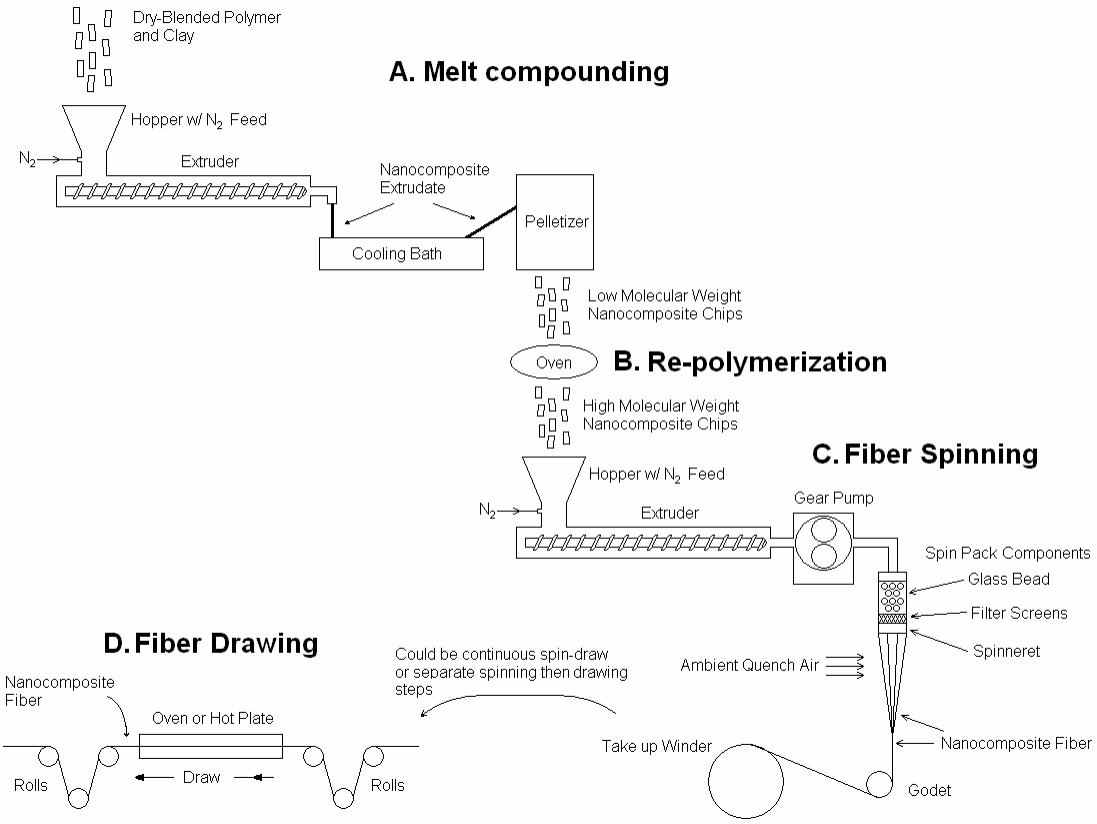

Figure 1. A Possible Schematic Representation of the Invented Method to Manufacture Polymer Nanocomposite Fibers of Improved Strength and Modulus.

APPENDIX B. RHEOLOGICAL DATA.

B.1 Frequency sweep data at 285 °C

SSP = Solid state polymerization

Pure PET – PF-601

	Before SSP			After SSP		
ω	G'	G"	|η*|	G'	G"	|η*|
rad/s	Pa	Pa	Pa s	Pa	Pa	Pa s
0.10000	0.46702	96.59	965.9	0.59198	151.0	1510.3
0.15848	2.2697	149.98	946.4	2.215	242.1	1527.6
0.25119	5.1026	235.51	937.8	4.324	387.3	1541.9
0.39810	9.4596	367.87	924.3	12.228	616.0	1547.5
0.63096	20.074	574.82	911.6	28.502	975.5	1546.7
1.0000	38.984	898.13	898.9	61.906	1536.1	1537.3
1.5849	76.151	1402.2	886.0	131.24	2410.3	1523.0
2.5120	140.04	2188.6	873.0	258.37	3762.3	1501.2
3.9813	267.25	3387.4	853.5	524.09	5841.9	1473.2
6.3100	487.87	5246.4	835.0	1048.2	9013.4	1438.1
10.000	938.75	8079.3	813.3	2002.7	13784	1392.8
15.850	1749.9	12339	786.3	3777.6	20840	1336.3
25.120	3264.4	18666	754.3	6960.7	31096	1268.5
39.813	5986.2	27915	717.1	12524	45653	1189.1
63.100	10742	41040	672.3	21838	65557	1095.1
100.00	18834	58982	619.2	36824	91587	987.1

1 wt% 20A

	Before SSP			After SSP		
ω	G’	G”	|η*|	G’	G”	|η*|
rad/s	Pa	Pa	Pa s	Pa	Pa	Pa s
0.10000	1.6563421	79.753456	797.70349	2.376395	200.2018	1783.095
0.15848	2.9174812	106.68741	673.40405	3.963651	301.0831	1692.006
0.25119	4.3640833	152.99449	609.32605	9.20216	458.3021	1625.228
0.39810	7.1665573	232.00972	583.0567	18.7832	710.6794	1590.378
0.63096	11.05226	357.59961	567.0199	42.66428	1101.611	1556.056
1.0000	18.065699	555.21063	555.48755	84.06075	1711.78	1526.283
1.5849	31.508354	866.20081	546.87384	166.0364	2662.98	1499.234
2.5120	51.473259	1348.8713	537.35675	323.1487	4118.428	1464.597
3.9813	102.51032	2113.8689	531.57025	632.2217	6376.269	1433.313
6.3100	200.75316	3292.6926	522.78546	1205.493	9787.119	1391.774
10.000	388.89227	5105.1655	511.95813	2273.348	14849.6	1337.8
15.850	752.74646	7868.5054	498.6991	4230.055	22345.79	1277.87
25.120	1465.9821	12060.539	483.63916	7696.762	33167.29	1207.111
39.813	2820.3613	18328.783	465.78467	13680.15	48436.67	1125.867
63.100	5326.6587	27476.441	443.54581	23618.43	69239.86	1032.528
100.00	9779.2266	40373.125	415.40613			

3 wt% 20A

	Before SSP			After SSP		
ω	G’	G”	|η*|	G’	G”	|η*|
rad/s	Pa	Pa	Pa s	Pa	Pa	Pa s
0.10000	2.311559	31.95245	320.35831	3.928414	179.7934	1786.477
0.15848	3.3054247	42.694668	270.19141	5.248075	281.3308	1763.489
0.25119	4.7329445	59.331196	236.95064	9.403791	425.8745	1684.637
0.39810	6.3331442	86.103439	216.86508	18.72227	652.863	1629.745
0.63096	8.1662312	127.58971	202.62698	38.83217	1009.036	1589.804
1.0000	11.164158	194.39339	194.70776	75.35477	1565.708	1557.117
1.5849	15.333256	298.38385	188.50783	145.9299	2429.532	1525.484
2.5120	23.752079	454.64124	181.23285	294.304	3756.705	1490.162
3.9813	37.795822	716.99847	180.34055	557.8682	5811.647	1456.75
6.3100	63.767277	1108.9049	176.02638	1070.329	8923.131	1414.84
10.000	98.659782	1721.828	172.45259	2000.347	13620.07	1367.423
15.850	193.6031	2658.6956	168.18416	3689.593	20481.17	1304.306
25.120	344.44769	4090.7898	163.42224	6710.058	30527.31	1236.021
39.813	642.16357	6273.5981	158.39807	11997.9	44806.26	1157.357
63.100	1192.8387	9559.9375	152.67795	20825.79	64485.02	1066.819
100.00	2214.1616	14374.287	145.43819	35119.99	90358.13	963.0291

5 wt% 20A

	Before SSP			After SSP		
ω	G’	G”	|η*|	G’	G”	|η*|
rad/s	Pa	Pa	Pa s	Pa	Pa	Pa s
0.10000	3.5668395	28.83083	290.50519	6.456542	153.3747	1976.86
0.15848	5.6649084	37.531605	239.49084	9.189181	231.1725	1880.923
0.25119	7.220294	51.414093	206.69041	14.44026	338.7836	1739.425
0.39810	9.5899973	72.841454	184.54733	26.69791	509.3897	1650.955
0.63096	13.01625	105.59453	168.62035	43.72223	775.5216	1586.24
1.0000	16.793222	158.45737	159.33987	72.04549	1190.956	1537.331
1.5849	21.971895	239.49763	151.74089	122.5565	1838.242	1497.749
2.5120	28.371817	364.74332	145.63759	217.8391	2836.232	1459.107
3.9813	40.150955	557.54114	140.40181	386.3081	4375.096	1421.472
6.3100	61.139088	860.16443	136.66029	711.6662	6738.676	1383.699
10.000	91.786629	1318.5062	132.16005	1308.705	10307.26	1338.678
15.850	146.68547	2023.0503	127.97153	2388.723	15700.63	1291.059
25.120	251.63403	3109.0608	124.17007	4369.028	23602.67	1231.229
39.813	439.9852	4753.2734	119.89893	7934.884	35058.36	1163.326
63.100	789.3335	7243.228	115.46819	13991.38	51246.91	1084.769
100.00	1426.4547	10887.477	109.80524	24274.24	73239.52	994.1902

1 wt% 30B

	Before SSP			After SSP		
ω	G’	G”	|η*|	G’	G”	|η*|
rad/s	Pa	Pa	Pa s	Pa	Pa	Pa s
0.10000	-0.52322102	46.068253	460.71048	1.600519	131.3008	1722.152
0.15848	-1.305017	69.848839	440.79355	2.756713	198.3644	1641.63
0.25119	1.6672941	106.24592	423.02209	5.573902	305.0643	1593.005
0.39810	0.84763628	168.9147	424.29749	14.03852	475.6965	1567.551
0.63096	2.6567001	263.91669	418.2951	30.0622	744.1767	1547.594
1.0000	5.9011526	414.54901	414.57837	61.28785	1162.843	1526.283
1.5849	12.910393	650.92462	410.76889	122.2149	1815.658	1504.378
2.5120	24.67552	1031.3752	410.6929	251.9146	2833.455	1482.673
3.9813	46.403461	1597.8004	401.49319	463.5161	4393.545	1451.888
6.3100	110.19578	2520.3787	399.80396	901.2364	6792.003	1418.718
10.000	258.43942	3926.3989	393.46069	1720.698	10412.78	1376.065
15.850	498.97296	6100.4961	386.17227	3244.348	15848.25	1326.802
25.120	990.36487	9411.5498	376.72314	6061.111	23848.65	1267.61
39.813	1969.2739	14420.674	365.56754	11084.6	35400.85	1197.98
63.100	3762.1904	21819.828	350.89676	19742.73	51569.16	1115.266
100.00	7101.3589	32422.703	331.91278			

3 wt% 30B

	Before SSP			After SSP		
ω	G’	G”	|η*|	G’	G”	|η*|
rad/s	Pa	Pa	Pa s	Pa	Pa	Pa s
0.10000	2.4385476	3.9797044	46.673756	3.630781	68.11331	1933.361
0.15848	0.69550031	22.878126	144.41798	4.677351	99.75935	1786.501
0.25119	2.4163015	31.937418	127.50774	6.606934	146.6735	1657.297
0.39810	0.5859257	50.60017	127.10968	13.48963	225.65	1608.748
0.63096	0.97001171	79.893509	126.63024	27.51844	351.0344	1579.133
1.0000	2.079134	124.81033	124.82384	62.52599	548.5645	1557.117
1.5849	3.307056	195.66348	123.46767	128.3768	859.2733	1539.086
2.5120	-3.9621994	327.63821	130.43753	296.2076	1345.713	1521.248
3.9813	7.5270262	492.9942	123.84116	549.6145	2108.505	1504.211
6.3100	24.501333	766.14056	121.47783	1157.392	3300.955	1486.697
10.000	44.159996	1186.1359	118.68707	2381.502	5135.123	1460.7
15.850	60.486916	1884.9827	118.98683	4853.16	7950.823	1429.382
25.120	139.65044	2930.6633	116.7961	9648.978	12222.87	1390.15
39.813	323.45483	4593.5474	115.66238	18933.18	18616.55	1341.719
63.100	552.52838	7173.792	114.02491	36251.47	27968.17	1280.366
100.00	1133.6715	11053.864	111.11846	67248.04	41118.43	1199.912

5 wt% 30B

	Before SSP			After SSP		
ω	G’	G”	|η*|	G’	G”	|η*|
rad/s	Pa	Pa	Pa s	Pa	Pa	Pa s
0.10000	-0.43966317	10.505489	105.14645	15.93136	105.6702	2177.71
0.15848	1.1813492	14.324224	90.686638	16.85591	147.9236	1949.845
0.25119	2.0521564	19.173779	76.767677	20.53183	199.9205	1799.773
0.39810	3.5120828	29.61586	74.912514	27.69668	294.3499	1671.421
0.63096	5.5641928	43.958199	70.223976	38.47294	441.1646	1580.445
1.0000	7.4797926	66.062531	66.482597	62.52599	680.118	1537.331
1.5849	10.593544	100.6649	63.863262	107.1889	1053.724	1502.901
2.5120	17.570951	147.94431	59.308388	220.2887	1636.405	1472.972
3.9813	12.902653	231.03975	58.121319	406.1571	2544.437	1445.41
6.3100	13.70655	371.2428	58.873581	794.1771	3965.542	1421.981
10.000	59.368736	581.04767	58.403	1647.121	6141.451	1390.892
15.850	43.685364	881.33978	55.672955	3324.921	9471.97	1355.668
25.120	81.446167	1385.0225	55.23016	6657.262	14498.98	1312.886
39.813	129.85327	2152.467	54.162075	13132.49	22008.06	1263.005
63.100	218.94127	3339.3123	53.034084	25264.6	32963.16	1201.971
100.00	414.15036	5150.3525	51.669773	47046.43	48275.87	1122.826

1 wt% Na^+

	Before SSP			After SSP		
ω	G’	G”	|η*|	G’	G”	|η*|
rad/s	Pa	Pa	Pa s	Pa	Pa	Pa s
0.10000	0.61727357	75.068947	750.71204	1.007724	128.7659	1564.434
0.15848	1.7156689	121.24515	765.08221	5.648793	219.8232	1565.217
0.25119	3.7086971	193.67775	771.18164	14.06824	357.6043	1607.286
0.39810	9.0894709	307.64764	773.10876	31.14404	562.0552	1595.143
0.63096	18.648859	485.74008	770.40253	61.14884	872.6332	1564.035
1.0000	37.558666	761.04041	761.94336	112.0905	1348.328	1526.283
1.5849	70.018127	1188.3806	751.08575	195.9263	2078.696	1486.108
2.5120	126.07462	1844.8584	736.12408	339.1368	3201.867	1445.97
3.9813	231.7045	2873.646	724.12408	585.9441	4920.45	1404.082
6.3100	427.0791	4452.6377	708.8797	1030.782	7516.48	1356.389
10.000	783.30939	6869.5249	691.35333	1838.136	11414.67	1304.211
15.850	1444.9333	10516.251	669.71533	3273.668	17197.8	1246.026
25.120	2667.8398	15964.825	644.33948	5789.985	25617.55	1179.461
39.813	4875.1187	23956.207	614.04388	10163.93	37630.91	1104.49
63.100	8793.5479	35395.398	577.98779	17482.03	54239.73	1018.833
100.00	15489.566	51115.922	534.11273			

3 wt% Na^+

	Before SSP			After SSP		
ω	G’	G”	|η*|	G’	G”	|η*|
rad/s	Pa	Pa	Pa s	Pa	Pa	Pa s
0.10000	-0.25894192	60.796608	607.9693	1.544392	202.879	1685.672
0.15848	1.1673477	101.2298	638.7597	7.351618	313.6714	1644.824
0.25119	3.5197008	163.23592	650.00092	17.73301	489.1383	1618.972
0.39810	8.0857229	260.73523	655.24841	40.54244	775.3503	1620.367
0.63096	16.286711	413.9975	656.64014	77.15339	1205.753	1590.98
1.0000	31.790037	650.60535	651.36169	141.9284	1868.791	1557.117
1.5849	58.574635	1016.8824	642.64551	253.588	2890.512	1521.06
2.5120	116.56386	1582.1334	631.53119	445.949	4445.918	1477.871
3.9813	187.16629	2454.5566	618.30756	814.6516	6847.085	1438.983
6.3100	339.793	3827.5645	608.96704	1484.065	10443.69	1388.95
10.000	636.13214	5911.9702	594.56604	2698.659	15837.62	1334.745
15.850	1130.343	9107.2666	578.99609	4863.903	23749.43	1270.774
25.120	2099.6025	13880.767	558.85046	8658.291	35139.55	1196.988
39.813	3866.5354	20974.828	535.70386	15151.3	51161.75	1113.513
63.100	7040.8887	31252.115	507.68832	25916	72898.6	1018.719
100.00	12590.977	45611.777	473.17722	42851.93	101043.4	911.9004

5 wt% Na^+

	Before SSP			After SSP		
ω	G’	G”	|η*|	G’	G”	|η*|
rad/s	Pa	Pa	Pa s	Pa	Pa	Pa s
0.10000	0.8898558	46.765415	467.737	2.454709	248.18	1793.271
0.15848	1.1197734	74.718987	471.49811	11.72767	371.5852	1694.938
0.25119	3.7563629	117.30848	467.24997	28.58963	580.7409	1672.57
0.39810	6.112586	186.87663	469.66125	55.24994	897.5952	1632.218
0.63096	10.202725	289.62668	459.30563	103.0205	1378.772	1583.34
1.0000	18.590582	453.19571	453.56302	180.4492	2119.992	1537.331
1.5849	35.520283	706.60181	446.37949	327.3247	3253.283	1490.628
2.5120	58.935127	1110.2255	442.58679	585.6886	4976.484	1441.335
3.9813	110.61684	1705.1135	429.17838	1026.517	7620.06	1395.453
6.3100	188.2531	2663.947	423.22751	1820.533	11538.48	1337.623
10.000	340.80603	4117.9917	413.17676	3251.95	17352.72	1275.587
15.850	631.27655	6375.0859	404.17825	5755.389	25800.86	1205.109
25.120	1169.8245	9783.7266	392.24435	10053.86	37898.5	1127.818
39.813	2189.9473	14912.19	378.5687	17328.23	54740.85	1042.07
63.100	4082.2886	22462.473	361.80984	29108.9	77369.45	946.5918
100.00	7498.7236	33264.586	340.99319	47400.08	106326.5	841.1664

B.2 Solid State Polymerization Data at 285 °C

Pure PET PF-601 Viscosity Data at Various Solid State Polymerization Times

ω rad/s	|η*| Pa s	|η*| Pa s	|η*| Pa s	|η*| Pa s	|η*| Pa s	|η*| Pa s
	0 hrs	10 hrs	20 hrs	30 hrs	40 hrs	50 hrs
0.10000	965.9	1728.8	***	5678.7	7047.9	8852.3
0.15848	946.4	1748.3	3117.1	5606.3	6770.5	8570.3
0.25119	937.8	1734.9	3076.0	5408.6	6597.3	8391.8
0.39810	924.3	1731.0	3030.1	5254.6	6414.5	8100.6
0.63096	911.6	1719.7	2977.9	5119.2	6210.1	7811.4
1.0000	898.9	1703.7	2911.6	4962.1	5987.2	7454.9
1.5849	886.0	1679.0	2830.7	4764.8	5708.6	7048.0
2.5120	873.0	1651.9	2742.3	4549.5	5403.1	6604.1
3.9813	853.5	1609.8	2630.6	4297.5	5063.0	6142.8
6.3100	835.0	1566.2	2510.1	4032.9	4708.0	5666.0
10.000	813.3	1507.1	2372.1	3746.2	4340.8	5178.0
15.850	786.3	1438.4	2222.2	3443.0	3953.2	4674.0
25.120	754.3	1359.7	2054.8	3121.3	3550.3	4159.2
39.813	717.1	1268.0	1873.4	2782.8	3134.2	3637.7
63.100	672.3	1162.0	1676.7	2431.0	2709.4	3113.5
100.00	619.2	1042.2	***	2071.5	2286.2	2602.0

0.5 wt% Cloisite 20A Viscosity Data at Various Solid State Polymerization Times

ω rad/s	|η*| Pa s	|η*| Pa s	|η*| Pa s	|η*| Pa s	|η*| Pa s	|η*| Pa s
	0 hrs	10 hrs	20 hrs	30 hrs	40 hrs	50 hrs
0.10000	858.02	1847.2	2649.9	3900.0	5761.4	3771.6
0.15848	843.05	1813.4	2565.2	3623.9	5314.0	3617.4
0.25119	824.97	1749.4	2485.2	3448.6	5066.9	3437.7
0.39810	815.04	1707.8	2444.5	3309.6	4867.1	3331.1
0.63096	810.81	1679.1	2389.6	3210.5	4704.6	3229.0
1.0000	803.11	1651.5	2333.7	3110.3	4553.6	3141.9
1.5849	793.68	1622.5	2280.6	3015.2	4387.3	3048.5
2.5120	781.72	1587.7	2213.4	2910.5	4202.1	2944.5
3.9813	769.93	1552.3	2148.7	2792.7	3994.9	2828.0
6.3100	755.84	1506.9	2066.3	2664.7	3768.9	2695.4
10.000	739.23	1454.7	1970.6	2518.4	3523.0	2547.5
15.850	717.64	1389.9	1863.5	2358.7	3256.5	2382.7
25.120	691.16	1315.3	1743.1	2183.3	2971.0	2201.9
39.813	659.66	1229.6	1608.6	1991.6	2669.0	2006.3
63.100	621.52	1131.5	1459.5	1785.3	2352.1	1794.8
100.00	575.09	1019.1	1295.5	1563.3	2022.8	1569.5

1 wt% Cloisite 20A Viscosity Data at Various Solid State Polymerization Times

ω rad/s	|η*| Pa s	|η*| Pa s	|η*| Pa s	|η*| Pa s	|η*| Pa s	|η*| Pa s
	0 hrs	10 hrs	20 hrs	30 hrs	40 hrs	50 hrs
0.10000	797.70	1070.7	1612.4	2699.4	3641.9	4589.9
0.15848	673.40	988.38	1441.5	2391.3	3071.6	3813.1
0.25119	609.32	920.78	1321.6	2167.4	2754.6	3402.6
0.39810	583.05	878.26	1249.4	2031.8	2548.1	3162.0
0.63096	567.01	848.81	1203.6	1935.2	2421.2	2994.0
1.0000	555.48	827.26	1168.0	1866.6	2324.9	2863.9
1.5849	546.87	810.18	1139.7	1811.2	2242.5	2754.2
2.5120	537.35	793.46	1111.7	1758.7	2161.2	2643.9
3.9813	531.57	776.80	1086.2	1701.8	2077.4	2533.1
6.3100	522.78	759.39	1054.2	1639.5	1987.7	2411.4
10.000	511.95	738.40	1019.4	1567.6	1886.5	2276.6
15.850	498.69	713.46	978.51	1486.9	1774.9	2128.9
25.120	483.63	684.69	931.33	1396.1	1651.8	1968.7
39.813	465.78	650.80	877.59	1294.6	1517.2	1795.2
63.100	443.54	611.00	815.67	1181.9	1369.9	1608.8
100.00	415.40	562.21	743.55	1053.8	1207.9	1407.3

1.5 wt% Cloisite 20A Viscosity Data at Various Solid State Polymerization Times

ω rad/s	|η*| Pa s	|η*| Pa s	|η*| Pa s	|η*| Pa s	|η*| Pa s	|η*| Pa s
	0 hrs	10 hrs	20 hrs	30 hrs	40 hrs	50 hrs
0.10000	589.37	1124.7	1810.6	2229.8	2327.5	2263.4
0.15848	551.17	1047.3	1659.4	1975.2	2006.2	1973.7
0.25119	523.11	990.79	1540.1	1815.5	1815.6	1798.7
0.39810	507.34	953.32	1463.5	1720.4	1713.2	1701.3
0.63096	492.01	927.48	1414.8	1657.4	1640.0	1631.3
1.0000	481.86	905.97	1375.7	1608.4	1583.8	1581.7
1.5849	472.93	888.49	1342.4	1567.4	1535.1	1536.9
2.5120	469.08	865.73	1306.0	1525.4	1484.9	1496.6
3.9813	457.17	850.56	1279.1	1478.6	1436.1	1446.9
6.3100	449.70	830.05	1239.7	1431.2	1387.2	1397.6
10.000	438.24	805.82	1196.0	1374.3	1328.2	1340.9
15.850	428.24	776.97	1144.2	1311.0	1260.3	1274.0
25.120	414.64	743.35	1085.6	1238.4	1187.2	1201.1
39.813	399.42	704.47	1019.3	1156.9	1105.7	1119.4
63.100	380.93	658.95	943.28	1065.0	1015.2	1028.1
100.00	358.24	604.97	855.47	959.86	912.53	924.65

3 wt% Cloisite 20A Viscosity Data at Various Solid State Polymerization Times

ω rad/s	|η*| Pa s	|η*| Pa s	|η*| Pa s	|η*| Pa s	|η*| Pa s	|η*| Pa s
	0 hrs	10 hrs	20 hrs	30 hrs	40 hrs	50 hrs
0.10000	320.36	625.94	1119.5	1678.3	2378.4	2366.9
0.15848	270.19	540.95	922.64	1392.9	1961.3	1936.9
0.25119	236.95	481.05	805.30	1227.4	1710.1	1698.9
0.39810	216.87	444.00	740.72	1127.2	1569.1	1564.8
0.63096	202.63	421.76	700.92	1064.4	1481.2	1481.9
1.0000	194.71	407.55	672.62	1024.0	1419.5	1424.7
1.5849	188.51	397.15	653.72	994.66	1374.2	1380.0
2.5120	181.23	389.40	638.11	963.42	1326.4	1338.9
3.9813	180.34	382.49	623.28	944.62	1288.4	1301.0
6.3100	176.03	374.12	606.23	916.30	1244.7	1256.6
10.000	172.45	365.72	589.09	884.86	1195.5	1205.8
15.850	168.18	356.37	568.60	848.16	1138.9	1149.3
25.120	163.42	345.36	546.43	808.14	1076.4	1085.8
39.813	158.40	333.03	521.04	763.32	1006.2	1015.2
63.100	152.68	318.60	491.63	712.39	928.76	936.23
100.00	145.44	299.81	455.03	651.92	839.24	845.52

5 wt% Cloisite 20A Viscosity Data at Various Solid State Polymerization Times

ω rad/s	|η*| Pa s	|η*| Pa s	|η*| Pa s	|η*| Pa s	|η*| Pa s	|η*| Pa s
	0 hrs	10 hrs	20 hrs	30 hrs	40 hrs	50 hrs
0.10000	290.51	433.99	526.79	777.50	949.68	1153.15
0.15848	239.49	355.62	441.74	615.83	732.77	924.08
0.25119	206.69	306.87	383.11	522.14	630.73	788.57
0.39810	184.55	276.71	352.39	465.35	563.91	709.76
0.63096	168.62	254.98	330.92	430.54	522.29	679.88
1.0000	159.34	240.87	316.83	407.59	496.45	652.03
1.5849	151.74	229.44	306.07	391.83	477.80	631.64
2.5120	145.64	219.19	298.94	379.16	462.00	615.20
3.9813	140.40	212.50	290.54	368.18	449.76	598.87
6.3100	136.66	205.62	284.12	358.66	438.11	582.31
10.000	132.16	198.98	275.92	347.34	424.97	562.47
15.850	127.97	192.57	267.82	336.66	410.32	541.87
25.120	124.17	185.75	258.80	324.69	395.24	518.58
39.813	119.90	178.65	249.06	311.78	378.58	492.67
63.100	115.47	171.25	238.02	297.55	359.92	463.79
100.00	109.81	161.48	223.50	279.09	336.12	427.87

1 wt% Cloisite 30B Viscosity Data at Various Solid State Polymerization Times

ω rad/s	|η*| Pa s	|η*| Pa s	|η*| Pa s	|η*| Pa s	|η*| Pa s	|η*| Pa s
	0 hrs	10 hrs	20 hrs	30 hrs	40 hrs	50 hrs
0.10000	460.71	906.56	1868.63	2625.88	4042.97	4459.01
0.15848	440.79	845.70	1675.54	2361.75	3579.49	3858.33
0.25119	423.02	803.86	1558.31	2175.50	3306.87	3545.41
0.39810	424.30	789.07	1483.81	2059.08	3135.66	3390.41
0.63096	418.30	770.81	1431.58	1979.73	3012.23	3252.55
1.0000	414.58	759.97	1394.88	1922.92	2904.62	3120.25
1.5849	410.77	749.03	1362.89	1868.05	2811.36	3013.43
2.5120	410.69	736.94	1342.43	1816.12	2714.31	2896.29
3.9813	401.49	731.22	1302.85	1759.48	2596.18	2771.75
6.3100	399.80	715.05	1262.71	1695.56	2472.34	2628.95
10.000	393.46	698.28	1219.52	1619.62	2333.40	2475.70
15.850	386.17	678.00	1166.68	1533.44	2181.15	2307.14
25.120	376.72	654.04	1106.19	1438.26	2015.68	2125.83
39.813	365.57	624.55	1036.74	1332.26	1838.13	1933.31
63.100	350.90	589.19	957.53	1214.75	1647.05	1727.50
100.00	331.91	545.76	865.97	1083.40	***	1508.41

3 wt% Cloisite 30B Viscosity Data at Various Solid State Polymerization Times

ω rad/s	|η*| Pa s	|η*| Pa s	|η*| Pa s	|η*| Pa s	|η*| Pa s	|η*| Pa s
	0 hrs	10 hrs	20 hrs	30 hrs	40 hrs	50 hrs
0.10000	46.67	416.55	1074.82	1506.60	1465.39	1657.63
0.15848	144.42	359.83	912.97	1284.36	1242.82	1421.89
0.25119	127.51	327.14	848.44	1174.55	1157.42	1312.23
0.39810	127.11	311.20	801.65	1103.09	1093.00	1210.00
0.63096	126.63	301.75	772.95	1062.74	1056.59	1166.28
1.0000	124.82	294.32	754.79	1031.44	1026.69	1135.33
1.5849	123.47	289.58	741.97	1011.49	1007.71	1112.33
2.5120	130.44	280.48	730.14	997.09	987.63	1091.87
3.9813	123.84	281.93	716.11	976.05	971.27	1071.25
6.3100	121.48	279.90	706.00	952.27	952.04	1048.50
10.000	118.69	275.43	689.16	927.28	925.52	1014.74
15.850	118.99	270.82	669.33	894.69	893.48	976.55
25.120	116.80	265.50	645.68	856.10	855.48	932.26
39.813	115.66	259.18	617.56	810.98	811.17	880.70
63.100	114.02	251.35	583.53	758.49	758.81	820.73
100.00	111.12	240.59	541.20	695.36	696.23	749.54

5 wt% Cloisite 30B Viscosity Data at Various Solid State Polymerization Times

ω rad/s	|η*| Pa s	|η*| Pa s	|η*| Pa s	|η*| Pa s	|η*| Pa s	|η*| Pa s
	0 hrs	10 hrs	20 hrs	30 hrs	40 hrs	50 hrs
0.10000	105.15	305.12	693.18	1008.85	1041.69	844.43
0.15848	90.69	264.08	580.11	861.64	891.97	702.80
0.25119	76.77	237.37	520.98	777.75	802.86	632.03
0.39810	74.91	225.45	488.14	722.64	754.52	577.55
0.63096	70.22	218.43	463.14	693.64	722.77	553.27
1.0000	66.48	212.23	449.72	674.66	700.95	537.37
1.5849	63.86	208.00	439.39	659.76	687.68	526.73
2.5120	59.31	201.97	431.59	645.63	677.04	518.53
3.9813	58.12	202.14	424.82	637.18	662.59	508.32
6.3100	58.87	198.62	418.03	624.35	652.09	500.15
10.000	58.40	194.99	410.75	611.03	636.21	491.39
15.850	55.67	192.63	402.08	594.83	620.78	479.49
25.120	55.23	189.38	391.96	575.96	598.87	465.44
39.813	54.16	185.70	379.39	551.53	574.61	448.80
63.100	53.03	180.82	364.33	523.67	544.66	428.36
100.00	51.67	174.25	344.68	488.29	507.30	402.58

1 wt% Cloisite Na^+ Viscosity Data at Various Solid State Polymerization Times

ω rad/s	|η*| Pa s	|η*| Pa s	|η*| Pa s	|η*| Pa s	|η*| Pa s	|η*| Pa s
	0 hrs	10 hrs	20 hrs	30 hrs	40 hrs	50 hrs
0.10000	750.7	1287.7	3039.5	4096.0	5697.8	6245.0
0.15848	765.1	1387.4	3004.0	4038.0	5566.1	6131.7
0.25119	771.2	1424.7	2927.6	3946.1	5468.4	5948.4
0.39810	773.1	1414.0	2889.4	3831.0	5360.4	5822.9
0.63096	770.4	1386.4	2825.0	3686.6	5194.8	5629.0
1.0000	761.9	1352.9	2765.5	3547.8	5004.0	5413.2
1.5849	751.1	1317.3	2690.1	3392.1	4784.6	5161.1
2.5120	736.1	1281.7	2602.9	3226.0	4539.5	4882.0
3.9813	724.1	1244.6	2504.1	3048.4	4279.6	4584.8
6.3100	708.9	1202.3	2394.3	2863.5	3998.7	4268.8
10.000	691.4	1156.1	2267.2	2659.7	3707.3	3934.7
15.850	669.7	1104.5	2128.7	2441.3	3393.5	3583.7
25.120	644.3	1045.5	1973.6	2210.3	3065.7	3216.4
39.813	614.0	979.0	1803.6	1967.0	2721.4	2838.8
63.100	578.0	903.1	1618.0	1716.7	2366.9	2456.3
100.00	534.1	1287.7	1418.1	1459.1	2003.2	2069.5

3 wt% Cloisite Na^+ Viscosity Data at Various Solid State Polymerization Times

ω rad/s	|η*| Pa s	|η*| Pa s	|η*| Pa s	|η*| Pa s	|η*| Pa s	|η*| Pa s
	0 hrs	10 hrs	20 hrs	30 hrs	40 hrs	50 hrs
0.10000	608.0	1017.1	2028.8	3478.0	4521.8	4757.5
0.15848	638.8	1038.1	1979.7	3477.2	4376.3	4602.3
0.25119	650.0	1046.6	1948.6	3375.8	4279.1	4477.4
0.39810	655.2	1050.3	1950.2	3342.6	4159.2	4341.6
0.63096	656.6	1042.3	1914.9	3265.1	4056.9	4202.7
1.0000	651.4	1029.3	1874.1	3177.7	3920.7	4060.9
1.5849	642.6	1011.3	1830.7	3079.2	3770.9	3893.9
2.5120	631.5	984.8	1778.7	2971.8	3614.7	3714.0
3.9813	618.3	973.8	1731.9	2852.1	3437.5	3525.5
6.3100	609.0	948.4	1671.7	2717.6	3247.9	3316.3
10.000	594.6	924.3	1606.5	2569.5	3043.1	3094.3
15.850	579.0	892.4	1529.5	2405.1	2822.0	2857.9
25.120	558.9	855.6	1440.7	2224.7	2585.5	2607.0
39.813	535.7	812.2	1340.2	2026.8	2333.4	2341.1
63.100	507.7	760.1	1226.1	1813.1	2066.2	2063.2
100.00	473.2	698.2	1097.5	1584.3	1785.3	1775.0

5 wt% Cloisite Na^+ Viscosity Data at Various Solid State Polymerization Times

ω rad/s	|η*| Pa s	|η*| Pa s	|η*| Pa s	|η*| Pa s	|η*| Pa s	|η*| Pa s
	0 hrs	10 hrs	20 hrs	30 hrs	40 hrs	50 hrs
0.10000	467.7	801.8	1407.9	2481.8	3615.9	4421.8
0.15848	471.5	805.8	1393.7	2345.7	3536.0	4297.5
0.25119	467.2	806.8	1384.7	2314.8	3459.2	4152.1
0.39810	469.7	797.4	1371.8	2258.9	3352.7	4004.2
0.63096	459.3	785.3	1346.4	2191.3	3256.8	3871.5
1.0000	453.6	770.6	1321.0	2127.6	3153.7	3709.5
1.5849	446.4	756.2	1293.9	2063.0	3049.3	3558.4
2.5120	442.6	738.4	1262.1	1994.7	2942.4	3399.6
3.9813	429.2	720.9	1233.7	1931.2	2817.3	3236.5
6.3100	423.2	707.7	1198.4	1851.2	2687.0	3052.8
10.000	413.2	689.6	1160.3	1765.4	2540.3	2859.9
15.850	404.2	667.5	1115.0	1667.8	2379.7	2654.9
25.120	392.2	641.7	1062.4	1560.8	2204.0	2435.1
39.813	378.6	613.0	1001.6	1442.2	2012.1	2201.8
63.100	361.8	577.8	930.1	1310.0	1804.8	1955.2
100.00	341.0	535.5	846.7	1164.1	1581.3	1695.3

B.3 Time Sweeps at 1 rad/s, 285 °C

PURE PET – PF-601

Time sec	G' Pa	G" Pa	|η*| Pa s
6	40.6767	1517.992	1518.537
17	40.4528	1520.03	1520.568
30	42.25919	1524.909	1525.495
42	42.55096	1532.061	1532.651
55	43.1629	1533.853	1534.46
67	45.94297	1535.954	1536.641
80	46.0625	1536.811	1537.502
92	46.46927	1537.845	1538.547
105	48.54755	1535.232	1535.999
117	47.83354	1533.391	1534.137
130	47.98519	1532.25	1533.001
142	49.88644	1530.265	1531.078
155	50.29154	1528.369	1529.196
167	50.38014	1525.397	1526.228
180	50.85224	1520.006	1520.856
193	51.62122	1518.038	1518.915
206	53.1115	1515.564	1516.494
218	53.10792	1515.461	1516.392
231	55.64389	1513.903	1514.926
243	56.01216	1513.854	1514.889
256	55.74696	1516.708	1517.732
268	57.2328	1519.238	1520.316
281	58.51129	1518.678	1519.805
293	58.97169	1516.195	1517.341
306	60.62159	1518.054	1519.264
318	63.17659	1521.474	1522.785
331	63.68005	1526.854	1528.181
343	65.15817	1533.076	1534.46
356	64.38609	1534.783	1536.133
368	66.69891	1531.861	1533.312
382	68.07689	1524.956	1526.475
394	68.43214	1522.485	1524.023
407	68.61726	1516.288	1517.84
419	69.1069	1506.744	1508.328
432	67.88466	1494.042	1495.583
444	68.1582	1486.059	1487.621
457	69.42792	1480.185	1481.812
469	72.60768	1476.714	1478.498
482	72.90249	1477.195	1478.993
494	74.71198	1477.231	1479.119
507	74.40265	1476.473	1478.347
519	77.58746	1478.622	1480.656
532	76.29923	1479.963	1481.929
545	77.12231	1480.115	1482.123
558	79.05091	1482.305	1484.412
570	81.21323	1483.682	1485.903
583	82.1012	1484.957	1487.225
595	84.5916	1487.181	1489.585
608	85.32716	1488.893	1491.336

1 wt% 20A with SSP

Time sec	G' Pa	G" Pa	|η*| Pa s
7	836.2731	6123.063	6179.907
18	824.5872	6026.527	6082.678
30	797.0402	5946.76	5999.936
43	780.2496	5873.207	5924.808
56	757.8162	5810.254	5859.465
68	741.2956	5752.013	5799.584
81	728.7712	5701.492	5747.879
93	715.7211	5654.268	5699.386
106	705.957	5610.108	5654.352
118	694.0206	5567.364	5610.455
131	684.106	5534.607	5576.726
143	676.6577	5496.391	5537.886
156	664.8099	5468.952	5509.211
168	658.6295	5431.948	5471.732
181	651.7855	5403.099	5442.27
193	644.7424	5375.063	5413.593
206	637.224	5345.49	5383.336
219	634.0243	5321.411	5359.049
231	631.1357	5294.417	5331.902
244	623.2041	5271.675	5308.384
256	622.053	5250.942	5287.659
269	614.2487	5226.014	5261.988
281	609.6357	5205.951	5241.525
294	604.3246	5185.252	5220.349
306	602.0897	5166.076	5201.044
319	599.9845	5142.554	5177.436
331	594.1323	5125.002	5159.325
344	592.4943	5105.424	5139.69
356	586.9153	5087.176	5120.92
369	586.4163	5069.262	5103.068
381	579.5673	5047.838	5081.001
394	576.3052	5030.264	5063.169
407	577.528	5011.182	5044.352
419	572.0432	4993.063	5025.724
433	570.7473	4976.379	5009.002
445	565.7785	4957.109	4989.292
458	566.2099	4942.147	4974.476
470	562.049	4924.432	4956.403
483	559.8818	4908.104	4939.934
495	557.2328	4890.183	4921.828
508	557.8276	4871.612	4903.445
520	550.4912	4854.725	4885.836
533	549.9077	4833.767	4864.946
545	545.5867	4816.724	4847.525
558	546.0329	4802.317	4833.259
570	542.6874	4788.515	4819.169
583	539.9947	4772.565	4803.017
596	539.943	4756.515	4787.064
608	534.3841	4741.109	4771.13

1 wt% 20A without SSP

Time	G’	G”	|η*|
sec	Pa	Pa	Pa s
6	25.1774	1068.674	1068.971
18	23.55053	1054.275	1054.538
30	23.13665	1041.441	1041.698
43	22.70484	1030.502	1030.752
55	22.70792	1019.341	1019.594
68	21.37664	1009.384	1009.61
81	22.16188	1000.313	1000.559
93	22.45835	991.8251	992.0794
106	21.6758	983.7968	984.0356
118	22.07869	975.6057	975.8554
132	21.84959	968.4219	968.6684
145	21.9726	962.5853	962.836
156	21.4172	956.1596	956.3994
168	22.78669	949.9615	950.2347
181	22.69601	943.7783	944.0512
193	21.8854	938.675	938.9301
206	22.31579	932.7047	932.9716
218	22.65891	928.094	928.3705
231	22.21601	923.8182	924.0853
243	23.27724	918.9393	919.2341
256	23.05118	914.4245	914.715
269	23.0501	909.9723	910.2642
281	23.2826	906.0436	906.3428
294	23.48795	901.1833	901.4894
306	22.62771	897.6257	897.9109
319	24.1656	893.6749	894.0017
331	23.83877	889.6262	889.9456
344	24.49235	885.7507	886.0892
356	24.17857	882.1982	882.5295
369	24.74509	879.3508	879.6989
381	24.68612	875.3553	875.7033
394	25.75461	871.7034	872.0838
407	25.72239	868.8164	869.1971
420	26.37812	865.9495	866.3511
432	26.45024	863.1237	863.5288
445	27.14653	860.1236	860.5519
457	26.27924	857.5437	857.9463
470	27.7141	854.9365	855.3856
483	27.4056	851.8418	852.2825
495	27.09449	848.6182	849.0507
508	27.87407	847.0982	847.5566
520	28.30077	844.3859	844.8601
533	28.36238	841.621	842.0988
545	28.97785	838.5962	839.0967
558	28.60173	836.5881	837.0768
570	29.54437	834.3339	834.8568
583	30.4676	831.6978	832.2557
595	30.53561	829.4031	829.965
608	30.66758	827.4928	828.0609

5 wt% 20A with SSP

Time sec	G' Pa	G" Pa	|η*| Pa s
6	181.2763	2470.749	2477.39
18	178.1182	2417.595	2424.148
30	168.8605	2372.962	2378.962
43	164.3033	2331.024	2336.807
55	157.8091	2292.752	2298.177
68	152.2538	2254.216	2259.351
80	149.7696	2223.49	2228.529
93	146.3487	2190.648	2195.532
105	141.1876	2158.958	2163.57
118	137.9382	2131.244	2135.704
130	133.1683	2107.434	2111.637
143	130.9213	2079.942	2084.059
155	127.443	2058.752	2062.693
168	125.2406	2035.259	2039.109
180	122.7106	2014.198	2017.933
193	118.9382	1992.342	1995.889
206	117.8772	1972.545	1976.064
218	114.6012	1955.813	1959.168
231	114.0884	1934.926	1938.286
243	110.483	1915.561	1918.745
256	110.2709	1897.78	1900.981
268	108.0767	1879.828	1882.933
281	107.3032	1866.374	1869.457
293	103.5789	1848.854	1851.753
307	102.9575	1833.754	1836.642
319	102.3596	1819.138	1822.016
332	99.56548	1804.829	1807.573
344	99.5301	1790.28	1793.045
357	98.24752	1776.994	1779.708
369	94.51217	1766.142	1768.669
382	93.79528	1752.746	1755.254
394	93.48175	1740.913	1743.421
407	92.37709	1728.221	1730.688
420	92.16569	1716.404	1718.877
432	90.05946	1704.379	1706.756
445	90.23168	1691.959	1694.363
457	90.7235	1681.877	1684.322
470	88.10801	1669.381	1671.705
482	87.64105	1658.61	1660.924
495	85.55491	1647.758	1649.978
507	85.2071	1635.277	1637.495
520	83.4351	1624.16	1626.302
532	83.96515	1615.236	1617.417
545	82.66808	1605.404	1607.531
557	81.61871	1594.5	1596.588
570	81.53395	1583.38	1585.477
582	80.84883	1573.815	1575.891
595	78.9434	1562.786	1564.779
607	77.52618	1555.456	1557.387

5 wt% 20A without SSP

Time	G'	G"	|η*|
sec	Pa	Pa	Pa s
6	98.34917	1006.471	1011.264
18	75.25726	947.2668	950.2516
30	70.41296	918.2293	920.9251
43	67.09885	894.3415	896.855
55	65.45596	871.7307	874.1847
68	62.62803	850.0491	852.353
80	61.19291	829.1889	831.4439
93	58.98664	810.7534	812.8963
105	58.85116	793.4981	795.6775
118	57.31419	775.9854	778.0991
130	56.06584	758.4536	760.523
143	53.84987	743.2841	745.2322
156	53.4869	729.0127	730.9722
168	51.64867	713.5056	715.3724
181	49.59201	699.3178	701.074
193	49.47829	687.0164	688.7958
206	48.04927	674.0643	675.7747
218	47.44815	660.5155	662.2175
231	46.36652	647.1163	648.7753
243	46.05154	634.5698	636.2385
256	45.15569	625.3978	627.0259
268	44.77548	614.9067	616.5347
281	43.88171	604.1597	605.7512
293	42.58487	594.8469	596.3693
306	42.58153	585.2701	586.8171
318	42.27882	575.2871	576.8386
331	41.32381	567.9832	569.4845
345	40.77943	558.6163	560.1028
357	40.67369	550.23	551.7313
370	40.07941	542.1906	543.6699
382	39.93834	534.5131	536.0031
395	39.37896	526.5942	528.0646
407	38.90952	519.8898	521.3438
420	38.75049	512.3029	513.7664
432	38.36825	505.1995	506.6544
446	38.90139	498.0108	499.5278
459	38.56704	491.2203	492.732
471	38.67862	484.975	486.5149
484	37.15673	479.1759	480.6144
496	37.21692	473.2069	474.6681
507	36.63678	466.1945	467.6319
520	36.99017	461.6708	463.1503
532	35.90402	456.8703	458.2789
545	37.05576	450.7383	452.2589
558	36.15751	444.4627	445.931
570	36.42148	440.7171	442.2195
583	35.18296	436.106	437.5229
595	35.58762	431.2683	432.7342
608	35.90441	426.8417	428.3492

1 wt% 30B with SSP

Time sec	G' Pa	G" Pa	|η*| Pa s
6	233.0317	3655.896	3663.315
17	225.8045	3604.895	3611.96
30	219.4226	3562.245	3568.997
42	215.4256	3521.876	3528.459
55	208.4838	3488.748	3494.972
67	203.7778	3456.048	3462.05
80	198.7215	3427.252	3433.008
92	196.5016	3399.739	3405.413
105	194.4258	3370.968	3376.57
117	188.8124	3344.66	3349.985
130	187.0993	3321.52	3326.785
143	183.1502	3298.015	3303.096
155	186.2355	3281.217	3286.498
168	182.723	3257.994	3263.114
180	178.8138	3237.774	3242.708
193	176.8956	3217.308	3222.167
205	176.3796	3197.242	3202.104
218	172.0519	3178.761	3183.414
230	171.4638	3160.745	3165.393
243	169.1587	3146.66	3151.204
255	171.5182	3133.46	3138.151
268	167.5892	3121.019	3125.515
280	167.8993	3105.553	3110.088
293	168.4393	3091.041	3095.627
305	165.2216	3076.925	3081.358
319	166.6822	3062.237	3066.77
331	163.925	3049.304	3053.707
344	164.0228	3033.85	3038.281
356	164.9217	3019.704	3024.205
369	161.6138	3002.892	3007.237
381	158.1515	2989.56	2993.741
394	158.404	2977.111	2981.322
407	156.9656	2963.715	2967.868
419	157.7695	2951.604	2955.817
432	158.4422	2937.28	2941.55
444	156.5698	2925.809	2929.995
457	157.1524	2913.369	2917.605
469	155.249	2901.128	2905.279
482	155.1314	2889.016	2893.178
494	153.9616	2877.07	2881.187
507	154.743	2862.206	2866.386
519	153.6318	2851.338	2855.474
532	150.0607	2839.905	2843.867
544	150.4031	2826.739	2830.737
557	150.5163	2815.909	2819.929
569	152.5226	2805.255	2809.398
582	150.7438	2794.563	2798.626
594	148.0909	2783.283	2787.22
607	148.9839	2771.372	2775.374

1 wt% 30B without SSP

Time	G’	G”	|η*|
sec	Pa	Pa	Pa s
6	15.08239	950.6096	950.7292
18	15.48642	932.9935	933.122
30	14.82036	916.4625	916.5823
43	14.7081	902.7045	902.8243
55	14.26923	889.0944	889.2089
68	14.30252	877.8121	877.9286
80	13.49129	867.0065	867.1115
93	14.23845	857.8085	857.9267
105	12.72768	847.872	847.9675
118	13.78219	839.585	839.6981
130	13.08848	831.3355	831.4385
143	13.4814	824.3272	824.4374
155	13.71744	817.4005	817.5156
168	14.25567	811.1113	811.2366
180	13.7	804.6516	804.7682
193	14.23821	799.0152	799.142
205	13.06236	792.7861	792.8937
218	13.98471	787.4874	787.6115
230	14.11973	781.6538	781.7813
243	13.5683	777.4025	777.5209
255	13.66417	772.0924	772.2133
268	14.56461	767.3762	767.5143
281	13.73877	763.1434	763.2671
293	14.12005	758.595	758.7264
306	14.4643	754.8064	754.945
319	14.18788	749.9394	750.0736
332	15.18015	746.9424	747.0966
344	14.74729	743.5145	743.6607
357	15.06947	739.2752	739.4287
369	15.18407	736.0778	736.2344
382	14.8096	733.1148	733.2643
394	14.97784	730.4044	730.558
407	15.57022	726.8279	726.9946
419	15.42291	724.079	724.2432
432	14.63824	720.2778	720.4265
444	15.41276	717.4321	717.5977
457	15.31087	714.7211	714.8851
469	15.51772	712.1964	712.3654
482	15.84212	709.1965	709.3734
495	16.17369	706.6534	706.8385
507	16.28001	703.7875	703.9758
520	16.65455	701.4602	701.6579
532	15.98076	698.2242	698.407
545	17.01092	696.7561	696.9638
557	17.01069	693.2782	693.4869
570	16.5421	691.389	691.5869
582	16.98537	688.8174	689.0268
595	17.62241	685.777	686.0034
607	16.85329	683.4609	683.6686

5 wt% 30B with SSP

Time	G'	G"	|η*|
sec	Pa	Pa	Pa s
6	69.71929	1649.887	1651.36
20	64.20892	1607.886	1609.168
32	60.97703	1573.213	1574.394
45	56.00976	1531.497	1532.521
61	52.71115	1504.139	1505.063
72	53.19394	1479.746	1480.702
84	48.50656	1454.43	1455.238
96	48.08951	1432.085	1432.893
109	45.10073	1409.102	1409.824
121	45.2841	1388.329	1389.068
134	43.46401	1367.1	1367.79
146	42.2214	1350.067	1350.727
159	42.32338	1331.862	1332.535
171	40.01986	1316.314	1316.922
184	38.74815	1301.287	1301.863
196	38.41031	1283.359	1283.933
209	37.10062	1269.395	1269.937
221	36.79052	1254.851	1255.39
234	35.88919	1239.605	1240.125
246	35.73666	1225.289	1225.81
259	33.93307	1211.666	1212.141
271	34.60397	1197.741	1198.241
284	34.53552	1187.214	1187.716
297	32.90472	1173.666	1174.127
310	32.08495	1162.15	1162.593
322	32.12516	1150.246	1150.694
335	32.87454	1139.688	1140.162
347	31.15141	1127.09	1127.52
360	30.07505	1116.522	1116.926
373	28.5205	1104.516	1104.884
385	29.1415	1093.643	1094.032
398	29.26608	1083.418	1083.813
410	28.96835	1071.79	1072.182
423	28.48486	1059.89	1060.273
435	27.82357	1050.201	1050.57
448	26.91397	1040.454	1040.802
460	26.435	1030.453	1030.792
473	27.13245	1023.525	1023.885
485	26.73247	1013.692	1014.044
498	26.34478	1003.639	1003.985
510	26.40745	996.1757	996.5256
523	25.23622	986.0719	986.3948
535	25.24822	977.2125	977.5386
548	26.56863	967.6956	968.0602
560	25.36992	961.467	961.8017
573	24.0502	951.0781	951.3821
585	26.02006	941.9524	942.3117
598	24.41101	936.5072	936.8253
612	23.60645	927.9268	928.227

5 wt% 30B without SSP

Time	G'	G"	|η*|
sec	Pa	Pa	Pa s
6	14.65011	446.0479	446.2884
18	12.09359	417.9674	418.1423
31	13.03613	395.4362	395.651
43	12.80018	375.0702	375.2885
56	13.4427	356.2569	356.5104
68	13.86646	338.9346	339.2181
81	13.52851	322.9521	323.2353
93	12.31536	309.342	309.5871
106	13.62539	296.2853	296.5984
118	12.95074	283.5003	283.796
131	13.37433	272.0106	272.3392
144	13.07907	262.4135	262.7393
156	12.96717	251.8209	252.1545
169	13.75719	244.2275	244.6146
181	13.59426	235.6982	236.0899
194	13.74553	228.8435	229.256
206	13.72705	221.7509	222.1753
219	13.72222	214.4551	214.8937
231	13.59611	208.0989	208.5426
244	12.75495	203.231	203.6309
256	12.45617	197.5062	197.8985
269	12.31952	192.349	192.7431
281	12.86399	186.73	187.1726
294	12.6169	183.1434	183.5775
306	12.38463	178.9752	179.4032
319	12.08757	175.616	176.0315
332	11.75185	171.3491	171.7516
344	11.30056	167.4641	167.8449
357	12.2153	164.8369	165.2889
369	12.21454	161.877	162.3372
382	11.52886	158.1938	158.6133
394	11.77094	155.4922	155.9371
408	11.76228	152.6542	153.1067
420	11.09579	150.1029	150.5124
433	12.38578	147.6773	148.1958
445	11.98914	144.9664	145.4613
458	11.61203	142.8476	143.3188
470	12.55512	140.9146	141.4728
483	12.23939	138.9053	139.4435
495	12.13586	136.2089	136.7485
508	13.09993	134.6543	135.29
521	12.80409	133.3872	134.0003
533	13.31291	131.2712	131.9446
546	13.03691	128.9417	129.599
558	12.50537	128.1372	128.7459
571	12.8483	126.2294	126.8816
583	12.76572	124.7379	125.3894
596	12.35536	121.7553	122.3806
608	12.4986	120.6013	121.2472

B.4 Cooling Curves

The effect of cooling rate and frequency on the solidification of PET filled with 2 wt% Cloisite 20A.

Figure 1. Complex Viscosity as a function of temperature for PET and PET nanocomposites, 5% strain, 1 rad/s

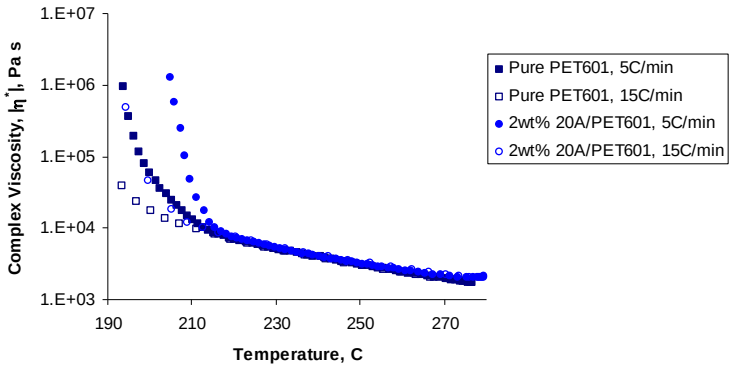

Figure 2. Complex viscosity as a function of temperature for PET and PET nanocomposites, 5% strain, 10 rad/s

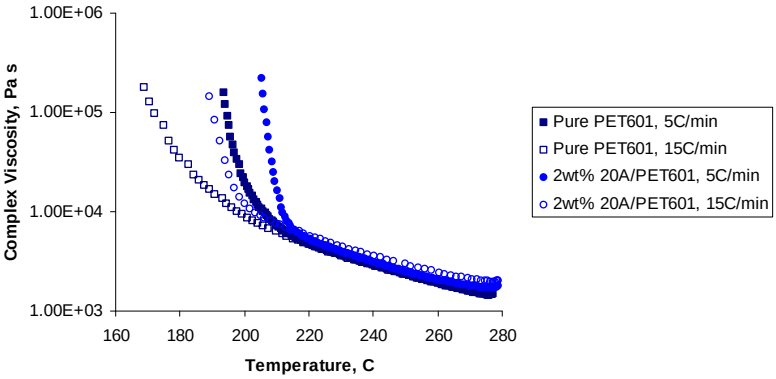

Figure 3. Complex viscosity as a function of temperature for PET and PET nanocomposites, 5% strain, 100 rad/s

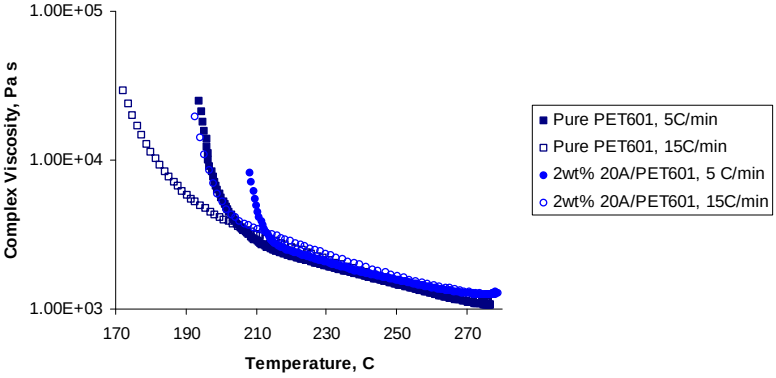

B.5 Transient Shear.

Conditions: 1 s^{-1}, 275 C, 25 mm Cone and Plate

PURE PET - PF-PET601 (1 s^{-1})

Time sec	η Pa s	N1 Pa	Torque g cm	Stress Pa
0	***	0	0	0
0.84375	1614.73	11.36945	67.35469	1614.73
1.74375	1619.013	15.2621	67.53336	1619.013
2.64375	1616.077	55.78676	67.4109	1616.077
3.54375	1614.922	77.73056	67.36272	1614.922
4.44375	1613.912	27.47475	67.32056	1613.912
5.118751	1610.976	50.42327	67.1981	1610.976
5.56875	1612.179	42.40178	67.24828	1612.179
6.01875	1609.821	68.08079	67.14991	1609.821
6.468751	1608.617	48.21389	67.09972	1608.617
6.91875	1604.671	116.8358	66.9351	1604.671
7.368751	1603.468	71.75975	66.88491	1603.468
7.593751	1604.286	72.06591	66.91904	1604.286
7.81875	1605.248	96.29907	66.95919	1605.248
8.043751	1600.724	72.06716	66.77048	1600.724
8.26875	1600.724	41.33708	66.77048	1600.724
8.493751	1601.542	86.39187	66.8046	1601.542
8.71875	1600.147	77.69932	66.74638	1600.147
8.94375	1598.943	57.49627	66.6962	1598.943
9.168751	1599.136	84.76858	66.70422	1599.136
9.39375	1597.596	52.86758	66.63998	1597.596
9.618751	1597.788	28.11832	66.64801	1597.788
9.84375	1596.826	2.493046	66.60786	1596.826
10.06875	1596.585	55.33064	66.59782	1596.585
15.01875	1593.072	112.1471	66.45126	1593.072
20.08125	1591.868	43.61457	66.40108	1591.868
25.03125	1590.473	62.83727	66.34286	1590.473
30.09375	1588.884	92.64011	66.2766	1588.884
35.04375	1587.729	70.57883	66.22842	1587.729
40.10625	1587.152	63.44334	66.20433	1587.152
44.94375	1582.964	92.9875	66.02967	1582.964

1 wt% 20A (1 s^{-1})

Time sec	η Pa s	N1 Pa	Torque g cm	Stress Pa
0	***	0	0	0
0.05625	1147.078	9.447022	47.84769	1147.078
0.16875	1757.045	-27.1533	73.29105	1757.045
0.28125	1808.929	-7.70301	75.45525	1808.929
0.39375	1830.876	-32.0716	76.37071	1830.876
0.50625	1845.7	-44.2744	76.98906	1845.7
0.61875	1856.336	-24.2813	77.43274	1856.336
0.73125	1859.898	-4.27426	77.5813	1859.898
0.84375	1864.807	5.589047	77.78608	1864.807
0.95625	1869.572	-1.29932	77.98483	1869.572
1.06875	1870.342	5.684021	78.01695	1870.342
1.18125	1870.101	43.43462	78.00691	1870.101
1.29375	1875.877	51.01873	78.24783	1875.877
1.40625	1870.919	57.8543	78.04104	1870.919
1.51875	1871.304	79.58691	78.0571	1871.304
1.63125	1874.674	64.2325	78.19763	1874.674
1.74375	1870.149	62.8029	78.00892	1870.149
1.85625	1871.112	98.98144	78.04907	1871.112
1.96875	1871.69	118.9708	78.07317	1871.69
2.08125	1867.358	124.6492	77.89248	1867.358
2.19375	1867.358	120.8728	77.89248	1867.358
2.30625	1868.369	119.1957	77.93464	1868.369
2.41875	1865.433	133.0268	77.81217	1865.433
2.531251	1865.192	142.8641	77.80214	1865.192
2.64375	1863.267	134.6689	77.72183	1863.267
2.75625	1860.475	149.8596	77.60539	1860.475
2.86875	1858.117	194.467	77.50702	1858.117
2.98125	1856.962	189.6883	77.45884	1856.962
3.093751	1856.577	169.3841	77.44277	1856.577
3.54375	1847.48	203.2495	77.06334	1847.48
3.99375	1835.833	197.1762	76.5775	1835.833
4.556251	1830.539	223.1889	76.35666	1830.539
5.00625	1822.453	232.0864	76.01939	1822.453
6.01875	1807.87	256.4395	75.41108	1807.87
7.031251	1795.693	203.2345	74.90316	1795.693
8.043751	1785.201	184.3599	74.4655	1785.201
9.056251	1774.179	179.1113	74.00576	1774.179
10.06875	1769.463	203.6794	73.80901	1769.463
15.01875	1753.917	134.7314	73.16056	1753.917
20.08125	1743.473	97.62932	72.72491	1743.473
25.03125	1729.852	147.0079	72.15675	1729.852
30.09375	1717.483	170.7387	71.6408	1717.483
35.04375	1702.852	134.4239	71.03049	1702.852
39.99375	1693.226	103.4627	70.62897	1693.226
44.94375	1689.52	162.391	70.47438	1689.52
45.0375	***	149.6122	37.70327	903.8804

3 wt% 20A (1 s^{-1})

Time sec	η Pa s	N1 Pa	Torque g cm	Stress Pa
0	***	0	0	0
0.05625	1174.692	67.38286	48.99953	1174.692
0.16875	1599.409	41.06341	66.71562	1599.409
0.28125	1635.458	21.03766	68.21932	1635.458
0.39375	1660.87	30.93189	69.27934	1660.87
0.50625	1670.111	52.88945	69.6648	1670.111
0.61875	1677.812	61.83442	69.98601	1677.812
0.73125	1684.935	56.23351	70.28313	1684.935
0.84375	1685.657	36.65715	70.31325	1685.657
0.95625	1687.823	61.92315	70.4036	1687.823
1.06875	1691.577	102.6916	70.56019	1691.577
1.18125	1690.614	47.75402	70.52004	1690.614
1.29375	1692.203	49.7922	70.58629	1692.203
1.40625	1691.962	68.04392	70.57625	1691.962
1.51875	1692.203	65.73583	70.58629	1692.203
1.63125	1690.614	71.95282	70.52004	1690.614
1.74375	1691.192	88.60062	70.54413	1691.192
1.85625	1689.652	89.05174	70.47988	1689.652
1.96875	1688.064	90.69253	70.41363	1688.064
2.08125	1688.015	92.80568	70.41162	1688.015
2.19375	1686.668	106.763	70.35541	1686.668
2.30625	1685.128	111.7491	70.29117	1685.128
2.41875	1683.732	111.7266	70.23295	1683.732
2.531251	1683.684	115.9304	70.23094	1683.684
2.64375	1682.336	138.719	70.17473	1682.336
2.75625	1678.197	133.5205	70.00208	1678.197
2.86875	1679.4	109.0224	70.05226	1679.4
2.98125	1676.224	144.1375	69.91976	1676.224
3.093751	1671.074	145.3996	69.70495	1671.074
3.54375	1667.56	165.4364	69.5584	1667.56
3.99375	1660.052	228.5486	69.24521	1660.052
4.556251	1647.25	234.172	68.71118	1647.25
5.00625	1639.164	231.5078	68.37391	1639.164
6.01875	1621.837	259.7248	67.65117	1621.837
7.031251	1604.944	303.5974	66.9465	1604.944
8.043751	1592.912	290.7211	66.4446	1592.912
9.056251	1580.302	304.5872	65.91861	1580.302
10.06875	1570.532	313.1198	65.51106	1570.532
15.01875	1537.25	189.6596	64.1228	1537.25
20.08125	1533.183	188.37	63.95316	1533.183
25.03125	1533.087	230.3331	63.94915	1533.087
30.09375	1521.079	144.3999	63.44825	1521.079
35.04375	1508.276	163.5895	62.91423	1508.276
39.99375	1494.872	203.1808	62.35511	1494.872
44.94375	1480.121	188.8198	61.73978	1480.121
45.0375	***	212.2032	32.77708	785.7825

PURE PET - PF-PET601 (10 s^{-1})

Time sec	η Pa s	N1 Pa	Torque g cm	Stress Pa
0	***	0	0	0
0.05625	1012.108	206.3668	422.1773	10121.08
0.16875	1506.416	1461.003	628.3663	15064.16
0.28125	1517.697	2856.089	633.0721	15176.97
0.39375	1515.079	3116.975	631.9799	15150.79
0.50625	1510.651	3154.005	630.1329	15106.51
0.61875	1505.299	3279.01	627.9005	15052.99
0.73125	1500.756	3379.461	626.0053	15007.56
0.84375	1495.866	3423.129	623.9656	14958.66
0.95625	1491.785	3502.227	622.2631	14917.85
1.06875	1487.087	3537.257	620.3037	14870.87
1.18125	1482.813	3527.179	618.521	14828.13
1.29375	1480.118	3482.232	617.3967	14801.18
1.40625	1477.808	3446.562	616.433	14778.08
1.51875	1474.959	3411.532	615.2446	14749.59
1.63125	1471.686	3447.602	613.8794	14716.86
1.74375	1470.415	3565.169	613.3494	14704.15
1.85625	1470.261	3491.19	613.2852	14702.61
1.96875	1469.299	3461.998	612.8836	14692.99
2.08125	1467.72	3558.691	612.2251	14677.2
2.19375	1465.833	3541.895	611.4382	14658.33
2.30625	1463.33	3492.149	610.3942	14633.31
2.41875	1461.559	3447.922	609.6554	14615.59
2.531251	1458.787	3510.864	608.499	14587.87
2.64375	1456.746	3527.739	607.6478	14567.46
2.75625	1454.051	3514.703	606.5236	14540.51
2.86875	1453.397	3552.372	606.2505	14533.97
2.98125	1451.394	3557.971	605.4153	14513.94
3.093751	1451.24	3599.879	605.3511	14512.4
3.54375	1449.161	3658.502	604.4838	14491.61
3.99375	1445.234	3641.387	602.8456	14452.34
4.556251	1443.039	3592.681	601.9301	14430.39
5.00625	1443.501	3591.322	602.1229	14435.01
6.01875	1436.455	3386.739	599.1837	14364.55
7.031251	1433.76	3275.171	598.0595	14337.6
8.043751	1432.528	3272.851	597.5455	14325.28
9.056251	1432.374	3325.237	597.4813	14323.74
10.06875	1429.832	3527.5	596.4213	14298.32
15.01875	1416.164	3372.983	590.7197	14161.64
19.96875	1405.46	3118.255	586.2548	14054.6
25.03125	1393.254	3069.549	581.1635	13932.54
30.09375	1374.503	3445.603	573.3419	13745.03
35.04375	1346.049	3408.733	561.4729	13460.49
40.10625	1330.031	3101.3	554.7916	13300.31
44.94375	1279.399	3140.649	533.6716	12793.99
45.0375	***	2827.937	249.4311	5979.744

1 wt% 20A (10 s^{-1})

Time sec	η Pa s	N1 Pa	Torque g cm	Stress Pa
0	***	0	0	0
0.05625	1170.813	266.9597	488.3774	11708.13
0.16875	1744.958	1591.031	727.8685	17449.58
0.28125	1750.81	3009.991	730.3098	17508.1
0.39375	1738.836	3566.154	725.3148	17388.36
0.50625	1725.899	3941.648	719.9184	17258.99
0.61875	1714.502	4299.467	715.1644	17145.02
0.73125	1705.03	4525.723	711.2134	17050.3
0.84375	1698.292	4642.25	708.4028	16982.92
0.95625	1692.131	4671.682	705.8331	16921.31
1.06875	1687.434	4592.424	703.8737	16874.34
1.18125	1683.198	4422.952	702.1069	16831.98
1.29375	1678.462	4340.415	700.1315	16784.62
1.40625	1675.344	4375.125	698.8305	16753.44
1.51875	1671.262	4322.1	697.1281	16712.62
1.63125	1667.951	4217.09	695.7468	16679.51
1.74375	1666.834	4076.97	695.2811	16668.34
1.85625	1665.14	3975.718	694.5744	16651.4
1.96875	1662.869	3885.344	693.6268	16628.69
2.08125	1659.442	3857.591	692.1974	16594.42
2.19375	1657.247	3869.908	691.2819	16572.47
2.30625	1655.822	3848.074	690.6877	16558.22
2.41875	1654.398	3812.084	690.0934	16543.98
2.531251	1652.858	3920.134	689.451	16528.58
2.64375	1650.663	3890.862	688.5355	16506.63
2.75625	1648.237	3906.698	687.5237	16482.37
2.86875	1646.389	3849.354	686.7528	16463.89
2.98125	1644.156	3812.724	685.8212	16441.56
3.093751	1642.462	3820.562	685.1146	16424.62
3.54375	1638.842	3850.713	683.6049	16388.42
3.99375	1636.032	3733.466	682.4324	16360.32
4.556251	1631.296	3633.974	680.4569	16312.96
5.00625	1627.06	3491.855	678.6903	16270.6
6.01875	1615.124	3433.631	673.7114	16151.24
7.031251	1610.85	3551.198	671.9287	16108.5
8.043751	1610.696	3720.35	671.8644	16106.96
9.056251	1608.194	3655.888	670.8204	16081.94
10.06875	1607.731	3689.639	670.6277	16077.31
15.01875	1575.196	3435.95	657.0563	15751.96
19.96875	1563.106	2976.96	652.0132	15631.06
25.03125	1534.305	2989.436	639.9997	15343.05
30.09375	1497.073	2993.755	624.4689	14970.73
35.04375	1424.609	3146.512	594.2424	14246.09
40.10625	1370.666	2850.676	571.7412	13706.66
44.94375	1329.313	2811.966	554.4919	13293.13
45.0375	***	2544.202	225.2007	5398.856

3 wt% 20A (10 s^{-1})

Time sec	η Pa s	N1 Pa	Torque g cm	Stress Pa
0	***	0	0	0
0.05625	1082.365	10823.65	448.0018	10823.65
0.16875	1601.469	16014.69	2149.891	16014.69
0.28125	1594.538	15945.38	3566.692	15945.38
0.39375	1571.282	15712.82	4199.793	15712.82
0.50625	1548.95	15489.5	4497.069	15489.5
0.61875	1529.275	15292.75	4623.354	15292.75
0.73125	1511.563	15115.63	4612.956	15115.63
0.84375	1497.817	14978.17	4491.791	14978.17
0.95625	1492.812	14928.12	4259.776	14928.12
1.06875	1489.039	14890.39	4144.849	14890.39
1.18125	1481.8	14818	4084.226	14818
1.29375	1475.986	14759.86	3996.89	14759.86
1.40625	1472.559	14725.59	3886.521	14725.59
1.51875	1470.826	14708.27	3744.801	14708.26
1.63125	1470.056	14700.56	3684.179	14700.56
1.74375	1470.018	14700.18	3732.805	14700.18
1.85625	1471.289	14712.89	3635.872	14712.89
1.96875	1471.905	14719.05	3558.534	14719.05
2.08125	1471.751	14717.51	3559.174	14717.51
2.19375	1470.981	14709.81	3481.276	14709.81
2.30625	1469.055	14690.55	3426.651	14690.55
2.41875	1467.669	14676.69	3422.652	14676.69
2.531251	1466.899	14668.99	3445.606	14668.99
2.64375	1465.783	14657.83	3428.331	14657.83
2.75625	1464.974	14649.74	3375.226	14649.74
2.86875	1464.204	14642.04	3375.785	14642.04
2.98125	1462.625	14626.25	3336.277	14626.25
3.093751	1461.509	14615.09	3329.079	14615.09
3.54375	1456.965	14569.65	3258.299	14569.65
3.99375	1455.117	14551.17	3339.476	14551.17
4.556251	1452.422	14524.22	3240.704	14524.22
5.00625	1450.343	14503.43	3355.231	14503.43
6.01875	1443.605	14436.05	3032.123	14436.05
7.031251	1442.488	14424.88	3125.776	14424.88
8.043751	1441.102	14411.02	3122.497	14411.02
9.056251	1439.061	14390.61	3079.869	14390.61
10.06875	1434.826	14348.26	3330.358	14348.26
15.01875	1422.389	14223.89	3151.929	14223.89
19.96875	1396.168	13961.68	3090.426	13961.68
25.03125	1386.427	13864.27	3124.816	13864.27
30.09375	1374.914	13749.14	2930.951	13749.14
35.04375	1391.586	13915.86	2856.652	13915.86
40.10625	1385.772	13857.72	2855.372	13857.72
44.94375	1373.336	13733.36	3138.892	13733.36
45.0375	***	7402.229	2747.003	10823.65

APPENDIX C. THERMAL ANALYSIS.

C.1 Thermal Shrinkage (at 177 C) for materials drawn to their maximum extents at an oven temperature of 100 C giving exit temperature of 83 C

Material	Shrinkage %	Error (95% confidence)
Pure PET	9.56	0.12
0.5 wt% 20A	14.8	0.2
1 wt% 20A	13.6	0.4
1.5 wt% 20A	13.1	0.1
3 wt% 20A	10.5	0.1
1 wt% 30B	12.4	0.4
3 wt% 30B	7.6	0.5
1 wt% Na^+	-	-
3 wt% Na^+	-	-

C.2 Thermal Shrinkage at 177 C for the Pure and 1 wt% 20A fibers drawn at various temperatures.

Material	Draw Temperature (Oven) °C	Shrinkage %	Error (95% confidence)
Pure PET	80	10.4	0.2
	100	9.6	0.1
	125	8.9	0.1
	150	6.4	0.4
1 wt% 20A	80	14.7	0.2
	100	13.6	0.4
	125	11.7	0.2
	150	8.9	0.1

C3. Determination of the exit temperature of the PET fibers through the hot air oven

Based on the design of our oven…

Assumming:
Negligible conduction through fiber due to small fiber radius
Negligible convection
Transient 1-D heat transfer
Negligible crystallization effects from T above Tg
Constant Properties, ρ, ε, c

$$\rho Vc\frac{dT}{dt} = -\varepsilon A_{s,r}\sigma(T^4 - T_{sur}^4)$$

$$\frac{\varepsilon A_{s,r}\sigma}{\rho Vc}\int_0^t dt = -\int_{T_i}^{T}\frac{dT}{(T^4 - T_{sur}^4)}$$

$$t = -\frac{\rho Vc}{4\varepsilon A_{s,r}\sigma T_{sur}^3}\left(\ln\left|\frac{T_{sur}+T_i}{T_{sur}-T_i}\right| + \ln\left|\frac{T_{sur}-T}{T_{sur}+T}\right|\right)$$

T = temperature of fiber
t = time to reach T
V = volume of fiber
$A_{s,r}$ = surface area of fiber
ρ = density of PET (1.35 g/cm^3)
c = specific heat of PET (1300 J/(kg K))
T_i = initial temperature of fibers (room temp 293 K)
T_{sur} = Temperature of surroundings
ε = emissivity of radiating surface (~ 0.8)
σ = Stefan Boltzmann constsnt (5.67 x 10^{-8} W/(m^{2}K^4))

Equation for modeling draw down:

$$2(V/A) = r(DR) = \frac{r_0}{\sqrt{DR}} = \frac{r_0}{\sqrt{v_1/v_2}}$$

r(DR) = radius of fiber after draw
V = volume of fiber
$A_{s,r}$ = surface area of fiber
DR = draw ratio
v_1 = line speed of first roll
v_2 = line speed of second roll

Radius as a function of denier

$$r_0(dpf) = \sqrt{\frac{dpf}{2.83 \cdot 10^6 \rho}} = \sqrt{\frac{9000\dot{m}}{2.83 \cdot 10^6 \rho v_L}}$$

dpf = denier per filament

$\dot{m}$ = mass flow rate of single fiber in g/s

v_L= take up speed or line speed in m/s

ρ = density of PET (1.35 g/cm^3)

r_0 = fiber radius in cm

Radius as a function of Draw Ratio and position in the oven (Linear Dependence)

$$r(DR, \xi) = r_0 - (r_0 - r(DR))\xi$$

ξ = dimensionless length = x/L

x = coordinate position in the oven

L = length of oven = 26in.

Final modeling equation:

$$t(T, DR, \xi) = -\frac{\rho c r(DR, \xi)}{8\varepsilon\sigma T_{sur}^3}\left(\ln\left|\frac{T_{sur} + T_i}{T_{sur} - T_i}\right| + \ln\left|\frac{T_{sur} - T}{T_{sur} + T}\right|\right)$$

Compare to residence time assuming linear acceleration of fiber line speed:

$$\tau = \frac{260}{v_1 + v_2}$$

τ = residence time in sec

v_1 = line speed of first roll in ft/min

v_2 = line speed of second roll in ft/min

260 s ft/min = 60 s/min * 2 * L in * ft/12in

L = length of the oven (26 in)

Oven Temperature °C	Fiber Exit Temperature °C
80	67.3
100	83.0
125	102.7
150	122.9

C.4. Temperature lag between sample and surroundings in Differential Scanning Calorimetry (DSC)

Analysis follows the outline by Isayev et al. (2006)[‡] of the work of Eder and Janeschitz-Kriegel (1993)[§].

Temperature lag corrections are required if the Nusselt number is less than one.

$$Nu = \frac{hL}{k_{th}}$$

Where h is the heat transfer coefficient between the pan and furnace; L is the thickness of the sample; and k_{th} is the thermal conductivity of sample.

To find h:

> Plot the ln(dq/dt) versus T_f in a heating run of a standard indium sample.
> The slope of the line will give $-hA/(m_iC_i+m_aC_a)T^*_f$

q = heat flow W/g
t = time, sec
T_f = temperature of the furnace
A = surface area of the pan
m_i = mass of indium
C_i = specific heat of indium = 234.3 J/kg K
m_a = mass of aluminum pan
C_a = specific heat of aluminum pan = 898.7 J/kg K
T^*_f = heating rate

k_{th} of PET = 0.19 W/m K
k_{th} of montmorillonite ~ 2.9 W/m K

$k_{parrallel} = x_{PET}k_{PET}+(1-x_{PET})k_{MMT}$
$k_{series} = ((x_{PET}/k_{PET}) + ((1-x_{PET})/k_{MMT}))$^-1

Material	Nu (Parallel aggregate)	Nu (Series aggregate)
Pure PET	0.332353	
1 wt% 20A	0.289985	0.329243
5 wt% 20A	0.187714	0.3168

Correction is needed at a cooling rate of 20 C/min.
Other cooling rates are required for meaning full interpretation of differences in temperature lag

[‡] Isayev et al. J. App. Polym. Sci. 102, 2847-2855 (2006)
[§] Wu et al. Colloid Polym. Sci. 271, 1116 (1993)

APPENDIX D. RAMAN SPECTROSCOPY.

D.1 Raman Spectroscopy for Determination of Molecular Orientation Distributions of Semi-crystalline Nanoparticle-Filled Polymers.

There are many methods to determine molecular orientation in a biaxially or uniaxially deformed polymer sample. In terms of broad classes of methods, birefringence, wide angle x-ray diffraction, small angle x-ray diffraction, and polarized laser and infrared light scattering are the more common methods to quantitatively assess molecular orientation. Qualitative methods such as electron microscopy and thermal shrinkage tests are capable of giving the general idea of the degree of molecular orientation but lack in any quantitative significance. Thus, in order to obtain meaningful molecular orientation data, x-ray or light scattering methods are required.

Considering the system at hand (a nanoparticle filled semi-crystalline polymer fiber), one can immediately begin to limit the options for assessing molecular orientation. For example, birefringence methods give too much of the system average and no clear solution can be given to treat the form birefringent effects of the inorganic-filler phase. Small angle x-ray scattering requires the use of a synchrotron radiation source available at national facilities, and may be an overstatement when compared to the remaining methods. Wide angle x-ray diffraction (WAXD) gives information pertaining to the crystalline orientation in the fiber, but not on the amorphous phase. Infrared dichroism requires samples to be highly transparent and very thin to limit reflectance of the incident beam and maximize absorbance. Complications from this methods can arise do to variataions on sample geometry that may have effects on extinction coefficients and

beam reflection. In addition, IR dichroism gives only the second moment of molecular orientation.

On the other hand, polarized Raman spectroscopy yields both the second and fourth moments of the molecular orientation distribution, is relatively quick in experiment time and is nondestructive to the sample. Like IR methods, Raman gives information on molecular bond structures and can test for new bond formation of the polymer chains to the nanoparticle surfaces. Raman methods give information about both the crystalline and amorphous orientation of the polymer phases and the composition and alignment of the inorganic particle. The Raman scattering intensity is linearly related to the number of chemical bonds in a sample and quantitative analysis is much easier than IR dichroism.

Yet, polarized Raman scattering has its drawbacks. The efficiency of Raman scattering is very low, in which the scattered light intensity is typically $10^{-8} – 10^{-6}$ of that of the incident beam and 10^{-3} of the elastic Rayleigh scattering [Bower and Maddams, 1989]. Secondly, the polymers fluoresce at these light intensities and require Fourier transform methods to resolve the time scales for scattering, in which for Raman and fluorescent scattering the scale are on the order of picoseconds and nanoseconds respectively. The optical discontinuity at the interface of the sample and its environment can cause scrambling of the polarized light, but can be corrected if the sample is submerged in a medium of equal refractive index. The equations to solve for the moments of distribution are coupled and non-linear, but algebraic and quadratic, and require very good initial guesses for the parameters. There are four roots to the five

equations for samples of cylindrical symmetry (fibers) and each solution must be examined for acceptability.

The acceptability criterion are based on the physical interpretations of the solid angle, θ, that the molecular makes with the principal axis of deformation and the definition of the second on fourth Legendre polynomials or as they have been referred to thus far, the orientation distribution functions. These functions are of the form:

$$P_2 = \langle P_2(\cos\theta)\rangle = \frac{\langle 3\cos^2\theta - 1\rangle}{2} \qquad \ldots(1)$$

$$P_4 = \langle P_4(\cos\theta)\rangle = \frac{\langle 35\cos^4\theta - 30\cos^2\theta + 3\rangle}{8} \qquad \ldots(2)$$

In which, P_2 and P_4 are the second and fourth moments of the molecular orientation distribution functions and are defined by the solid angle cosines. Three sets of data points (P_2, P_4) describe the extremes of molecular orientation. First, at (0, 0) the molecular orientation is random or molecular orientation does not exist. Second, at (1,1) the molecules are perfectly oriented along the axis of deformation (fiber axis). Finally, at (-1/2, 3/8) there is perfect molecular orientation perpendicular to the axis of deformation. Therefore from these points, the following acceptability criteria are made [Tanaka and Young 2006].

$$-1/2 \le P_2 \le 1 \qquad \ldots(3)$$

$$-3/7 \le P_4 \le 1 \qquad \ldots(4)$$

$$\frac{35P_2^2 - 10P_2 - 7}{18} \le P_4 \le \frac{5P_2 + 7}{12} \qquad \ldots(5)$$

Stated briefly above, a comment was made that there were five equations and five unknowns for a sample with cylindrical or fiber-like symmetry. The theoretical development of these equations began with Bower, Purvis, and Ward [Purvis et al., 1972] and was later summarized by Citra [Citra et al., 1995] and reviewed by Tanaka and Young [2006]. For purposes of brevity, the complete theory is not reviewed here and the five non-linear equations are summarized below.

$$I_{33} = I_0 \sum \alpha_{33}^2 = f_1(k, a_1, a_2, P_2, P_4) \qquad \ldots(6)$$

$$I_{11} = I_0 \sum \alpha_{11}^2 = f_2(k, a_1, a_2, P_2, P_4) \qquad \ldots(7)$$

$$I_{31} = I_0 \sum \alpha_{31}^2 = f_3(k, a_1, a_2, P_2, P_4) \qquad \ldots(8)$$

$$I_{21} = I_0 \sum \alpha_{21}^2 = f_4(k, a_1, a_2, P_2, P_4) \qquad \ldots(9)$$

$$I_{31}(45) \approx I_0 \sum \alpha_{22}\alpha_{33} = f_5(k, a_1, a_2, P_2, P_4) \qquad \ldots(10)$$

In which the variables are defined as follows: I_{ij} is the intensity of a reflection with the polarizer aligned in the *i*-axis and analyzer aligned in the *j*-axis, I_0 is the incident intensity and is better summarized in the *k* term, $k = I_0 N_0 \alpha_3^2$. Here N_0 is the number of scattering units, and α_1, α_2, and α_3 are the principal components of the Raman tensor and are combined into ratios to give the terms $a_1(=\alpha_1/\alpha_3)$ and $a_2(=\alpha_2/\alpha_3)$. Due to the symmetry

argument, $I_{21}=I_{12}$ and $I_{13}=I_{31}=I_{32}=I_{23}$. Lastly, the $I_{31}(45)$ is an intensity relation in which the fiber is at a 45° angle to the 3-axis or Z-axis. Figure 1 shows the five geometric representations to obtain the intensities to solve equations 6-10 (A, B, C, E, and G) plus two more as checks (D and F).

As shown in Figure D1 and stated in the previous paragraph, there are seven polarizer/analyzer/fiber arrangements that are needed to accurately determine P_2 and P_4. To begin, Figure D1A shows that the laser light becomes polarized in the z-axis (or 3-axis), then the light hits the sample and scatters in all directions, the analyzer filters out all scattered radiation except for that polarized in the z-axis. The recorded intensity for figure 1A is then the I_{33}. Similarly, Figure D1B gives I_{31}, but Figure D1D gives I_{13}. Therefore, because of the symmetry rule applied here, I_{11} (Figure 1C) is corrected by:

$$I_{11}^{corr} = \frac{I_{31}I_{11}}{I_{13}} \qquad \ldots(11)$$

Such a correction should be made to check for depolarization and to correct for any variance in incident intensity on the sample by changing polarization directions. Additionally, the right angle scattering geometries (Figure D1 E and F) need to be corrected to remove any sample effects, e.g. reflections. Figure D1E gives I_{32} and Figure D1F gives I_{12}.

$$I_{21}^{corr} = \frac{I_{31}I_{21}}{I_{32}} \qquad \ldots(12)$$

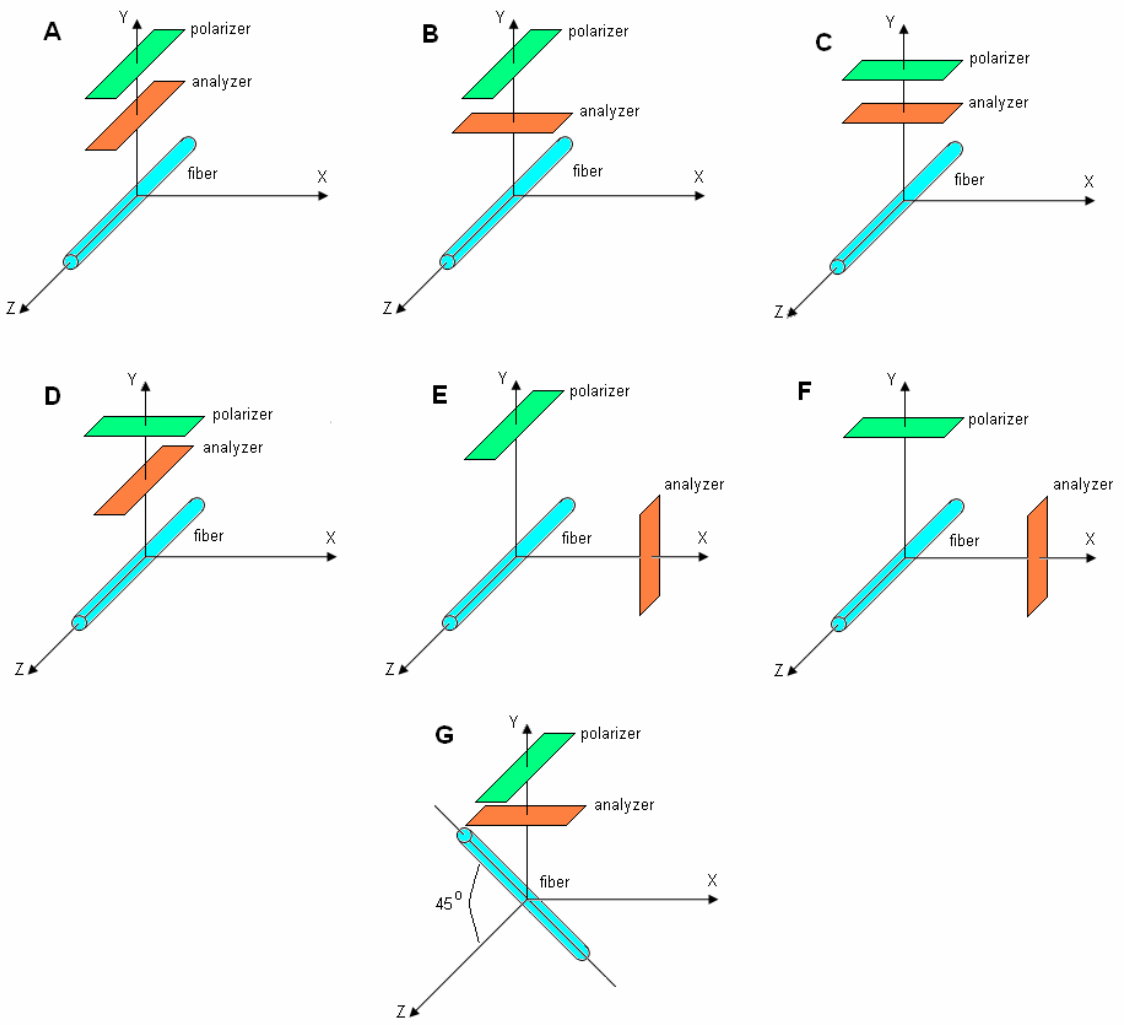

Figure D1. The seven polarizer/analyzer/fiber arrangements to obtain the Raman intensities to calculate the second and fourth molecular orientation distribution functions. See text for a description of the diagrams. The incident light beam is always directed along the –Y axis (Natarajan and Michielsen 1999)

The above procedure has been proven to provide the molecular orientation parameters and coefficients required to estimate the most probable distribution of oriented chains N(θ). However, by making some simplifying assumptions, N(θ) can be determined directly by taking spectra at specified angles using only backscattering arrangements of the sample and polarized light. The most significant assumption is that the Raman tensor is symmetric with its principal axis aligned with the axis of the filament, such that there is no tilt of the ellipsoid and any rotation of the filament about its principal axis produces an equivalent spectrum. This is more clearly illustrated in Figure D2. The Raman tensor is the differential polarizability of a molecular bond, $\left(\frac{\partial \alpha}{\partial q_k}\right)_{q_k} = 0$. This assumption is not very much different from those made by the authors above, who in each case have made an assumption as to the form of the Raman tensor. Although taking 20 spectra over 10° increments is more time consuming and coarse in the determination of N(θ), results do agree with those that have looked at PET orientation at various draw ratios, shown in table D1.

Table D1. Orientation averages for some uniaxially oriented PET samples from Bower, 1997

Sample Draw Ratio	P_2	P_4
1.87	0.16	0.04
2.19	0.14	0.08
3.16	0.41	0.35

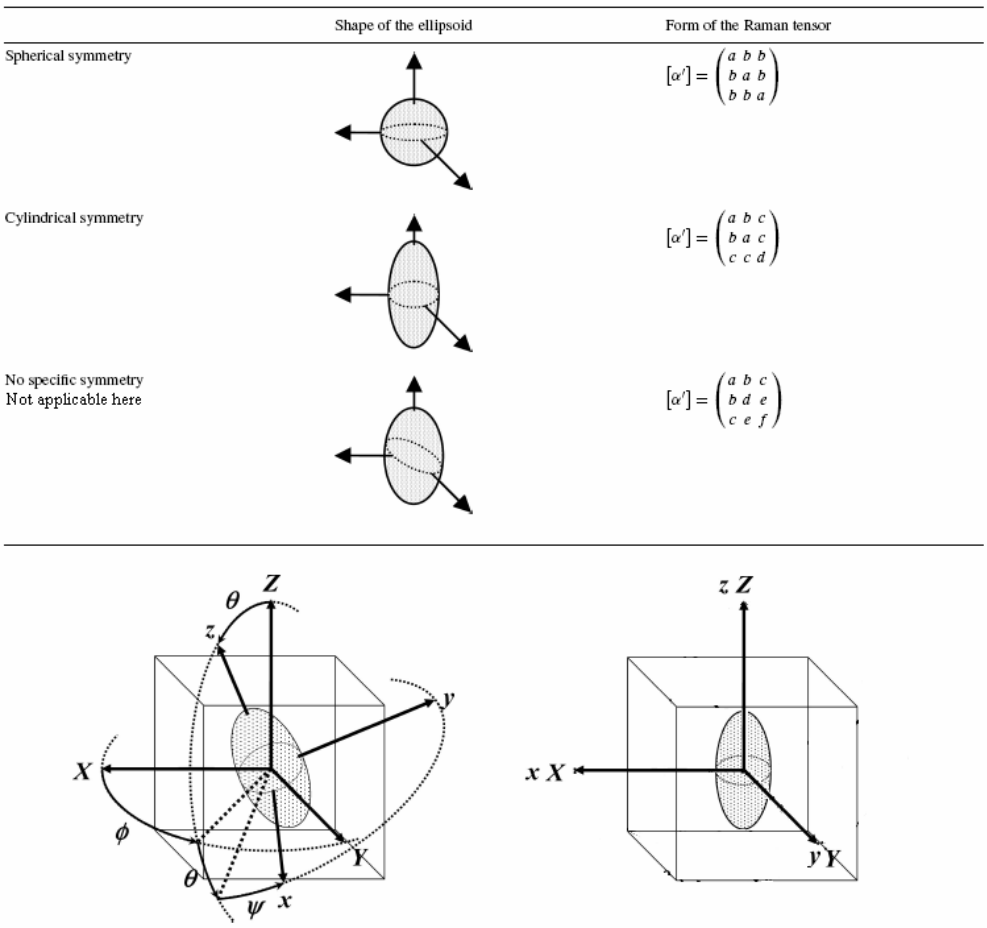

Figure D2 Form of the Raman tensor for various symmetries and the depiction of the tilted angles (θ, ψ, ϕ) of the Raman ellipsoid (sample (z,y,x)) with the fiber axis (Z,Y,X) and the assumption that the sample and fiber axis are coincidental.

The method used to determine P_2 and P_4 from N(θ):

First, spectra were taken every 10° (90-180 and 90-0, where 90 is the arrangement of the filament parallel to the orientation of the incident light vector) from a filament glued across the opening in a steel washer, mounted on a rotating stage and placed in the pathway of the laser beam. The intensities were recorded as a function of the angle to determine N(θ).

Then, N(θ) is normalized such that:

$$\frac{1}{2\pi} = \int_0^{\pi} N(\theta)\sin\theta d\theta$$

Next, the molecular orientation coefficients P_2 and P_4 are determined by the relationships given by Tanaka and Young (2004), which are

$$P_2 = \frac{1}{2}\left[3\left\langle\cos^2\theta\right\rangle - 1\right]$$

$$P_4 = \frac{1}{8}\left[35\left\langle\cos^4\theta\right\rangle - 30\left\langle\cos^2\theta\right\rangle + 3\right]$$

where

$$\left\langle\cos^l\theta\right\rangle = \frac{\int_0^{\pi} N(\theta)\cos^l\theta\sin\theta d\theta}{\int_0^{\pi} N(\theta)\sin\theta d\theta}$$

Although P_4 can be calculated by this method, due to the assumption that the sample chains and fiber axis are coincidental the reliability of these values is more questionable than the P_2 values due to compounding errors during calculation. Therefore the P_4 values serve mainly as a check for validity of the solution by testing them against criteria outlined by Bower and reviewed by Tanaka and Young (2004).

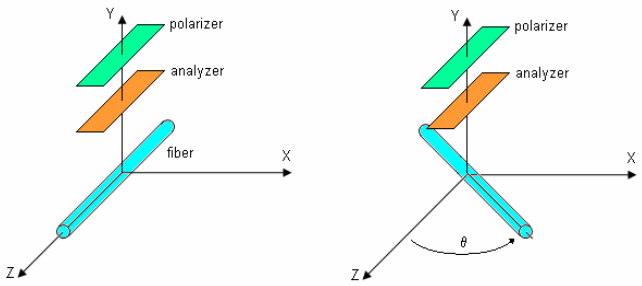

Now, the question remains as to which Raman intensity should be chosen for molecular orientation. The applied energy causes vibrations to occur in the molecules and different parts of the molecules jiggle, vibrate, and/or stretch. More scientifically speaking, when the incident light encounters a molecule, the electric field induces a dipole moment in the molecule due to its polarizability. For poly(ethylene terephthalate), the phenyl ring begins to vibrate in the 1400-1700 cm^{-1} range. In particularly, at 1614 cm^{-1} the symmetric stretch of the C-C bond of the phenyl ring occurs in both the amorphous and crystalline state. This 1614 cm^{-1} peak is the typical peak used for molecular orientation of PET in both fibers and films as it is insensitive to crystallization [e.g. see Lesko et al., 2000].

There are other peaks for PET other than 1614 cm^{-1} that could be used for molecular orientation or the assessment of crystallinity, but these peaks pertain to the vibrations of the ethylene glycol groups. At 998 cm^{-1} there is a mixed mode –C-C- stretch of the ethylene glycol unit and the -O-CH_2- stretch of the ester linkage. The intensity at 998 cm^{-1} increases with the addition of *trans* conformers. The *trans* conformation of the ethylene glycol unit is associated with higher crystallinity, as this conformation is where the chain is more greatly extended. The opposite conformation is *gauche* and disrupts the extended chain morphology and contributes to the amorphous phase composition. In terms of other crystallinity indicators, the intensity peak at 1175 cm^{-1} shifts to 1182 cm^{-1} on an increase in crystal content. Natarajan and Michielsen [1999] correlated peak intensities at 998 cm^{-1} and 1616 cm^{-1} with a reference peak at 702 cm^{-1} to birefringence data. The authors also found that the peaks at 998 and full width at half maximum at 1725 cm^{-1} correlated well with density measurements. However,

choosing peaks to examine for molecular orientation becomes difficult if the peaks are convoluted with other peaks, such that vibrational frequencies of different stretching groups occur near simultaneously to give either broader peaks or peaks with shoulders. Then the data must be de-convoluted, typically using a Gaussian-Lorentz sum function [Meier, 2005]. Such is the case when peaks are not obvious.

Adding a second component of significantly different chemistry and more importantly symmetry to the polymer at hand could possibly lead to peak convolution. For example if we fill a PET melt with inorganic nanoparticles, then would any peak convolution occur. A filler like a layered-silicate has typical vibration frequencies in either the very low (50-1200 cm^{-1}) or very high (2000-3500 cm^{-1}) range [Frost and Rintoul, 1996; Huang et al., 1999]. The low ranges are due to the metal cations and silicate tetrahedral, while the high ranges are due to stretching of the hydroxyl groups. As an example, for montmorillonites the distinguishable (un-convoluted) peaks are the 210 cm^{-1} stretch of the interlayer octahedron (MO_6, where M is a metal element such as Fe, Mg, Mn,.. etc), the 710 cm^{-1} stretch associated with the silicate outer-layer tetrahedral (SiO_4) and sheet-like stretch of the Si_2O_5 group, and the 3200 cm^{-1} stretch associated with the bound hydroxyl groups.

Therefore, for the case of PET filled with an organically modified montmorillonite, the Raman intensities of the two constituents should not overlap and allow the facile calculation of molecular orientation of the PET chain and the particle orientation of the filler. In which the peaks used to assess molecular orientation and particle orientation are the 1614 cm^{-1} of PET and the 710 cm^{-1} for the particle

respectively. However, the caveat is that the organic modifier can not contain a phenyl group or benzene type ring structure.

References:

Bower, D.I. and Maddams, W.F. *The Vibrational Spectroscopy of Polymers.* Cambridge University Press; Cambridge: 1989.

Bower, D.I. Infrared dischroism, polarized fluorescence, and Raman spectroscopy. In *Structure and Properties of Oriented Polymers 2nd ed.* Edited by I.M. Ward, Chapman and Hall, London; 1997.

Citra, M.J.; Chase, D.B.; Ikeda, R.M.; Gardner, K.H. Molecular Orientation of High Density Polyethylene Fibers Characterized by Polarized Raman Spectroscopy. *Macromolecules*, **28**, (1995) 4007-4012.

Frost, R.L. and Rintoul, L. Lattice vibrations of montmorillonite: an FT Raman and X-ray diffraction study. *Appl. Clay Sci.* **11**, (1996) 171-183.

Huang, Y.; Jiang, Z.; Schwieger, W. Vibrational Spectroscopic Studies of Layered Silicates. *Chem. Mater.* **11** (1999) 1120-1217.

Lesko, C.C.C.; Rabolt, J.F.; Ikeda, R.M., Chase, B.; Kennedy, A. Experimental determination of the fiber orientation parameters and Raman tensor of the 1614 cm^{-1} band of poly(ethylene terephthalate). *J. Molec. Structure* **521** (2000) 127-136.

Meier, R.J. On the art and science in curve-fitting vibrational spectra. *Vibrational Spectr.* **39** (2005) 266-269.

Natarajan, S. and Michielsen, S. Determination of Density and Birefringence of Poly(ethylene terephthalate) Fibers Using Raman Microscopy. *J. Appl. Poly. Sci.* **73** (1999) 943-952.

Purvis, J.; Bower, D.I.; Ward, I.M. Molecular Orientation in PET studied by polarized Raman scattering. *Polymer* **14** (1973) 398-400.

Tanaka, M. and Young, R.J. Review: Polarised Raman Spectroscopy for the study of molecular orientation distributions in polymers. *J. Mater. Sci.* **41** (2006) 963-991.

D.2 FORTRAN77 Code**.**

Code to solve the system of 5 non-linear algebraic equations (equations 6-10 in the review)

```
C     ------------------------------------------------------------------
C
C     Orientation_by_Raman.f     FORTRAN77
C
C     ------------------------------------------------------------------
C      IMSL SUBROUTINE NEQNF ("Solve a system of non-linear eqns using
C       modified Powell hybrid alogorithm and a finite-diffrence approx
C       to the Jacobian.")
C      Declare variables
       INTEGER ITMAX, N
       REAL ERRREL
C      PARAMETER N - the number of equations and hence the number
C       of unknown variables to solve.
       PARAMETER (N=5)
C
       INTEGER K, NOUT
       REAL FNORM, X(N), XGUESS(N)
       EXTERNAL FCN, NEQNF, UMACH
C      Set values of initial guess should be 5 guesses
C      ***NOTE THE EQNS BELOW ARE QUADRATIC IN X(2) AND X(3) SUCH THAT
C         THERE ARE FOUR TO THE SET OF FIVE EQNS.  GUESSES SHOULD BE
C         MADE SUCH THAT ALL FOUR ROOTS ARE OBTAINED. THEN THE ACCEPT-
C         ABILITY CRITERION SHOULD BE APPLIED*** SEE CITRA ET AL. 1995
C      XGUESS = ( 1.0 0.5 0.5 0.5 0.5 )
C
       DATA XGUESS/1.0, 0.5, -0.5, 0.5, 0.5/
C
       ERRREL = 0.0001
       ITMAX = 100
C
       CALL UMACH (2, NOUT)
C      Find the solution
       CALL NEQNF (FCN, ERRREL, N, ITMAX, XGUESS, X, FNORM)
C      Output
       WRITE (NOUT,99999) (X(K),K=1,N), FNORM
99999  FORMAT (' The solution to the system is', /, ' X = (', 5F10.5,
     & ')', /, ' with FNORM =', F5.4, //)
       END
C      User-defined subroutine
       SUBROUTINE FCN (X, F, N)
       INTEGER N
       REAL X(N), F(N)
C
C      These are the five equations to be solved by the subroutine
C        The only variables that may change are the intensities Iij
C        which are taken from the Raman spectra peak intensities for
C        a given vibrational energy
C      According to Citra et al. [Macromolecules (1995) v.28 p.4007]
C        For cylindrical symmetry:
C        F(1) - Io SUM(alpha22)^2
C        F(2) - Io SUM(alpha33)^2
C        F(3) - Io SUM(alpha21)^2
C        F(4) - Io SUM(alpha23)^2
C        F(5) - Io SUM(alpha22*alpha33)
C             where alphaij are the components of the Raman tensor
```

```
C        X(1) = b = Io*No*alpha3^2
C        X(2) = a1 = alpha1/alpha3
C        X(3) = a2 = alpha2/alpha3
C        X(4) = P2 = second moment of the orientation distribution
C        X(5) = P4 = fourth moment of the orientation distribution
C
        REAL ISUM_A22A22, ISUM_A33A33, ISUM_A21A21, ISUM_A23A23,
     & ISUM_A22A33
C       ENTER ISUM_AijAij DATA
        ISUM_A33A33 = 1.0
        ISUM_A22A22 =
        ISUM_A21A21 =
        ISUM_A23A23 =
        ISUM_A22A33 =
C       THE EQUATIONS SIMPLIFIED BY CITRA ET AL. 1995
        F(1) = X(1)*(((3.0*X(2)**2.0+3.0*X(3)**2.0+3.0+2.0*X(2)*X(3)+
     & 2.0*X(2)+2.0*X(3))/15.0)+X(4)*((3.0*X(2)**2.0+3.0*X(3)**2.0-
     & 6.0+2.0*X(2)*X(3)-X(2)-X(3))/21.0)+3.0*X(5)*((3.0*X(2)**2.0+3.0*
     & X(3)**2.0+8.0+2.0*X(2)*X(3)-8.0*X(2)-8.0*X(3))/280.0))-
     & ISUM_A22A22
C
        F(2) = X(1)*(((3.0*X(2)**2.0+3.0*X(3)**2.0+3.0+2.0*X(2)*X(3)+
     & 2.0*X(2)+2.0*X(3))/15.0)-2.0*X(4)*((3.0*X(2)**2.0+3.0*X(3)**2.0-
     & 6.0+2.0*X(2)*X(3)-X(2)-X(3))/21.0)+X(5)*((3.0*X(2)**2.0+3.0*
     & X(3)**2.0+8.0+2.0*X(2)*X(3)-8.0*X(2)-8.0*X(3))/35.0))-
     & ISUM_A33A33
C
        F(3) = X(1)*(((X(2)**2.0+X(3)**2.0+1.0-X(2)*X(3)-X(2)-
     & X(3))/15.0)+X(4)*((X(2)**2.0+X(3)**2.0-2.0-4.0*X(2)*X(3)+
     &  2.0*X(2)+2.0*X(3))/21.0)+X(5)*((3.0*X(2)**2.0+3.0*X(3)**2.0+8.0+
     & 2.0*X(2)*X(3)-8.0*X(2)-8.0*X(3))/280.0))-ISUM_A21A21
C
        F(4) = X(1)*(((X(2)*X(2)+X(3)*X(3)+1.0-X(2)*X(3)-X(2)-
     & X(3))/15.0)-X(4)*((X(2)*X(2)+X(3)*X(3)-2.0-4.0*X(2)*X(3)+
     & 2.0*X(2)+2.0*X(3))/42.0)-X(5)*((3.0*X(2)**2.0+3.0*X(3)**2.0+8.0+
     & 2.0*X(2)*X(3)-8.0*X(2)-8.0*X(3))/70.0))-ISUM_A23A23
C
        F(5) = X(1)*(((X(2)**2.0+X(3)**2.0+1.0+4.0*X(2)*X(3)+4.0*X(2)+
     &  4.0*X(3))/15.0)-X(4)*((X(2)**2.0+X(3)**2.0-2.0+10.0*X(2)*X(3)-
     & 5.0*X(2)-5.0*X(3))/42.0)-X(5)*((3.0*X(2)**2.0+3.0*X(3)**2.0+8.0+
     & 2.0*X(2)*X(3)-8.0*X(2)-8.0*X(3))/70.0))-ISUM_A22A33
        RETURN
        END
```

D.3 Raman Data

Pure PET – As-spun					
Wavenumber cm^{-1}	Angle °	Intensity a.u.	Wavenumber cm^{-1}	Angle °	Intensity a.u.
1616.26	80	5766.8	998.1	0	86.3
1615.22	70	5674.7	999.3	10	97.5
1615.22	60	5647.0	999.3	20	93.4
1615.22	50	5758.3	1000.4	30	87.4
1615.22	40	6803.5	999.3	40	93.5
1615.22	30	6803.5	999.3	50	98.5
1615.22	20	7217.5	999.3	60	88.8
1615.22	10	7333.0	998.2	70	82.1
1615.22	0	7479.6	999.3	80	94.6
1616.26	-10	7455.6	998.2	90	100.7
1616.26	-20	6665.0			
1615.22	-30	6688.3			
1615.22	-40	6173.7			
1615.22	-50	6134.4			
1615.22	-60	5764.8			
1615.22	-70	5793.6			
1616.26	-80	5350.5			
1616.26	-90	5803.4			
1616.26	-100	5423.4			

Pure PET – Drawn					
Wavenumber cm^{-1}	Angle °	Intensity a.u.	Wavenumber cm^{-1}	Angle °	Intensity a.u.
1613.54	80	1925.6	999.282	0	645
1613.54	70	2413.1	999.282	10	708
1613.54	60	3194.9	1000.42	20	653
1613.54	50	4095.5	998.146	30	540
1613.54	40	5295.4	998.146	40	440
1613.54	30	6455.3	999.282	50	323
1613.54	20	8371.0	998.146	60	257
1614.58	10	10009.2	998.146	70	212
1614.58	0	10433.7	999.282	80	136
1614.58	10	10065.6	999.282	90	94
1614.58	20	9515.9			
1614.58	30	7837.5			
1614.58	40	7847.7			
1614.58	50	5642.5			
1614.58	60	4474.2			
1614.58	70	3583.9			
1614.58	80	2950.0			
1614.58	90	2170.3			
1615.62	80	2476.5			

0.5 wt% 20A – As-spun					
Wavenumber cm^{-1}	Angle °	Intensity a.u.	Wavenumber cm^{-1}	Angle °	Intensity a.u.
1615.21	0	13460.4	999.282	0	106.2
1615.21	0	14119.9	999.282	0	210.4
1615.21	45	12898.7	1000.42	45	22.4
1614.16	45	12038	999.282	45	129.1
1614.16	90	10319	999.282	90	34.1
1615.21	90	14109.8	998.146	90	107.1

0.5 wt% 20A – Drawn					
Wavenumber cm^{-1}	Angle °	Intensity a.u.	Wavenumber cm^{-1}	Angle °	Intensity a.u.
1614	-30	24643.4	998.146	-30	1383.4
1614	-20	28892	1000.42	-20	1775.93
1614	-10	32487.9	999.282	-10	1992.35
1614	0	34735.6	1001.55	0	2129.87
1614	0	33924.1	1000.42	0	2253.58
1614	10	34822.9	1001.55	10	2374.87
1614	20	34974.3	999.282	20	2287.36
1614	30	30306.1	999.282	30	1763.71
1614	40	25775	998.146	40	1393.34
1614	50	19828.9	999.282	50	1103.69
1614	60	14671.8	997.012	60	760.068
1614	70	11176.1	1000.42	70	474.397
1614	80	8304.6	1000.42	80	235.029
1614	90	7020.32	998.146	90	8.56738
1614	90	7153.64	999.282	100	323.338
1614	100	6937.96	1000.42	110	224.761
1614	110	8857.91	1000.42	120	299.256
1614	120	12262.9	1001.55	130	554.125
1614	130	15132.8	999.282	140	751.824
1614	140	20538.3	998.146	150	1046.32

1 wt% 20A – As-spun					
Wavenumber cm^{-1}	Angle °	Intensity a.u.	Wavenumber cm^{-1}	Angle °	Intensity a.u.
1615.21	0	14852.3	999.282	0	290.5
1615.21	0	13744.9	998.146	0	195.0
1615.21	45	15261.5	1000.42	45	158.7
1615.21	45	14090	999.282	45	209.2
1615.21	90	13424.9	998.146	90	175.5
1615.21	90	13842.5	999.282	90	-279.8

1 wt% 20A – Drawn					
Wavenumber cm^{-1}	Angle °	Intensity a.u.	Wavenumber cm^{-1}	Angle °	Intensity a.u.
1615.21	-30	6730.73	-30	1000.4	384.357
1615.21	-20	8120.46	-20	998.136	536.212
1615.21	-10	8325.25	-10	999.262	497.003
1615.21	0	9874.36	0	999.262	875.605
1615.21	0				
1615.21	10	9456.11	10	1000.4	608.609
1615.21	20	10746.1	20	999.262	833.387
1615.21	30	9155.09	30	999.262	659.838
1615.21	40	8138.4	40	998.136	550.155
1615.21	50	9434.52	50	1000.4	616.518
1615.21	60	8487.8	60	999.262	431.055
1615.21	70	6418.56	70	998.146	216.26
1615.21	80	4699.94	80	998.146	242.548
1615.21	90	3348.59	90	1000.42	112.723
1615.21	90	3709.92	90	1000.42	262.765
1615.21	100	3746.49	100	998.146	99.6118
1615.21	110	3654.2	110	998.146	155.21
1615.21	120	4169.74	120	999.262	340.995
1615.21	130	4931.37	130	1000.4	223.119
1615.21	140	5525.48	140	998.136	445.729

1.5 wt% 20A – As-spun					
Wavenumber cm^{-1}	Angle °	Intensity a.u.	Wavenumber cm^{-1}	Angle °	Intensity a.u.
1613.5	120	3688.0	999.3	0	123.5
1613.5	110	2812.0	998.2	10	115.7
1613.5	100	2384.9	999.3	20	92.25
1612.46	90	2084.7	999.3	30	183.52
1613.5	80	2658.9	1000.4	40	246.4
1613.5	70	3476.5	1000.4	50	233.4
1613.5	60	4672.9	999.3	60	215.74
1613.5	50	6098.9	1000.4	70	160.04
1613.5	40	8065.0	1000.4	80	134.52
1614.54	30	9596.3	998.2	90	101.78
1614.54	20	12146.3			
1614.54	10	12942.6			
1614.54	0	13391.0			
1614.54	-5	13573.4			
1614.54	-10	13270.6			
1614.54	-20	11222.7			
1614.54	-30	10279.3			
1614.54	-40	8425.8			
1614.54	-60	4606.5			

1.5 wt% 20A – Drawn					
Wavenumber cm^{-1}	Angle °	Intensity a.u.	Wavenumber cm^{-1}	Angle °	Intensity a.u.
1614.58	90	1844.0	998.146	0	613
1615.62	80	2245.3	1000.42	10	432
1614.58	70	2929.3	999.282	20	345
1614.58	60	3975.6	1001.55	30	234
1614.58	50	4649.4	1000.42	40	154
1615.62	40	5363.7	1001.55	50	119
1615.62	30	7387.9	999.282	60	96
1615.62	20	8849.0	999.282	70	69
1615.62	10	9459.7	998.146	80	202
1615.62	0	9656.3	999.282	90	73
1615.62	10	8761.0			
1615.62	20	7935.8			
1615.62	30	6411.9			
1615.62	40	5534.9			
1615.62	50	4286.9			
1615.62	60	3409.9			
1615.62	70	2641.6			
1615.62	80	2306.2			
1615.62	90	2438.1			

3 wt% 20A – As-spun					
Wavenumber cm^{-1}	Angle °	Intensity a.u.	Wavenumber cm^{-1}	Angle °	Intensity a.u.
1614	0	9464.8	998.146	0	227.1
1614	0	9978.12	1000.42	0	75.1
1614	45	10596.6	998.146	45	159.5
1614	45	7744.96	997.012	45	69.9
1614	90	7217.99	998.146	90	-119.6
1614	90	8234.73	998.146	90	-56.6

3 wt% 20A – Drawn					
Wavenumber cm^{-1}	Angle °	Intensity a.u.	Wavenumber cm^{-1}	Angle °	Intensity a.u.
1614	50	13895.6	1000.42	50	877.202
1614	60	9151.67	998.146	60	406.821
1614	70	7195.58	998.146	70	437.662
1614	80	6101.32	1000.42	80	175.846
1614	90	5045.58	1000.42	90	132.759
1614	90	4237.74	998.146	90	152.713
1614	80	3981.97	1000.42	80	98.8311
1614	70	4037.45	1000.42	70	152.873
1614	60	4951.48	999.282	60	336.245
1614	50	8006.43	1000.42	50	435.987
1614	40	9100.41	998.146	40	249.003
1614	30	11569.2	999.282	30	542.618
1614	20	13629	998.146	20	798.862
1614	10	14150	999.282	10	1209.82
1614	0	18111.6	1000.42	0	1184.05
1614	0	20503.3	1000.42	0	1273.42
1614	10	20541.3	998.146	10	1344.59
1614	20	21590	1000.42	20	1404.9
1614	30	20181.2	999.282	30	1224.1
1614	40	15667.3	999.282	40	1002.73

APPENDIX E. NANOCOMPOSITE FIBER MORPHOLOGY

E.1 XRD Data

As-Spun PET Nanocomposite relative to pure Cloiste 20A nanoclay. FFT filter applied to smooth raw data points

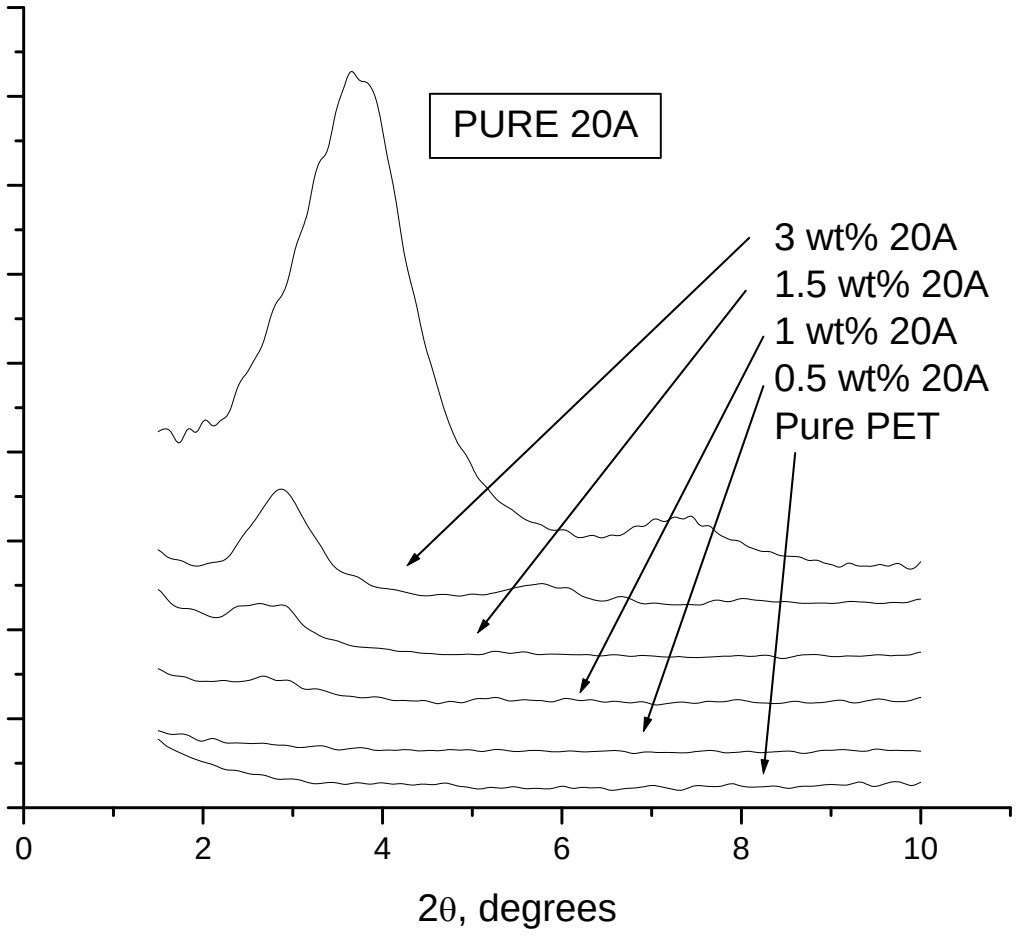

Drawn Fiber relative to pure Cloiste 20A nanoclay. FFT filter applied to smooth raw data points.

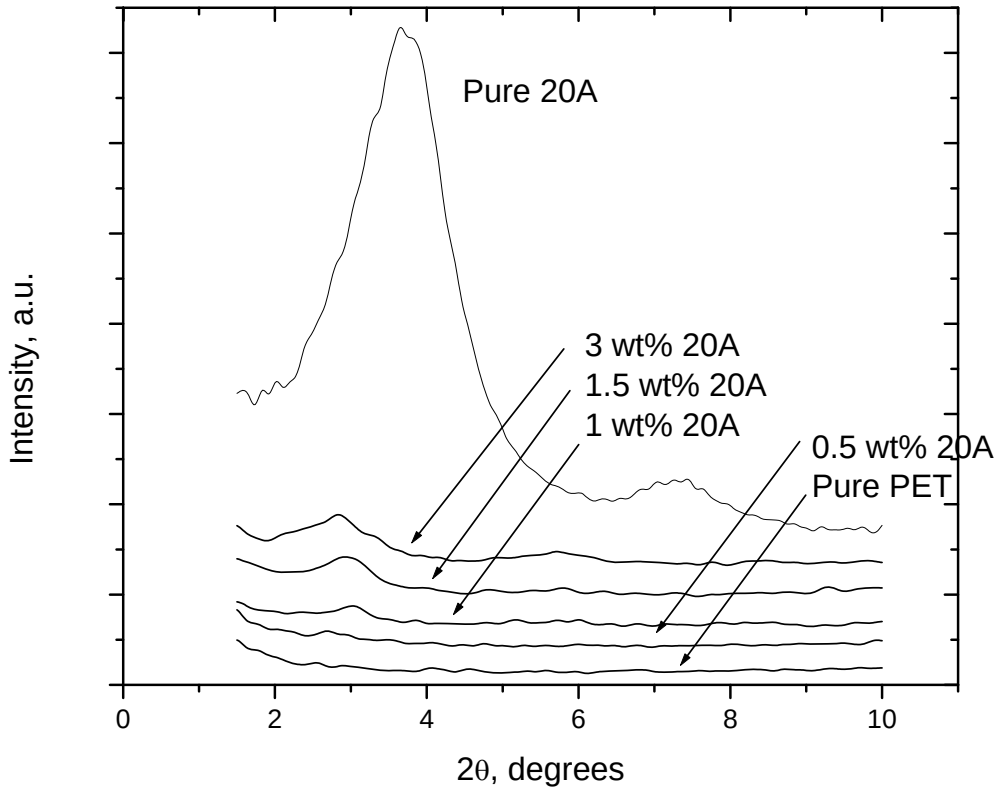

E.2 SEM images

E2-A images of fiber spun and drawn at Virginia Tech

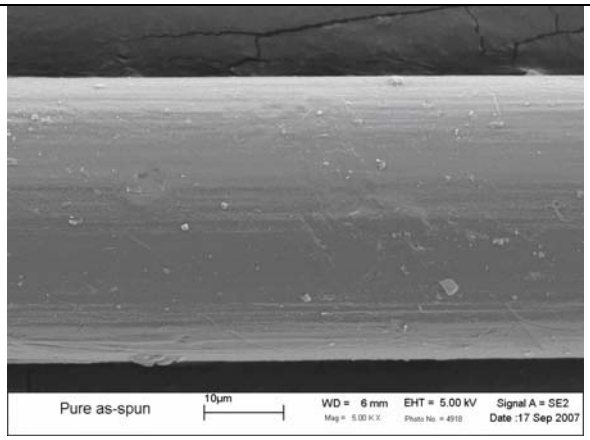

"Pure as-spun" – Unfilled PET fiber in its as-spun state obtained directly from the spin line. Fiber has not been attenuated further by a drawing process. White rectangular crystals are NaCl from the tap water used during aspiration.
Comments:
Overall, surface is smooth

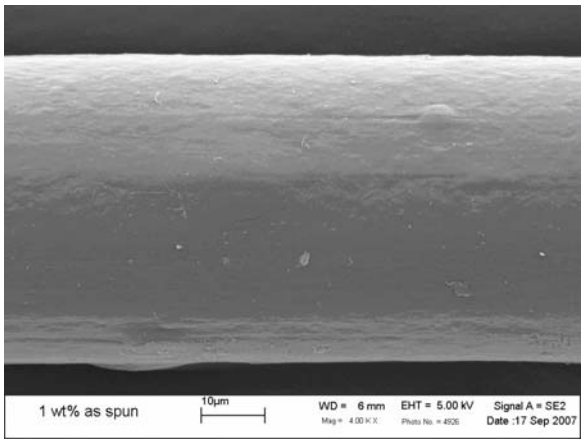

"1 wt% as-spun" – PET fiber filled with 1% by weight of Cloisite 20A organically modified montmorillonite. Fiber has not been attenuated further by a second step draw.
Comments:
Surface becoming abnormal. Note the bulge in the upper right hand corner, a possible agglomerate of nanoclay.

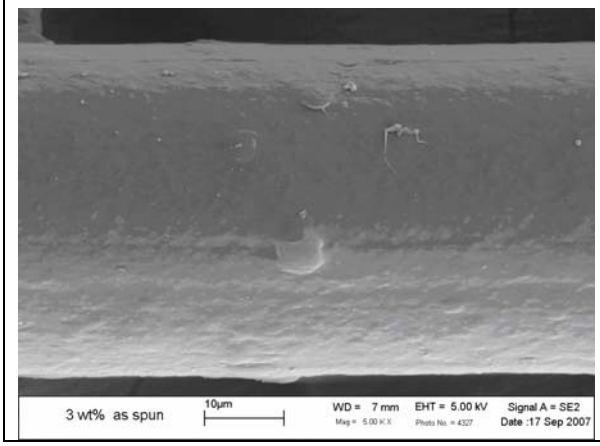

"3 wt% as-spun" – PET fiber filled with3% by weight of Cloisite 20A organically modified montmorillonite. Fiber has not been oriented in a second step draw.
Comments:
Surface is much "rougher" and abnormal that the standard pure sample and the population of bulges has increased, possibly larger agglomerates of nanoclay are present.

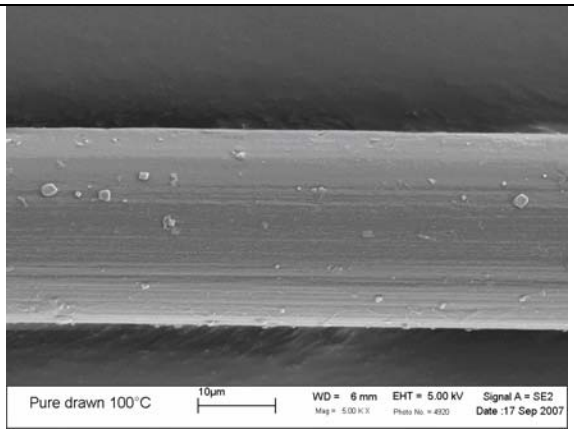

"Pure drawn 100°C" – Unfilled as-spun PET fiber drawn to its maximum extent (draw ratio, A_0/A, of 2.625) through a hot air oven at 100 °C. Temperature of filaments is roughly 85 °C at maximum as they pass through the oven. Again, white rectangular crystals are NaCl from aspiration process.
Comments:
Overall surface is "smooth"

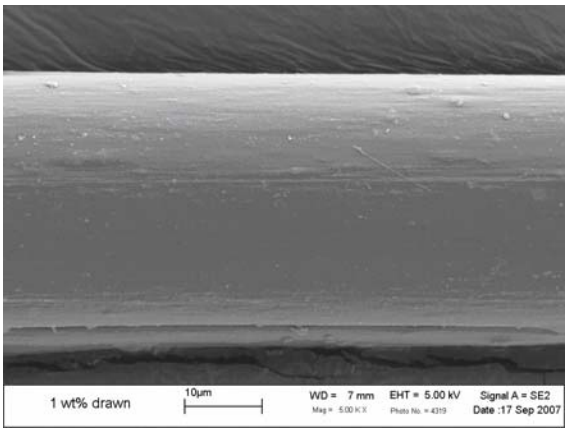

"1 wt% drawn" – The as-spun 1wt% Cloisite 20A / PET fiber drawn to its maximum extent (DR of 3.75) through a hot air oven at 100°C.
Comments:
Filament surface is smoother than expected, but we can see at this magnification some pock marks or the "bulges" signifying that agglomeration is still present.
But the size of the agglomerates is greatly reduced, upon comparing the bulge sizes of the as-spun and drawn fiber samples.

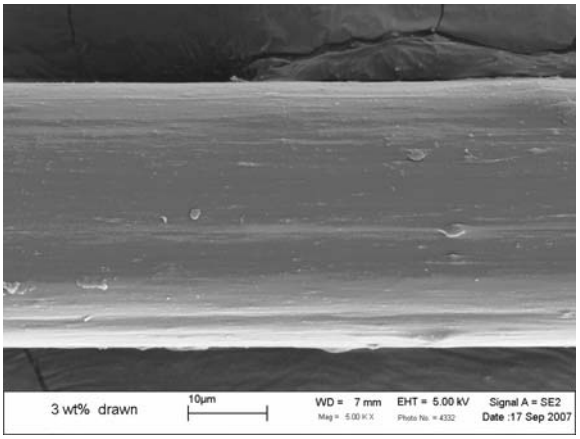

"3wt% drawn" – The as-spun 3 wt% Cloisite 20A / PET fiber drawn to its maximum extent (DR of 3.75) through a hot air oven at 100 °C.
Comments:
Compared to the drawn 1% and pure samples the surface is much more irregular, and the bulge sizes are larger signifying higher degree of agglomeration.

Abnormalities greater than the fiber diameter

For the nanoclay filled PET fibers, the presence of large "bulbs" several times the diameter of the filament were observed. Approximately and on average, two such bulbs were noted per foot of fiber, with no periodic regularity. Shown in figure 2 are SEM images of the irregularities at 1 and 3 wt%. The 3 wt% fiber is shown in both the as-spun and oriented state, in which the filaments passed through a hot air oven heating the fiber just above the glass transition.

Some points are of note in figure E2. In terms of processing, the fibers remain continuous (i.e. processing proceeded uninterrupted) and effective filament take-up was not affected by the bulbs. Upon drawing, the bulbs become more elongated, aiding in nanoclay dispersion and PET chain orientation. Additionally, nanoclay filled fiber mechanical properties in the drawn state are greater than the pure fibers, which do not possess the occurrence of similar anomalies. Traditional thinking prescribes irregular surfaces and fiber cross section with inferior tensile mechanical properties. Defects such as these are thought of as stress concentrators that cause premature failure upon deformation, which contradicts our observations. The last note pertains to the chemical make-up of the "bulbs." X-ray elemental analysis (see figure E3) reveals that these abnormalities are slightly richer in silicon and aluminum than the more uniform segments of the filament, which leads to the conclusion that these bulbs are indeed large agglomerates of nanoclay.

Unfortunately, light scattering measurements for molecular orientation of PET chains were inconclusive in determining if the PET phase is oriented or crystalline within these bulbs. Therefore, the conclusion that can be reached is that upon drawing in a

second step the large irregularities in fiber cross section referred to as “bulbs” become elongated and disperse the agglomerated nanoclay stacks. The fiber mechanical properties are thus improved despite the fact that the irregularities act as stress concentrators. So therefore, the processing aid effect of the nanoclay in PET fiber – leading to high molecular orientation of the PET phase – out weighs the negative effects of increased population of defect sites.

Figure E2. Scanning electron micrograph images of nanoclay filled PET filaments at two magnifications and nanoclay concentrations.

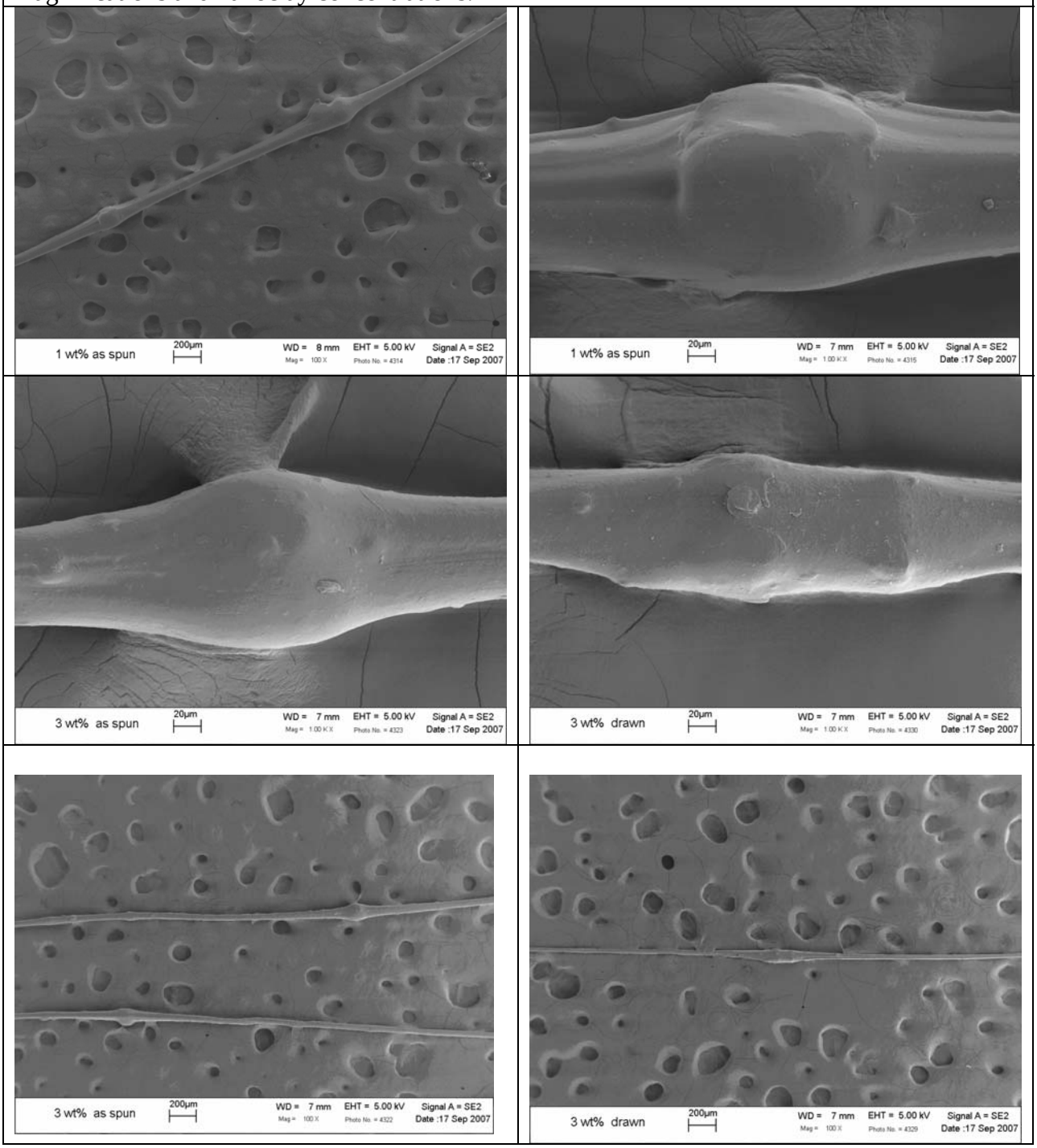

Figure E3. Elemental analysis of fiber cross section irregularities, “bulbs,” for 1 and 3wt% Cloisite 20A filled PET fibers.

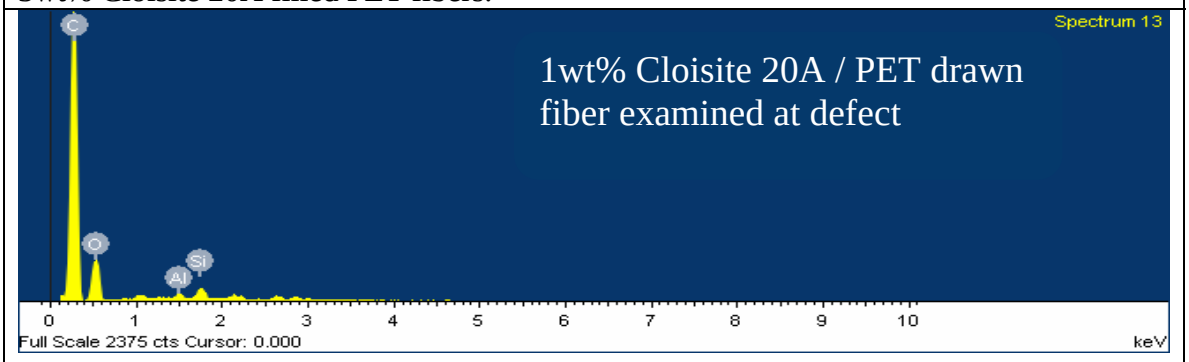

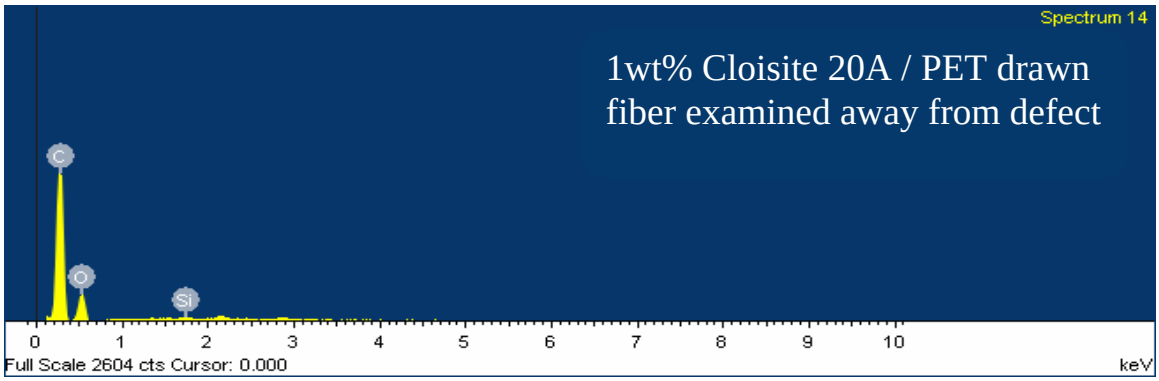

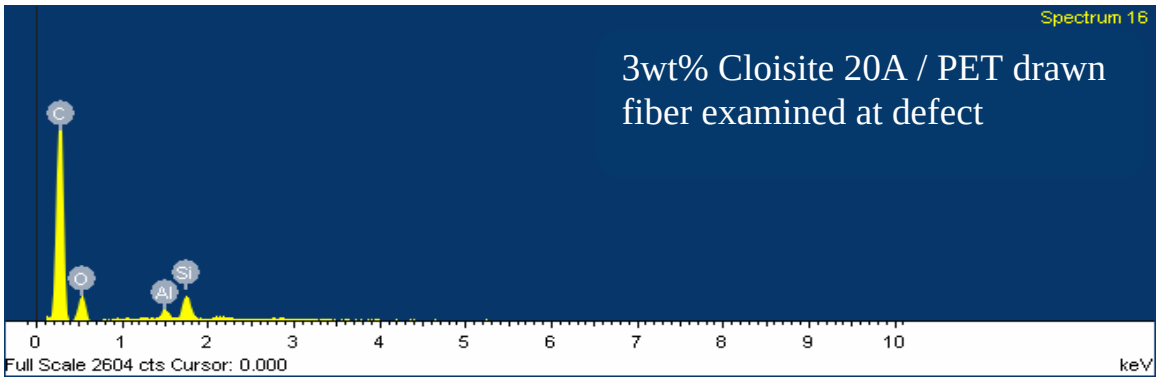

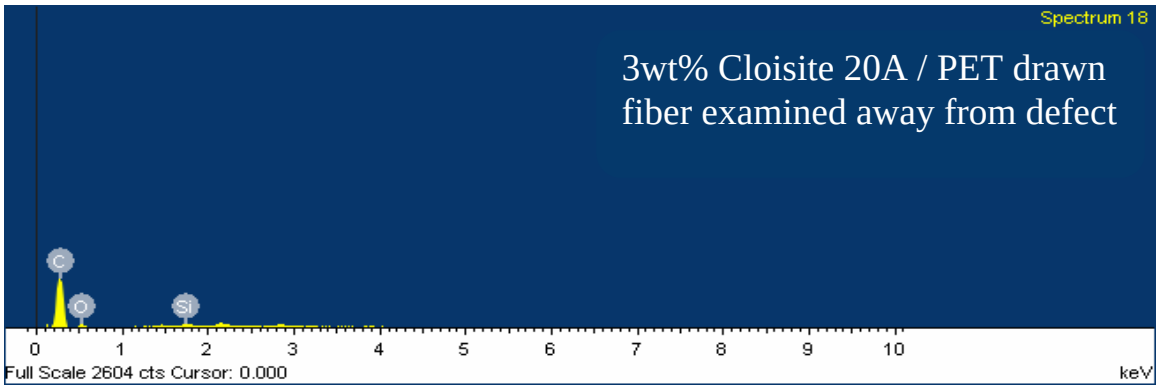

E2-B images of PET nanocomposite fiber drawn by Performance Fibers

The following 4 images were obtained from August Schneider at a Performance Fibers Inc site in Germany.

Performance Fibers scientists attempt to reproduce our results disclosed in this dissertation.

Note the splitting around the large agglomerates at higher drawing speeds. Drawing speeds and fiber mechanical properties are confidential.